UNIVERSITÀ DEGLI STUDI DI PADOVA
Dipartimento di Fisica e Astronomia Galileo Galilei

SCUOLA DI DOTTORATO DI RICERCA IN ASTRONOMIA
CICLO XXVIII

Interacting supernovae and supernova impostors

Direttore della scuola: Ch.mo Prof. Giampaolo Piotto
Supervisore: Dr. Andrea Pastorello

Dottorando: Leonardo Tartaglia

Abstract

Massive stars are thought to end their lives with spectacular explosions triggered by the gravitational collapse of their cores. Interacting supernovae are generally attributed to supernova explosions occurring in dense circumstellar media, generated through mass-loss which characterisie the late phases of the life of their progenitors. In the last two decades, several observational evidences revealed that mass-loss in massive stars may be related to violent eruptions involving their outer layers, such as the luminous blue variables. Giant eruptions of extragalactic luminous blue variables, similar to that observed in η Car in the 19th century, are usually labelled 'SN impostors', since they mimic the behaviour of genuine SNe, but are not the final act of the life of the progenitor stars. The mechanisms producing these outbursts are still not understood, although the increasing number of observed cases triggered the efforts of the astronomical community to find possible theoretical interpretations. More recently, a number of observational evidences suggested that also lower-mass stars can experience pre-supernova outbursts, hence becoming supernova impostors. Even more interestingly, there is growing evidence of a connection among massive stars, their outbursts and interacting supernovae. All of this inspired this research, which has been focused in particular on the characterisation of supernova impostors and the observational criteria that may allow us to safely discriminate them from interacting supernovae. Moreover, the discovery of peculiar transients, motivated us to explore the lowest range of stellar masses that may experience violent outbursts. Finally, the quest for the link among massive stars, their giant eruptions and interacting supernovae, led us to study the interacting supernova LSQ13zm, which possibly exploded a very short time after an LBV-like major outburst.

Sommario

Le stelle massive terminano la loro vita con spettacolari esplosioni innescate dal collasso gravitazionale del loro nucleo. Le supernove interagenti sono tipicamente associate a questo tipo di esplosioni in mezzi circumstellari densi, generati da episodi di perdita di massa durante le fasi finali dell'evoluzione dei loro progenitori. Negli ultimi due decenni, diverse evidenze osservative hanno rivelato come questi episodi siano spesso correlati ad eruzioni violente che coinvolgono gli strati esterni degli inviluppi di stelle massive, come le 'luminous blue variables'. In qualche caso questi eventi sono stati osservati come 'supernova impostors' (impostori), transienti che imitano il comportamento di supernove reali, ma non costituiscono l'atto finale della vita dei loro progenitori. Questi sono spesso associati alle eruzioni giganti di luminous blue variable extragalattiche. I meccanismi che innescano queste eruzioni non sono ancora del tutto compresi, nonostante il crescente numero di casi osservati abbia attirato l'attenzione della comunitá astronomica nel tentativo di trovare delle spiegazioni teoriche a questi fenomeni. Píu di recente, un certo di numero di evidenze osservative ha portato ad ipotizzare che anche stelle meno massive possano mostrare eruzioni giganti che imitano gli osservabili delle supernove interagenti. Tutto questo, unitamente alla possibile connessione recentemente proposta tra le stelle massive, le loro eruzioni giganti e alcune supernove interagenti, ha ispirato questo lavoro di ricerca, che si é focalizzato in particolare sulla caratterizzazione del fenomeno degli impostori e sui possibili criteri osservativi che permettono di distinguere con sicurezza le supernove interagenti dagli impostori. Inoltre, la scoperta di oggetti peculiari ci ha motivato nell'analisi dell'estremo inferiore dell'intervallo di masse interessate da episodi eruttivi violenti. La caccia al collegamento tra le stelle massive, le loro eruzioni giganti e le supernove interagenti, ha portato alla scoperta della supernova peculiare LSQ13zm, che potrebbe essere esplosa poco tempo dopo un'eruzione gigante simile a quelle osservate nelle luminous blue variables.

Contents

List of Tables

List of Figures

Chapter 1

Introduction

A supernova (SN) is a spectacular event occurring at the endpoint of the evolution of stars. It consists in the terminal catastrophic stellar explosion which, in some cases, may lead to the complete destruction of the progenitor stars or, in other cases, to the formation of a compact remnant. At maximum light, the total radiated energy may exceed that of an entire host galaxy (Figure 1.1), and the total energy output is comparable with that of a solar-like star over its entire lifetime. SNe owe their name to their much higher luminosity with respect to the classical Galactic *novae*, which also led Baade & Zwicky (1934) to consider '*supernovae*' those transient events with absolute magnitudes brighter than -14 mag. As a consequence, about 15 classical *novae* discovered in the period between 1885 and 1939, we re-classified as SNe, and systematic SN searches led to the discovery of thousands of new objects in the following years.

Despite the results of statistical studies on outer galaxies (Cappellaro et al. 1999) suggest a rate of $\sim 2-3$ events per century for the Milky Way, only a handful of Galactic SNe have been observed by naked eye during the past ~ 2 thousand years. Nonetheless, the detection of two other relatively young SN remnants (Reynolds et al. 2008), indicates that other events may have remained undetected by the human eye (e.g. due to strong Galactic extinction).

SNe play a crucial role in the chemical composition and evolution of galaxies, enriching the inter-stellar medium (ISM) of nucleosynthetised elements. Although a large fraction of stars end their life quietly (mostly lower-mass stars), internal instability may trigger catastrophic explosions and the ejection of a huge amount of high-velocity ($v \gtrsim 10^4$ km s^{-1}) material. The energy released during a SN explosion also plays a major role in the star formation, since the resulting shock waves may trigger the initial collapse of nearby molecular clouds. Most of this energy is released as neutrinos ($E_\nu \simeq 10^{53}$ erg) and other accelerated particles, which are the main source of high energy cosmic particles. For all these reasons, the study of SNe is a fundamental tool for our understanding of the stellar evolution theories, the physical mechanisms governing the final stellar evolutionary stages, the nucleosynthesis processes and the properties of the remnants. SNe also plays a key role in determining the physical, dynamical and chemical properties of galaxies, and are also a fundamental tool in constraining extragalactic distances (being, up to date, among the most precise distance indicators) as well as the star formation history in nearby galaxies.

In this Chapter, the SN phenomenon is introduced: the classification criteria and the different classes are described in Section 1.1, while in Sections 1.2 and 1.3 the main explosion mechanisms are presented. In Section 1.4, newly discovered peculiar SN Types are also briefly illustrated.

Figure 1.1: The Type Ia SN 1994D (which is the bright source on the lower-left corner; Drenkhahn & Richtler 1999) in NGC 4526. NASA/ESA, The Hubble Key Project Team and The High-Z Supernova Search Team. `http://www.spacetelescope.org/images/opo9919i/`

1.1 Classification of supernovae

The SN classification has been a matter of discussion since the discovery of the first extragalactic transient in 1885. From the first SN search (1936-1941 using the Palomar 18 inches Schmidt telescope, Mount Palomar, California, United States of America) to date, the significant improvements in technologic tools have led to an increasing accuracy in the determination of the observational features characterising the different SN classes.

A first rough classification scheme was introduced by Minkowski (1941), based solely on the presence/absence of H lines in the spectra. The first 'Type I' class was exceptionally homogeneous, showing no H lines in their spectra, while the second ('Type II') was particularly heterogeneous, showing a wide range of spectroscopic properties, although all objects exhibited Balmer lines in their spectra. Three additional classes were later proposed by Zwicky (1965), who introduced the Types III, IV and V. All transients of this extended classes showed H lines in their spectra and peculiar light-curves. SN 1961V (Utrobin 1984; Goodrich et al. 1989; Bower et al. 1993; Filippenko et al. 1995) is the prototype for the Type V group, although these objects are now believed to be giant stellar outbursts resembling the 'Great Eruption' of η-Car in the 18th century (see Chapter 3) rather than genuine SN explosions.

Later on, the Type I class was further divided in the 'Ia' and 'Ib' sub-classes (Porter & Filippenko 1987), based on the presence or absence of the Si II (λ6355 Å) absorption line respectively. The 'Ic' class was introduced later to discriminate Type I SNe characterised by the absence of He lines in their spectra. In addition, the Type II SN class was subsequently splitted by Barbon et al. (1979), on the basis of observed photometric features, and the novel II-L (*linear*) and II-P (*plateau*) Types were introduced.

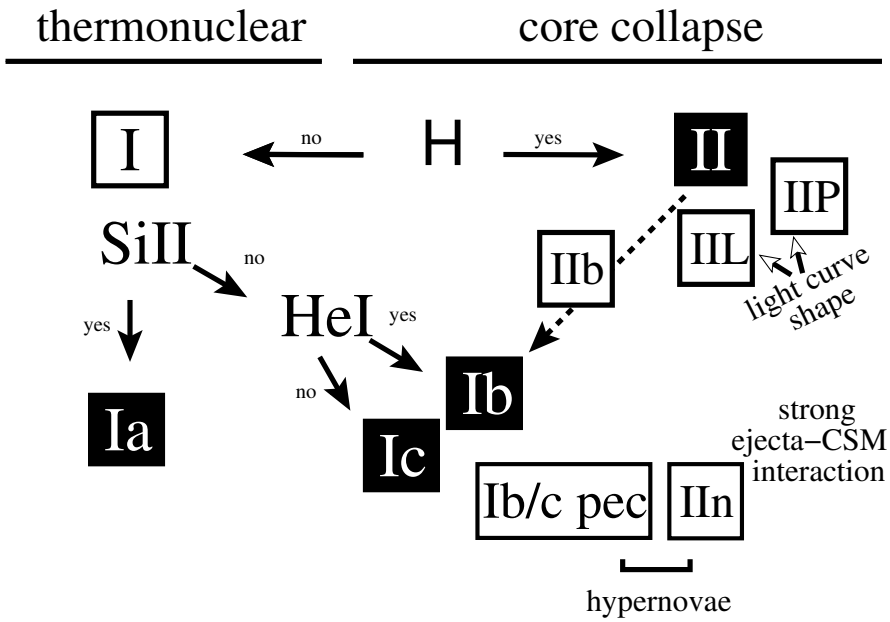

Figure 1.2: Overview of the basis for the modern classification scheme for SNe. (Figure from Turatto 2003). The four primary classes are marked with black boxes.

In the 80's, thanks to the introduction of the *charge-coupled devices* (CCDs), but also to the significant increase of comparison spectra, a new classification scheme was improved based mainly on early-time spectroscopy, while photometric properties were used to improve the classification of Type II SNe. Lower- and upper-case suffixes were added to the classical nomenclature to highlight the classification criteria. Lower-case suffixes were used to refer to classifications based on spectroscopic features (e.g. the absence or presence of particular lines in the spectra), while upper-case suffixes were used to refer to the shapes of the light-curves. An overview of this classification scheme and an example of spectra at different phases are showed in Figures 1.2 and 1.3 respectively. The four main classes along with their characterising features, are:

1. **Ia:** no H, strong Si II lines (same as the Minkowski Type I class);
2. **Ib:** no H (although very weak Hα lines may also be occasionally present; Branch et al. 2002) or Si II lines, spectra dominated by He I lines;
3. **Ic:** no H and He I lines, although very weak helium features may also be present. Si II lines are relatively weak;
4. **II:** dominated by Balmer lines at all epochs.

According to the shapes of light-curves (Figure 1.4) and to photometric features, Type II SNe are also divided into:

1. **II-L:** showing a linear and constant decline after maximum;
2. **II-P:** showing a constant luminosity (or a '**plateau**'), lasting approximatively 2-3 months after maximum.

but other two additional sub-classes do exist, mainly based on their spectroscopic properties:

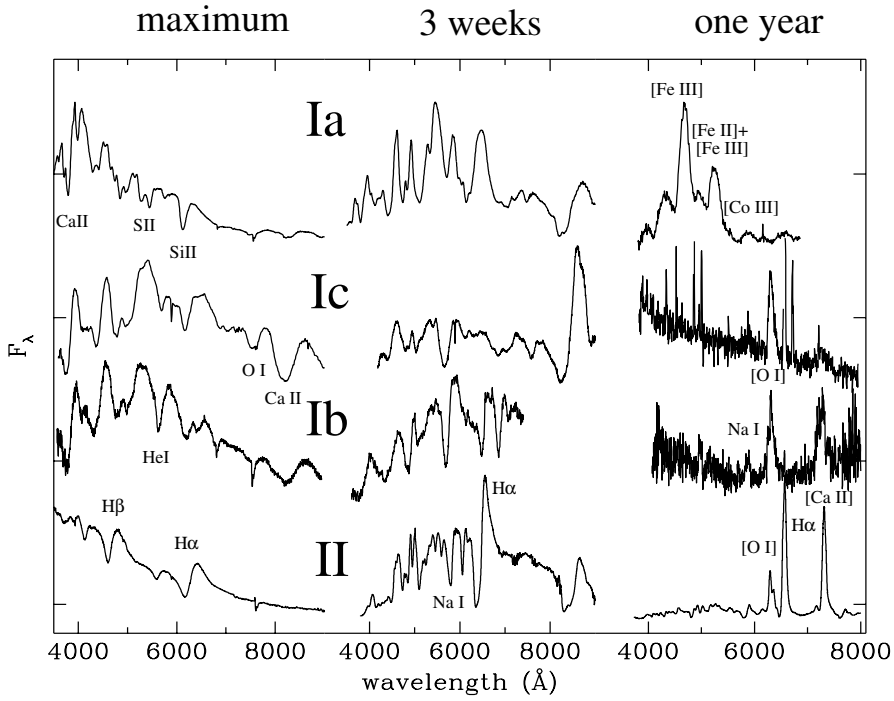

Figure 1.3: Overview of the spectroscopic evolution of the main SN classes. (Figure from Turatto 2003). Spectra of prototypical objects of the four main classes are shown: **left:** at maximum; **center:** 3 weeks after maximum; **right:** one year after maximum light. The positions of the main spectroscopic features are also marked with labels.

1. **IIb:** showing light-curves similar to those of Type Ib/Ic SNe, with strong H I lines during the first few weeks of the spectroscopic evolution weakening with time. He I lines become strong at later phases.

2. **IIn:** showing multi-component Balmer lines with prominent narrow emission components at any phase of their spectroscopic evolution. Their spectra are characterised by a blue continuum, with emission lines typically without broad P-Cygni absorption components, clearly detected in other SN types.

1.2 Type Ia: thermonuclear supernovae

1.2.1 Observational properties

Type Ia SNe are the most common explosive events in the Universe. They are observed in all types of galaxies, from elliptical (Barbon et al. 1999) to the latest types. The fact that there is no tight correlation with the arms of spirals or other star-forming regions suggests that they can occur both in young and old stellar population environments. These explosions leave no remnants behind.

Given their extremely homogeneous light-curves and spectra, as well as their extraordinary peak luminosities, they are the best known 'standardisable candles' for measuring cosmological distances. For this reason, in the last decades they became very popular due to their fundamental role in determining the geometry of the Universe (Riess et al. 1998;

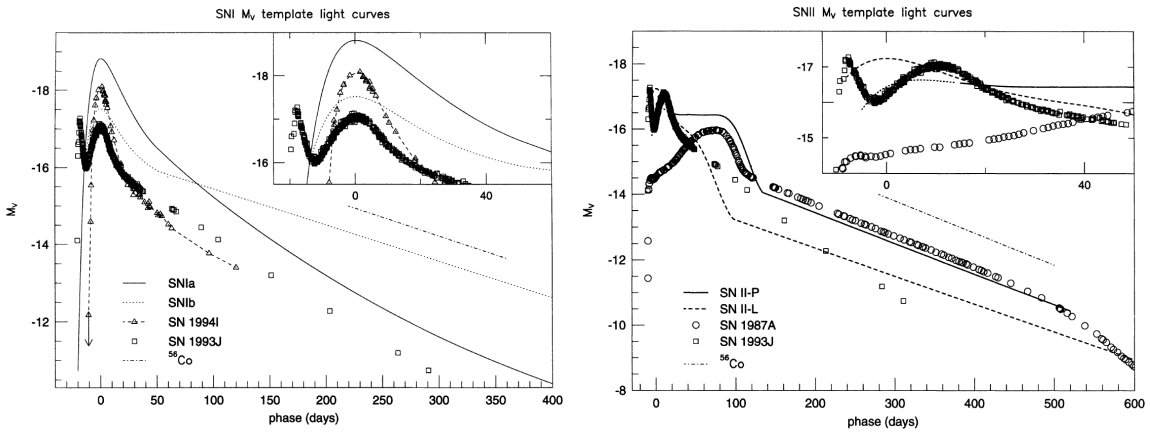

Figure 1.4: Light-curves of the main classes of SNe. (Figures from Wheeler & Benetti 2000).

Perlmutter et al. 1999).

Spectra of Type Ia SNe at early phases (Figure 1.6) are characterised by the lack of H and He lines, and are dominated by intermediate mass elements (Si II, S II and Ca II). At later phases the spectra evolve, and metal lines (especially Fe and Co lines) become dominant, while nebular spectra at very late phases are characterised by strong [Fe II] and [Fe III] emission lines (see Figure 1.3), as well as forbidden lines of Co and Ni.

Light-curves are very homogeneous (Figure 1.4), with an average absolute magnitude $V = -19.48 \pm 0.07$ mag (Gibson et al. 2000). In the recent past, a range of absolute peak-magnitudes wider than previously thought has been observed, challenging the role of Type Ia SNe as cosmological standard candles. Nonetheless, a relation between the peak B-band absolute magnitude and the post-maximum decline rate (Δm_B^{15}, i.e. the difference between the peak absolute magnitude and its value at +15 d after the B-band maximum) does exist (Phillips 1993; Phillips et al. 1999), suggesting that brighter objects have also broader light-curves, and that SNe Ia can still be used as cosmological distance indicators. This correlation has been interpreted as a signature of different masses of ^{56}Ni produced in the explosion (Mazzali et al. 2007).

Despite their predicted homogeneity, many peculiar Type Ia SNe have been observed in the recent past, challenging the validity of the proposed explosion mechanisms, the knowledge on the progenitor systems, as well as the use of Type Ia SNe as distance indicators. SN 1991T (Filippenko et al. 1992a; Ruiz-Lapuente et al. 1992; Phillips et al. 1992) presented bright, slowly declining ($\Delta m_{15} < 1$ mag) light-curves, while also its spectroscopic features revealed the unusual presence of Fe III at early phases rather than single ionised lines from intermediate-mass elements. Also the characteristic deep absorption in the red part of the Si II never reached the strength usually observed in Type Ia SNe (Fisher et al. 1999). Moreover, it showed evidences of a late light-echo from circumstellar dust (Schmidt et al. 1994). This was observed also in the Type Ia SN 1999bu (Cappellaro et al. 2001).

SN 1991bg (Filippenko et al. 1992b; Leibundgut et al. 1993; Turatto et al. 1996), on the other hand, showed faint, red and fast declining ($\Delta m_{15} > 1.7 - 1.8$ mag) light-curves. Since the first phases around maximum, it also showed a relatively red spectral continuum, with very strong Si II lines and the slower expansion velocity (see e.g. Benetti 1991). Nevertheless,

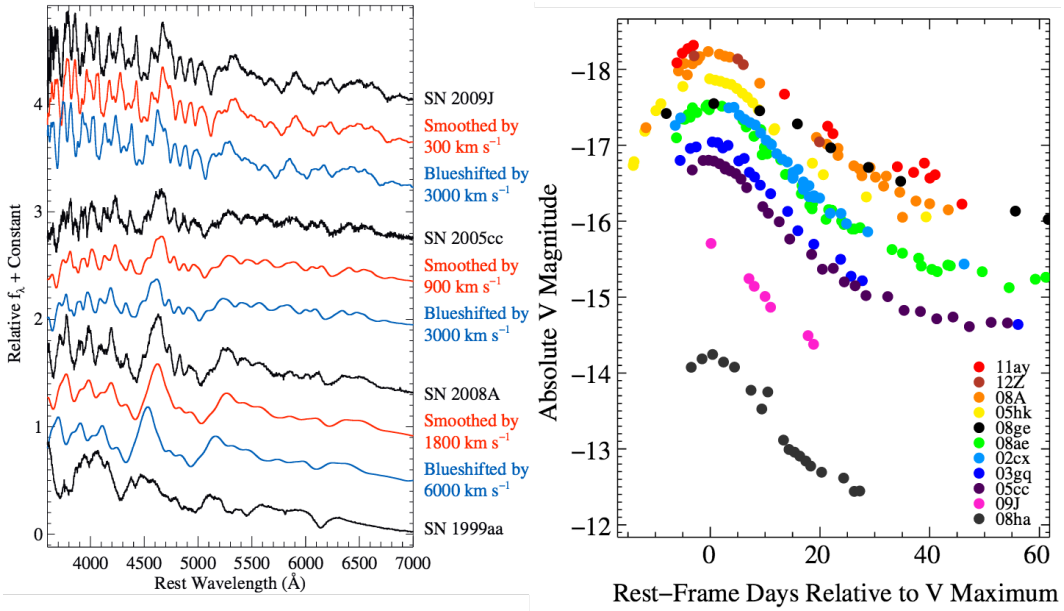

Figure 1.5: Early time spectra and absolute V-band light-curves of a sample of Type Iax SNe. (Figures from Foley et al. 2013).

in the following years, these unusual properties were observed in other objects (e.g. SN 1992K; Hamuy et al. 1992). Despite their unusual photometric and spectroscopic properties, both SNe 1991T and 1991bg (and similar objects) follow the Phillips (1993) relation between the absolute B-band peak magnitude and Δm_{15}, supporting the idea that also these objects both result from the explosion of Chandrasekhar mass WDs. Nonetheless, the subsequent discovery of objects with even more peculiar observables proved the existence of some SNe Ia that do not follow the Phillips (1993) relation and seem to arise from progenitor systems incompatible with the canonical Chandrasekhar mass limit.

SN 2009dc, a very luminous SN Ia, had a number of spectroscopic features barely resembling those of typical Type Ia SNe, with early spectra dominated by intermediate-mass elements and a fraction of unburned material, although the presence of strong C II lines until $\sim +14$ d after maximum was never been observed before in other Ia SNe. Also the expansion velocities (determined from the minima of the P Cyg absorption profiles) were significantly lower (i.e. not exceeding $\sim 10^4$ km s^{-1} for any line considered) with respect to those of other SNe Ia, while no signatures of ejecta-CSM interaction were detected. Late phase spectra, on the other hand, were characterised by lines from Fe-group elements. In addition, SN 2009dc revealed particularly slow evolving light-curves ($\Delta m_{15} = 0.71$ mag in the B-band) characterised by an extraordinary bolometric luminosity (with a slower decline and higher luminosity than those derived for SN 1991T), with a peak value of $\log L \simeq 43.47$ erg (Taubenberger et al. 2011). Estimates of the total ejected mass (~ 2.8 M$_\odot$)[1], moreover, supported the conclusion that SN 2009dc arose from a 'super-Chandrasekhar' mass progenitor, likely generated in a WD stellar merger (but see Section 1.2.2). Similar objects are SNe 2003fg (Howell et al. 2006), 2006gz (Hicken et al. 2007) and 2007if (Scalzo et al. 2010).

SNe 2002cx (Li et al. 2003) and 2005hk (Phillips et al. 2007), on the other hand, showed light-curves fainter (in some cases largely fainter) than those of SN 1991bg. SN 2002cx, in

[1]Derived from analytic models assuming that the light-curve is powered solely by radioactive decay (Taubenberger et al. 2011).

particular, was suggested to be the prototype for a class of thermonuclear SNe labelled 'Type Iax' (Foley et al. 2013), showing spectra similar to those of high-luminosity SNe Ia (e.g. SN 1991T, see Figure 1.5), although with much lower expansion velocities around maximum (in the $2000 - 8000$ km s^{-1} range, inferred from the narrow P Cyg lines in their spectra), lower peak magnitudes (between -14.2 mag and -18.9 mag in the V-band, suggesting a modest ejected mass of ^{56}Ni). Moreover, nebular spectra did not resemble those of canonical SNe Ia (namely dominated by forbidden Fe lines), but showed intermediate-mass elements usually observed in core-collapse SNe. As mentioned above, the absolute light-curves do not follow the Phillips (1993) relation, and are characterised by a large dispersion in their peak magnitudes, decline rates and the rise times. Nevertheless, a general trend according to the most luminous Iax SNe have broader light-curves seems to exist (although different from that predicted for normal Ia SNe), as well as a correlation among absolute peak magnitudes rise times and decline rates, in which faintest objects are related to shorter rises and faster declines (Foley et al. 2013).

1.2.2 Theoretical interpretations

Type Ia SNe are believed to be the result of the thermonuclear explosion of white dwarf (WD) stars in close binary systems. When the WD accretes mass and reaches the Chandrasekhar limit ($\simeq 1.38$ M$_\odot$), carbon ignition in the degenerate WD core leads to the complete destruction of the progenitor star. At least two explosion mechanisms have been proposed, in which the burning front may propagate subsonically (deflagration; Nomoto et al. 1986) or supersonically (detonation; Woosley et al. 1986). A Type Ia SN typically enriches the interstellar medium with ~ 0.7 M$_\odot$ of Fe-peak elements, while a total of 0.4 M$_\odot$ of intermediate-mass elements (such as Si and S) and 0.3 M$_\odot$ of unburned α-elements (C,O) are expected. The pure deflagration model fairly explains the expected the small amount of unburned material through the effects of turbolence (due to Reyleih-Taylor instabilities; Röpke et al. 2007), which accelerates the expansion ensuring the required critical density to sustain the burning flame (Hillebrandt & Niemeyer 2000). On the other hand, the expected large-scale mixing in the deflagration model does not match the observations, and its expected synthetised mass on ^{56}Ni is to low (~ 0.6 M$_\odot$) to explain the brightest Ia SNe observed (Röpke et al. 2007). Nonetheless, pure detonation models also fails to explain the observables, since rapidly moving burning flames are not expected to produce any (or very little) unprocessed material and hence a small amount of intermediate-mass elements. A combination of this two models has hence been proposed to explain the observed photometric and spectroscopic properties of Type Ia SNe, where the explosion is triggered as a deflagration followed, after the star sufficiently expanded, by a transition into a detonation flame (Khokhlov 1991). A 'delayed detonation', triggered by a starting deflagration front, would account for the fraction of burned and unburned material observed, also avoiding the effects of strong mixing in the SN ejecta. Moreover, the radius at which the deflagration-detonation transition occurs would explain the differences in the observed luminosity differences among Ia SNe (Hoeflich & Khokhlov 1996). Nevertheless, a few aspects of this model still need revision (i.e. the exact mechanisms triggering the deflagration-to-detonation transition; Niemeyer 1999).

Two main scenarios have been proposed to describe the physical properties of the progenitor systems: the single-degenerate (SD) and the double degenerate (DB) scenarios. In both scenarios the final explosion is triggered by the carbon ignition in the degenerate core of a WD star. In the SD scenario, the WD accretes mass from a red-giant (RG) companion (although mass can be accreted also from sub-giants or even main-sequence - MS stars) until the Chandrasekhar limit is reached. In the DD scenario, the SN explosion is triggered by

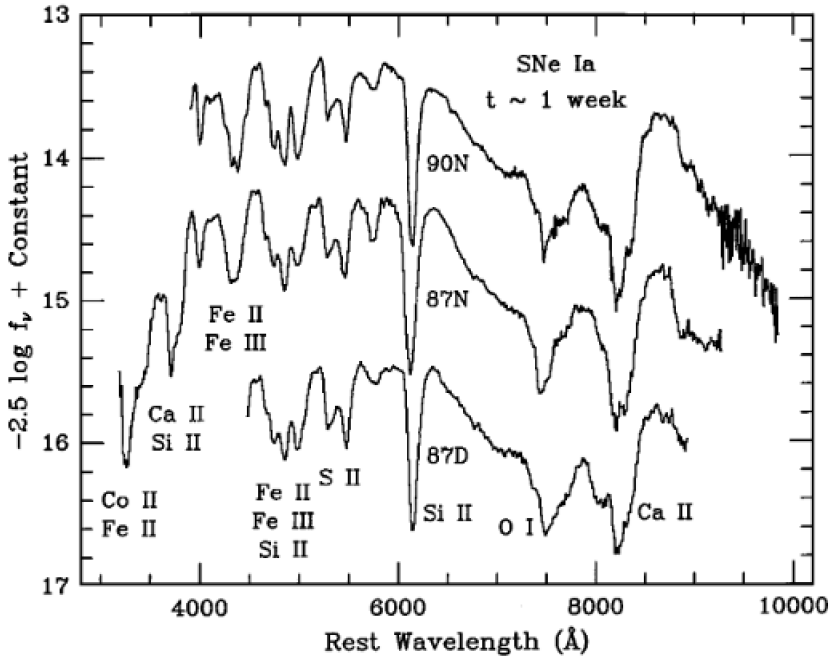

Figure 1.6: Optical spectra of Type Ia SNe $\sim$ 1 week after maximum. Strong Si II and Fe II and Fe III lines are clearly visible. These spectra are also characterised by the presence of moderate strength O I and Ca II lines. (Figure from Filippenko 1997).

merging two WDs whose combined mass reaches or exceeds the Chandrasekhar limit (Hicken et al. 2007). The DD scenario well matches the observed spectroscopic properties, since it is expected to produce Type Ia SNe with little or no H and He in their spectra.

Although theoretical models favour the formation of an O-Ne-Mg WD and the subsequent collapse to a neutron-star (SN Bravo & García-Senz 1999), the DD scenario was proposed to explain the very peculiar features observed in the 'super-Chandrasekhar' mass SN 2003fg (Howell et al. 2006, although this scenario was later questioned by Hillebrandt et al. 2007). SN 2003fg showed an unusual spectroscopic behaviour similar to that of SN 2009dc, with a relatively low expansion velocity, but high luminosity (2.2 times brighter than canonical SNe Ia). Alternatively, luminous Type Ia SNe like SN 2009dc have been also proposed to arise from the explosion of super-Chandrasekhar-mass WDs (Howell et al. 2006; Branch et al. 2006), in which strong differential rotation would provide the stability needed to sustain such high mass values, although Pfannes et al. (2010) showed that too high rotations would hinder the formation of Rayleigh-Taylor instabilities, rather resulting in a sub-luminous event.

An alternative interpretation to the observed properties of super-luminous Ia SNe was proposed by Hillebrandt et al. (2007), who showed that a sufficient luminosity can be obtained from an off-centre C ignition in a normal M_{Ch}-WD observed under an appropriate angle. Moreover, these objects do not follow the empirical relation between the absolute peak luminosity and the shape of the light-curve around maximum. For this reason, the discovery of 'super-Chandra' SNe Ia raises questions about the applicability of Type Ia supernovae as standard candles, since the total mass of the two merging WD can be significantly different from case to case, resulting also in very different luminosities. On the other hand, if the SD scenario is the preferred one, it is not unreasonable to expect the presence of H-rich material around Type Ia progenitors, and hence H lines in the spectra of Type Ia SNe, as observed, for example, in the spectra of the peculiar SN 2002ic (Hamuy et al. 2003) and SN PTF11kx

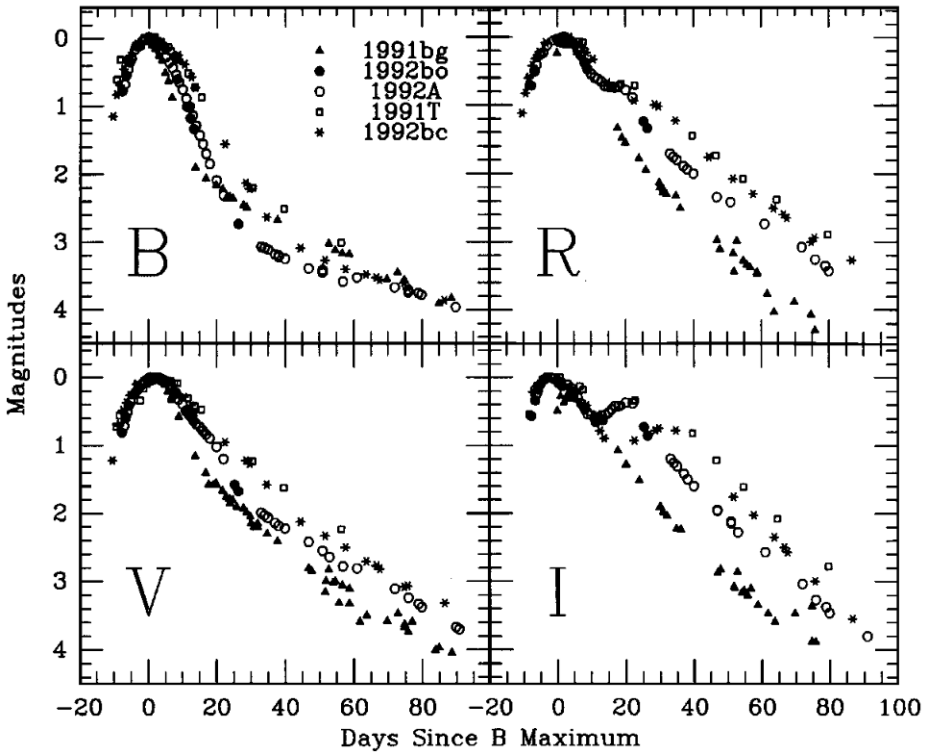

Figure 1.7: *BVRI* light-curves of a sample of Type Ia SNe. (Figure from Filippenko 1997).

(Dilday et al. 2012).

Sub-luminous transients producing such as Type Iax SNe, have been proposed to be the thermonuclear explosions of sub-Chandrasekhar-mass WDs (Weaver & Woosley 1980; Nomoto 1980; Woosley et al. 1980). These explosions are believed to be the result of a detonation mechanism triggered in the outer accreted He layer on the surface of the WD. The resulting shock wave would then propagate into the CO stellar core triggering a second C detonation. Although this mechanism predicts lower luminosities than those observed in normal Typa Ia SNe, more recent 2D simulations suggest a produced amount of ^{56}Ni too high to account for the luminosities of peculiar sub-luminous objects (Fink et al. 2007), suggesting that these models need further revisions. Finally, a few Type Iax SNe has been proposed to be produced by the explosion of WDs accreting He-rich gas (Foley et al. 2013; Wang et al. 2013) which may not always result in the complete destruction of the progenitor star (McCully et al. 2014).

1.3 Core-collapse supernovae

Stripped envelope supernovae

Type Ib/c SNe are thought to arise from the gravitational collapse of the core of massive stars, which have lost a significant amount of their envelopes during the latest phases of their life. In analogy with Type II SNe, they are associated to young stellar populations, and therefore to the star-forming regions in late type galaxies (Barbon et al. 1999). Both Type Ib and Ic SN spectra show Ca II, O I, Na ID, Fe II and Ti II lines at photospheric phases, while nebular spectra are dominated by [Mg II], [O I], [Ca II] and [Fe II] lines (Millard et al. 1999;

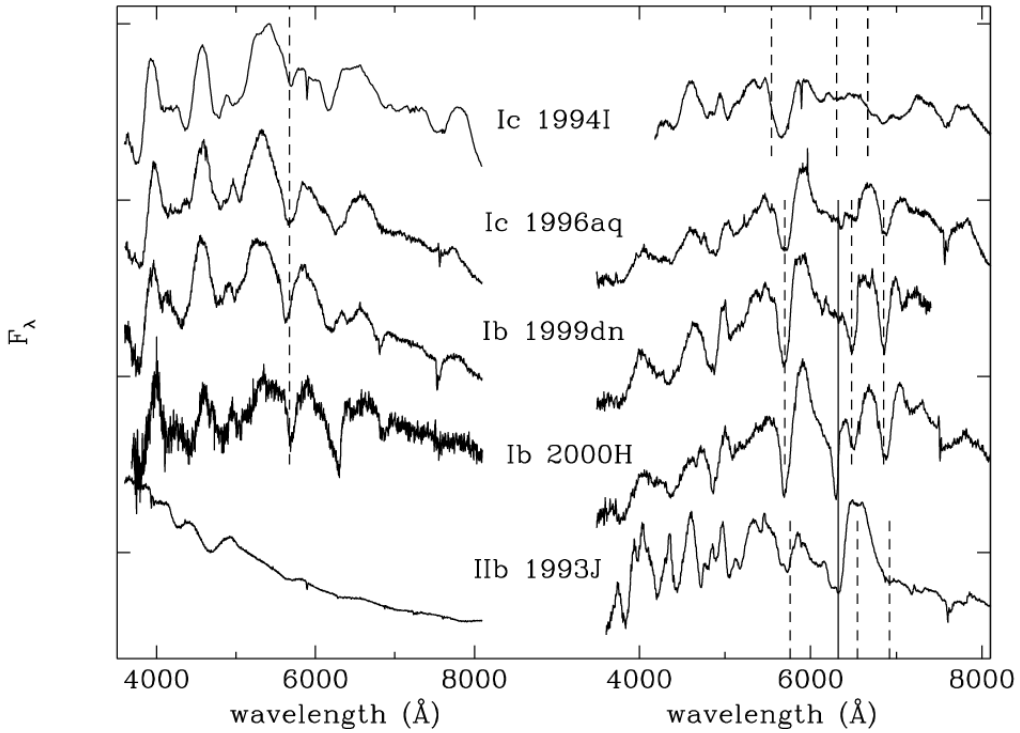

Figure 1.8: Spectroscopic evolution of a sample of Type Ib/c supernovae. The spectra were obtained at maximum **(left)** and 3 weeks after maximum (**right**. Figure from Turatto 2003).

Matheson 2001).

The spectra of Type Ib SNe (Figure 1.8) are characterised by prominent He lines (which are absent in SNe Ic), which strengthen with time, and weak (or no) H and Si features. Nonetheless, Hα absorptions were identified in the spectra of the Ib SNe 1983N and 1984L (Wheeler et al. 1994). This, along with the results on the comparison of similar objects with synthetic spectra, supported the conclusion that detached H-rich gas may be frequent in Type Ib SNe (Branch et al. 2002). Strong He lines indicate non-thermal excitation, since He lines are not easily excited at the typical temperatures of SN photospheres. Moreover, strong ionisation and large amount of He are also needed to produce the observed spectra (Fryer et al. 2007).

The light-curves of both Ib/c SNe (Figure 1.9) are similar to those displayed by SNe Ia, being powered by the radioactive decay of ^{56}Ni and ^{56}Co during the photospheric and nebular phases, respectively. Their light-curves usually show peaks followed by radioactive tails without any secondary maximum either in the optical or NIR domains, although they reach absolute magnitudes fainter than those of Type Ia SNe (Richardson et al. 2002).

The discovery of two Ic SNe, 1997ef and 1998bw suggested the presence of a subclass of stripped-envelope SNe showing very broad spectral features, with massive progenitors producing very energetic explosions, 1-2 order of magnitude more energetic than the prototypical Type Ic SN 1994I (Nomoto et al. 1994; Sasaki et al. 1994; Houck & Fransson 1994; Laaksonen et al. 1994; Wheeler et al. 1994). For these reasons the new label of 'hypernovae' was introduced. Nonetheless, observational evidences revealed the presence of broad line Type Ic SNe less energetic and massive than SN 1997ef and SN 1998bw, suggesting that high energies

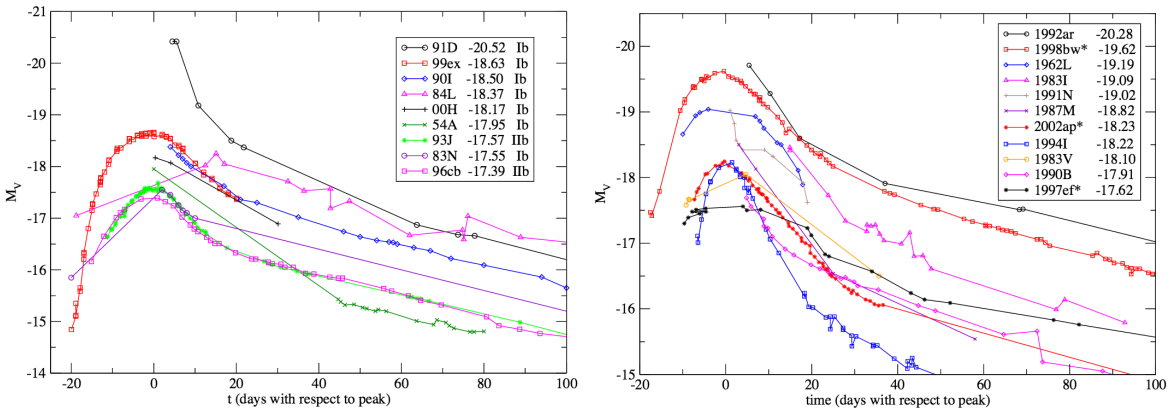

Figure 1.9: Light-curves of Type Ib/c supernovae. **Left panel:** a sample of Ib SNe compared to 3 Type IIb SNe. **Right panel:** a sample of Ic SNe. (Figure from Richardson et al. 2006).

are not distinctive features of this sub-group, and the less constraining label of 'broad line Ic' was introduced.

The candidate progenitors for Type Ib/c SNe are single Wolf-Rayet (WR) stars which lost their H envelope via strong stellar winds, although mass loss scenarios involving single massive stars disfavour the complete loss of the H envelope through stellar wind, justifying the residual H features observed in their spectra. Type Ib progenitors are hence believed to retain an external massive envelope He shells ($\gtrsim 1$ $M_\odot$; Woosley et al. 2002). Type Ic progenitors, on the other hand, lost both their H and He layers, and are believed to be low metallicity WC and WO stars in binary systems (Dessart et al. 2015). Nonetheless, lower mass stars in binary systems, stripped by the interaction with the companion star, cannot be ruled out (Smartt 2009; Eldridge et al. 2015).

Type II supernovae

Type II SNe are CCSNe whose spectra are characterised by the presence of prominent H lines. The Hα line (λ6562.8 Å) is particularly intense, but also other lines of the Balmer series can be easily detected. Early spectra are usually dominated by a blue continuum with Balmer lines progressively strengthening with time. SN II explosions usually occur in spiral galaxies (Barbon et al. 1999), being strongly related to the star-forming regions of their hosts (Van Dyk et al. 1999).

They exhibit a very wide heterogeneity in both photometric (Patat et al. 1994) and spectroscopic (Filippenko 1997) observational features. According to the shape of their optical light-curves, they may be classified as Type II-P or Type II-L (see Section 1.1 for more details on the classification criteria). These two subclasses constitute $\sim 85\%$ of all the Type II SNe[2]. On the basis of their spectroscopic properties, a fraction of SNe II may also be classified as Type IIn and Type IIb SNe (see below).

Type II-P and II-L SNe show similar spectroscopic evolution (Figure 1.10). Their spectra are dominated by Balmer lines in emission at all phases, while He I lines are visible at very early phases only (< 2 weeks). Photospheric spectra are dominated by Na I, Ca II, Fe II, Sc II,

[2]from the Asiago SN archive; `http://web.oapd.inaf.it/supern/cat`

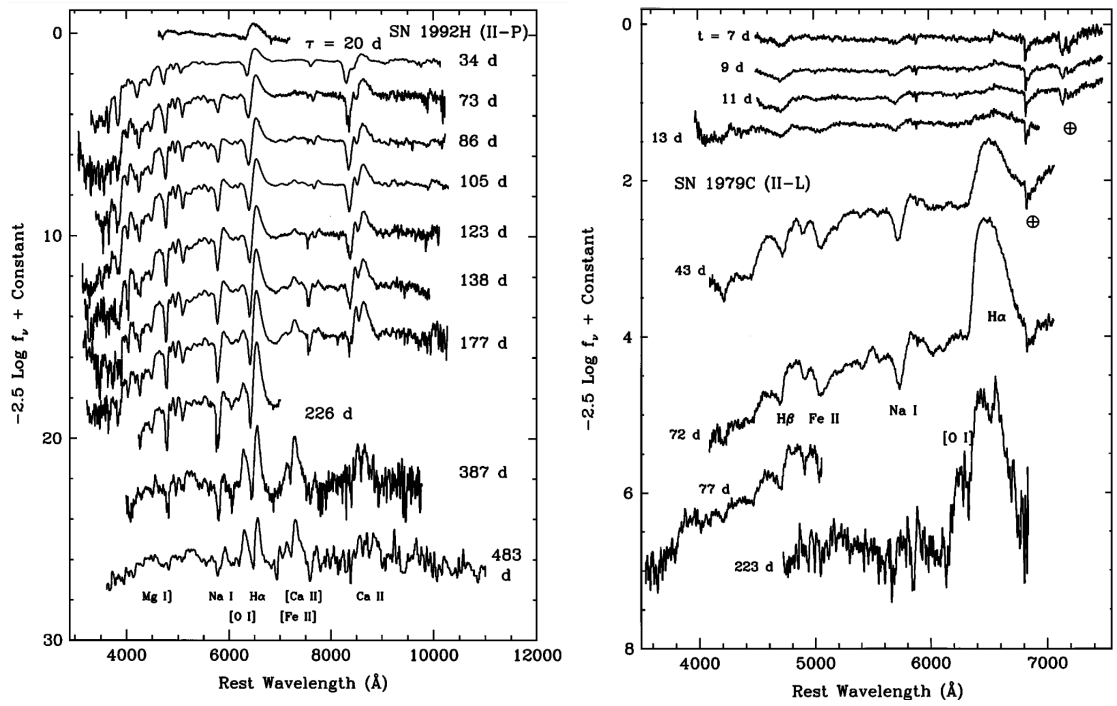

Figure 1.10: Optical spectroscopic evolution of the Type II-P SN 1992H **(left)** and the Type II-L **(right)** SN 1979C. (Figures from Filippenko 1997 and Branch et al. 1991.)

Ti II, Ba II, Sr II lines, while nebular spectra are characterised by strong lines of H, [O I], Ca II, [Ca II] and weak [Fe II].

Type II-P SNe have light-curves showing a wide range of properties, both in shapes and peak luminosities. Their absolute peak magnitudes have an average value of $M_B \simeq -17$ mag, although they are characterised by a large dispersion ($\sigma = 1.12$ mag Richardson et al. 2002). After maximum, the luminosity rapidly declines, and is followed by a plateau, a period of almost constant luminosity lasting from 2 to ∼3 months. After this period, the light-curves show a linear decline, similar to those displayed by Type II-L SNe (Figure 1.4) and following the slope predicted by the ^{56}Co decay, although tail luminosities may strongly differ, due to different amounts of expelled radioactive material.

Type II-L are generally brighter than II-P SNe, with light-curves characterised by a linear uninterrupted decline in luminosity after maximum. Their light-curves are similar to those displayed by Ib/c SNe (although with a smaller scatter; Richardson et al. 2002). At approximatively +150 d after the explosion, their curves usually settle onto an exponential decline, following the slope predicted by the ^{56}Co decay.

According to their spectroscopic features and evolution, Type II SNe may also be classified as Type IIb or IIn. Type IIb SNe arise from the CC of massive stars showing early spectra similar to canonical Type II SNe (e.g. showing prominent Balmer lines), but with late spectra resembling those of Ib/c SNe (see e.g. the comparison in the left panel of Figure 1.8). The first observed Type IIb was SN 1987K (Filippenko 1988), although the best studied object was certainly SN 1993J in M 81 (Barbon et al. 1995). With an unusual double-peaked shape, the light-curves of SN 1993J resembled those displayed by the well studied SN 1987A, although with a significant faster evolution, settling on an almost exponential tail (although with a

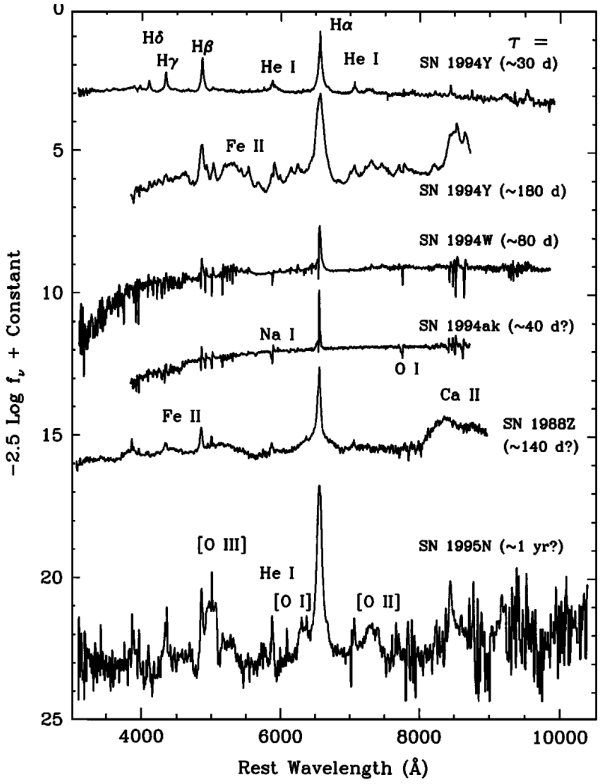

Figure 1.11: Optical spectra of a sample of Type IIn SNe. The spectra refer to different epochs, which are reported in the figure. The epochs refer to the light-curves maxima (Figure from Filippenko 1997).

decline rate faster than typically observed in other Type II SNe) over 50 d after the explosion.

Type IIn SNe (Schlegel 1990) are most frequently attributed to the explosion of massive stars in a dense H-rich CSM. Their early phase spectra are characterised by a blue continuum, with narrow Balmer lines in emission (Figure 1.11). These components have inferred *full-width-at-half-maximum* (FWHM) velocities from a few tens to a few hundreds km s^{-1}, and are believed to arise from photoionised, slowly expanding gas which recombines and emits photons. This gas, most likely expelled by the progenitor star during the last phases of its life (namely years to decades prior to the SN explosion), is located in the outer CSM and is not perturbed by the SN ejecta, at least during the early phases of the SN evolution. At later phases, the collision of the high velocity ejecta (a few 10^4 km s^{-1}) with the dense pre-existing CSM, may generate intermediate-velocity line components (FWHM of a few thousands km s^{-1}). Although the interaction may mask the innermost ejecta (as well as the explosion mechanism; Chevalier & Fransson 1994), in some cases, particular geometric configurations may also favour the detection of high-velocity components (namely a few 10^4 km s^{-1}) arising from the photo-ionised SN ejecta. As a consequence, the spectra of Type IIn SNe are generally characterised by multicomponent spectral lines, while narrow components are always visible at all stages of the spectroscopic evolution. At late phases, the interaction can dominate the properties of the light-curves and the spectra of these transients, masking the expected signatures of the SN explosion, such as the decline rate predicted from the ^{56}Co decay, or the presence of elements produced in the stellar/explosive nucleosynthesys (including O, C, Mg). The contribution of the interaction in the light-curves and spectra is mainly due to the conversion of kinetic energy into radiation If the CSM is dense enough, the interaction may lead to a deceleration and the subsequent conversion of a fraction of the

ejecta kinetic energy into radiation. The duration of this phase strongly depends on the mass and the velocity of the SN ejecta, as well as the amount and density of gas in the CSM. As a consequence, the spectroscopic and photometric studies of very late phases of Type IIn SN evolution are crucial to recover important information about the progenitor star and on the explosion mechanism. The physical and observational properties of Type IIn SNe will be further discussed in Chapter 3.

1.3.1 Explosion scenarios

Core-collapse SNe (CCSNe) arise from the collapse of the nuclei of massive stars ($M \gtrsim 8$ M$_\odot$; e.g. Smartt 2009). During the last phases of their evolution, these stars retain enough mass to allow temperature and pressure conditions necessary to undergo non-degenerate C ignition. Heavier elements may also be synthesised (although this requires an initial mass $\gtrsim 10$ M$_\odot$)[3], preventing the stellar collapse until an iron core is formed. Despite the basic evolution of stars is relatively well understood, the last phases of the evolution of massive stars are still poorly constrained. As a consequence, the fate of stars within the range $8-11$ M$_\odot$ is still somewhat uncertain, although stellar evolution models predict the formation of degenerate O-Ne cores after the C-burning, resembling the central structures of asymptotic giant branch (AGB) stars, and are hence labelled 'super-AGB' stars (Ritossa et al. 1996; Gil-Pons et al. 2005; Siess 2006; Poelarends et al. 2008; Doherty et al. 2010).

After the C-burning, the core evolution is characterised by a relatively fast evolutionary phase during which nuclear burnings and core contractions alternates in quick succession as core- and shell-burnings take place (Woosley et al. 2002). During these phases, a major role is played by neutrino losses, and the core evolution is so fast that the star's envelope usually evolves independently from the rest of the structure. Iron cores are produced once the central temperature exceeds $\sim 3 \times 10^9$ K and the silicon burning starts in the core of the star (see e.g. Woosley et al. 1973). Silicon burning consists in a combination of photo-disintegration and α-capture reactions, until a state close to nuclear statistical equilibrium (NSE) is reached, characterised by an overabundance of nuclei with the lowest binding energy at the core temperatures (i.e. elements of the iron group, mostly ^{56}Fe and ^{52}Cr at a temperature of 4×10^9 K, see e.g. Woosley & Janka 2005). Subsequent core- and shell-burnings lead to the typical 'onion' structure, consisting of heavier elements at increasing depth separated by burning shells, although the convection may also partially mix the inner layers.

Once the inert iron core is formed, no further energy can be produced by nuclear fusion, and there is no energy source to contrast the collapse of the core. This is a consequence of the high temperature and density ($\gtrsim 10^9$ g cm^{-3}), since a relativistic electron gas cannot prevent the CC even if the core is degenerate (Janka et al. 2007).

This phase is characterised by strong neutrino losses, but also electron captures and photo-disintegration play a fundamental role in accelerating the collapse (see e.g. Heger et al. 2001). Electron captures, or 'inverse β-decay', occur at very high densities when free electrons can be captured and bound into unstable heavy nuclei. As a consequence, the electron pressure decrease and the gas increasingly becomes neutron-rich (the process is also labelled 'neutronization'), triggering the collapse of the core and decreasing the effective Chandrasekhar mass, which may also lead to the collapse of stars with initial masses $\lesssim 11$ M$_\odot$ (see Woosley & Heger 2015). Photo-disintegration occur when the temperature in the

[3]Stars with initial masses of 8-10 M$_\odot$ are instead believed to develop an ONeMg core with a thin carbon shell surrounded by a dilute and loosely bound He-shell (Mayle & Wilson 1988)

contracting core is $\simeq 10^{10}$ K and the energy of the photons breaks up heavy elements (e.g. ^{56}Fe) into α particles and neutrons following the reaction:

$$^{56}\mathrm{Fe} + \gamma \leftrightarrow 13 \quad ^{4}\mathrm{He} + 4\mathrm{n}. \tag{1.1}$$

This process is similar to the ionisation of hydrogen, lowering the adiabatic exponent γ_{ad} below the critical $\frac{4}{3}$ value, and contributing to the dynamic instability of the core of very massive stars. β decay and the photodisintegration of iron-group nuclei to α particles partially dissipate the core energy and reduce the electron density of the core, accelerating the collapse (Clayton 1984).

The collapse is eventually and abruptly stopped by the repulsive component of the short-range nuclear force when the central density reaches $4-5\times10^{14}$ g cm^{-3}, and while the outer shells are still collapsing, the rebound on the inner core generates a shock wave (Burrows 2000). Nonetheless, the initial wave cannot propagate all the way out of the core, but rather loses its energy due to strong neutrino losses and photodisintegration (Wilson et al. 1986; Myra & Bludman 1989; Bruenn 1993; Swesty et al. 1994). Although the exact scenario is still uncertain, the most likely mechanism to revive the shock is the one predicted by the 'delayed neutrino' model (Bethe & Wilson 1985). In this model, neutrinos are absorbed by the layers behind the shock and provide the required energy to accelerate the shock in a runaway process. As the shock wave reaches the stellar photosphere, a flash of thermal ultra-violet (UV) or X-ray radiation is expected to break through. This phase is usually labelled as 'shock break-out', usually lasts a few hours, and marks the beginning of the observable supernova phenomenon (Falk & Arnett 1977).

The gravitational energy released during the CC is $E_{grav} \simeq 3\times10^{53}$ erg, more than enough to expel the entire envelope of the star, which evolves independently from the inner part ($E_{env} \simeq 3\times10^{52}$ erg if $M = 10$ M$_\odot$). Only a small fraction of the explosion energy is spent to unbind the outer layers and contributes to kinetic energy.

Our knowledge about CCSNe mostly originates from detailed studies on the famous Type II SN 1987A (Hamuy et al. 1987). Given the extremely proximity of its host galaxy (the LMC, located at $\sim$ 5.1 Kpc) with respect to the other extragalactic SNe, the explosion site was extensively monitored over the years, allowing a complete and accurate characterisation of the SN environment, its progenitor and the physical processes occurring in this CCSN at all phases of its evolution. The data spanned a period from the UV-flash in the very first hours after the CC, to the reprocessing of radioactive energy over the following decades (McCray 1993; Fransson et al. 2015). These observations played also a major role in confirming theoretical models, in particular regarding the expected neutrino emission in CCSNe, recorded by three different instruments (i.e. BAKSAN, Kamiokande II and IMB detectors; Alekseev et al. 1987; Burrows & Lattimer 1987) a few hours before the first optical detection. The progenitor star was detected in historical plates and identified with the blue hypergiant Sanduleak -69° 202 (Sanduleak 1970, and references therein), although stellar evolution theories of that time did not predict such progenitor type for Type II SNe. Finally, late-time HST images showed an inner/outer ring structure (Figure 1.12) surrounded by a diffuse region of emitting gas, supporting the idea that at very late phases the energy output is dominated by the conversion of kinetic energy into radiation through shock interactions between the SN ejecta and a surrounding dense CSM (e.g. Larsson et al. 2011).

Figure 1.12: Late-time HST image of the ring surrounding SN 1987A. The evolution of the ejecta-CSM collision from 1994 to 2014 is showed (Figure from Fransson et al. 2015).

1.4 Peculiar supernovae

1.4.1 New supernova types: observational properties

In the last few years, the discovery of a number of peculiar objects suggested the need for a revised and finer classification scheme (see Figure 1.13). Many of these objects turned out to be transitional phases between existing classes, but others still show unique, and still poorly explained properties.

- A handful of peculiar, extremely bright objects have light curves with 'bell-like' shapes and at late phases do not show the canonical radioactively-powered tails. For these reasons, their observational properties cannot be explained with canonical CC explosion mechanisms (see e.g. Gal-Yam 2012). Among the others, SN 2005ap, SCP06F6, PTF09atu, PTF09cnd and SN 2010gx (Quimby et al. 2011) are members of this new class. All of them show extremely blue spectra at early phases, with unprecedented deep absorptions of Si III, C II, Mg II and O II, while no H features are observed at any phase of their evolution. As mentioned before, their light-curves are characterised by high luminosities, which at maximum can be one order of magnitudes more luminous than most Type Ia SNe. As all these objects emit a large fraction of their energy in the UV domain (in the observer's frame), they are observable at very large distances (up to redshift ~ 4; Quimby et al. 2011).

- Type Ib SNe showing narrow He I lines in their spectra were proposed to belong to a new class of interacting transients labelled as 'Type Ibn' (Pastorello et al. 2008). The prototypical object for this class is SN 2006jc (Pastorello et al. 2007b; Foley et al. 2007), but also other cases of interacting Type Ib SNe have been observed (e.g. SNe 1999cq;

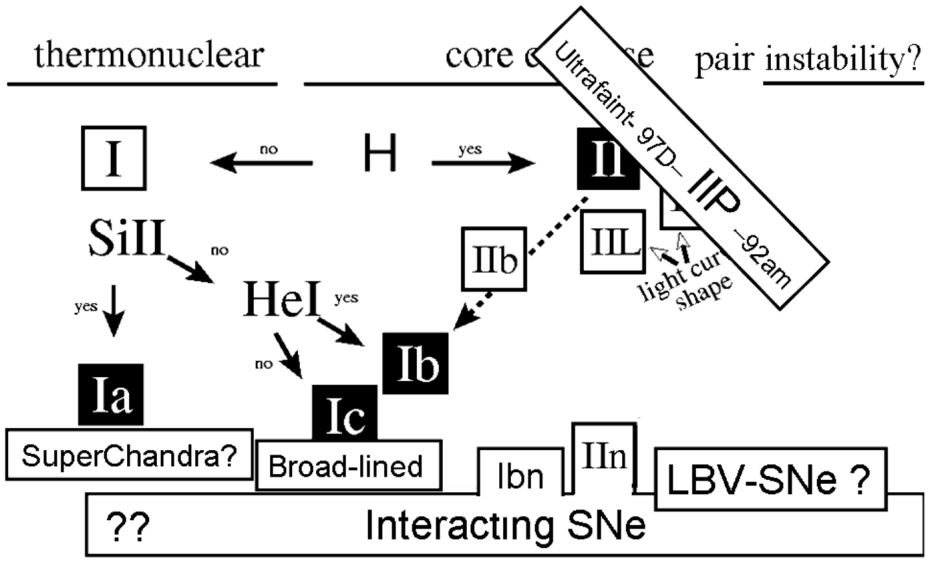

Figure 1.13: A new classification scheme for SNe reporting the latest findings and open issues. (Figure from Turatto et al. 2007)

Matheson et al. 2000, and the sample in Pastorello et al. 2016).

- The discovery of the very faint Type II-P SN 1997D (Turatto et al. 1998; Benetti et al. 2001) suggested that faint SNe do exist and that they might form a new sub-class of faint transients do exist and that they might form a new sub-class of faint CCSNe. Other objects belonging to this class are SNe 1999br, 1999eu, 2001dc; (Pastorello et al. 2004), 2003Z; (Utrobin et al. 2007; Knop et al. 2007; Spiro et al. 2014) and 2005cs; (Pastorello et al. 2009a).

1.4.2 Proposed explosion scenarios

The discovery of new types of transients, has suggested the need to introduce new explosion scenarios (Figure 1.14).

Pair Instability SNe (PISNe) are expected to be the final evolutionary stage of very massive stars ($M > 140$ M$_\odot$) developing a critical O mass ($M \simeq 50$ M$_\odot$) in their cores. High temperatures and relatively low densities, lead to the production of free electrons and positrons prior to the O ignition. This phenomenon is powered by the collisions of nuclei with energetic gamma rays and lead to a reduction of the thermal pressure in the cores, eventually triggering their collapse followed by the explosive O ignition (Rakavy & Shaviv 1967; Barkat et al. 1967; Bond et al. 1984; Heger & Woosley 2002; Scannapieco et al. 2005; Waldman 2008). In very massive stars ($M \simeq 100$ M$_\odot$; e.g. Heger & Woosley 2002; Waldman 2008), a large amount of radioactive material is subsequently produced (mostly ^{56}Ni), leading to an extremely luminous explosion. Such massive stars are expected to be observed in very low metallicity environments, and the progenitors of PISN are therefore believed to be population III stars at very high redshift, although recent observations revealed that luminous objects matching the requisites of the PISN model may also occur in the local Universe (Gal-Yam 2012). The first case of proposed PISN was the 'superluminous SN' (SLSN Gal-Yam 2012) 2007bi (Gal-Yam et al. 2009), which showed an extremely bright absolute peak-magnitude

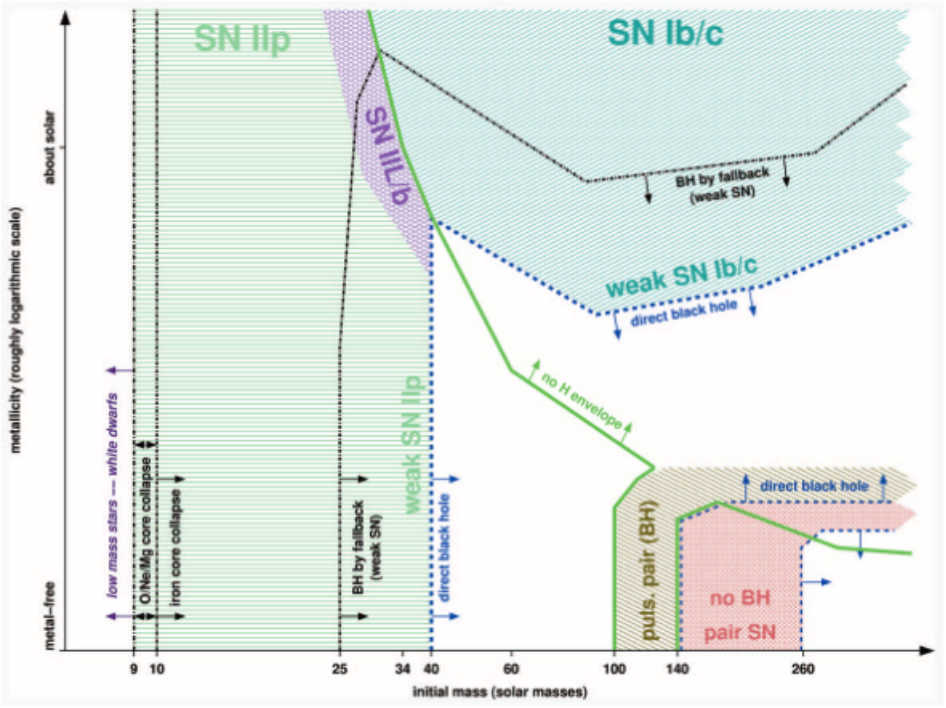

Figure 1.14: Supernova types produced by single non-rotating stars, as a function of initial metallicity and mass. (Figure from Heger et al. 2003).

($R = -21.3$ mag) and a large expelled ^{56}Ni mass ($M \simeq 5\ \mathrm{M}_{\odot}$). Moreover, its spectra did not show evident H features. However, despite the PPI mechanism was appealing for SN 2007bi, alternative and more reliable scenarios have been proposed (e.g. H-free ejecta-CSM interaction or magnetar spin-down; Nicholl et al. 2014; Sorokina et al. 2015).

A similar mechanism, the 'pulsational pair instability' (PPI; Woosley et al. 2007) was also proposed to explain the observable displayed by extremely luminous transients, but also some SN impostors (see Chapter 3). Although the direct consequence of the PPI mechanism is not the complete disruption of the progenitor star, violent ejections of shells, and their subsequent collisions, are triggered by the same mechanism producing PISN. In the PPI mechanism (expected in stars in the $90 - 140\ \mathrm{M}_{\odot}$ mass range) the electron-positron production and the subsequent explosive burning are not sufficient to unbind the star, and the core contracts reaching a new stable burning state. When the following explosion occurs, the massive shells collide, producing up to 10^{50} erg of radiated energy (Woosley et al. 2007).

Weak CCSNe can be explained by invoking different scenarios, although still involving a gravitational CC. A CCSN with fall-back explosion mechanism has been proposed to explain also underluminous transients. Fallback SNe arise from the collapse of massive stars when the explosion has not enough energy to unbind the inner mantle, which instead falls back onto the newly formed neutron star. As a result, a fraction of the stellar envelope does not contribute to the total amount of ejected material, therefore affecting both the resulting photometric and spectroscopic SN features.

Electron-capture (EC) reactions may also be an alternative mechanism triggering the final collapse of ONeMg-rich cores of super-AGB stars with initial masses of $10 - 11\ \mathrm{M}_{\odot}$. As the central density exceeds a critical level, Mg nuclei may capture free electrons and lower

the degenerate pressure of the core, triggering the gravitational collapse (Miyaji et al. 1980). The resulting SN is called ECSN, and this mechanismmay explain weak SNe. A promising ECSN candidate is SN 2008S (Botticella et al. 2009), which showed a faint absolute peak magnitude ($\simeq -14$ mag) and SN-like light-curves with a radioactive tail consistent with that predicted by the ^{56}Co decay (although it shared some similarities with SN impostors; Steele et al. 2008).

References

Alekseev, E. N., Alekseeva, L. N., Krivosheina, I. V., & Volchenko, V. I. 1987, European Southern Observatory Conference and Workshop Proceedings, 26, 237

Baade, W., & Zwicky, F. 1934, Contributions from the Mount Wilson Observatory, vol. 3, pp.73-78, 3, 73

Barbon, R., Ciatti, F., & Rosino, L. 1979, A&A, 72, 287

Barbon, R., Buondí, V., Cappellaro, E., & Turatto, M. 1999, A&AS, 139, 531

Barbon, R., Benetti, S., Cappellaro, E., et al. 1995, A&AS, 110, 513

Barkat, Z., Rakavy, G., & Sack, N. 1967, Physical Review Letters, 18, 379

Benetti, S. 1991, IAU Circ., 5405, 2

Benetti, S., Turatto, M., Balberg, S., et al. 2001, MNRAS, 322, 361

Bethe, H. A., & Wilson, J. R. 1985, ApJ, 295, 14

Bond, J. R., Arnett, W. D., & Carr, B. J. 1984, ApJ, 280, 825

Botticella, M. T., Pastorello, A., Smartt, S. J., et al. 2009, MNRAS, 398, 1041

Bower, G. C., Filippenko, A. V., Ho, L. C., et al. 1993, Bulletin of the American Astronomical Society, 25, #19.03

Branch, D., Nomoto, K., & Filippenko, A. V. 1991, Comments on Astrophysics, 15, 221

Branch, D., Benetti, S., Kasen, D., et al. 2002, ApJ, 566, 1005

Branch, D., Dang, L. C., Hall, N., et al. 2006, PASP, 118, 560

Bravo, E., & García-Senz, D. 1999, MNRAS, 307, 984

Bruenn, S. W. 1993, Nuclear Physics in the Universe, 31

Burrows, A., & Lattimer, J. M. 1987, ApJ, 318, L63

Burrows, A. 2000, Nature, 403, 727

Candia, P., Krisciunas, K., Suntzeff, N. B., et al. 2003, PASP, 115, 277

Cappellaro, E., Evans, R., & Turatto, M. 1999, A&A, 351, 459

Cappellaro, E., Patat, F., Mazzali, P. A., et al. 2001, ApJ, 549, L215

Chassagne, R. 2000, IAU Circ., 7528, 1

Chevalier, R. A., & Plait, P. C. 1988, ApJ, 331, L109

Chevalier, R. A., & Fransson, C. 1994, ApJ, 420, 268

Clayton, D. D. 1984, Principles of stellar evolution and nucleosynthesis.. D. D. Clayton.2nd edition. The University of Chicago Press, Chicago

Dessart, L., Hillier, D. J., Woosley, S., et al. 2015, MNRAS, 453, 2189

Dilday, B., Howell, D. A., Cenko, S. B., et al. 2012, Science, 337, 942

Doherty, C. L., Siess, L., Lattanzio, J. C., & Gil-Pons, P. 2010, MNRAS, 401, 1453

Drenkhahn, G., & Richtler, T. 1999, A&A, 349, 877

Eldridge, J. J., Fraser, M., Maund, J. R., & Smartt, S. J. 2015, MNRAS, 446, 2689

Falk, S. W., & Arnett, W. D. 1977, ApJS, 33, 515

Filippenko, A. V. 1988, AJ, 96, 1941

Filippenko, A. V., Richmond, M. W., Matheson, T., et al. 1992a, ApJ, 384, L15

Filippenko, A. V., Richmond, M. W., Branch, D., et al. 1992b, AJ, 104, 1543

Filippenko, A. V., Barth, A. J., Bower, G. C., et al. 1995, AJ, 110, 2261

Filippenko, A. V. 1997, ARA&A, 35, 309

Fink, M., Hillebrandt, W., Rópke, F. K. 2007, A&A, 476, 1133

Fisher, A., Branch, D., Hatano, K., & Baron, E. 1999, MNRAS, 304, 67

Foley, R. J., Smith, N., Ganeshalingam, M., et al. 2007, ApJ, 657, L105

Foley, R. J., Challis, P. J., Chornock, R., et al. 2013, ApJ, 767, 57

Fransson, C., Chevalier, R. A., Filippenko, A. V., et al. 2002, ApJ, 572, 350

Fransson, C., Larsson, J., Migotto, K., et al. 2015, ApJ, 806, L19

Fryer, C. L., Mazzali, P. A., Prochaska, J., et al. 2007, PASP, 119, 1211

Gal-Yam, A., Mazzali, P., Ofek, E. O., et al. 2009, Nature, 462, 624

Gal-Yam, A. 2012, Science, 337, 927

Gibson, B. K., Stetson, P. B., Freedman, W. L., et al. 2000, ApJ, 529, 723

Gil-Pons, P., Suda, T., Fujimoto, M. Y., & García-Berro, E. 2005, A&A, 433, 1037

Goodrich, R. W., Stringfellow, G. S., Penrod, G. D., & Filippenko, A. V. 1989, ApJ, 342, 908

Hamuy, M., Phillips, M. M., & Seargent, D. A. J. 1987, IAU Circ., 4398, 1

Hamuy, M., Maza, J., Antezana, R., et al. 1992, IAU Circ., 5468, 1

Hamuy, M., Phillips, M. M., Suntzeff, N. B., et al. 2003, Nature, 424, 651

Heger, A., Langanke, K., Martínez-Pinedo, G., & Woosley, S. E. 2001, Physical Review Letters, 86, 1678

Heger, A., & Woosley, S. E. 2002, ApJ, 567, 532

Heger, A., Fryer, C. L., Woosley, S. E., Langer, N., & Hartmann, D. H. 2003, ApJ, 591, 288

Hicken, M., Garnavich, P. M., Prieto, J. L., et al. 2007, ApJ, 669, L17

Hillebrandt, W., & Niemeyer, J. C. 2000, ARA&A, 38, 191

Hillebrandt, W., Sim, S. A., Rópke, F. K. 2007, A&A, 465, L17

Hoeflich, P., & Khokhlov, A. 1996, ApJ, 457, 500

Houck, J. C., & Fransson, C. 1994, Bulletin of the American Astronomical Society, 26, #79.07

Howell, D. A., Sullivan, M., Nugent, P. E., et al. 2006, Nature, 443, 308

Hillebrandt, W., Sim, S. A., Röpke, F. K. 2007, A&A, 465, L17

Howell, D. A., Sullivan, M., Nugent, P. E., et al. 2006, Nature, 443, 308

Knop, S., Hauschildt, P. H., Baron, E., & Dreizler, S. 2007,A&A, 469, 1077

Khokhlov, A. M. 1991, A&A, 245, 114

Jakobsen, P., Albrecht, R., Barbieri, C., et al. 1991, ApJ, 369, L63

Janka, H.-T., Langanke, K., Marek, A., Martínez-Pinedo, G., Müller, B. 2007, Phys. Rep., 442, 38

Laaksonen, B. D., Romanishin, W., & Marschall, L. A. 1994, Bulletin of the American Astronomical Society, 26, #79.13

Larsson, J., Fransson, C., Östlin, G., et al. 2011, Nature, 474, 484

Leibundgut, B., Kirshner, R. P., Phillips, M. M., et al. 1993, AJ, 105, 301

Li, W., Filippenko, A. V., Gates, E., et al. 2001, PASP, 113, 1178

Li, W., Filippenko, A. V., Chornock, R., et al. 2003, PASP, 115, 453

Martin, P., Li, W. D., Qiu, Y. L., & West, D. 2002, IAU Circ., 7809, 3

McCray, R. 1993, ARA&A, 31, 175

Matheson, T., Filippenko, A. V., Chornock, R., Leonard, D. C., & Li, W. 2000, AJ, 119, 2303

Matheson, T. 2001, PASP, 113, 1155

Mayle, R., & Wilson, J. R. 1988, ApJ, 334, 909

Mazzali, P. A., Röpke, F. K., Benetti, S., & Hillebrandt, W. 2007, Science, 315, 825

McCully, C., Jha, S. W., Foley, R. J., et al. 2014, Nature, 512, 54

Miyaji, S., Nomoto, K., Yokoi, K., & Sugimoto, D. 1980, PASJ, 32, 303

Millard, J., Branch, D., Baron, E., et al. 1999, ApJ, 527, 746

Minkowski, R. 1941, PASP, 53, 224

Myra, E. S., & Bludman, S. A. 1989, ApJ, 340, 384

Nicholl, M., Smartt, S. J., Jerkstrand, A., et al. 2014, MNRAS, 444, 2096

Niemeyer, J. C. 1999, ApJ, 523, L57

Nomoto, K. 1980, Space Sci. Rev., 27, 563

Nomoto, K., Thielemann, F.-K., Yokoi, K., & Branch, D. 1986, Ap&SS, 118, 305

Nomoto, K., Yamaoka, H., Pols, O. R., et al. 1994, Nature, 371, 227

Pastorello, A., Zampieri, L., Turatto, M., et al. 2004, MNRAS, 347, 74

Pastorello, A., Della Valle, M., Smartt, S. J., et al. 2007, Nature, 449, 1

Pastorello, A., Mattila, S., Zampieri, L., et al. 2008, MNRAS, 389, 113

Pastorello, A., Valenti, S., Zampieri, L., et al. 2009, MNRAS, 394, 2266

Pastorello, A., Wang, X.-F., Ciabattari, F., et al. 2016, MNRAS, 456, 853

Patat, F., Barbon, R., Cappellaro, E., & Turatto, M. 1994, A&A, 282, 731

Perlmutter, S., Aldering, G., Goldhaber, G., et al. 1999, ApJ, 517, 565

Phillips, M. M., Wells, L. A., Suntzeff, N. B., et al. 1992, AJ, 103, 1632

Phillips, M. M. 1993, ApJ, 413, L105

Phillips, M. M., Lira, P., Suntzeff, N. B., et al. 1999, AJ, 118, 1766

Phillips, M. M., Li, W., Frieman, J. A., et al. 2007, PASP, 119, 360

Pfannes, J. M. M., Niemeyer, J. C., Schmidt, W., & Klingenberg, C. 2010, A&A, 509, A74

Poelarends, A. J. T., Herwig, F., Langer, N., & Heger, A. 2008, ApJ, 675, 614

Porter, A. C., & Filippenko, A. V. 1987, AJ, 93,1372

Quimby, R. M., Kulkarni, S. R., Kasliwal, M. M., et al. 2011, Nature, 474, 487

Rakavy, G., & Shaviv, G. 1967, ApJ, 148, 803

Reynolds, S. P., Borkowski, K. J., Green, D. A., et al. 2008, ApJ, 680, L41

Richardson, D., Branch, D., Casebeer, D., et al. 2002, AJ, 123, 745

Richardson, D., Branch, D., & Baron, E. 2006, AJ, 131, 2233

Riess, A. G., Filippenko, A. V., Challis, P., et al. 1998, AJ, 116, 1009

Ritossa, C., Garcia-Berro, E., & Iben, I., Jr. 1996, ApJ, 460, 489

Röpke, F. K., Hillebrandt, W., Schmidt, W., et al. 2007, ApJ, 668, 1132

Ruiz-Lapuente, P., Cappellaro, E., Turatto, M., et al. 1992, ApJ, 387, L33

Sanduleak, N. 1970, Contributions from the Cerro Tololo Inter-American Observatory, 89

Sasaki, M., Kosugi, G., Ishigaki, T., et al. 1994, PASJ, 46, L187

Scalzo, R. A., Aldering, G., Antilogus, P., et al. 2010, ApJ, 713, 1073

Scannapieco, E., Madau, P., Woosley, S., Heger, A., & Ferrara, A. 2005, ApJ, 633, 1031

Schlegel, E. M. 1990, MNRAS, 244, 269

Schmidt, B. P., Kirshner, R. P., Leibundgut, B., et al. 1994, ApJ, 434, L19

Siess, L. 2006, A&A, 448, 717

Smartt, S. J. 2009, ARA&A, 47, 63

Sorokina, E., Blinnikov, S., Nomoto, K., Quimby, R., & Tolstov, A. 2015, arXiv:1510.00834

Spiro, S., Pastorello, A., Pumo, M. L., et al. 2014, MNRAS, 439, 2873

Steele, T. N., Silverman, J. M., Ganeshalingam, M., et al. 2008, Central Bureau Electronic Telegrams, 1275, 1

Swesty, F. D., Lattimer, J. M., & Myra, E. S. 1994, ApJ, 425, 195

Taubenberger, S., Benetti, S., Childress, M., et al. 2011, MNRAS, 412, 2735

Turatto, M. 2003, Supernovae and Gamma-Ray Bursters, 598, 21

Turatto, M., Benetti, S., Cappellaro, E., et al. 1996, MNRAS, 283, 1

Turatto, M., Mazzali, P. A., Young, T. R., et al. 1998, ApJ, 498, L129

Turatto, M., Benetti, S., & Pastorello, A. 2007, Supernova 1987A: 20 Years After: Supernovae and Gamma-Ray Bursters,937, 187

Utrobin, V. P. 1984, Ap&SS, 98, 115

Utrobin, V. P., Chugai, N. N., & Pastorello, A. 2007, A&A, 475,973

Van Dyk, S. D., Peng, C. Y., Barth, A. J., & Filippenko, A. V. 1999, AJ, 118, 2331

Van Dyk, S. D., Peng, C. Y., King, J. Y., et al. 2000, PASP, 112, 1532

Waldman, R. 2008, IAU Symposium, 252, 329

Wang, B., Justham, S., & Han, Z. 2013, A&A, 559, A94

Weaver, T. A., & Woosley, S. E. 1980, Supernovae Spectra, 63, 15

Wheeler, J. C., Harkness, R. P., Clocchiatti, A., et al. 1994, ApJ, 436, L.135

Wheeler, J. C., & Benetti, S. 2000, Allen's Astrophysical Quantities, 451

Wilson, J. R., Mayle, R., Woosley, S. E., & Weaver, T. 1986, Annals of the New York Academy of Sciences, 470, 267

Woosley, S. E., Arnett, W. D., & Clayton, D. D. 1973, ApJS, 26, 231

Woosley, S. E., Weaver, T. A., & Taam, R. E. 1980, Texas Workshop on Type I Supernovae, 96

Woosley, S. E., Taam, R. E., & Weaver, T. A. 1986, ApJ, 301, 601

Woosley, S. E., Heger, A., & Weaver, T. A. 2002, Reviews of Modern Physics, 74, 1015

Woosley, S., & Janka, T. 2005, Nature Physics, 1, 147

Woosley, S. E., Blinnikov, S., & Heger, A. 2007, Nature, 450, 390

Woosley, S. E., & Heger, A. 2015, ApJ, 810, 34

Zampieri, L., Pastorello, A., Turatto, M., et al. 2003, MNRAS, 338, 711

Zwicky, F. 1965, Stellar Structure - Stars and Stellar Systems, VIII, 367

Chapter 2

Data reduction

2.1 Preliminary reduction

Preliminary steps for both photometry and spectroscopy reduction consisted in overscan, bias and flat-field corrections. Pre-reductions were performed using standard IRAF tasks. Master-biases were obtained averaging a number of single bias frames obtained during the same nights, while flat fields were obtained median combining a number of dome or sky flats in the case of spectroscopic or photometric flats respectively. Master-biases and master-flats were obtained using the tasks ZEROCOMBINE and FLATCOMBINE respectively. Science images were first corrected for overscan, trimmed in order to keep scientifically relevant regions only, and finally corrected for master-biases and master-flats. These steps were performed sequentially using the task CCDPROC. Pre-reduction steps for Near Infra-Red (NIR) images included also sky subtraction. Sky images were obtained by median-combining dithered images and then subtracted to the individual frames. Stacked NIR images were generated by combining these frames, in order to increase the signal-to-noise ratio (SNR).

2.2 Spectroscopy

The spectra of the sources were processed using standard IRAF tasks included in the CTIOSLIT package. Monodimensional spectra were obtained performing an optimised extraction along the dispersion axis, after subtracting night sky lines and the contribution of the host galaxy using the task APALL.

Wavelength calibration was performed using the spectra of comparison lamps (usually He, Ne, Ar and/or Cd) obtained with the same instrumental configuration and identifying the arc lines through the IDENTIFY task. The accuracy of the wavelength calibration was then checked comparing the positions of the night sky lines in the spectra, and a rigid shift in wavelength was applied in case of discrepancy. The final accuracy is, in general, < 1 Å. At this stage, the spectral resolution was also computed using the mean values of the *full-width-at-half-maximum* (FWHM) of unblended night sky lines (usually the same lines used to check the wavelength calibration).

The flux calibration was the performed using the spectra of standard stars from the ESO spectrophotometric standards list[1]. The accuracy of the flux calibration is typically $10-15\%$, and is limited by the sky conditions and/or slit losses due to non perfect positioning of the slit on the target. Most of the spectra used in this project were obtained using slit aligned with

[1] `https://www.eso.org/sci/observing/tools/standards/spectra/stanlis.html`

the parallactic angle in order to minimize the effects of the atmospheric differential refraction on the flux calibration (Filippenko 1982).
The spectra were also corrected fror reddening originating either in the host galaxy and foreground Galactic extinction along the line of sight. For the objects studied in this thesis, the absence of narrow absorption lines of the Na ID doublet at the recessional velocity of the parent galaxies suggests a negligible contribution of the hosts to the total extinction. For this reason, the only contribution considered for the reddening was the Galactic extinction, provided by the recalibration of the infrared-based dust map of Schlegel et al. (1998) performed by Schlafly & Finkbeiner (2011). These values were available in the NASA/IPAC Extragalactic Database (NED[2]) or the HyperLeda database[3] (Makarov et al. 2014). This map is based on dust emission from COBE/DIRBE and IRAS/ISSA, assuming a reddening law with $R_V = 3.1$ (Cardelli et al. 1989; Fitzpatrick 1999).

The flux calibrations were finally checked against multi-band photometry obtained on the nearest nights and, if necessary, a scaling factor was applied. This check was performed using the IRAF task CALCPHOT included in the Space Telescope Science Data Analysis System (STSDAS[4]) package, which gives the magnitudes in a given passband for a specific spectrum. The scaling factor was computed from the comparison of these magnitudes and those obtained by multi-band photometry using the Pogson relation:

$$\frac{I}{I_0} = 10^{-0.4(M_{i,phot} - M_{i,spec})}. \tag{2.1}$$

When possible, broad telluric absorption features were subtracted using the spectra of standard stars. Differential refraction, uncertain sensitivity curves at the extremes or second order contaminations strongly affect the results of this correction, which is not always accurate. Calibrated spectra were finally corrected for the redshifts of the host galaxies, derived from the recessional heliocentric velocities reported in the NED or HyperLeda archives, or from the positions of the host galaxy narrow lines.

An example of spectrum obtained with IRAF and following the steps described below is shown in Figure 2.1.

2.3 Photometry

Photometric observations of the objects presented in this thesis were carried out using a number of instruments equipped with broad-band $UBVRI$ and $ugriz$ filters for the optical part, while JHK filters were used to obtain NIR photometry. Measured magnitudes were first computed using the relation:

$$m_\lambda = m\prime_\lambda + 2.5 \log (t_{exp}) - K_\lambda \times airm \tag{2.2}$$

where K_λ is the atmospheric extinction coefficient which depends on the observing site, t_{exp} is the exposure time and *airm* is the airmass of the object at the moment of the observation.

Two main techniques can be used to obtain SN photometry. Simple aperture photometry is the measurement of counts occurring inside a particular aperture, usually circular, of a given size ($3 - 4$ times the typical image *full-width-at-half-maximum*: FWHM). In this tech-

[2] `https://ned.ipac.caltech.edu`
[3] http://leda.univ-lyon1.fr/
[4] `http://www.stsci.edu/institute/software_hardware/stsdas/download-stsdas`

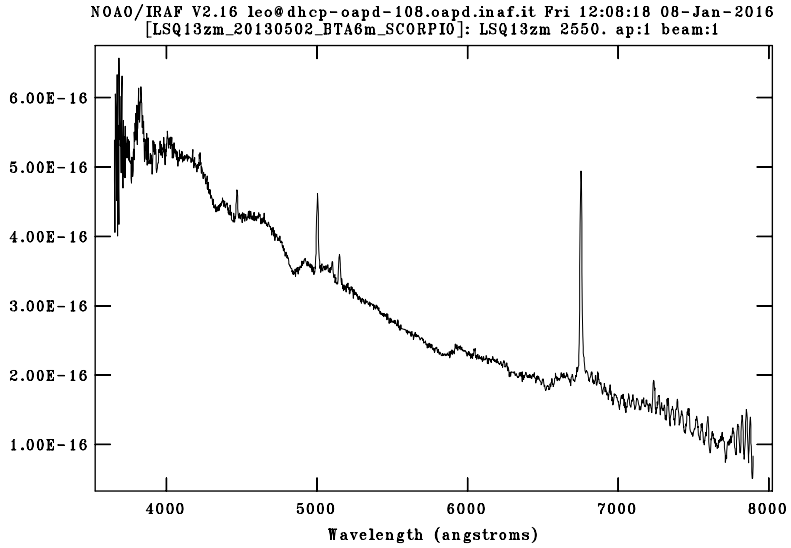

Figure 2.1: A spectrum of LSQ13zm (Tartaglia et al. submitted to MNRAS), obtained following the steps described in Section 2.2. The spectrum was calibrated using photometric data obtained during the closest night.

nique, the background is generally estimated (and subsequently subtracted) by measuring the foreground flux in an annulus around the source. Mode or median values of these counts are usually adopted as the final background estimate in order to account for bad pixels or cosmic rays that may be detected in the proximity of the source, although this implicitly assumes a constant background around the source of interest. While this assumption is valid in the case of isolated objects on a flat background, in general it fails in the case of SNe, when the source is relatively faint, or when the background has a more complex profile (e.g. when the source lies in a relatively crowded (or bright) region of its host galaxy.

The template-subtraction technique gives most accurate results when the SN lies in bright regions (e.g. the nucleus) of the host, but still presents some complications. Template images, for example, are not always available, and in many cases must be obtained more than 1 year after maximum to be confident that the object completely faded below the detection threshold. Moreover, additional complications arise if the template image is obtained with different telescopes (and instruments), and different sky conditions. Ideally, templates images should be obtained in the same observational conditions, since differences in these external conditions strongly affect the quality of the resulting subtracted images.

A slightly different approach to this technique was adopted by Richmond et al. (1995) for the photometric analysis of SN 1994D. In that particular case, the SN exploded in the proximity of the bright nucleus of NGC 4526 and aperture photometry produced unreliable results[5]. Given the axial symmetry of the host galaxy, their approach consisted into producing an artificial template using a specular image of the SN field (Figure 2.2).

Accurate SN photometry has to account for the contamination from different sources of disturbance. While at early phases the luminosity of the transient can be well above the back-

[5]Nonetheless, given the very low contribution of the host galaxy at the Ultra-Violet wavelengths, U-band magnitudes were obtained through the aperture photometry techinque.

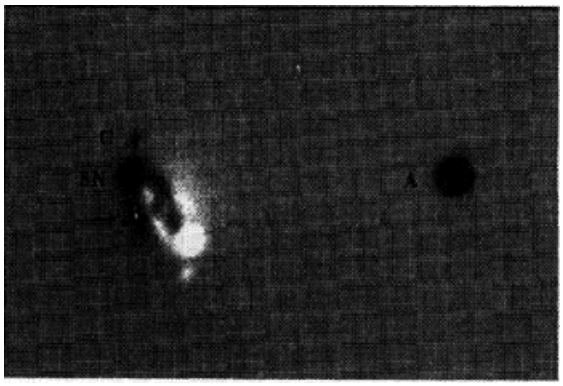

Figure 2.2: Central region of the subtracted image obtained for NGC 4526 with the technique described in Richmond et al. (1995).

ground level, as the luminosity decreases after the maximum light, the SNR of the source declines accordingly. A major complication is often related to the contamination from the host galaxy at the position of the transient. The contribution of this contamination source varies from event to event, and strongly depends on the position of the SN within the galaxy, but also on the morphological properties of the host itself. Photometric reduction strategies have hence to account for these sources of uncertainty, in particular at late phases, when the luminosity of the transient fades. Simple aperture photometry, useful in the case of isolated sources, or when the SNR of the transient is high, is not an efficient tool in the case of SN photometry.

An alternative approach to obtain good-quality photometric measurements is the *point-spread-function* (PSF) fitting technique. PSF-fitting is also largely adopted to obtain photometry of crowded fields, such as globular clusters, open clusters, as well as some Galactic fields. It mainly consists in the measurement of the local PSF using a few selected stars in the field. The background is estimated through a low order polynomial function and subtracted, and finally the modeled PSF is fitted to the source in order to get a final instrumental magnitude.

The calibration of instrumental magnitudes obtained with the aperture photometry or the PSF-fitting technique is generally performed through the comparison of the magnitudes of standard fields stars from known catalogues (e.g. SDSS, Landolt, 2MASS) with those obtained for the same set of stars during photometric nights. Each observed star provides the following set of equations:

$$\Delta m_{i,\lambda} = m_{0,i,\lambda} - m_{i,\lambda} = a_{i,\lambda} + b_{i,\lambda} \times (colour)_{\lambda} \tag{2.3}$$

where Δm represents the difference between the measured and calibrated magnitudes of the *i-th* standard star, $m_{0,\lambda}$ is the archival magnitude of the single standard star, m_{λ} is the instrumental magnitude obtained from Equation 2.2, while a_{λ} and b_{λ} are the instrumental zero point (ZP) and colour-term (CT), respectively. The solution of this set of equations gives the mean a_{λ} and b_{λ} values, which are then used to calibrate the SN magnitudes. No CT corrections were applied to the NIR calibrations. ZPs and CTs allowed also to calibrate local sequences of reference stars, that were used to calibrate images obtained during non-photometric nights.

Final multi-band colours and absolute magnitudes were computed taking into account the total reddening at the positions of the different sources (as discussed in Section 2.2), while

distance moduli were usually derived, using the 'Virgo Infall' velocities[6], through the Ned Wright's Cosmological Calculator[7] adopting a standard cosmology ($H_0 = 73$ km s^{-1} Mpc^{-1}, $\Omega_\Lambda = 0.7$ and $\Omega_M = 0.3$).

2.4 SN photometry using SNOoPY

The final magnitudes of the objects presented in this thesis were obtained using the PSF-fitting technique and calibrated using the equations reported above, using a dedicated pipeline: SuperNOva PhotometrY (SNOoPY; Cappellaro 2014). SNOoPY is a reduction pipeline specifically designed to perform PSF-fitting or template subtraction on multi-band photometric data obtained with different instruments and telescopes. The pipeline consists in a collection of PYTHON scripts calling standard IRAF tasks through PYRAF. Other specific analysis tools are also used, namely SEXTRACTOR[8] (Bertin & Arnouts 1996) for source extraction and star/galaxy separation, DAOPHOT[9] (Stetson 1987) to compute the magnitudes of the sources through the PSF-fitting technique and HOTPANTS[10] to perform template subtraction. Information on specific instruments (CCD features such as *gain, read-out-noise: RON, pixel-scales* and *datamin/datamax*, filters, UTs, sites and exposures) are available for a number of telescopes, but other specific instruments can be included in a configuration file (called 'snoopy.default'), so that photometry can be computed also from images obtained with different instrumental set-up configurations. An example of configuration file (for the instrument AFOSC mounted at the 1.82 m Copernico telescope located at Mount Ekar, Asiago, Italy) is reported below:

```
[AFOSC]
site:       ASIAGO
datamin:    -100
datamax:    60000.
epadu:      0.9
readnoise:  7.8
object:     OBJECT
exposure:   EXPTIME
mjd:        MJD
dateobs:    DATE-OBS
airmass:    AIRMASS
filter:     FILTER
scale:      0.52
seeing:     PSF_FWHM
UBVRI:      U,B-Bessel,V-Bessel,R-Bessel,I
ugriz:      u-Sloan,g-Sloan,r-Sloan,i-Sloan,z-Sloan
```

Different instruments can be included in the configuration file, so the photometric analysis can be performed simultaneously on different images. CCD gain and RON are used for cosmic-rays rejections. The pixel-scale is another fundamental feature, which is mostly used in the PSF determination. The keyword relative to the 'Modified Julian Date' (defined as JD − 2400000.5) is also used by the pipeline in the calibration of the instrumental magnitudes (as will be described in Section 2.4.5).

[6] based on the model of Mould et al. (2000) considering the influence of the Virgo Cluster only

[7] http://www.astro.ucla.edu/~wright/CosmoCalc.html

[8] http://www.astromatic.net/software/sextractor

[9] http://www.star.bris.ac.uk/~mbt/daophot/

[10] http://www.astro.washington.edu/users/becker/v2.0/hotpants.html

2.4.1 Preliminary steps

Pre-reduced images (see Section 2.1) can be organised in lists and different pre-requisites can be tested using the command ECLIST, which performs different checks on the image headers, giving error messages when any crucial keywords or information on the instrumental set-up are missing. An example of an ECLIST output is reported below:

```
-------------------------------------------------------------------------------------------------
 filename     object    instrument     dateobs       mjd        filter   b expos airm seei
science_r PSNJ09p76 ALFOSC_FASU 2015-06-22 57195.906 r-Sloan r  120  1.98 0.99
science_i PSNJ09p76 ALFOSC_FASU 2015-06-22   ERROR   i-Sloan i  120  1.90 0.98
science_z PSNJ09p76 ALFOSC_FASU 2015-06-22 57196.012 z_Sloan z  120  1.90 ERROR
-------------------------------------------------------------------------------------------------
********** Completed in  0 sec
```

where the 'MJD' is missing in the i-band image, while the z-band image does not include the keyword relative to the seeing. In the first case, the task ECMJD can be used, which reads basic information in the image header (such as the UT date of the observation) and computes the MJD of the frame's exposure:

```
usage: ecmjd.py [-h] [-d DATEOBS] [-t TIMESTART] [-e EXPTIME] [-m MJDKWR] [-r]
                [-v]
                list

Compute MJD and update keyword

positional arguments:
  list                  file list

optional arguments:
  -h, --help            show this help message and exit
  -d DATEOBS, --dateobs DATEOBS
                        DATE OBS keywork or 1900/01/31 (default: DATE-OBS)
  -t TIMESTART, --timestart TIMESTART
                        UT start OBS keyword or 00:00:00 (default: 00:00:00)
  -e EXPTIME, --exptime EXPTIME
                        EXPTIME keyword or seconds (default: 0)
  -m MJDKWR, --mjdkwr MJDKWR
                        MJD keyword (default: MJD-OBS)
  -r, --redo            Re-do (default: False)
  -v, --verbose         Print diagnostic informations (default: False)
```

The seeing can be computed using the ECSEEING task:

```
usage: ecseeing.py [-h] [-r] [-t THRESHOLD] [-i] imglist

Measure seeing

positional arguments:
  imglist               iraf format

optional arguments:
  -h, --help            show this help message and exit
  -r, --rseeing         re-measure seeing (default: False)
  -t THRESHOLD, --threshold THRESHOLD
                        Source detection threshold (default: 10.0)
  -i, --interactive     interactively select stars (default: False)
```

which measures the mean FWHM from non-saturated stars. Note that in the given image, or list of images, a valid astrometric calibration must already be performed. New keywords

are hence added to the image headers, corresponding to the name given in the SNOoPY default file.

Astrometric calibration has to be performed before starting. Astrometry can be checked using the CHECK option in the ECLIST task. The task ECASTROAUTO automatically performs astrometric calibration on an image (or a list of images) comparing the positions of the stars in the field with either the USNO-A2.0 catalog of astrometric standards[11] or the 2MASS catalogs:

```
usage: ecastroauto.py [-h] [-r REFERENCE | -s SNCOO] [-t THRESHOLD]
                      [-c {ua2,2mass}] [-f {rscale,rxyscale,general}]
                      [-x XFRAME] [-w WSEEING] [-i] [-v]
                      imglist

Astrometric calibration

positional arguments:
  imglist               iraf format list (if * use quote)

optional arguments:
  -h, --help            show this help message and exit
  -r REFERENCE, --reference REFERENCE
                        reference image (input files must be all of the same
                        field (default: None)
  -s SNCOO, --sncoo SNCOO
                        field center: RA,DEC or file with RA DEC(input files
                        must be all of the same field) (default: None)
  -t THRESHOLD, --threshold THRESHOLD
                        Source detection threshold (default: 10.0)
  -c {ua2,2mass}, --catalog {ua2,2mass}
                        astrometric catalog (ua2|2mass) (default: 2mass)
  -f {rscale,rxyscale,general}, --fitgeometry {rscale,rxyscale,general}
                        plate solution geometry to be used (default: rscale)
  -x XFRAME, --xframe XFRAME
                        Trim border (default: 10)
  -w WSEEING, --wseeing WSEEING
                        seeing [fwhm in arcsec] (default: 1.0)
  -i, --interactive     Interactive mode (default: False)
  -v, --verify          verify mode (default: False)
```

This task is based on the IRAF task CCMAP, which uses the (RA, Dec) coordinates to generate an astrometric solution for the single frame. If a list of images is given, the first astrometric solution is used as a reference to calibrate the astrometry for all the other images.

When the source is particularly faint, and in order to avoid saturation, it is common to take a number of exposures instead of a very long one. Multiple exposures, in fact, can be median-combined in order to increase the SNR of the single images. SNOoPY combines consecutive images using the task ECDITHER:

```
usage: ecdither.py [-h] [-i] [--seeing SEEING] [-t THRESHOLD] [-x XFRAME]
                   [-l TOLERANCE] [-s] [-w] [-b BPM] [-v]
                   imglist outfile

Combine dithered images. WARNING: it herits the setting of the saved imcombine
parfile

positional arguments:
  imglist               img1,img2,... or @list
  outfile               output file name
```

[11] http://tdc-www.harvard.edu/catalogs/ua2.html

```
optional arguments:
  -h, --help            show this help message and exit
  -i, --interactive     Interactive mode (default: False)
  --seeing SEEING       seeing FWHM [arcsec] (default: 1.0)
  -t THRESHOLD, --threshold THRESHOLD
                        Source detection threshold (default: 5.0)
  -x XFRAME, --xframe XFRAME
                        Trim border (default: 5)
  -l TOLERANCE, --tolerance TOLERANCE
                        Tolerance in pixel (default: 1.0)
  -s, --sky             Subtract sky (default: False)
  -w, --wcs             use wcs (default: False)
  -b BPM, --bpm BPM     use bad pixel mask (give name)? (default: )
  -v, --verbose         Enable progress report (default: False)
```

which is based on the IRAF task IMCOMBINE. The alignment is made on the basis of the position of common sources in two different exposures, which can be selected manually (using the -i option), or automatically (e.g. selecting the -w option, if the images have already been astrometrically calibrated).

2.4.2 PSF

Several factors contribute to the variation of the PSF from one image to another, like different seeing and hence atmospheric conditions, telescope tracking, or geometric distortion over the field of view. For all these reasons, the PSF should be determined separately on each available frame.

The PSF is usually generated by averaging the profiles of a few stars in the field. Given the importance of a correct PSF determination, these sources must be selected among the best exposed, unsaturated (see Figure 2.3 for a visual example of saturated and unsaturated stars) and isolated stars in the field.

SNOoPY includes a task which automatically selects the best stars in the field using SEXTRACTOR algorithms. The automatic rejection of saturated stars is made on the basis of the *datamin* and *datamax* values included in the 'snoopy.default' file for each instrument. The task ECPSF uses the SN RA and Dec [J 2000] coordinates in an input file and returns the local average PSF. The source to be fitted is not used to compute the local PSF. Positional and optional arguments (although in general the automatic selection gives the best results) are reported below:

```
usage: ecpsf.py [-h] [-w WSEEING] [-f FITRAD] [-t THRESHOLD] [-p PSFSTARS]
                [-d DISTANCE] [-r] [-g] [-i] [-s] [-v]
                img sncoo

Automated psf creation

positional arguments:
  img                   file name
  sncoo

optional arguments:
  -h, --help            show this help message and exit
  -w WSEEING, --wseeing WSEEING
                        seeing [FWHM in pixel] (default: None)
  -f FITRAD, --fitrad FITRAD
                        fit radius (FWHM units) (default: 1.0)
  -t THRESHOLD, --threshold THRESHOLD
                        Source detection threshold (default: 10.0)
  -p PSFSTARS, --psfstars PSFSTARS
```

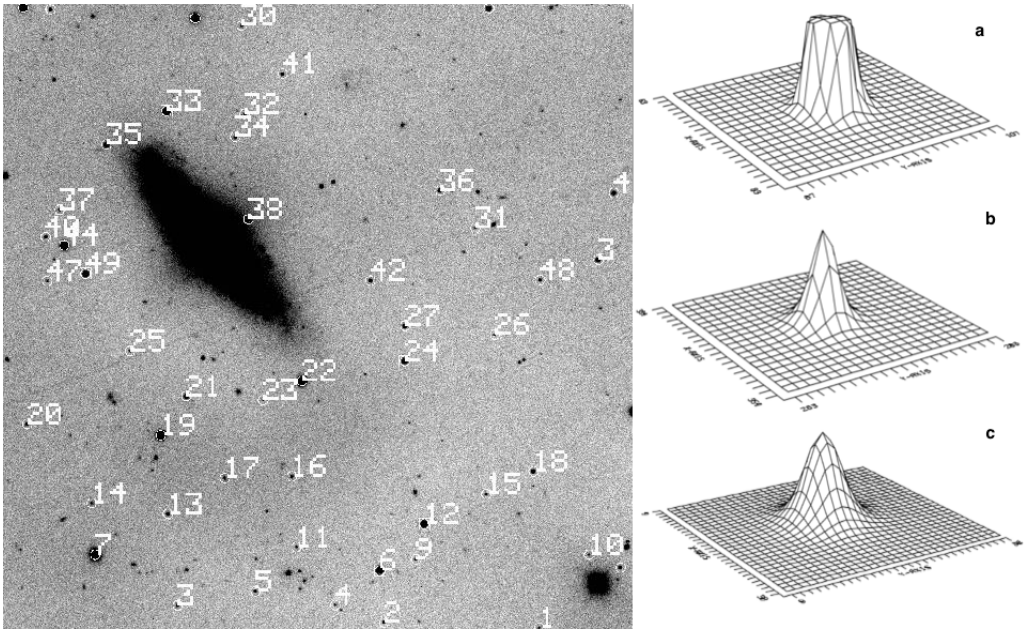

Figure 2.3: Output image of the task ECPSF. All the stars measured are labelled with a number and are marked with circles. The stars used to compute the local PSF are marked by squared circles. The procedure automatically exclude saturated or the non-isolated stars of the frame. Aperture magnitudes of all the measured stars in the field are written on a specific output file. Example of saturated **(a)** and unsaturated **(b)** star. PSF stars must be selected among the best exposed, unsaturated and isolated stars in the field. An example of a resulting PSF is also shown **(c)**.

```
                        Maximum number of psf stars (default: 5)
-d DISTANCE, --distance DISTANCE
                        Minimum star separation (in unit of FWHM) (default:
                        10)
-r, --redo              Re-do (default: False)
-g, --generic           Generic instrument (default: False)
-i, --interactive       Interactive mode (default: False)
-s, --show              Show PSF output (default: False)
-v, --verbose           Print diagnostic informations (default: False)
```

Selected stars are also displayed (see Figure 2.3 and the resulting PSF can be also checked (panel c of the same Figure) using the *-s* option. PSF stars can also be selected manually and single star profiles checked using the *-i* option.

The output consists in a file named '*.psf.fits' which contains the PSF analytical model and the residuals. A file named '*.sn' is also created, including a number of information needed for the following steps, such as the aperture photometry for all the measured stars in the field along with the magnitudes of the stars used to compute the PSF (stars labelled with circles and squared circles respectively in Figure 2.3), but also information on the instrument, filters, airmass, exposure times and MJD of the observation. An example of this output file is reported below:

```
PSNJ09p76r_sloan-image 1of2    ALFOSC_FASU    2015-06-22T21:44:17.991     57195.91 r
Exptime 120.0    Airmass 1.98006959315    FWHM[pix]    5.4    Ap.Corr. -0.029 +/- 0.033
          RA           DEC  magp(2)  magph(3)  err     mph(4)    magfit     err   diff
 9:13:13.828   76:24:45.92   -6.468   -6.522  0.028   -6.576    -6.459   0.024
 9:13:48.613   76:24:55.99   -7.220   -7.256  0.015   -7.273    -7.131   0.017
 9:13:22.041   76:24:56.16   -5.711   -5.777  0.057   -5.830    -5.751   0.038
 9:13:35.497   76:25:04.31   -6.415   -6.533  0.027   -6.614    -5.889   0.040
```

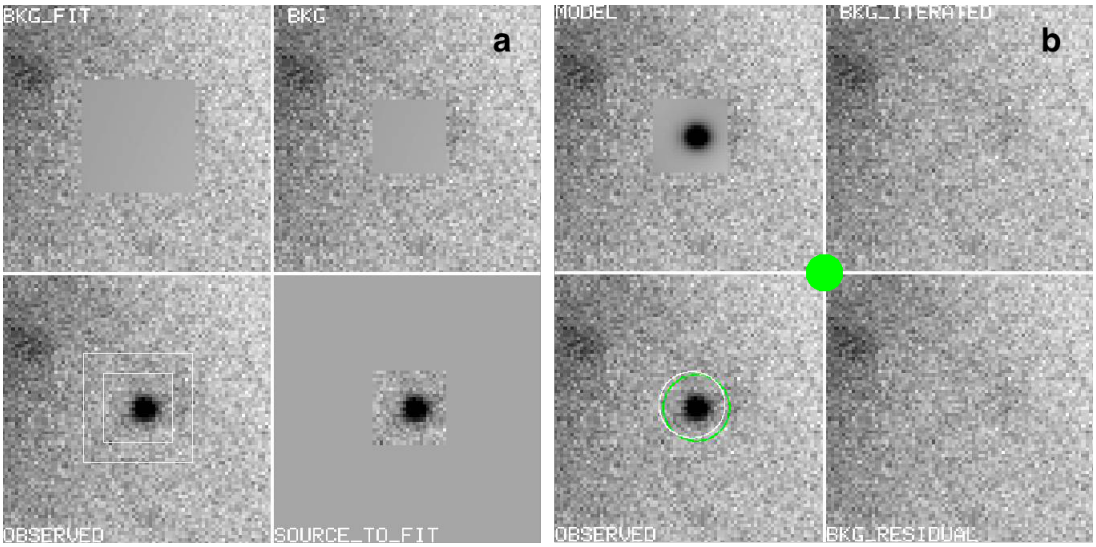

Figure 2.4: Example of image output in the interacting mode of ECSNFIT. **a)** First, background is estimated and subtracted to the region of the source, the source is then fitted and subtracted, in ordere to compute a new estimate of the background. **)** Finally, the source is fitted again using the iterated background estimate, and the residuals are shown to check the quality of the final fit. An accurate estimate of the source's centroid is also performed and the result is displayed by the green open circle in the **b** panel, while the central filled green circle indicates that the SNR estimate at the position of the sources is $\gtrsim 10$ (see Section 2.4.3).

```
 9:13:14.527   76:25:16.57  -10.224  -10.264   0.002  -10.279  -10.225   0.007  -0.039
 9:12:33.974   76:25:17.98   -6.417   -6.433   0.036   -6.488   -6.549   0.025
 9:13:08.437   76:25:23.21   -5.490   -5.507   0.069   -5.406   -5.431   0.062
 9:12:39.271   76:25:25.68   -5.339   -5.310   0.093   -5.175   -5.423   0.055
 9:13:28.584   76:25:30.50   -5.679   -5.745   0.057   -5.751   -5.680   0.040
 9:13:07.033   76:25:44.16  -10.449  -10.487   0.002  -10.501  -10.483   0.008  -0.004
```

This file contains comprehensive information about the frame, including the final instrumental magnitude of the source and the errors.

2.4.3 PSF fitting

SNOoPY performs automatic PSF-fitting with the specific task ECSNFIT:

```
usage: ecsnfit.py [-h] [-b BKG_PAR] [-f FITRAD] [-w WSIZE] [--recenter] [-r]
                  [-i] [-m] [-g] [-v]
                  img

SN fit

positional arguments:
  img                   file name

optional arguments:
  -h, --help            show this help message and exit
  -b BKG_PAR, --bkg_par BKG_PAR
                        Bgk fit annulus (in,out) and order (x,y) (default:
                        2.,3.,2,2)
  -f FITRAD, --fitrad FITRAD
                        fit radius (FWHM units) (default: 1.0)
  -w WSIZE, --wsize WSIZE
                        display window size (FWHM units) (default: 15)
  --recenter            recentering (default: True)
  -r, --redo            Re-do (default: False)
  -i, --interactive     Interactive (default: False)
```

```
  -m, --manual          Manual adjustment (default: False)
  -g, --generic         Generic instrument (default: False)
  -v, --verbose         Print diagnostic informations (default: False)
```

A file named '*.res.fits' is also generated, containing the residual of the PSF-fit (see Figure 2.4). The fitting procedure is performed as follows: the local analytic PSF is fitted to the source, whose position is obtained in pixel coordinates in the '.sn' pre-generated file (see Section 2.4.2). The procedure interactively asks the user if the input coordinates actually refer to the desired source, and a specific algorithm re-centers the target's coordinates when necessary (Figure 2.4). The local background is then estimated, and the analytic local PSF is fitted to the selected source. Using the inferred instrumental magnitude, the source is then subtracted and the background is better estimated on the 'clean' frame. This new 'iterated' background is then used to fit the analytic PSF to the source.

As SNe are transient objects, their luminosity typically fades at late phases and eventually their apparent magnitudes become fainter than the limiting magnitudes of astronomical instruments. A crucial role in determining the limiting magnitude of an astronomical image is played by the SNR for a given source in the field:

$$(SNR)_{x,y} = \frac{(I + BKG) \times adu}{\sqrt{(I + BKG) \times adu + ron^2}}, \tag{2.4}$$

which affects the precision of the photometry. The limiting magnitude is typically affected by the contribution of different sources of noise, but strongly depends on the atmospheric conditions. Sky transparency, moon light contamination and seeing are the most important sources of noise in ground-based images. The SNR of the fitted source is reported in the fit summary (Figure 2.4): a green circle is printed when the SNR is $\gtrsim 10$, a blue square appears if the SNR is between 3 and 10 and a red triangle indicated that the SNR is < 3. When no sources are detected at the SN position, SNOoPY automatically compute the limiting magnitude of the image adopting a limiting SNR of 2.5 (Figure 2.5, although this value can be changed by the user) using the task ECLIMIT:

```
usage: eclimit.py [-h] [-s SNR] [-w WSIZE] [-r] [-i] [-g] img

Estimate upper limit with artificial star

positional arguments:
  img                   file name

optional arguments:
  -h, --help            show this help message and exit
  -s SNR, --snr SNR     S/N threshold for limit (default: 2.5)
  -w WSIZE, --wsize WSIZE
                        display window size (FWHM units) (default: 15)
  -r, --redo            Re-do (default: False)
  -i, --interactive     Interactive (default: False)
  -g, --generic         Generic instrument (default: False)
```

Photometric errors are obtained through the 'artificial star' technique, in which a fake star with the same magnitude and profile of the fitted source is placed, in the background iterated PSF-fit residual image, in a position close, although not coincident, with the SN position. The artificial image is then processed through the same steps, and the magnitude of the fake star recovered using the procedures described above. The dispersion of different measurements obtained from a number of these experiments (with the artificial star placed in slightly different positions) is then taken as an estimate of the instrumental magnitude error, and combined in

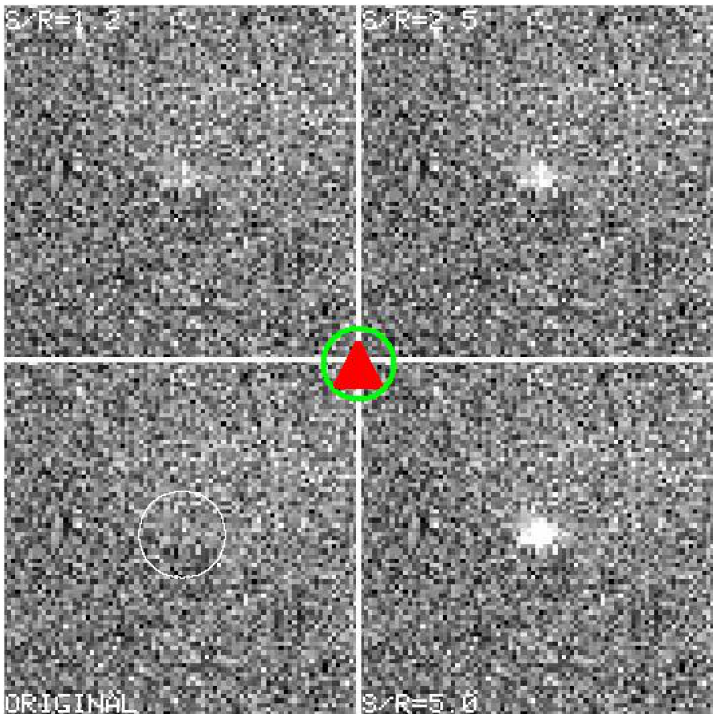

Figure 2.5: Example of limiting magnitude computation. The limiting SNR in this example was left to default value of 2.5. The circled triangle symbol indicate that the source was not detected in the image.

quadrature with the PSF-fit error returned by DAOPHOT. SNOoPY automatically performs artificial stars experiments using the task ECARTERR:

```
usage: ecarterr.py [-h] [-a ARTSHIFT] [-v] [-g] img

Artificial star experiments for latest sn fit

positional arguments:
  img                   file name

optional arguments:
  -h, --help            show this help message and exit
  -a ARTSHIFT, --artshift ARTSHIFT
                        shift [pix] for artstar experiments (default: 2.0)
  -v, --verbose         Print diagnostic informations (default: False)
  -g, --generic         Generic instrument (default: False)
```

2.4.4 Template subtraction

When a template image is available, this can be subtracted to images in which the SN is clearly visible. As stated above, this technique is particularly useful in the case of strong host galaxy contamination, or when the magnitude of the source is comparable to the background. This is performed in SNOoPY through a number of steps:

- First, a geometric transformation is computed, in order to scale the template image to the selected frame. This step is performed using several common stars in the fields, taking advantage of the astrometric calibration, which must already be performed.
- The template image is subtracted using the PSF match, degrading the image with the best seeing.

Finally, either aperture or PSF-fitting photometry can be used to the subtracted images, although SNOoPY adopts by default PSF-fitting photometry on the subtracted images also, as it proved to be less sensitive to residual background variations. SNOoPY performs the subtraction of template images using HOTPANTS, through the task ECSNDIFF :

```
usage: ecsndiff.py [-h] [-t THRESHOLD] [-s SNR] [-x XTASKS] [-i] [-v]
                   [-f FITGEOMETRY] [--nrxy NRXY] [--nsxy NSXY] [--ko KO]
                   [--bgo BGO] [--afssc] [--psfstars PSFSTARS]
                   [--distance DISTANCE] [--bkg_par BKG_PAR] [--wsize WSIZE]
                   [--recenter] [--fitrad FITRAD]
                   img ref sncoo

Image difference with hotpants and SN mag with psf fit

positional arguments:
  img                   new image
  ref                   reference
  sncoo                 sn coo

optional arguments:
  -h, --help            show this help message and exit
  -t THRESHOLD, --threshold THRESHOLD
                        Source detection threshold (default: 5.0)
  -s SNR, --snr SNR     S/N threshold for limit (default: 2.5)
  -x XTASKS, --xtasks XTASKS
                        task to be performed r-register, d-ifference, f-it
                        (default: rdf)
  -i, --interactive     interactive mode (default: False)
  -v, --verbose         Enable task progress report (default: False)

image registration:
  -f FITGEOMETRY, --fitgeometry FITGEOMETRY
                        ccmap fit geometry (rscale,rxyscale,general ...)
                        (default: rscale)

hotpants difference:
  --nrxy NRXY           number of image region in x y directions (default:
                        1,1)
  --nsxy NSXY           number of region stamps in x y directions (default:
                        8,8)
  --ko KO               spatial order of kernel variation within region
                        (default: 1)
  --bgo BGO             spatial order of background variation within region
                        (default: 1)
  --afssc               use selected stamps (default: False)

psf fit:
  --psfstars PSFSTARS   maximum number of psf stars (default: 5)
  --distance DISTANCE   minimum star separation (in unit of FWHM) (default: 5)
  --bkg_par BKG_PAR     bgk fit annulus (in,out) and order (x,y) (default:
                        2.,3.,1,1)
  --wsize WSIZE         display window size (FWHM units) (default: 15)
  --recenter            recenterig (default: True)
  --fitrad FITRAD       fit radius (FWHM units) (default: 1.0)
```

2.4.5 Calibration

The calibration of instrumental magnitudes to the final apparent magnitudes is based on the set of equations (2.3), in which the a_λ and b_λ terms play a crucial role. These terms are the ZP and CT respectively, and are fundamental parameters that should be inferred for each instrument and observational night. In SNOoPY, photometric calibration is performed using a set of selected stars in the SN field, calibrated using ZPs and CTs obtained during photometric nights with the task ECPH:

```
usage: ecph.py [-h] [-m MAG] [-p {johnson,sloan}] [-w] [-s] [-i] [-d] imglist

Measure standard field and derive zero points

positional arguments:
  imglist               list of images

optional arguments:
  -h, --help            show this help message and exit
  -m MAG, --mag MAG     Magnitude limit for standards (V band) (default: 20.0)
  -p {johnson,sloan}, --photosys {johnson,sloan}
                        photometric system (johnson|sloan) (default: johnson)
  -w, --web             Retrive Sloan table from DRS10 (default: False)
  -s, --stetson         Include stetson table (default: False)
  -i, --interactive     Interactive (default: False)
  -d, --display         Display matched star (default: False)
```

which writes ZPs and CTs for each specific instrument and photometric night in an output file. An example of this file (called 'phot.ph') is reported below:

```
### AFOSC 2012-02-28    57073
U UB 19.929 0.011 0.196 0.018
B BV 22.881 0.010 0.026 0.017
V BV 23.706 0.011 0.021 0.019
V VR 23.705 0.012 0.037 0.035
R VR 23.492 0.007 -0.019 0.020
R RI 23.492 0.007 -0.018 0.019
I RI 22.622 0.007 -0.107 0.021
u ug 21.277 0.014  0.109 0.008
g gr 24.322 0.011  0.044 0.013
r gr 24.102 0.020 -0.057 0.029
r ri 24.065 0.025  0.007 0.101
i ri 23.452 0.014  0.007 0.035
z iz 23.338 0.030 -0.358 0.219
```

The observations of 'standard' fields, namely fields of stars with well known magnitudes and range of colours is helpful to calibrate photometric data. The comparison of measured magnitudes with calibrated magnitudes directly provides ZPs and CTs for specific nights and instrumental set-ups, which can be used to calibrate the local standard sequence. Nonetheless, the observation of standard stars fields (e.g. from the lists of Landolt 1973, 1983, 1992) must be performed during photometric nights only.

Photometric conditions are ensured when the uncertainties in the final magnitudes are not affected by variations in the atmospheric throughput as well as instrumental sensitivity, and instrumental conditions are therefore constant over the sky and the observation time (Stetson 2013).

The local sequence of calibrated stars can be generated using the task ECREFSTAR:

```
usage: ecrefstar.py [-h] [-p PHOTLOG] [-i] [-c CTOLERANCE] [-v] [-a] list

Calibrate local reference stars

positional arguments:
  list                  file list

optional arguments:
  -h, --help            show this help message and exit
  -p PHOTLOG, --photlog PHOTLOG
                        Photo calibration file (default: )
  -i, --interactive     Interactive (default: False)
```

```
  -c CTOLERANCE, --ctolerance CTOLERANCE
                        coordinate matching tolerance [arcsec] (default: 1.0)
  -v, --verbose         Print diagnostic informations (default: False)
  -a, --astro           Check astrometry (default: False)
```

Alternatively, the local sequence can be obtained using the ECZEROPOINT task:

```
usage: eczeropoint.py [-h] [-p PHOTLOG] [-m MAGLIM] [-i] [-w]
                      [-c {sloan,apass}]
                      imglist

measure photometric zero point against sloan or apass

positional arguments:
  imglist               image list

optional arguments:
  -h, --help            show this help message and exit
  -p PHOTLOG, --photlog PHOTLOG
                        Photo calibration file (default: )
  -m MAGLIM, --maglim MAGLIM
                        Magnitude limit for selection (default: 19.0)
  -i, --interactive     Interactive (default: False)
  -w, --write           write catalog (default: False)
  -c {sloan,apass}, --catalog {sloan,apass}
                        photometric catalog) (default: sloan)
```

The *-w* option, in particular, checks for archival SDSS magnitudes for the given frame, and automatically writes a file containing the local standard Sloan magnitudes, but also derives (and writes in an output file) the $UBVRI$ Johnson-Cousins magnitudes using the relations obtained by Chonis & Gaskell (2008, see Equations 2.5).

$$\begin{aligned} B &= g + (0.327 \pm 0.047)(g - r) + (0.216 \pm 0.027) \\ V &= g - (0.587 \pm 0.022)(g - r) - (0.011 \pm 0.013) \\ R &= r - (0.272 \pm 0.092)(r - i) - (0.159 \pm 0.022) \\ I &= i - (0.337 \pm 0.191)(r - i) - (0.370 \pm 0.041) \end{aligned} \tag{2.5}$$

Archival photometric ZPs and CTs obtained during photometric nights are needed to calibrate non photometric nights, and must be provided in a separate file. These parameters are used by SNOoPY to determine the magnitude of the local standards in the frames obtained during non-photometric nights. Finally, these values are compared to those obtained during photometric nights using the task ECNIGHTCAL:

```
usage: ecnightcal.py [-h] [-p PHOTLOG] [-i] [-c CTOLERANCE] [-d] list localref

Check zero point fro each night/filter

positional arguments:
  list                  file list
  localref              local reference

optional arguments:
  -h, --help            show this help message and exit
  -p PHOTLOG, --photlog PHOTLOG
                        Photo calibration file (default: None)
  -i, --interactive     Interactive (default: False)
  -c CTOLERANCE, --ctolerance CTOLERANCE
                        coordinate matching tolerance [arcsec] (default: 1.0)
  -d, --display         Display position of local reference (default: False)
```

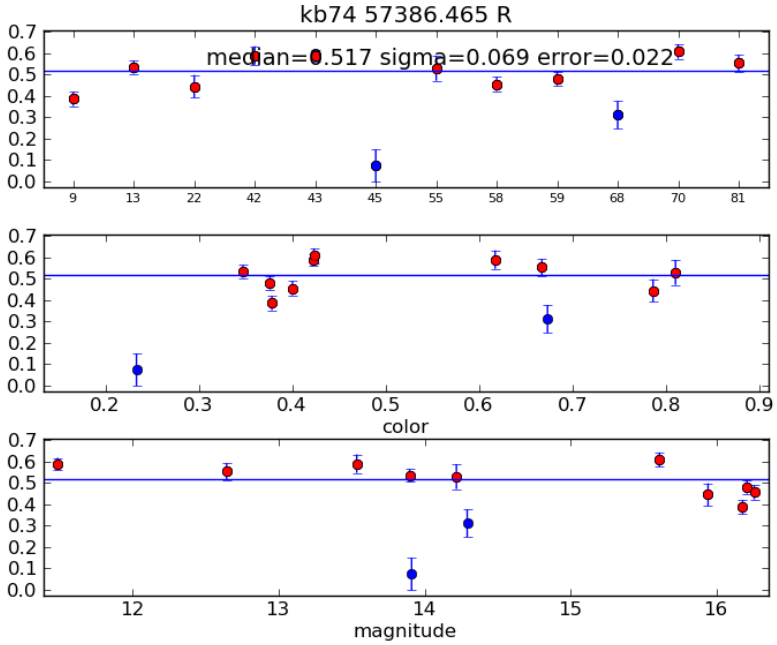

Figure 2.6: Comparison of the measured magnitudes of the stars of the local sequence in a non-photometric night with the calibrated ones. Blue stars are rejected and are not used to compute the ZP correction. Calibration errors are also reported, along with basic information on the specific frame.

producing a list of corrections to the ZPs to be applied to the images obtained during non-photometric nights which is then written in a file named 'zerocor.dat':

```
kb74 57057.320 B  0.395 0.084 V  0.499 0.029 R  0.459 0.034 I  0.417 0.046
kb74 57067.490 B  1.665 0.066 V  1.857 0.065 R  1.820 0.080 I  1.820 0.079
kb74 57073.475 B  0.439 0.063 V  0.559 0.040 R  0.520 0.027 I  0.485 0.046
```

2.4.6 Final apparent magnidutes

The final apparent magnitudes are obtained using the command ECSNCAL, which is summarised below:

```
usage: ecsncal.py [-h] [-p PHOTLOG] [-z ZEROCORFILE] [-i] list

Derive SN apparent magnitude and checks reference stars

positional arguments:
  list                  file list

optional arguments:
  -h, --help            show this help message and exit
  -p PHOTLOG, --photlog PHOTLOG
                        Photo calibration file (default: None)
  -z ZEROCORFILE, --zerocorfile ZEROCORFILE
                        File with zeropoint for each night (default: None)
  -i, --interactive     Interactive (default: False)
```

where photometric ZPs and CTs along with the information on their corrections must be provided. Corrected ZPs and CTs are applied to the instrumental magnitudes obtained in

the previous steps and final apparent magnitudes are written on a file named 'snlc.dat'. The results can be also displayed using the *-i* option.

References

Bertin, E., & Arnouts, S. 1996, A&AS, 117, 393

Cappellaro, E. (2014). SNOoPy: a package for SN photometry, `http://sngroup.oapd.inaf.it/snoopy.html`

Cardelli, J. A., Clayton, G. C., & Mathis, J. S. 1989, ApJ, 345, 245

Chonis, T. S., & Gaskell, C. M. 2008, AJ, 135, 264

Filippenko, A. V. 1982, PASP, 94, 715

Fitzpatrick, E. L. 1999, PASP, 111, 63

Landolt, A. U. 1973, AJ, 78, 959

Landolt, A. U. 1983, AJ, 88, 439

Landolt, A. U. 1992, AJ, 104, 340

Makarov, D., Prugniel, P., Terekhova, N., Courtois, H., &Vauglin, I. 2014, A&A, 570, A13

Mould, J. R., Huchra, J. P., Freedman, W. L., et al. 2000, ApJ, 529, 786

Poznanski, D., Prochaska, J. X., & Bloom, J. S. 2012, MNRAS, 426, 1465

Richmond, M. W., Treffers, R. R., Filippenko, A. V., et al. 1995, AJ, 109, 2121

Schlafly, E. F., & Finkbeiner, D. P. 2011, ApJ, 737,103

Schlegel, D. J., Finkbeiner, D. P., & Davis, M. 1998, ApJ, 500, 525

Stetson, P. B. 1987, PASP, 99, 191

Stetson, P. B. 2013, Planets, Stars and Stellar Systems. Volume 2: Astronomical Techniques, Software and Data, 1

Chapter 3

Luminous blue variables and supernova impostors

Massive stars end their life with spectacular explosions, during which they expel their mantle, leaving back compact remnants (neutron stars or black holes; see Section 1.3), whose physical properties and nature strongly depend on the stellar initial masses, but also on the mass-loss history of the progenitor stars.

Moreover, the properties of their environments strongly affect the spectroscopic and photometric features observed in SN explosions. In fact, SNe exploding in a dense CSM typically show prominent signatures of interaction of their ejecta with the pre-existing material (namely low and intermediate-width profiles in the emission lines of their spectra), and give unique clues on the progenitor's mass-loss rate. Hence, they are helpful to constrain the late evolution of very massive stars ($M > 30 - 50$ M$_\odot$), a still standing problem of modern stellar evolution theories.

The interaction between SN ejecta and dense pre-existing CSM is an hallmark feature of interacting SNe (see Section 1.3). Dense CSM is usually the result of strong winds, eruptions, or even giant eruptions (like the one experienced in the last centuries by η Car or P Cyg in the Milky Way) during the last phases of the progenitor star's evolution.

Strong eruptive events and mass loss episodes are a common feature in a class of very massive stars labelled 'luminous blue variables', which will be widely discussed in Section 3.1. Section 3.2 will introduce one of the main topic of this thesis, which is the description of a peculiar class of optical transients labelled 'SN impostors'. The proposed link among luminous blue variables, their major eruptions and some Type IIn is one of the main topics of this thesis, and it will be widely illustrated in Section 3.3.

3.1 Luminous blue variables

Luminous blue variables (LBVs, also referred to as 'Hubble-Sandage variables'; Wolf 1986; Lamers 1986) are a class of evolved, very massive ($M > 30$ M$_\odot$) unstable stars, showing wide photometric and spectroscopic variability. Given their high bolometric luminosities ($-9 \geqslant M_{\rm bol} \geqslant -11$, see e.g. Humphreys & Davidson 1994), they are very close to the so-called 'Eddington limit', defined as:

$$L_{Edd} = \frac{4\pi cGM}{k} \tag{3.1}$$

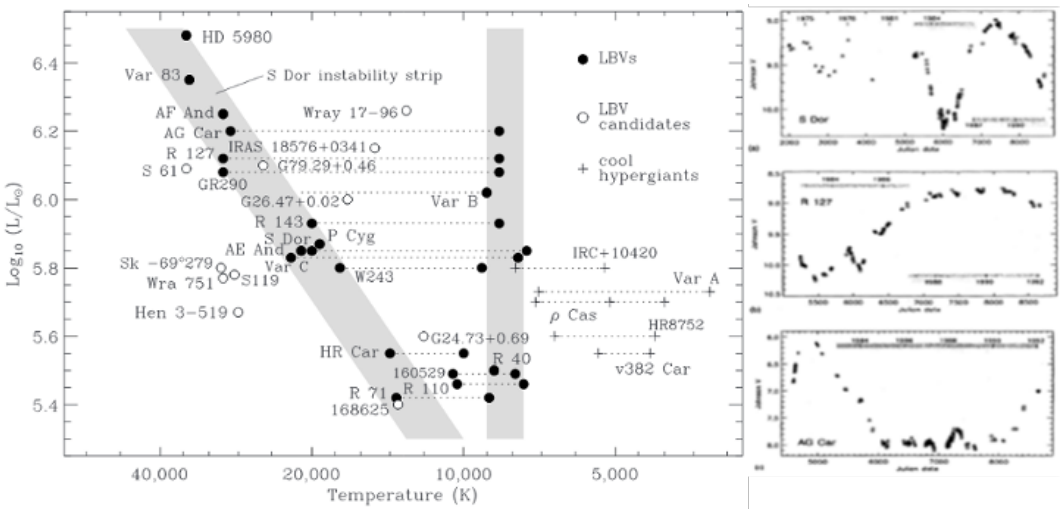

Figure 3.1: Hertzsprung-Russel diagram of quiescent and erupting LBV stars (**left**. Figure from Smith et al. 2004). Light-curves of a sample of LBV stars during the S Dor phase. (Figure from Humphreys & Davidson 1994).

which is the maximum luminosity (at a given stellar mass M) for a structure in hydrodynamic equilibrium, where k is the opacity per unit mass. The dimensionless 'Eddington parameter', therefore:

$$\gamma = \frac{kL}{4\pi cGM} = (7.66 \times 10^{-5}\, g\, cm^{-2})\, k\, (\frac{L}{L_\odot})(\frac{M}{M_\odot})^{-1} \tag{3.2}$$

(e.g. Vink 2012) is the theoretical upper limit to the ratio between the luminosity (L) and the mass (M) of a stellar atmosphere in hydrodynamic equilibrium. The equilibrium between the radiative and the gravity pressures requires that γ does not exceed unity. If Equation 3.2 is applied to classic ionised stellar photospheres, k can be assumed to be entirely due to scattering by free electrons, which gives the minimum possible opacity value, and hence the maximum allowed L/M ratio. LBVs are also characterised by high effective temperatures ($8500 \leqslant T_{eff} \leqslant 35000$ K), which are responsible for their blue colours.

Their temperature-luminosity limits correspond to a particular region of the Hertzprung-Russel diagram (HRD) called the 'S-Doradus instability strip' (see Figure 3.1; Wolf 1989; Smith et al. 2004), which is therefore the locus of the quiescent LBV stars in the Hertzsprung-Russel Diagram (HRD). As pointed out by Smith et al. (2004), there appears to exist a gap in the LBV population in the S Dor instability strip. This is observed in the luminosity range $5.6 \lesssim \log(L/L_\odot) \lesssim 5.8$ (see Figure 3.1), although temperature and luminosity estimates could be affected by large uncertainties, and hence some LBV could still be found to lie within the gap. Nonetheless, it has been argued that is gap is real, and could be linked to the so-called 'bi-stability jump[1]' (Lamers et al. 1995a; Vink et al. 1999) in the line-driven winds of supergiant stars. This gap could hence be explained simply by significant changes in the line-driven wind mechanism, leading to the production of a pseudo-photosphere through instabilities in the star's winds. Such photosphere would be responsible for a shift toward cooler temperatures in the HRD (Smith et al. 2004).

LBVs are among the rarest observed stars, with a handful of confirmed strong S Dor-

[1]related to the fast decrease in the wind terminal velocities between supergiants earlier and later than spectral type B1

like variability in the Galaxy. AG Car, HR Car and WRA 751 have been therefore observed for a sufficient long time to fully characterise their photometric and spectroscopic variability. In particular, high rotational velocity has been inferred from the spectroscopic analysis of AG Car during its S Dor minimum (Groh et al. 2006). Similar results, namely $v_{rot}/v_{crit} \geqslant 0.86$, where v_{crit} is the critical velocity for break-up[2], were obtained from the spectroscopic analysis of HR Car (Groh et al. 2009). This analysis supported the conclusion of Groh et al. (2009) that all strong-active LBVs are fast rotators, and that such high velocities may be in some way responsible for the instabilities causing the S Dor cycles.

During quiescence, LBVs show spectroscopic features typical of OB stars (e.g. Wolf et al. 1981), while they become redder during outbursts (typically after the formation of a cool, extended pseudo-photosphere), showing different spectroscopic and photometric features, according to the nature of the transitional phase. According to their photometric behaviour, they show three main types of variability:

- **S-Doradus variability**, consisting in eruptive episodes involving the outer layers of the star (see Figure 3.1);
- **Giant eruptions**, during which a considerable fraction of the mass of the envelope (up to 10 $M_\odot$) is expelled;
- **Small oscillations and micro-variations**, commonly observed also in normal supergiants (van Genderen et al. 1989).

Outbursts during the S-Dor variability phase usually have time-scales from years to decades (see e.g. the cases of the prototypical AG Car, e.g. Vink & de Koter 2003; Groh et al. 2008a; or the recurring variable S Dor in the Large Magellanic Cloud, Thackeray 1974; Wolf et al. 1980; Leitherer et al. 1985; Stahl & Wolf 1982), characterised by cyclical variations of 1–2 mag in their visual magnitude. It is widely accepted that S Dor variability leads simply to a shift in the stellar Spectral Energy Distribution (SED), and hence produces negligible changes in the bolometric magnitude (e.g. Humphreys & Davidson 1994). Nonetheless, a recent analysis revealed minor fluctuations in the bolometric luminosity of AG Car during the S Dor cycles which argue against this assumption. In particular, Groh et al. (2009) noticed a decrease in the bolometric luminosity by a factor of 1.5 during the S Dor cycle of AG Car. A similar result was also obtained for S Dor itself (Lamers 1995b), and interpreted as a consequence of the loss of energy required to expand the outer layers of the star. Overimposed to these cyclic changes of luminosity, small variations of 0.1 to 0.5 mag on time-scales of a few hundred days along with micro-variations of a few tenths of magnitudes with much faster periods (10-14 days) have also be observed in the prototypical AG Car (van Genderen et al. 1988, 1990).

The S Dor phase is also characterised by variations in the spectroscopic features of LBVs. During minima, they show relatively blue spectra with strong He I, H I, N II and Fe II lines, usually characterised by P Cyg profiles with typical expansion velocities of a few hundreds km s^{-1}, while the 4686 Å He II emission line is generally weak. At visual maximum, on the other hand, they have cooled spectra similar to those displayed by extreme A-type hypergiants, showing strong H I, Fe II, Ti II lines (Wolf & Stahl 1982; Stahl 2001), while transitional spectra between the two phases are characterised by peculiar features, like multiple components in the absorption features, pronounced Lorentzian wings in the emission profiles

[2]The break-up velocity is defined as $v^2_{crit} = \frac{GM}{R}(1-\gamma)$ (Langer 1997, 1998), where γ is the Eddington factor (Equation 3.2) and correspond to a total acceleration $\vec{g}_{tot} = \vec{g}_{grav} + \vec{g}_{rot} + \vec{g}_{rad} = 0$ where $\vec{g}_{rad}$ is the acceleration due to the radiation field (Maeder & Meynet 2000).

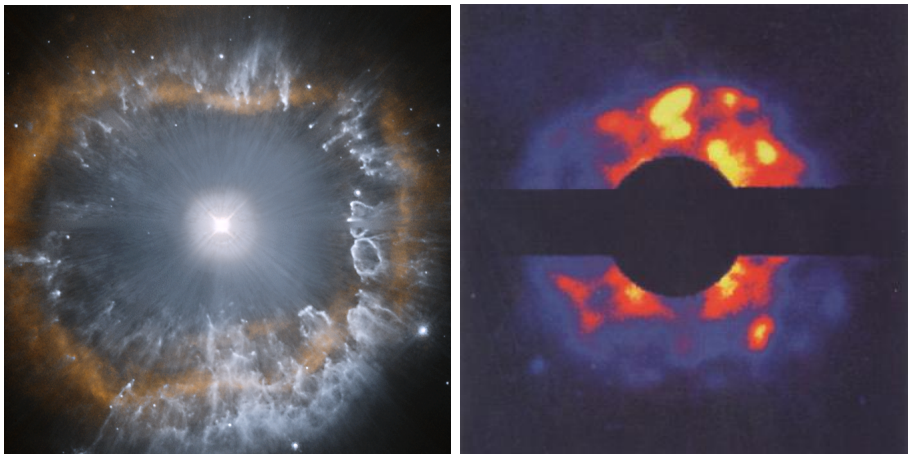

Figure 3.2: The Galactic LBVs AG Car (**left**) and P Cyg (**right**). NASA, Hubble Space Telescope images: `http://www.spacetelescope.org/images/`.

and signatures of inverse P Cyg profiles in particular in the He I lines (Leitherer et al. 1994).

Giant eruptions are characterised by a dramatic and sudden increase in the stellar luminosity (3-6 mag; Humphreys & Davidson 1994) with absolute bolometric peak magnitudes < -14 mag. These brightenings are generally related to the ejection of a significant fraction of the stellar envelope. The spectra also show a significant metamorphosys, showing blue continuum with prominent narrow Balmer lines in emission, hence resembling those of Type IIn SNe (see Section 3.2 for a detailed discussion). The most famous examples are the 'Giant Eruption' experienced by η Car in the 19th century, and the outburst of P Cyg in the 17th century, both in the Milky Way. In both cases the progenitor LBV stars probably violated the Eddington limit (3.2) by a large amount.

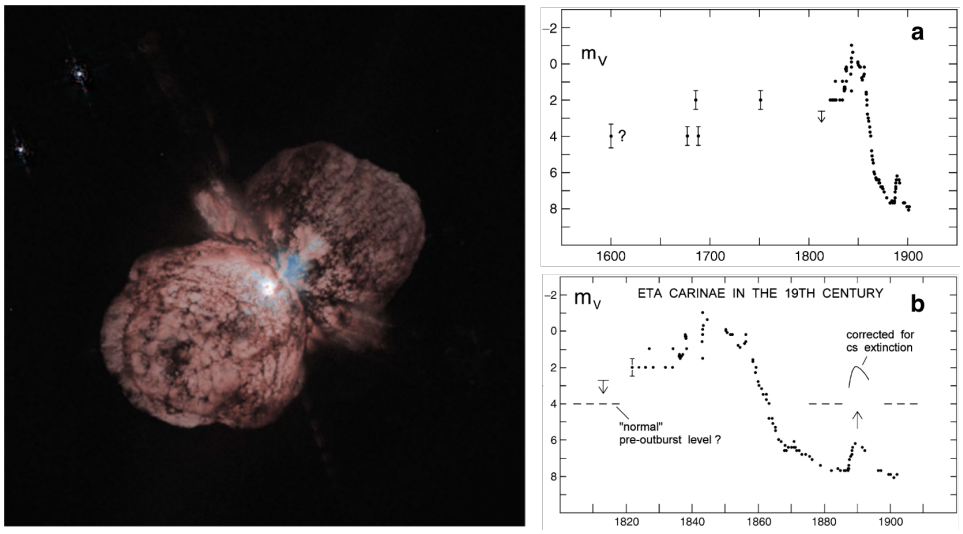

Figure 3.3: The 'Homunculus nebula' around η Car (**left**; NASA HST image). Historical light-curve of η Car from 1600 to 1900 (**a**. Figure from Humphreys et al. 1999) and a blow-up including the outburst, from 1800 to 1920 (**b**. Figure from Humphreys et al. 2008).

During quiescence, LBVs show typical supergiants mass-loss rates in the range of 10^{-7} –

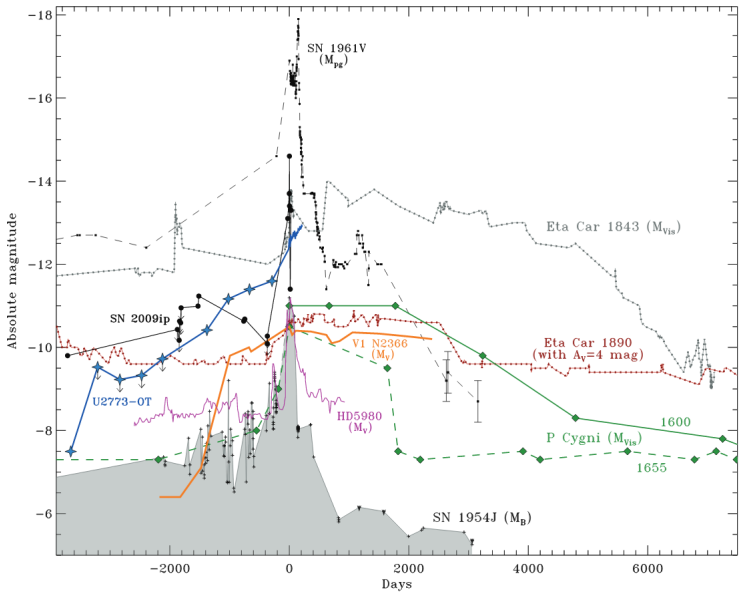

Figure 3.4: Absolute light-curves covering ~ 30 years for a sample of LBV-like eruptions. (Figure from Smith et al. 2011a).

10^{-5} $M_\odot$ yr^{-1} (Davidson et al. 1989), while this values increase to $10^{-5} - 10^{-4}$ $M_\odot$ yr^{-1} during normal eruptions. Giant eruptions, instead, are characterised by dramatic mass-loss enhancements, with rates largely exceeding $\sim 10^{-4} - 10^{-3}\,M_\odot\ yr^{-1}$, and up to a few $M_\odot$ yr^{-1} in the most extreme cases). The mechanisms triggering these giant eruptive events are still not fully understood, but several attempts have been made (e.g. reconsidering the effects of instabilities in stellar evolution codes; Smith & Arnett 2014).

η Car is one of the most massive and luminous star in the Milky Way. It is famous for its 'Giant Eruption' occurred in the 19th century (from 1837 to 1858). During the Giant Eruption the star ejected ~ 10 $M_\odot$ of its envelope, producing the so-called 'Homunculus nebula' (see Figure 3.3). Given its proximity, η Car is an invaluable tool for our understanding of pre-SN variability of the most massive stars in the local Universe (Smith 2012). This major eruption was the energetic non-terminal explosion of an LBV, and is considered assimilable to the extragalactic 'SN impostors' (see Section 3.2). A similar sequence of events was experienced by the LBV P Cyg, which, along with η Car, is one of the most luminous stars of our Galaxy.

3.2 Supernova impostors

SN impostors are believed to be the extra-galactic counterparts of the famous Giant Eruption of η Car, during which the star exceeded by a large factor the Eddington Limit (equation 3.2) with an increase of $\simeq 2$ mag in its bolometric magnitude, corresponding to a total luminosity output of $\simeq 10^{50}$ erg (Van Dyk & Matheson 2012). Such an energy output is comparable to those of CCSNe, therefore these events can easily be confused with genuine SNe. For this reason, mostly in the past, some of them obtained a SN designation (see e.g. the cases of SN 1954J, SN 2000ch and SN 2009ip). Violent eruptions of massive stars can occasionally mimic the SN behaviour, showing, in particular, spectra similar to those of Type IIn SNe. A blue continuum with narrow Balmer lines in emission is, in fact, a common feature in the spectra of both Type IIn SNe and such major outbursts. While SNe IIn are terminal SN

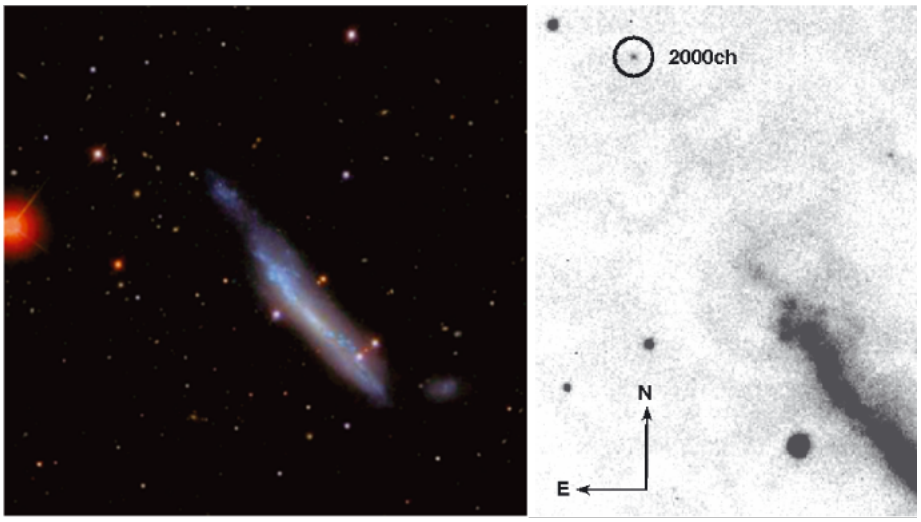

Figure 3.5: SDSS field of NGC 3432 (**left**). A zoom-in of the region of the recurrent SN 2000ch (**right**). (Figure from Pastorello et al. 2010b).

explosions, most frequently produced by the core-collapse leaving back a compact remnant (a neutron star or a black hole), in the outbursts described above, the massive star survives these eruptions. For this reason, the latter are usually labelled as 'impostors' (Van Dyk et al. 2000).

SN 1961V (Goodrich et al. 1989; Filippenko et al. 1995) was the first proposed extragalactic η Car analog in the galaxy NGC 1058. Given its relatively small distance ($\simeq 8$ Mpc, as reported in the NASA/IPAC Extragalactic Database[3], NED), and its extraordinary luminosity, its progenitor was clearly detectable in archival plates dated 1937 (Bertola 1964; Zwicky 1964) with absolute magnitude $M_{pg} = -12.1$ mag. The spectra were characterised by narrow (FWHM ~ 2000 km s^{-1}) H, He and Fe II lines in emission and typical colours of an F supergiant. Its peculiar light-curve (see Figure 3.4) was interpreted by Goodrich et al. (1989) as a 'super-outburst' (like the one experienced by η Car) of an extremely massive LBV star. Nonetheless, the true nature of SN 1961V, many decades after the outburst, is still debated (see e.g. Van Dyk et al. 2013).

Another remarkable example of an extragalactic impostor likely produced by a massive LBV is SN 2000ch in NGC 3432 (Wagner et al. 2004; Pastorello et al. 2010b). Like η Car in the 19th century, it is currently experiencing a giant eruption started at least a couple of decades ago. In one of the major re-brightenings, it reached an absolute magnitude ≈ -12.7 mag. Several other sharp luminosity peaks characterise its long-term light-curve, in which the absolute magnitudes fluctuate between ~ -9 to ~ -12.5 mag (see Figure 3.6 Pastorello et al. 2010b). Optical spectra obtained soon after discovery revealed a blue continuum with prominent narrow (FWHM ~ 1550 km s^{-1}) and asymmetric H, He I λ5876 and He II λ4686 features in emission, without evidence of forbidden lines, suggesting an excess in the density of free electrons of $\sim 10^{-8}$ cm^{-3} (Wagner et al. 2004).
[h!]

SN 1997bs in M 66 showed a single major outburst, followed by an almost linear decline. It opened the door to the discovery of a subset of impostors showing the same photometric behaviour (see e.g. SN 2007sv and PSN J09132750+7627410, discussed in Chapter 4 and 5 respectively). In that case, both photometric and spectroscopic properties resembled those

[3] `https://ned.ipac.caltech.edu/`

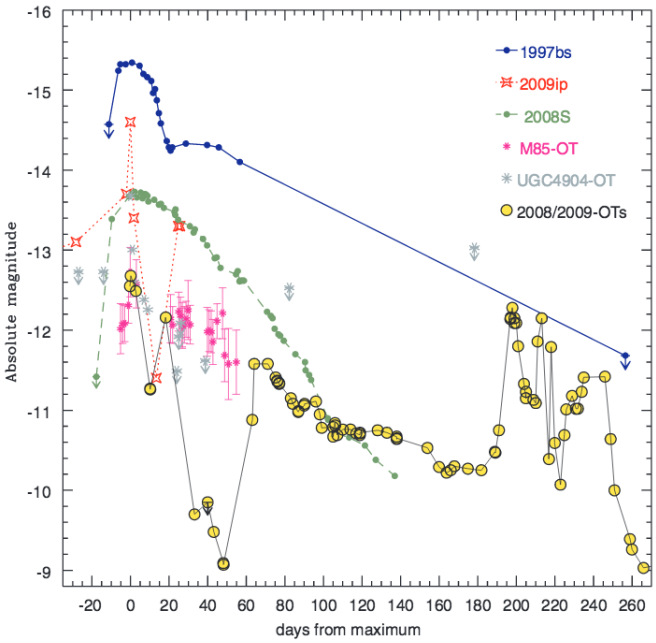

Figure 3.6: Comparison among the light-curves of transient with similar nature. (Figure from Pastorello et al. 2010b).

typically observed in Type IIn SNe, making difficult a secure classification of the transient. Nonetheless, the photometric analysis revealed that likely SN 1997bs was not a genuine Type IIn SN, but the major outburst of a massive star. At early phases, the spectra showed a blue continuum with overimposed narrow Balmer lines (with FWHM velocity of a few thousands km s^{-1}) and weak Fe II lines, with a dominant emission component. The photometric evolution and, even more, the low absolute peak magnitude, led Van Dyk et al. (2000) to conclude that SN 1997bs was a SN impostor rather than a genuine CCSN. Absolute peak magnitudes are, in fact, one of the indicators usually adopted to unmask SN impostors. However, a subset of sub-luminous CCSNe has been discovered (Turatto et al. 1998; Benetti et al. 2001; Pastorello et al. 2004; Spiro et al. 2014), suggesting that photometric analysis alone is not always sufficient to safely discriminate between genuine SNe and SN impostors (Tartaglia et al. 2015). A detailed discussion about this problem will be performed in Chaper 4.

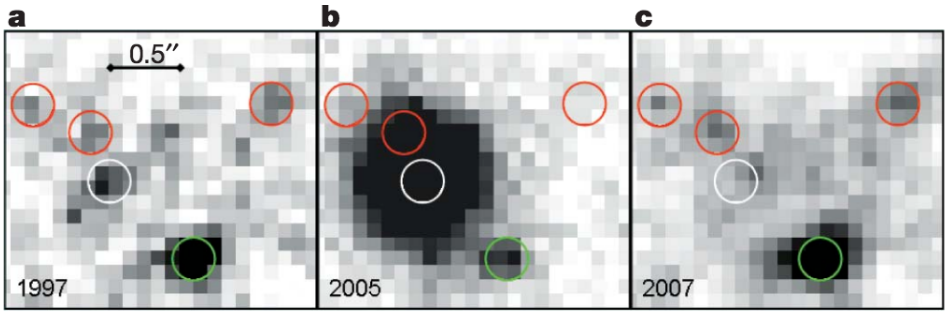

Figure 3.7: Archival HST image of the region of SN 2005gl obtained with the Wide Field and Planetary Camera 2 (WFPC2) (**a**). High resolution image of the same region using the Near Infrared Camera 2 (NIRC2) at the Keck II telescope in Mauna Kea (**b**). Late HST image obtained with the same instrument of the previous one (**c**). (Figure from Gal-Yam & Leonard 2009).

3.3 Massive stars, impostors and interacting supernovae connection

In the last decade, a tight connection among LBVs, their giant eruptions and SNe IIn has been proposed, based on studies of the pre-SN photometric variability of the precursor stars as well as on the analysis of spectroscopic features observed in some Type IIn SNe. In particular, the detection in deep archival *Hubble Space Telescope* (HST) images of the progenitor stars of SN 2005gl (Gal-Yam et al. 2007; Gal-Yam & Leonard 2009), SN 2009ip (Smith et al. 2010; Foley et al. 2011) and SN 2010jl (Smith et al. 2011a) strongly supports this interpretation. In addition, some Type IIn SNe showed evidences of S Dor variability before exploding, namely SNe 2001ig, 2003bg (Kotak & Vink 2006) and 2005gj (Trundle et al. 2008), supporting the conclusion that fast rotations may eventually trigger supernova explosions during the LBV phase.

SN 2005gl in NGC 266 was the first case in which the LBV progenitor star was detected in deep archival HST images (see Figure 3.7). In their paper, Gal-Yam & Leonard (2009) presented the results of their analysis of archival images obtained 8 years before the explosion (occurred on 2005 October 5), which revealed the presence of an intrinsically luminous source, most likely an LBV, at the same position of the SN. More importantly, a second image of the region of the SN obtained on 2007 September 27, confirmed the association the SN with the candidate stellar precursor, since the point source detected in the pre-SN image was no longer visible (Figure 3.7). Nonetheless, one may note that the derived absolute magnitude of the progenitor was very bright ($V \simeq -10.3$ mag) even for a quiescent LBV, so the hypothesis of an erupting LBV cannot be ruled out.

Other objects showed pre-SN variability a short time before their terminal SN explosions. SN 2010mc showed clear signatures of pre-SN variability only 40 d before its explosion as a Type IIn SNe (Ofek et al. 2013a), when it reached absolute R-band magnitude $\simeq -15$ mag (corresponding to $\simeq 2.25 \times 10^{41}$ erg s^{-1}). Also SN 2011ht showed a similar sequence of events, with an eruptive event ~ 1 year before the SN explosion (Fraser et al. 2013b), although, in these two cases, no direct detections of the quiescent progenitor stars was available in images collected in the science archives.

One of the best studied SN impostors in the recent past was surely the controversial SN 2009ip (Pastorello et al. 2013; Fraser et al. 2013a; Smith et al. 2013; Ofek et al. 2013; Prieto et al. 2013; Soker & Kashi 2013; Margutti et al. 2014; Smith et al. 2014; Mauerhan et al. 2014; Graham et al. 2014; Levesque et al. 2014; Moriya 2015; Martin et al. 2015; Fraser et al. 2015), which experienced a sequence of outbursts resembling those observed in SN 2000ch, and possibly ended its eruptive phase with a SN explosion. The putative SN explosion happened about 3 years after the discovery of the impostor, on August 2009. In August 2012, a major outburst (labelled 2012a event) followed ~ 3 weeks after by an even brighter luminosity peak (2012b event), were registered, supporting the idea that the progenitor star finally exploded as a Type IIn SN (e.g. Mauerhan et al. 2014; Smith et al. 2014). Also in this case, the inspection of deep archival HST images revealed the presence of a very massive stars ($M \simeq 60$ M$_\odot$), likely an LBV, at the position of the transient (Foley et al. 2011; Smith et al. 2014) strengthening the idea that a strong connection between LBVs and a few Type IIn SNe may exist.

Although the nature of the 2012a,b events (Pastorello et al. 2013) is still not safely determined (see Chapter 6 for a detailed discussion), the sequence of events observed in

SN 2009ip is a challenge for our knowledges of the latest evolutionary phases of massive stars. In fact, despite the observational evidences, current stellar evolution theories predict a different fate for very massive stars. The LBV phase is expected to last $\geqslant 2.5 \times 10^4$ yr, and to be strongly characterised by episodic and frequent eruptive episodes with one or more major η Car-like eruptions. The estimated amount of mass lost during this stage is expected to be $\gg 5$ $M_\odot$ (Humphreys & Davidson 1994), which is compatible with the total mass expelled by very massive stars (e.g. in the $50 - 100$ $M_\odot$ range) after the H burning phase to become stripped WR stars (Maeder & Meynet 1987). WR stars constitute an extremely heterogeneous class of massive stars which have completely lost their H-rich envelopes through stationary winds, outbursts or major eruptions. All of them show broad lines, generally with P Cyg profiles, originating from strong winds involving the residual outer layers of their envelopes. Different spectroscopic features determine their classification, and several subclasses of WR stars do exist (see e.g. Crowther 2007, for a review). According to the current theoretical models, the total life of a massive star in the WR phase is $\simeq 5 \times 10^5$ yr (Maeder & Meynet 1987), and massive stars are therefore not expected to explode as SNe during the LBV phase. Nonetheless, observational evidences strongly suggest that at least a fraction of LBVs may experience major eruptive episodes followed in a relatively short time (a few weeks to a few decades), by terminal SN explosions (e.g., Ofek et al. 2014a).

Although the mechanisms triggering LBV outbursts are, in general, not completely understood, a few scenarios were proposed to explain the observed properties of SN impostors. The PPI scenario (described in Section 1.4) could easily explain the major brightenings commonly observed in SN impostors (Woosley et al. 2007). In this case, the observed light-curves would be entirely powered by the interaction between subsequent shells expelled during different phases of instability in the stellar core (although also the ionisation and subsequent recombination of an outer unperturbed CSM may be an important source of radiated energy). A different scenario was proposed by Moriya (2014), who invoked that the unexpected mass-loss enhancements observed shortly before the terminal explosion of a number of SNe (e.g. SNe 2006jc; Pastorello et al. 2007, SN 2006oz; Leloudas et al. 2012 and iPTF13beo; Gorbikov et al. 2014) may be related to the high neutrino luminosities of the progenitors during the very late phases of their evolution. Since the neutrino luminosity increases as massive stars evolve, a strong emission of these particles is expected at the phases preceding the CC (up to $\sim 10^{-4}$ $M_\odot$ yr^{-1} ~ 1 year before the collapse) lowering the total mass of the core. This may lead the progenitor to exceed the classical Eddington limit and hence induce the violent ejection of its outer layers. Although mass losses due to high neutrino luminosities after the CC were already discussed by Nadezhin (1980) and Lovegrove & Woosley (2013), Moriya (2014) found that very mass loss rates of 1.4×10^{-3} and 3.3×10^{-3} $M_\odot$ yr^{-1} may occur shortly before the final CC for progenitor stars of 25 $M_\odot$ and 50 $M_\odot$, respectively.

Additional explanations involve strongly interacting massive binaries as precursors of LBV-like outbursts. Violent instabilities triggered at the periastron passages in eccentric binary systems are the mechanism proposed by Smith (2011) to interpret an abrupt mass ejection. Nonetheless, Justham et al. (2014) suggested that also binary mergers could explain isolated major eruptions of LBV stars and, in some cases, eventually lead to SN explosions. The binary collision mechanism is supported by the nature of η Car, which is believed to be a binary system with relatively well estimated orbital parameters (see Figure 3.8). The observed peaks in its light-curve, as well as the current estimates of the system parameters support this scenario. In particular, these strongly suggest that collisions between the envelopes of the two companions actually happen (Madura et al. 2013). If the primary evolved star rapidly expands its envelope (with time-scales from years to decades), it may eventually

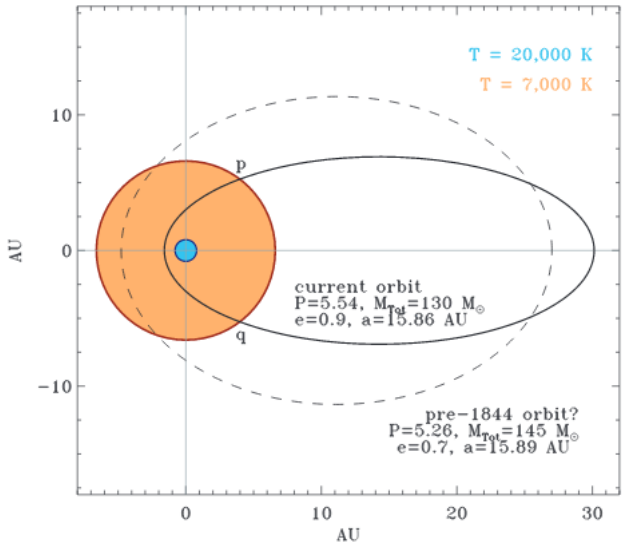

Figure 3.8: Orbital parameters of the proposed binary system for η Car (Figure from Smith 2011).

reach the point in which its radius exceeds the periastron separation between stars in eccentric orbits, triggering violent eruptive episodes. Multiple encounters may eventually produce the observed peaks in the light-curves of many erupting LBVs (a similar scenario can also be proposed to explain the modulated light-curves of SN 2000ch (Pastorello et al. 2010b) and - during the period 2009-1012 - SN 2009ip, see Chapter 6). Binarity can hence play an important role in determining the exact mechanisms characterising the LBV evolutionary phase, as well as their instabilities.

Although the most common SN impostors well fit the observational properties expected in erupting LBVs (namely prominent H lines with inferred velocities of a few hundreds km s^{-1}, fully comparable to those expected in LBV winds), a few observational evidences support the idea that at least a fraction of the observed SN impostors could arise from outbursts of lower-mass stars (Smith et al. 2011a) or even from H-stripped WR stars (Pastorello et al. 2007).

SN 2006jc was a peculiar object showing an outburst $\sim$ 2 years before its terminal SN explosion. Nonetheless, its spectroscopic features showed broad features of α- elements typically observed in Type Ic SNe (see Section 1.1), although the detection of prominent He I emission lines with relatively narrow (FWHM $\sim$ 2200 km s^{-1}) profiles supported the classification as a peculiar Type Ib SN. Narrow features are indeed the hallmark feature of interacting transients and, for this reason, SN 2006jc was properly classified as a Type Ibn SN (Pastorello et al. 2008, see also Section 1.1). Similar objects, although extremely rare, were already observed for example in UGC 11268 and UGC 9299 (SNe 1999cq and 2002ao; e.g. Matheson et al. 2000; Filippenko & Chornock 2002; Pastorello et al. 2008, respectively). Moreover, the SN spectroscopic and photometric analysis, led Pastorello et al. (2007) to conclude that the progenitor star of SN 2006jc was most likely a massive ($60 - 100$ M$_\odot$) CO WR star with a residual LBV-like behaviour (see also Tominaga et al. 2008).
Another interesting object was the impostor SNhunt248 in NGC 5806, which showed three distinct peaks in its light-curve, with the brightest one reaching the absolute magnitude $R \simeq -15.0$ mag, making it among the brightest impostor events ever recorded, but still fainter than typical CCSNe (Kankare et al. 2015). Early spectra showed Balmer lines in emission,

characterised by P Cyg profiles, indicating an expansion velocity of ~ 1100 km s^{-1}, with blue wings extending up to ~ 3000 km s^{-1}. The absorption features disappeared at the time of the second peak, re-appeared during the rise to the third light-curve maximum. The same expansion velocities were inferred at both phases. Also in this case, pre-burst archival images revealed the presence of a (likely) quiescent source with an inferred SED compatible with that of a yellow hypergiant (YHG) star close to the so-called 'Yellow Void', hence not a proper LBV. Nonetheless, like LBVs, also YHG are characterised by instabilities of the outer layers, and some of them are believed to be surrounded by dense, dusty circum-stellar environments (de Jager 1998).

SNe 2006jc and SNhunt248 are hence two important examples supporting our claim that SN impostors are not linked only to LBVs, but, as already argued by Smith et al. (2011a), the impostor phenomenon might be extended to masses below the standard LBV mass range (namely from $10-20$ M$_\odot$, see e.g. the case of UGC 2773 2009OT-1; Smith et al. 2010; Foley et al. 2011; Smith et al. 2016), or even to H-stripped massive stars. A further discussion on the variety of stars producing SN impostors will be presented in Chapter 5.

References

Benetti, S., Turatto, M., Balberg, S., et al. 2001, MNRAS, 322, 361

Bertola, F. 1964, Annales d'Astrophysique, 27, 319

Cappellaro, E., della Valle, M., Iijima, T., & Turatto, M. 1990, A&A, 228, 61

Chiosi, C., & Maeder, A. 1986, ARA&A, 24, 329

Chugai, N. N. 1994, Circumstellar Media in Late Stages of Stellar Evolution, 148

Ciatti, F., Rosino, L., & Bertola, F. 1971, Mem. Soc. Astron. Italiana, 42, 163

Crowther, P. A. 2007, ARA&A, 45, 177

Davidson, K., Moffat, A. F. J., & Lamers, H. J. G. L. M. 1989, IAU Colloq. 113: Physics of Luminous Blue Variables, 157

de Jager, C. 1998, A&ARv, 8, 145

Filippenko, A. V. 1989, AJ, 97, 726

Filippenko, A. V., Barth, A. J., Bower, G. C., et al. 1995, AJ, 110, 2261

Filippenko, A. V., & Chornock, R. 2002, IAU Circ., 7825, 1

Foley, R. J., Berger, E., Fox, O., et al. 2011, ApJ, 732, 32

Fraser, M., Inserra, C., Jerkstrand, A., et al. 2013a, MNRAS, 433, 1312

Fraser, M., Magee, M., Kotak, R., et al. 2013b, ApJ, 779, L8

Fraser, M., Kotak, R., Pastorello, A., et al. 2015, MNRAS, 453, 3886

Gal-Yam, A., Leonard, D. C., Fox, D. B., et al. 2007, ApJ, 656, 372

Gal-Yam, A., Leonard, D. C. 2009, Nature, 458, 865

Goodrich, R. W., Stringfellow, G. S., Penrod, G. D., & Filippenko, A. V. 1989, ApJ, 342, 908

Gorbikov, E., Gal-Yam, A., Ofek, E. O., et al. 2014, MNRAS, 443, 671

Graham, M. L., Sand, D. J., Valenti, S., et al. 2014, ApJ, 787, 163

Groh, J. H., Hillier, D. J., & Damineli, A. 2006, ApJ, 638, L33

Groh, J. H., Damineli, A., & Hillier, D. J. 2008a, Revista Mexicana de Astronomia y Astrofisica Conference Series, 33, 132

Groh, J. H., Damineli, A., & Hillier, D. J. 2008b, Mass Loss from Stars and the Evolution of Stellar Clusters, 388, 173

Groh, J. H., Damineli, A., Hillier, D. J., et al. 2009, ApJ, 705, L25

Humphreys, R. M., & Davidson, K. 1994, PASP, 106, 1025

Humphreys, R. M., Davidson, K., & Smith, N. 1999, PASP, 111, 1124

Humphreys, R. M., Davidson, K., & Koppelman, M. 2008, AJ, 135, 1249

Kankare, E., Kotak, R., Pastorello, A., et al. 2015, A&A, 581, L4

Kotak, R., & Vink, J. S. 2006, A&A, 460, L5

Justham, S., Podsiadlowski, P., & Vink, J. S. 2014, ApJ, 796, 121

Lamers, H. J. G. L. M. 1986, Luminous Stars and Associations in Galaxies, 116, 157

Lamers, H. J. G. L. M., Snow, T. P., & Lindholm, D. M. 1995a, ApJ, 455, 269

Lamers, H. J. G. L. M. 1995b, IAU Colloq. 155: Astrophysical Applications of Stellar Pulsation, 83, 176

Langer, N. 1989, A&A, 220, 135

Langer, N. 1997, Luminous Blue Variables: Massive Stars in Transition, 120, 83

Langer, N. 1998, A&A, 329, 551

Leitherer, C., Appenzeller, I., Klare, G., et al. 1985, A&A, 153, 168

Leitherer, C., Allen, R., Altner, B., et al. 1994, ApJ, 428, 292

Leloudas, G., Chatzopoulos, E., Dilday, B., et al. 2012, A&A, 541, A129

Levesque, E. M., Stringfellow, G. S., Ginsburg, A. G., Bally, J., & Keeney, B. A. 2014, AJ, 147, 23

Lovegrove, E., & Woosley, S. E. 2013, ApJ, 769, 109

Madura, T., Gull, T., Corcoran, M., et al. 2013, Massive Stars: From alpha to Omega, 164

Maeder, A., & Meynet, G. 1987, A&A, 182, 243

Maeder, A. 1990, A&AS, 84, 139

Maeder, A., & Meynet, G. 2000, ARA&A, 38, 143

Margutti, R., Milisavljevic, D., Soderberg, A. M., et al. 2014, ApJ, 780, 21

Martin, J. C., Hambsch, F.-J., Margutti, R., et al. 2015, AJ, 149, 9

Matheson, T., Filippenko, A. V., Chornock, R., Leonard, D. C., & Li, W. 2000, AJ, 119, 2303

Mauerhan, J., Williams, G. G., Smith, N., et al. 2014, MNRAS, 442, 1166

Moriya, T. J. 2014, A&A, 564, A83

Moriya, T. J. 2015, ApJ, 803, L26

Ofek, E. O., Rabinak, I., Neill, J. D., et al. 2010, ApJ, 724, 1396

Ofek, E. O., Lin, L., Kouveliotou, C., et al. 2013a, ApJ, 768, 47

Ofek, E. O., Sullivan, M., Cenko, S. B., et al. 2013b, Nature, 494, 65

Ofek, E. O., Sullivan, M., Shaviv, N. J., et al. 2014, ApJ, 789,104

Nadezhin, D. K. 1980, Ap&SS, 69, 115

Pastorello, A., Zampieri, L., Turatto, M., et al. 2004, MNRAS, 347, 74

Pastorello, A., Smartt, S. J., Mattila, S., et al. 2007, Nature, 447, 829

Pastorello, A., Mattila, S., Zampieri, L., et al. 2008, MNRAS, 389, 113

Pastorello, A., Botticella, M. T., Trundle, C., et al. 2010, MNRAS, 408, 181

Pastorello, A., Cappellaro, E., Inserra, C., et al. 2013, ApJ, 767, 1

Prieto, J. L., Brimacombe, J., Drake, A. J., & Howerton, S. 2013, ApJ, 763, L27

Richardson, D., Branch, D., Casebeer, D., et al. 2002, AJ, 123, 745

Schlegel, E. M. 1990, MNRAS, 244, 269

Smith, N. 2011, MNRAS, 415, 2020

Smith, N. 2012, Eta Carinae and the Supernova Impostors, 384, 145

Smith, N., Vink, J. S., & de Koter, A. 2004, ApJ, 615, 475

Smith, N., Miller, A., Li, W., et al. 2010, AJ, 139, 1451

Smith, N., Li, W., Miller, A. A., et al. 2011, ApJ, 732, 63

Smith, N., Mauerhan, J. C., Kasliwal, M. M., & Burgasser, A. J. 2013, MNRAS, 434, 2721

Smith, N., Mauerhan, J. C., & Prieto, J. L. 2014, MNRAS, 438, 1191

Smith, N., & Arnett, W. D. 2014, ApJ, 785, 82

Smith, N., Andrews, J. E., Mauerhan, J. C., et al. 2016, MNRAS, 455, 3546

Soker, N., & Kashi, A. 2013, ApJ, 764, L6

Spiro, S., Pastorello, A., Pumo, M. L., et al. 2014, MNRAS, 439, 2873

Stahl, O., & Wolf, B. 1982, A&A, 110, 272

Stahl, O. 2001, Eta Carinae and Other Mysterious Stars: The Hidden Opportunities of Emission Spectroscopy, 242, 163

Tartaglia, L., Pastorello, A., Taubenberger, S., et al. 2015, MNRAS, 447, 117

Thackeray, A. D. 1974, MNRAS, 168, 221

Tominaga, N., Limongi, M., Suzuki, T., et al. 2008, ApJ, 687, 1208

Trundle, C., Kotak, R., Vink, J. S., & Meikle, W. P. S. 2008, A&A, 483, L47

Tsvetkov, D. Y., & Pavlyuk, N. N. 1997, Astronomy Letters, 23, 26

Turatto, M., Mazzali, P. A., Young, T. R., et al. 1998, ApJ, 498, L129

Van Dyk, S. D., Peng, C. Y., King, J. Y., et al. 2000, PASP, 112, 1532

Van Dyk, S. D., & Matheson, T. 2012, Eta Carinae and the Supernova Impostors, 384, 249

Van Dyk, S. D., Filippenko, A. V., Cenko, B. S., & Shields, J. C. 2013, Massive Stars: From alpha to Omega, 134

van Genderen, A. M., The, P. S., Augusteijn, T., et al. 1988, A&AS, 74, 453

van Genderen, A. M., Bovenschen, H., Engelsman, E. C., et al. 1989, A&AS, 79, 263

van Genderen, A. M., The, P. S., Heemskerk, M., et al. 1990, A&AS, 82, 189

Vink, J. S. 2012, Eta Carinae and the Supernova Impostors, 384, 221

Vink, J. S., de Koter, A., & Lamers, H. J. G. L. M. 1999, A&A, 350, 181

Vink, J. S., & de Koter, A. 2003, A Massive Star Odyssey: From Main Sequence to Supernova, 212, 259

Wagner, R. M., Vrba, F. J., Henden, A. A., et al. 2004, PASP, 116, 326

Wang, L., Wheeler, J. C., Li, Z., & Clocchiatti, A. 1996, ApJ, 467, 435

Wegner, G., & Swanson, S. R. 1996, MNRAS, 278, 22

Wolf, B., Appenzeller, I., & Cassatella, A. 1980, A&A, 88, 15

Wolf, B., Appenzeller, I., & Stahl, O. 1981, A&A, 103, 94

Wolf, B., & Stahl, O. 1982, A&A, 112, 111

Wolf, B. 1986, Luminous Stars and Associations in Galaxies, 116, 151

Wolf, B. 1989, A&A, 217, 87

Woosley, S. E., Langer, N., & Weaver, T. A. 1993, ApJ, 411, 823

Woosley, S. E., Blinnikov, S., & Heger, A. 2007, Nature, 450, 390

Zwicky, F. 1964, ApJ, 139, 514

Chapter 4

The supernova impostor SN 2007sv in UGC 5979

As discussed in Section 3, the label *supernova impostors* (Van Dyk et al. 2000) is used to indicate a class of transient events showing luminous outbursts mirroring the behaviour of genuine SNe. In particular, they show spectra similar to those of Type IIn SNe, and experience eruptions with comparable energies as those of real SNe. The basic difference is that an impostors is a non-terminal explosion, and the star (most commonly an LBV) survives the outburst.

Active LBVs can show erratic variability and sometimes fast optical declines after the outbursts. A connection among LBVs, their major eruptions and SN explosions is strongly supported by a few observational evidences (Kotak & Vink 2006). The direct detection of LBVs as SN progenitors in deep archival HST images (see e.g. Gal-Yam & Leonard 2009; Smith et al. 2011a), as well as spectral evidences of structured H-rich CSM with inferred velocities consistent with those of LBV winds (a few hundreds km s^{-1}, Trundle et al. 2008, 2009), support this link. We remark that nearly identical lines are detected also in the spectra of SN impostors.

η Car and P Cyg are the only two major LBV eruptions occurred in the Milky Way in the last few centuries; these events can be considered as Galactic examples of SN impostors, and their study is fundamental for our understanding of the nature of eruptive phenomena, since their physical parameters are well constrained.

The safe discrimination between genuine SN explosions and supernova impostors has been challenged by the discovery of a new class of puzzling interacting transients. SN 2008S, in particular, was a controversial cases. Its peak absolute magnitude (~ -14 mag) was faint compared to those of genuine SNe, although other observational properties (like its decline rate consistent with that expected from the radioactive ^{56}Co decay; Botticella et al. 2009) supported a SN classification. SN 2009ip was another widely debated case, and its nature has not been firmly determined yet (a detailed discussion on the nature of this transient will be presented in Chapter 6).

In this context, the discovery of a weak transient event with Type IIn-like spectra, SN 2007sv, has been an excellent opportunity to test the criteria of discrimination between interacting SNe and impostors. The study of SN 2007sv illustrated in this Chapter has been published in Tartaglia et al. (2015). The transient was discovered on 2007 December 20.912 UT (Duszanowicz et al. 2007), and was located 6".9 West and 6".7 South of the centre of

UGC 5979, at the following coordinates: RA = 10:52:41.16 and Dec = +67:59:18.8 [J2000]. UGC 5979 is a diffuse (dI) galaxy[1], with a radial velocity corrected for the Local Group infall onto the Virgo cluster of about 1376 km s^{-1} (z = 0.0045). From the above value of the recessional velocity, the inferred distance for UGC 5979 is 18.85 ± 1.03 Mpc, implying a distance modulus $\mu = 31.38 \pm 0.27$ mag (adopting $H_0 = 73$ km s^{-1} Mpc^{-1}). The assumed foreground Galactic extinction in the direction of SN 2007sv is $A_V = 0.048$ mag, as reported in the NED[2] archive. No additional host galaxy extinction contribution is adopted, as a detailed analysis of the spectra of 2007sv revealed no evidence of narrow absorptions of the NaID doublet at the recessional velocity of the host galaxy (Section 4.2). The resulting absolute magnitude of SN 2007sv is $M_B = -15.5$ mag.

The detection was confirmed with an unfiltered CCD image by T. Boles on 2007 December 25.971 UT, whilst there was no source detected at the position of SN 2007sv on an archive image taken on 2007 September 13.093 UT (Duszanowicz et al. 2007). The spectra showed a blue continuum at early phases and prominent Balmer lines in emission. Nonetheless, the absolute magnitude at the epoch of the discovery ($M_R = -14.25 \pm 0.38$ mag) suggested it to be most likely a SN impostor. This classification was also supported by the lack of evidence of very high velocity material in the spectra, as expected in expanding SN ejecta. In addition, the spectra showed no unequivocal evidence of broad lines of α- and/or Fe-peak elements. Finally, the comparison with the absolute light-curves of similar interacting transients highlights the overall similarity with the prototypical impostor SN 1997bs. All these observational features supported the claim that SN 2007sv was a SN impostor rather than a genuine SN explosion.

In the following, SN impostors will be referred to without the 'SN' prefix in their names, in order to emphasize their different nature compared to genuine SNe. What follows is an excerpt of the results published in Tartaglia et al. (2015).

4.1 Photometry

4.1.1 Data reduction and light-curves

Our photometric monitoring campaign started on 2007 December 30, and spanned a period of about 100 days. We also collected sparse observations (mostly unfiltered) from amateur astronomers. Information about the photometric data and the instruments used are reported in Table 4.1.

All data were pre-processed using standard procedures in IRAF[3] including bias and flat field corrections. To measure the magnitudes we used a dedicated pipeline (Cappellaro 2014) consisting in a collection of PYTHON scripts calling standard IRAF tasks (through PYRAF) and other specific analysis tools, in particular SEXTRACTOR for source extraction and star/galaxy separation, DAOPHOT to measure the source magnitude via PSF fitting and HOTPANTS[4] for image difference with PSF match.

[1] http://leda.univ-lyon1.fr/

[2] http://ned.ipac.caltech.edu

[3] IRAF is distributed by the National Optical Astronomy Observatory, which is operated by the Associated Universities for Research in Astronomy, Inc., under cooperative agreement with the National Science Foundation.

[4] http://www.astro.washington.edu/users/becker/hotpants.html

Table 4.1: Optical magnitudes of 2007sv and associated errors.

Date	MJD	U(err)	B(err)	V(err)	R(err)	I (err)	Instrument
20070913	54356.09	-	-	-	>18.8	-	SX MX7
20071220	54454.91	-	-	-	17.16(0.26)	-	SX MX7
20071227	54461.86	-	-	17.98(0.36)	17.50(0.14)	-	MX916
20071230	54464.15	-	18.50(0.08)	18.16(0.04)	17.79(0.02)	17.43(0.02)	AFOSC
20080104	54469.04	19.15(0.15)	18.86(0.03)	18.22(0.01)	17.81(0.02)	-	RATCam
20080106	54471.08	19.21(0.06)	18.91(0.04)	18.27(0.02)	17.88(0.02)	17.35(0.02)	RATCam
20080108	54473.21	19.26(0.09)	18.96(0.03)	18.26(0.02)	17.80(0.03)	17.33(0.02)	RATCam
20080110	54475.14	-	19.04(0.07)	18.22(0.03)	17.86(0.03)	17.33(0.03)	AFOSC
20080110	54475.20	19.35(0.08)	19.06(0.02)	18.25(0.02)	17.78(0.03)	17.34(0.02)	RATCam
20080112	54477.25	19.37(0.03)	19.12(0.02)	18.31(0.03)	17.93(0.03)	17.52(0.03)	ALFOSC
20080113	54478.00	19.42(0.08)	19.17(0.03)	18.32(0.02)	17.83(0.03)	17.38(0.04)	RATCam
20080116	54481.12	19.54(0.14)	19.21(0.02)	18.35(0.03)	17.77(0.03)	17.45(0.03)	RATCam
20080118	54483.20	19.93(0.21)	19.39(0.10)	18.36(0.03)	17.95(0.13)	-	RATCam
20080120	54485.94	-	-	-	17.98(0.27)	-	SX MX7
20080128	54493.16	-	19.51(0.11)	18.57(0.03)	18.02(0.07)	17.47(0.09)	CAFOS
20080128	54493.95	-	19.53(0.04)	18.52(0.02)	17.91(0.02)	17.41(0.02)	RATCam
20080207	54503.93	-	19.89(0.04)	18.70(0.02)	18.03(0.03)	17.51(0.03)	RATCam
20080209	54505.94	-	-	-	18.02(0.18)	-	Apogee Ap7
20080211	54507.85	-	-	-	18.18(0.21)	-	SBIG ST-7
20080213	54509.94	-	-	-	18.17(0.22)	-	SX MX7
20080301	54526.88	-	20.53(0.05)	19.21(0.03)	18.33(0.04)	17.84(0.06)	RATCam
20080304	54529.01	-	-	-	18.60(0.26)	-	SX MX7
20080305	54530.98	-	>20.4	19.47(0.06)	18.46(0.07)	17.85(0.04)	CAFOS
20080331	54556.00	-	>21.2	20.80(0.06)	19.46(0.06)	18.94(0.05)	ALFOSC
20080401	54557.93	-	>21.4	21.07(0.05)	19.75(0.04)	19.18(0.18)	RATCam

The observations were carried out using the 2.56 m Nordic Optical Telescope (NOT) with ALFOSC and the 2 m Liverpool Telescope with RATCam (both located at the Roque de Los Muchachos, La Palma, Canary Islands, Spain), the Calar Alto 2.2 m Telescope with CAFOS (Sierra de Los Filabres, Spain) and the 1.82 m Copernico Telescope with AFOSC (Mount Ekar, Asiago, Italy). Additional observations (mostly unfiltered) were obtained by amateur astronomers.
The magnitudes obtained from SX MX7, Apogee Ap7 and SBIG ST-7 were computed from unfiltered images, whose magnitudes were rescaled to R-band.
MX916: 0.45 m f4.5 newtonian telescope with a MX916 CCD Camera, at Mandi Observatory (Pagnacco, Udine, Italy)
SX MX7: 0.32 m f/3.1 reflector and a Starlight Xpress MX716 CCD camera at Moonbase Observatory (Akersberga, Sweden)
Apogee AP7: C-14 Celestron Schmidt Cassegrain reflector and an Apogee AP7 CCD camera (Suffolk, United Kingdom)
SBIG ST-7: 0.44 m f4.43 telescope with a SBIG ST-7 Dual CCD Camera at Sandvretens Observatorium (Uppsala, Sweden)

The magnitudes were measured using the PSF-fitting technique, first subtracting the sky background calculated using a low order polynomial fit (typically a 2nd order polynomial). The PSF was obtained by averaging the profiles of isolated field stars. The fitted source is removed from the original frames, then a new estimate of the local background is derived and the fitting procedure is iterated. Finally, the residuals are visually inspected to validate the fit.

Error estimates were obtained through artificial star experiments in which a fake star, with magnitude similar to that of the SN, is placed in the PSF-fit residual image, in a position close (though not coincident) with that of the real source. The simulated image is processed through the PSF fitting procedure and the dispersion of measurements out of a number of experiments (with the fake star in slightly different positions), is taken as an estimate of the instrumental magnitude error. This is combined (in quadrature) with the PSF-fit error

Table 4.2: Magnitudes of the stellar sequence used for the photometric calibration. The stars are shown in Figure 4.1.

label	ra [J2000] (hh:mm:ss)	dec [J2000] (dd:mm:ss)	U(err)	B(err)	V(err)	R(err)	I(err)
1	10:53:02.62	67:58:18.77	-	-	20.159(0.056)	19.202(0.015)	-
2	10:53:01.92	67:59:46.33	18.451(0.020)	17.110(0.015)	15.861(0.029)	14.983(0.022)	14.214(0.027)
3	10:52:54.29	67:58:14.49	15.692(0.009)	15.675(0.007)	15.127(0.020)	14.800(0.016)	14.429(0.030)
4	10:52:50.03	67:57:21.82	-	20.571(0.010)	19.113(0.024)	18.195(0.015)	16.425(0.014)
5	10:52:49.13	67:58:39.87	17.682(0.007)	17.088(0.011)	16.212(0.012)	15.688(0.008)	15.180(0.012)
6	10:52:43.00	67:57:22.46	16.401(0.004)	16.329(0.005)	15.661(0.010)	15.295(0.006)	14.887(0.003)
7	10:52:27.18	68:00:26.52	-	-	18.245(0.013)	17.770(0.005)	17.299(0.015)

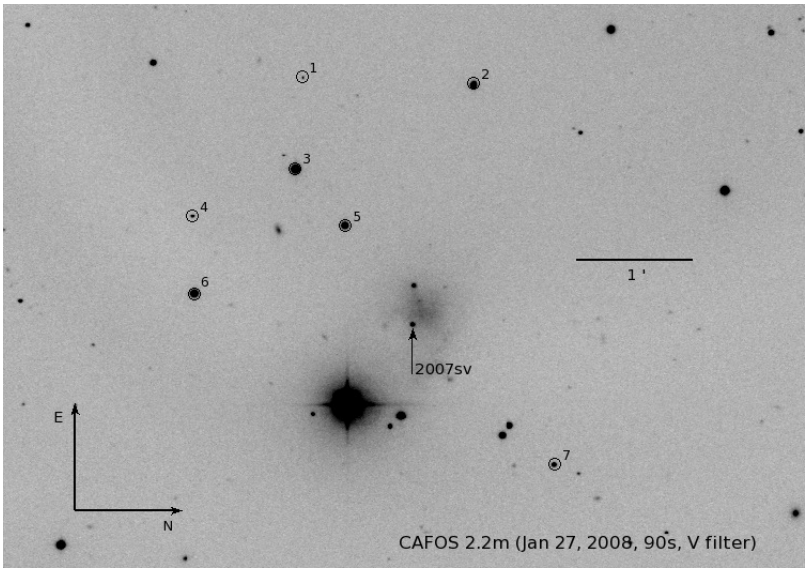

Figure 4.1: Finding chart of 2007sv. The stars used for the photometric calibration are labelled with a number, the position of the transient is marked with an arrow. Information about the intrumental set-up is also reported (bottom-right corner).

returned by DAOPHOT.

The SN photometry was calibrated as follows. Among the observational data, we selected the frames obtained in photometric nights in which standard photometric fields (from the list of Landolt 1992) were observed. These standard frames were used to derive zero points and colour terms for the specific instrumental set-up and to calibrate the magnitudes of selected stars in the SN field (Table 4.2 and Figure 4.1). This local sequence was used to calibrate the SN magnitudes in non-photometric nights. The final magnitudes were computed using first-order colour-term corrections.

The resulting magnitudes of 2007sv are reported in Table 4.1 along with the photometric errors, and the light-curves are shown in Figure 4.2.

4.1.2 Constraining the SN age

Since no observation was obtained a short time before the discovery of 2007sv, the epochs of the outburst on-set and the light-curve maximum cannot be precisely constrained. Nonethe-

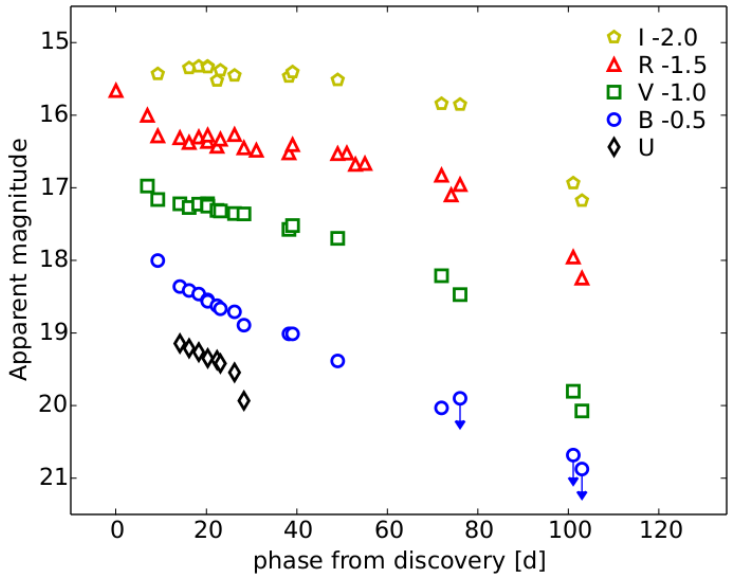

Figure 4.2: Multi-band light-curves of 2007sv. The $UBVRI$ magnitudes are listed in Table 4.1. The phases are from the discovery epoch.

less, we have adopted the epoch of the discovery as reference time for the light-curve phases, assuming that the transient was discovered in the proximity of the maximum light. In other words, hereafter we will adopt as an indicative epoch for the light-curve maximum the discovery time (December 20, 2007; JD = 2454455.41). The goodness of our assumption is supported by the photometric and spectroscopic analysis that will be widely discussed in the next sections. Briefly, our choice is motivated on the basis of the following line of thinking. As we will discuss in the forthcoming sections, 2007sv shows very fast temperature/colour evolutions during the first 3-4 weeks, suggesting that the transient was discovered very young, a few days after the burst. This also implies that it is unlikely that 2007sv reached a peak magnitude much brighter than the discovery magnitude $R = 17.16$ mag (Table 4.1). If we adopt for 2007sv the distance modulus and the reddening value discussed above, we obtain an absolute magnitude $M_R = -14.25 \pm 0.38$ mag at the discovery, which is an indicative estimate for the absolute peak magnitude. This weak absolute magnitude at maximum is an indication that 2007sv was very likely a SN impostor rather than a genuine SN explosion.

4.1.3 Absolute magnitude and colour curves

In Figure 4.3, we compare the absolute R-band light curve of 2007sv with those of the SN impostor 1997bs (Van Dyk et al. 2000), SN 2008S (Botticella et al. 2009) and the Type IIn SN 1999el (Di Carlo et al. 2002). As highlighted in this comparison, the absolute peak magnitude of 2007sv is similar to those measured for the SN impostor 1997bs and the enigmatic transient SN 2008S (see Section 4.2.3), while it is significantly fainter than that of the canonical Type IIn SN 1999el. Although the faint absolute magnitude supports the SN impostor scenario for 2007sv, this argument alone is not sufficient to rule out a true SN explosion, as we will discuss in Section 5.

The $B - V$, $V - R$ and $V - I$ colour curves of 2007sv are compared in Figure 4.4 with those of the same SNe considered in Figure 4.3, showing that 2007sv becomes rapidly red (in analogy with other SN impostors discovered soon after the burst) as the temperature of the ejecta rapidly decreases (Section 4.2). On the other hand, the regular Type IIn SN 1999el

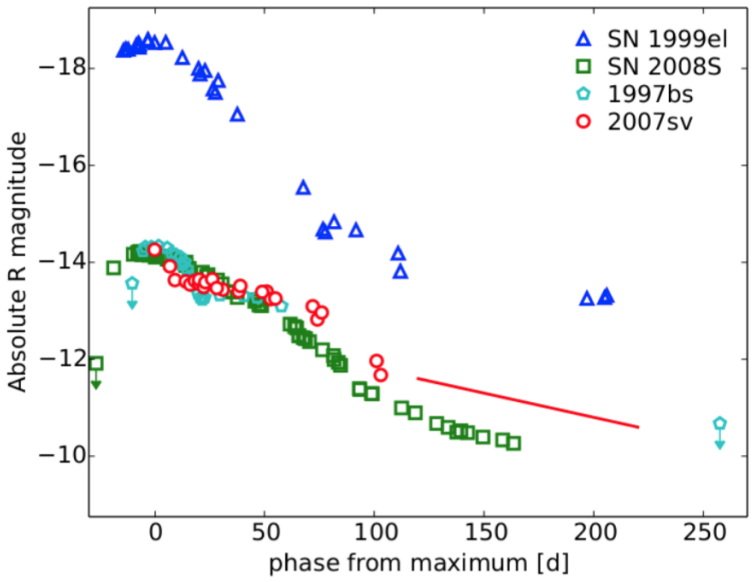

Figure 4.3: Comparison of the absolute R-band light-curves of the impostors 2007sv and 1997bs, the enigmatic transient SN 2008S, and the classical Type IIn SN 1999el. The red line indicates the slope of the ^{56}Co decay.

Table 4.3: Log of the spectroscopical observations of 2007sv. The phase refers to the discovery.

Date	MJD	Phase (days)	Instrumental setup	Grism or grating	Spectral range (Å)	Resolution (Å)	Exp. times (s)
20071229	54463.96	9	Ekar182+AFOSC	2×gm4	3450 – 7800	24	2×1800
20080105	54470.05	15	TNG+LRS	LR-B	3600 – 7770	19.9	2700
20080110	54475.08	20	Ekar182+AFOSC	gm2+gm4	3450 – 8100	34; 24	2×1800
20080113	54478.26	23	TNG+LRS	LR-R	5070 – 10100	10.7	1800
20080114	54479.12	24	NOT+ALFOSC	gm4	3300 – 9100	9.6	1800
20080119	54484.43	30	HET	LRS	4300 – 7300	6.2	2×1350
20080128	54493.17	38	CAHA+CAFOS	b200	3200 – 8800	12.3	3600
20080201	54497.12	42	WHT+ISIS	spec	3200 – 10300	4.8; 9.8	1200
20080301	54526.25	71	HET	LRS	4300 – 7300	6.0	4×1125
20080308	54533.04	78	CAHA+CAFOS	b200+g200	4800 – 10700	13.8	2×2400

The spectra were obtained using the 1.82 m Telescopio Copernico with AFOSC, the 3.58 m Telescopio Nazionale Galileo (TNG) with DOLoRes (La Palma, Canary Islands, Spain), the 4.2 m William Herschel Telescope with ISIS (La Palma, Canary Islands, Spain), the 2.56 m Nordic Optical Telescope (NOT) with ALFOSC, the Calar Alto 2.2 m telescope with CAFOS and the 11.1x9.8 m Hobby-Eberly Telescope (HET, Mt. Fowlkes, Texas, USA) with LRS.

remains bluer for a longer time. In particular, it has much bluer colours than the other transients at phases later than 100 days.

The comparisons shown above highlight some of the similarities between the SN impostors 2007sv and 1997bs and the peculiar transient SN 2008S, whose nature has not been firmly established yet (genuine electron-capture SN or SN impostor, see Prieto et al. 2008; Botticella et al. 2009; Smith et al. 2009; Thompson et al. 2009; Pumo et al. 2009; Wesson et al. 2010; Kochanek 2011; Szczygieł et al. 2012, and Section 4.2.3), all showing a fainter maximum and a different evolution in the light-curve when compared with the light-curve of the interacting SN 1999el.

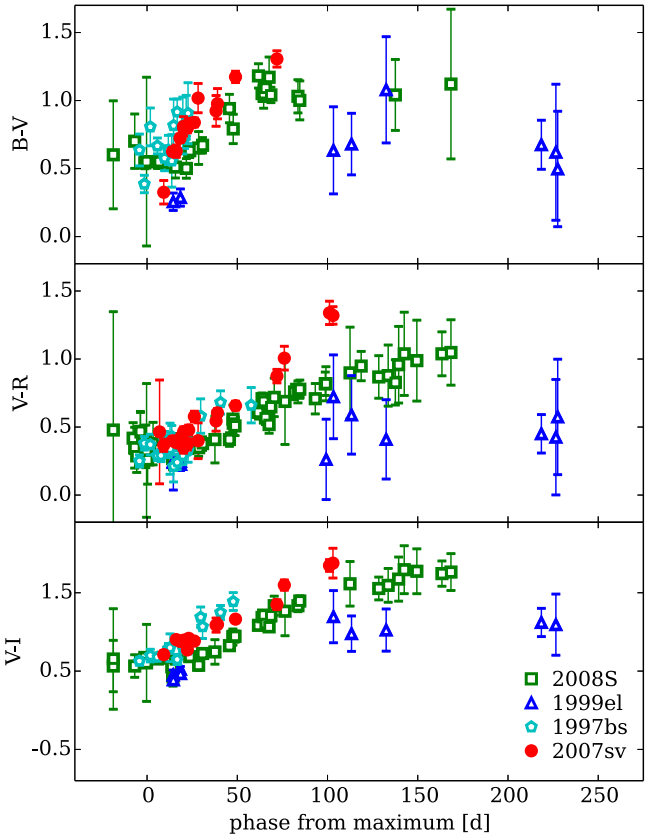

Figure 4.4: Comparison among the $B-V$ (top), $V-R$ (middle) and $V-I$ (bottom) colour curves of the same sample as in Figure 4.3. All phases are from the epoch of the maximum, which we assumed to be coincident with the discovery epoch of 2007sv .

4.2 Spectroscopy

Spectroscopic observations were carried out from December 29, 2007 (i.e. 9 days after the discovery) to March 7, 2008 (+78 days). Basic information on the spectra and the instrumental configurations is reported in the log of the spectroscopic observations (Table **??**).

All data were processed using standard IRAF tasks in order to perform the pre-reduction analysis (bias, flat and overscan corrections) and the extraction of the mono-dimensional spectra. Wavelength calibration was performed using the spectra of comparison lamps obtained with the same instrumental setup. Flux calibration was performed using the spectrum of standard stars. The accuracy of the wavelength calibration was verified measuring the wavelength of night sky lines (in particular [O I] at 5577.34 Å and 6300.30 Å), and a shift was applied in case of discrepancy. Spectral resolution was measured from the *full-width-at-half-maximum* (FWHM) of isolated night sky lines, adopting their mean value as final resolution estimate. The final spectral flux calibration was checked against multi-band photometry obtained on the nearest night and, when necessary, a scaling factor was applied. Telluric corrections were applied when spectra of references stars obtained during the same nights were available. The spectral sequence obtained with the above procedures is shown in Figure 4.5.

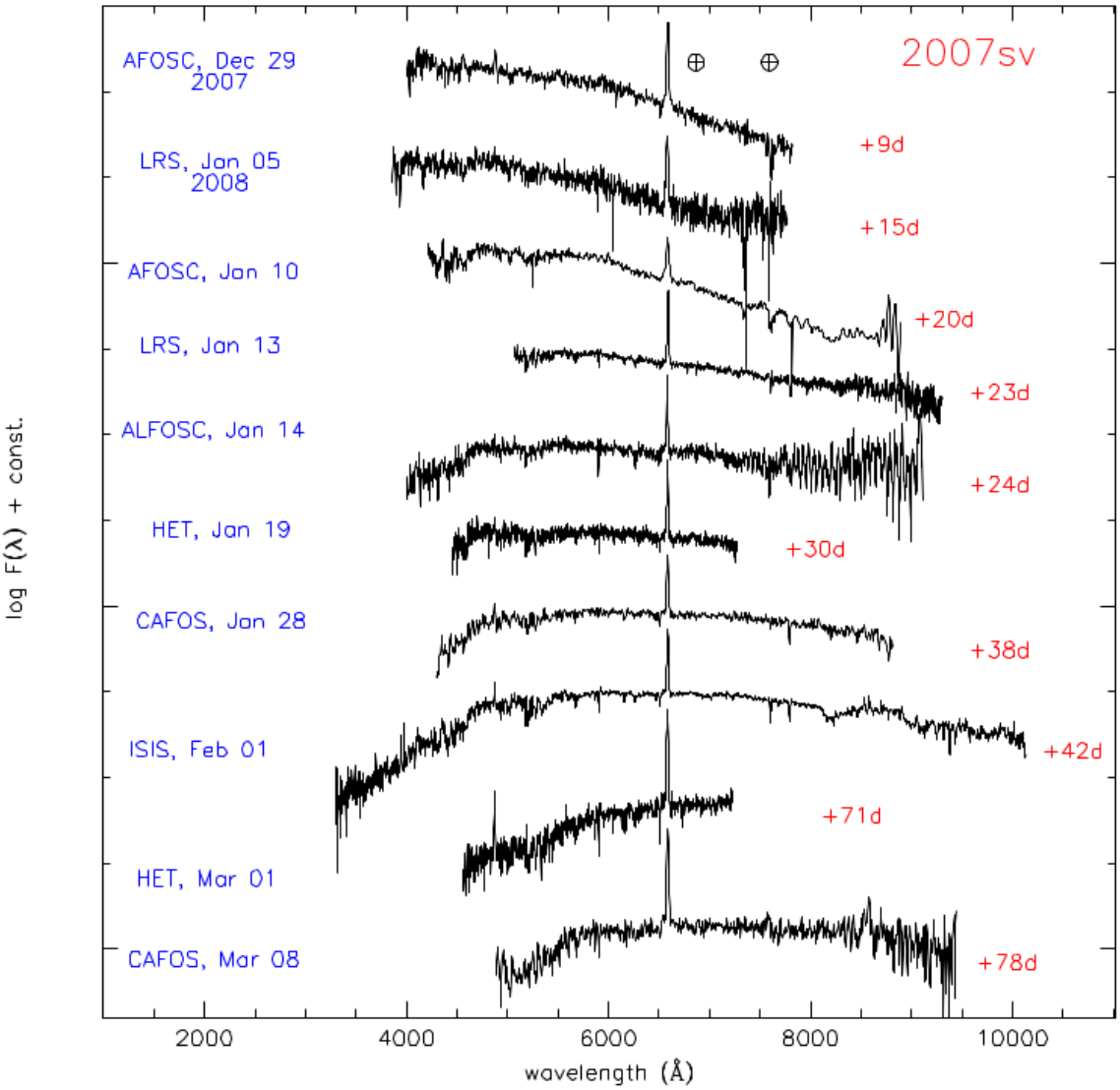

Figure 4.5: Spectral sequence of 2007sv. The date and the instrumental set-up are reported on the left, the phase (in days after the discovery) is indicated on the right. Spectra are flux-calibrated. The ⊕ symbols mark the positions of the visible telluric absorptions.

4.2.1 Spectral evolution and line identification

From Figure 4.5, we note that all spectra of 2007sv are dominated by a prominent and narrow Hα emission line. We also remark that there is relatively little evolution in the spectral features during the almost 80-days coverage window, except for the continuum becoming progressively redder with time. As the spectra are characterized by a significant continuum contribution to the total flux, we estimated the temperature of the emitting region through a black-body fit. The temperature experienced a rapid decline from $\simeq$ 8000 K in the +9 d spectrum to $\simeq$ 5000 K at phase $\sim$ 20 d. Thereafter, the temperature slowly declines to $\simeq$ 4000 K in the late-time spectra (71$-$78 d; Figure 4.5, see also Section 4.2.2). This evolution is consistent with that of the broad-band colours (Figure 4.4). As mentioned above, there is little spectral evolution during the almost 80 d of spectral coverage. However, it should be noticed that the spectra have relatively poor resolution and low S/N. Therefore, it is difficult to measure evolution in the weak and narrow spectral features. In order to investigate the presence of low-contrast spectral lines, we inspected in detail one of our highest S/N spectrum

(ISIS, phase +42 d).

The line identification is shown in Figure 4.6. The identification was performed by comparing the spectra of 2007sv with that of the SN impostor UGC2773-20009OT1 from the Padova-Asiago SN archive (also shown in Figures 4.6 and 4.9; resolution11 Å). A comprehensive line identification for UGC2773-2009OT1 was performed by Smith et al. (2010) and Foley et al. (2011). Figure 4.6 shows that, despite the different resolution, the spectra of the two transients are very similar, with a number of lines in common (see e.g. Figures 8 to 12 in Smith et al. 2010). We determined an indicative photospheric velocity in the spectrum of 2007sv ($\simeq 500$ km s^{-1}) from the blue-shifted absorption component of the Ba II 6496.6 Å line, and the expected positions of all other absorption lines were derived by adopting this velocity for all ions. The lines with strong emission components (e.g Hα, Hβ, H&K Ca II and the NIR Ca II) were identified using their rest wavelengths. We marked only multiplets with an intensity of the strongest line 5σ above the noise level. We also identified O I (multiplets 1 and 4), Ba II (multiplets 1 and 2), Na ID (doublet at 5889.9 and 5895.9 Å), Sc II (multiplets 13, 28, 29, 31), Fe II (multiplets 27, 28, 37, 38, 40, 42, 46, 48, 49, 74, 199, 200). These lines show a narrow P-Cyg profile (blueshifted by about 650 km s^{-1}), although a shallow high-velocity component in the NIR Ca II triplet cannot be ruled out (see Section 4.2.3). We also marked the positions of the [Ca II] doublet lines at 7292 Å and 7324 Å, which are prominent in the spectrum of UGC2773-20009OT1 but not in the 2007sv spectrum[5].

4.2.2 Hα profile and evolution of the main observables

The evolution of the Hα profile during the almost 80d of spectral coverage is highlighted in Figure 4.7. We notice that there is no significant change in the wavelength position of the Hα emission peak.

The Hα line profile is relatively complex. A narrow component is detected in our higher resolution spectra of 2007sv, but a simple Gaussian or Lorentzian line fit does not well reproduce the entire line profile. For this reason, we adopted a combination of multiple line components to improve the accuracy of the spectral line fit. A broad component (decreasing from ≥ 2000 to $\simeq 1700$ km s^{-1}) is visible in the two earliest spectra (phases +9 d and +15 d). This component is only marginally detected in the two subsequent spectra (+20 d and +23 d), and disappears at later phases. In fact, the broad component is below the detection threshold in the +24 d ALFOSC spectrum. Starting from the LRS spectrum at +23 d, we improved our fits by including an intermediate-width component (FWHM velocity ≈ 600 km s^{-1}). While we cannot rule out that the intermediate component was also present at earlier phases, the modest resolution of the +9 d to +20 d spectra prevents us its discrimination from the narrow component. In the spectra collected at later phases, a two-component (intermediate + narrow) fit well reproduces the observed line profile.

The Hα line profile is relatively complex. A narrow component is detected in our higher resolution spectra of 2007sv, but a simple Gaussian or Lorentzian line fit does not well reproduce the entire line profile. For this reason, we adopted a combination of multiple line components to improve the accuracy of the spectral line fit. A broad component (decreasing from ≥ 2000 to $\simeq 1700$ km s^{-1}) is visible in the two earliest spectra (phases +9 d and +15 d). This component is only marginally detected in the two subsequent spectra (+20 d and +23 d), and disappears at later phases. In fact, the broad component is below the detection threshold

[5]We also note that a telluric feature matches the wavelength position of the [Ca II] doublet, therefore no robust conclusion can be inferred on the identification of this feature in the 2007sv spectrum.

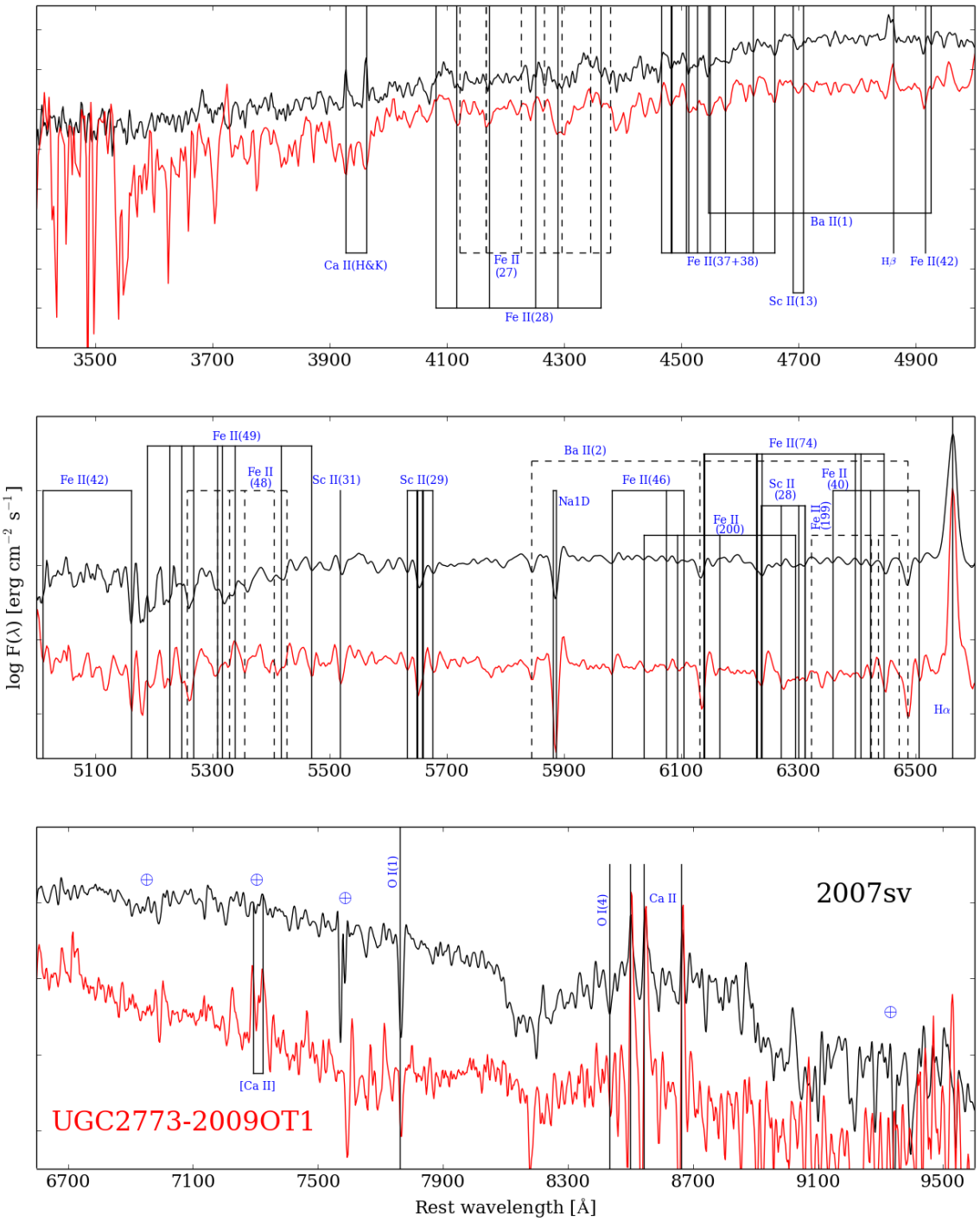

Figure 4.6: Line identification of the ISIS spectrum obtained on February 1, 2008 of 2007sv. A comparison with the spectrum of the transient UGC2773-2009OT1 obtained with the Telescopio Nazionale Galileo + LRS on Oct 11, 2009 (slightly before maximum, Padova-Asiago SN archive) is also shown. The spectra are flux-calibrated and redshift-corrected. H and Ca II lines are marked at their rest wavelengths; the marks for the other lines are blue–shifted by $\simeq 500$ km s^{-1}. The $\oplus$ symbols mark the positions of prominent telluric absorption bands.

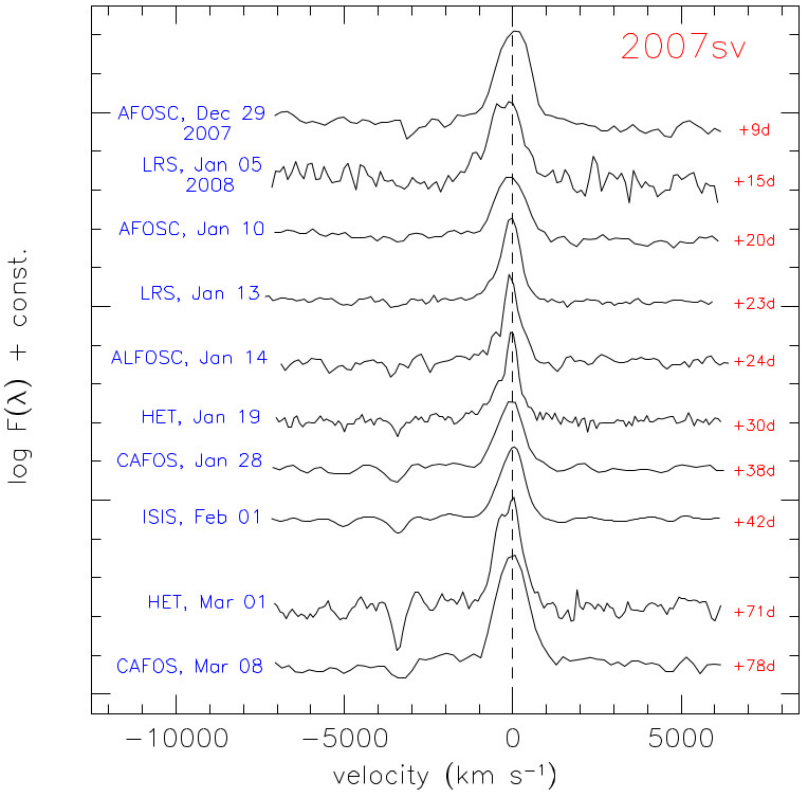

Figure 4.7: Evolution of the profile of Hα in the velocity space.

in the +24 d ALFOSC spectrum. Starting from the LRS spectrum at +23 d, we improved our fits by including an intermediate-width component (FWHM velocity $\approx 600\,\mathrm{km\ s^{-1}}$). While we cannot rule out that the intermediate component was also present at earlier phases, the modest resolution of the +9 d to +20 d spectra prevents us its discrimination from the narrow component. In the spectra collected at later phases, a two-component (intermediate + narrow) fit well reproduces the observed line profile.

In order to analyse the evolution of the velocity of the different Hα components and the total line flux, we first corrected the spectra for redshift (adopting 1116 km s^{-1} as the mean heliocentric radial velocity[6]) and for foreground Galactic extinction (using the reddening values mentioned above). Then we measured the total line flux, and the full-width-at-half-maximum (FWHM) velocities of the three Hα line components. In most spectra, the narrow component was unresolved, and even the intermediate component was occasionally below (or near) the resolution limits. In these cases, a multicomponent fit using a combination of Gaussian functions provided good fits. However, in some cases (namely for the two higher resolution HET spectra), we used a Gaussian function for the intermediate component and a Lorentzian profile for the narrow component. Figure 4.8 (top panel) shows the evolution of the velocity of the ejected material for the three line components.

As mentioned above, the narrow component was unresolved in most cases. When the narrow Hα was unresolved, we used the spectral resolution as an upper limit for the velocity of the slowest-moving material.

[6] http://leda.univ-lyon1.fr/

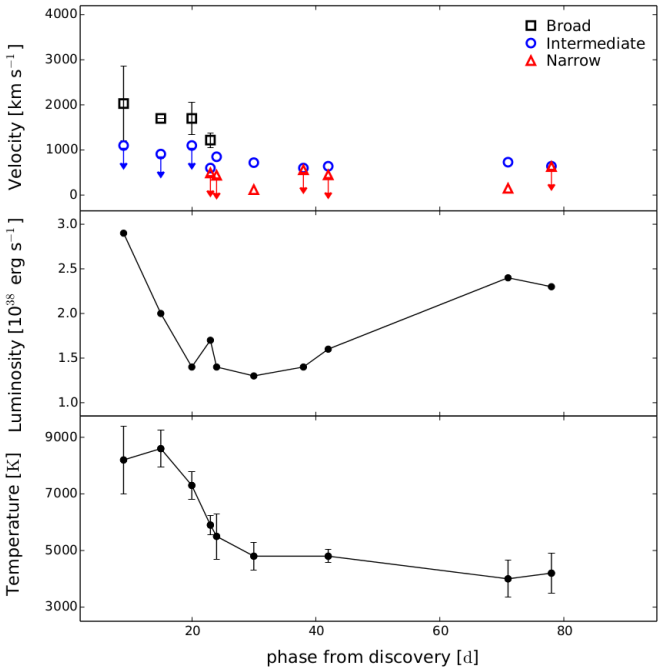

Figure 4.8: **Top.** FWHM evolution for the broad (black squares, solid line), the intermediate (blue circles) and the narrow Hα (red triangles) components. **Middle.** Evolution of the total luminosity of Hα. We assume a 10% error in the measures, due only to the error in the flux calibration. **Bottom.** Evolution of the spectral continuum temperature.

When the narrow line component was resolved, we first corrected the measured FWHM for the spectral resolution ($width = \sqrt{\mathrm{FHWM}^2 - \mathrm{res}^2}$) and then computed the velocity ($v = \frac{width}{6562.8} \times c$). In the highest resolution HET spectra at phases +30 and +71 d, we measured the FWHM of the narrower component as 120±30 km s^{-1} and 150±40 km s^{-1}, respectively. The intermediate component remains at roughly constant velocity around $600-800$ km s^{-1} at all epochs. Finally, the broad component is characterized by a fast decline from $\simeq 2000$ km s^{-1} in our first spectrum to ≈ 1200 km s^{-1} in the +23 d spectrum. We note that these values are significantly smaller that the typical values of $\simeq 10000$ km s^{-1} measured in the ejecta of young SNe.

Multiple line components in the spectra of interacting objects are known to arise from different emitting gas shells (see e.g. Turatto et al. 1993a). The very small velocities inferred for the narrow Hα in the HET spectra ($120-150$ km s^{-1}) are consistent with those expected in the wind of an LBV. The velocity evolution of the broad component is consistent with material violently ejected, and in particular with the velocities observed in the fastest hydrogen-rich material expelled in major eruptions of LBVs (Smith 2008; Pastorello et al. 2010b, 2013). More puzzling is the interpretation of the intermediate component. According to the interpretation usually adopted in interacting SNe (see e.g. Chevalier & Fransson 1994), the intermediate velocity component arises in the gas region between the forward shock and the reverse shock. In the case of 2007sv, the relative strength of this component progressively increases with time with respect to that of the narrow component. This would support the idea that a significant fraction of the line flux at late phases arises from the gas interface between the two shock fronts, hence from the shocked gas region. In addition, one may note that the intermediate component is significantly blue-shifted with respects to the narrow one. In the ejecta/CSM interaction scenario, a blue-shifted intermediate component

Table 4.4: Main parameters inferred from the spectra of 2007sv.

Phase (days)	FWHM($H_{\alpha,broad}$) (km s^{-1})	FWHM($H_{\alpha,intermediate}$) (km s^{-1})	FWHM($H_{\alpha,narrow}$) (km s^{-1})	H_α Luminosity (10^{38} erg s^{-1})	Resolution (km s^{-1})
9	2030 ± 830	< 1100	-	2.9	1100
15	1700:	< 910	-	2.0	910
20	1700 ± 360	< 1100	-	1.4	1100
23	1220 ± 160	600 ± 100	< 490	1.7	490
24	-	850 ± 180	< 440	1.4	440
30	-	720 ± 100	120 ± 30	1.3	280
38	-	600 ± 120	< 560	1.4	560
42	-	640 ± 100	< 450	1.6	450
71	-	730 ± 100	150 ± 40	2.4	270
78	-	640 ± 130	< 630	2.3	630

The measured FWHM of the broad, intermediate and narrow components of H_α are reported in columns 2, 3 and 4, respectively. The measure marked with the : symbol is uncertain.
The total luminosity of Hα is in column 5, the spectral resolution in column 6.

may be explained with an attenuation of the red line wind due to prompt dust formation in a post-shock cool dense shell, as observed in a number of interacting SNe (e.g. SN 2006jc, Smith et al. 2008; Nozawa et al. 2008; Mattila et al. 2008). Alternatively, very asymmetric and blue-shifted line profiles may be interpreted in terms of a highly asymmetric geometrical distribution of the CSM (see, e.g., the interpretation of Stritzinger et al. 2012, for the Type IIn SN 2006jd).

A progressive enhancement of ejecta/CSM interaction emission can be inferred observing the evolution of the total Hα flux in the latest spectra (phase > 70 d; Table **??** and Figure 4.8, middle panel). The flux decreases from about 7×10^{-15} erg s^{-1} to 3×10^{-15} erg s^{-1} during the first ~ 40 days. Later on, we note an increase by a factor almost two in the Hα flux, approximatively to about 5.5×10^{-15} erg s^{-1} in the last two spectra. As mentioned above, this can be interpreted as an increased contribution of the intermediate component arising in a shocked gas region which dominates the flux contribution at late phases over the other line components.

4.2.3 Spectral comparison with other interacting transients

An important issue is to determine whether the spectroscopy alone allows us to discriminate between genuine Type IIn SNe and SN impostors. For this goal, we compare in Figure 4.9 the early-time AFOSC spectrum (phase +9 d) of 2007sv with spectra of young transients with narrow emissions, viz. the impostors 1997bs (Van Dyk et al. 2000) and UGC2773-2009OT1 (Padova–Asiago SN Archive; Pastorello et al. in preparation), the classical Type IIn SN 1999el (Di Carlo et al. 2002) and SN 2008S (Botticella et al. 2009). SN 2008S is the prototype of a small family of intermediate-luminosity transients (see Thompson et al. 2009, and references therein) whose nature has been widely debated. Although many observables of SN 2008S are similar to those of SN impostors, the detection of prominent, narrow [Ca II] (7292–7324 Å) lines and, even more, the late-time light-curve with a decline rate consistent with that expected from the ^{56}Co decay (Botticella et al. 2009), provide reasonable arguments to support a faint SN scenario. The progenitor star of SN 2008S was detected in mid-infrared archive Spitzer images, whilst there was no detection in deep optical and near-IR pre-explosion frames (e.g. Prieto et al. 2008). This was interpreted as a clear signature that the progenitor was a highly reddened star, embedded in a dusty environment. Although there is general agreement

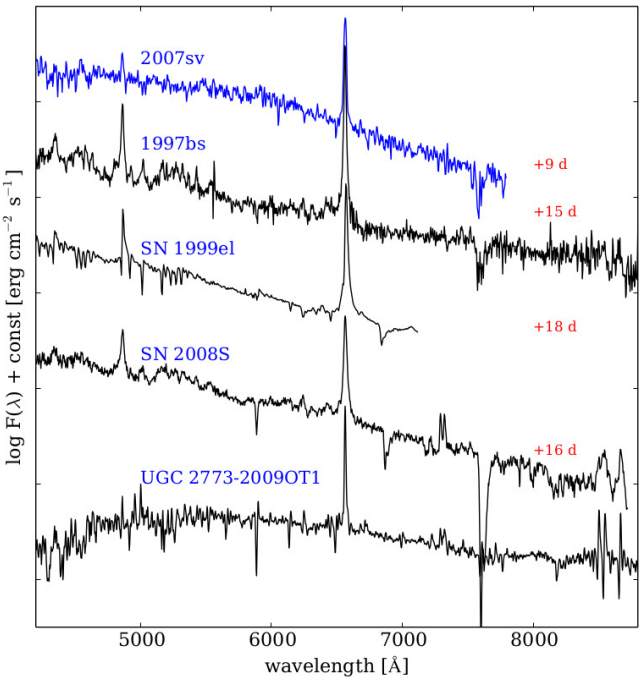

Figure 4.9: Comparison of early-time spectra of the impostors 2007sv, 1997bs (unpublished spectrum from the Padova–Asiago SN archive obtained on 1997 April 30th with the ESO1.52 m telescope, resolution 10 Å, located at La Silla, Chile) and UGC2773-2009OT1 (spectrum obtained slightly before maximum), the enigmatic transient SN 2008S, and the linearly-declining Type IIn SN 1999el. The spectra are flux-calibrated and redshift-corrected.

that the progenitor star of SN 2008S was a moderate-mass star[7], the characterization of the stellar type is somewhat different in the different papers, ranging from a ~ 9 $M_\odot$ extreme asymptotic giant branch star (AGB; e.g. Prieto et al. 2008; Khan et al. 2010; Kochanek 2011; Szczygieł et al. 2012) to a ≤ 20 $M_\odot$ supergiant (Smith et al. 2009). The most debated issue is whether the observed 2008 outburst was a terminal stellar explosion, most likely as an electron-capture SN from a super-AGB star (Pumo et al. 2009; Tominaga et al. 2013) or an LBV-like outburst of a mildly massive star (Smith et al. 2009, 2011).

From the comparison in Figure 4.9, it is evident that the spectra of all these transients are rather similar, and have many spectral lines in common. Therefore this is an indication that the spectra alone may not be sufficient to discriminate between impostors and true SNe. As mentioned before, the narrow [Ca II] doublet at 7292–7324 Å is the hallmark feature for SN 2008S-like transients and is sometimes used as an argument to support the SN nature of these objects. We note that there is no clear evidence for the presence of [Ca II] lines in the spectra of 2007sv or 1997bs. However, we have to admit that the [Ca II] feature was detected in UGC2773-2009OT1 (which is clearly an impostor, see Smith et al. 2010; Foley et al. 2011). Therefore, the [Ca II] feature is not a good discriminant of the nature of these explosions.

In Figure 4.10, the 7800–8700 Å wavelength window of the +42d ISIS spectrum of 2007sv is compared with spectra of SN 2008S and UGC2773-2009OT1. In all of them, we find the Ca II triplet at 8498.0 Å, 8542.1 Å and 8662.1 Å, which is another very common feature in many types of transients, although some differences in the line strengths and velocities can be

[7] A similar conclusion was also inferred for the detected progenitor of the 2008S-analogous NGC300-2008OT1 (Bond et al. 2009; Berger et al. 2009)

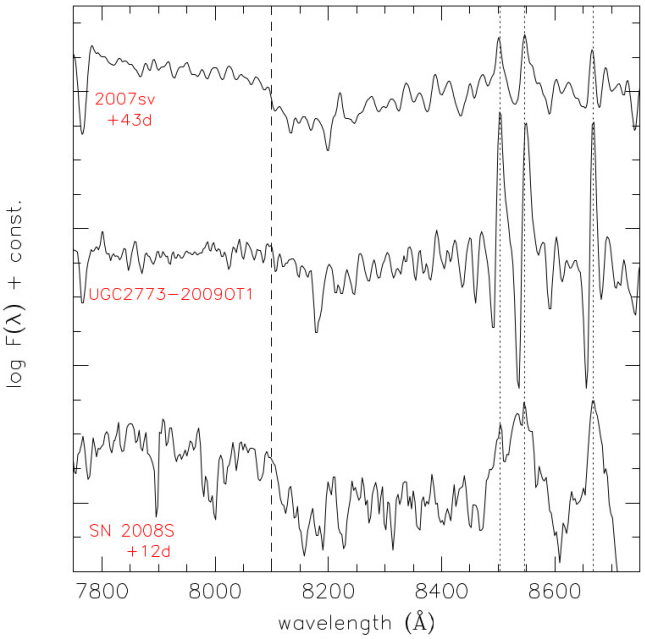

Figure 4.10: Comparison of the NIR Ca II triplet line profiles in three different types of faint transients, viz. 2007sv, UGC2773-2009OT1 and SN 2008S (from top to bottom). The three dotted lines mark the positions of the lines of the Ca II triplet at 8498.0 Å 8542.1 Å and 8662.1 Å. The dashed line indicatively marks the velocity close to the terminal velocity of the gas. The spectra are flux-calibrated and redshift-corrected.

appreciated. The three spectra show narrow features with velocities of a few hundreds km s^{-1}, and these mark the presence of slow-moving material. However, a very broad depression with a minimum at about 8200 Å is visible in all the spectra of Figure 4.10, suggesting that a small amount of material can be ejected at high velocities (above 10000 km s^{-1}) also in SN impostors. The presence of fast-moving material has been also reported in the η Car circumstellar environment (Smith 2008). Therefore, the detection of high-velocity gas alone should not be considered a robust argument to favor a SN scenario[8].

4.3 Discussion

In Sections 4.1 and 4.2, the photometric and spectroscopic properties of the optical transient 2007sv have been described. The main goal is now to provide convincing insights on its nature (SN vs. SN impostor). Already from a quick investigation of the spectra of 2007sv, the similarity with the spectra of well-known SN impostors (e.g. 1997bs and UGC2773-2009OT1, Van Dyk et al. 2000; Smith et al. 2010; Foley et al. 2011) is evident. However, some similarity can also be found with the spectra of genuine interacting SNe (such as SNe 1999el and 1995G, Di Carlo et al. 2002; Pastorello et al. 2002). The comparisons shown in Section 4.2.3 confirm that there are only subtle differences between spectra of LBV-like eruptions and genuine Type IIn SNe, giving evidence that from the spectroscopic analysis alone, it is sometimes tricky to discriminate between the two types of transients.

However, from an in-depth inspection of our spectral sequence of 2007sv, we can obtain crucial information on this object. The increased total luminosity of Hα and the enhanced strength of the intermediate-velocity component in the late time spectra suggest that the

[8]We note, however, that this argument is instead used by many authors to favor the SN explosion scenario for the debated SN 2009ip.

material ejected in the outburst is interacting with the pre-existing CSM. We also find that along with the expected narrow components, Hα and the Ca II NIR triplet show broader wings (Figure 4.10), suggesting an outflow of material at velocities comparable with those observed in SN ejecta. The maximum velocity registered for the outflowing material (dashed line in Figure 4.10) is about 14000 km s^{-1} (although it is clear that the bulk of this material is expanding at much lower velocity, viz. $\sim$ 8000 km s^{-1}). The detection of prominent broad spectral features from typical nucleosynthesis products observed in SN ejecta would be a more robust tool to distinguish between SNe and impostors. We do not detect any broad line of α- or Fe-peak elements in the late-time spectra (approx. +80 d) of 2007sv, except for the shallow absorption attributed to the Ca II NIR triplet. For this reason, the general spectral properties of 2007sv favour a non-terminal explosion scenario for this transient, although we have to admit that these can not be considered as conclusive proofs to unveil the nature of this interacting transient.

A more robust constraint can be obtained from the photometric analysis. In some cases, impostors were unmasked through their erratic light-curves. It is worth mentioning the optical transient observed during the period 2000-2009 in NGC 3432 (aka 2000ch, Wagner et al. 2004; Pastorello et al. 2010b) and also the 2009-2012 recurrent transient observed in NGC 7259 (known as 2009ip, Smith et al. 2010; Foley et al. 2011; Pastorello et al. 2013). The latter was followed by a major eruption in mid-2012 that has been proposed to be a terminal SN explosion (Smith et al. 2014, and references therein). More frequently, impostors reveals themselves through a single episode, characterized by a fast-evolving but regular light-curve. A classical example is 1997bs (Van Dyk et al. 2000), whose light-curve shape is not trivially discernible from that of a regular SN. And the light-curve of 2007sv is remarkably similar to that of 1997bs. However, the colours of 2007sv rapidly become redder as the object evolves, due to the decreasing temperature of the emitting region (this finding is confirmed by the temperature evolution inferred through black-body fits to the spectral continuum). The colour/temperature transition is observed to occur on much shorter timescales than in typical SNe IIn (see e.g. Fig. 4.4).

Finally, the peak luminosity still remains the most used method to discriminate between SNe and impostors. With a distance modulus of 31.38 ± 0.27 mag, we derive for 2007sv an absolute magnitude of $M_R = -14.25 \pm 0.38$ mag. This value is 4 to 6 magnitudes fainter than the absolute magnitudes typically measured in Type IIn SNe (e.g. Richardson et al. 2002).

4.3.1 Which mechanisms can produce 2007sv-like events?

The faint absolute magnitude at the discovery and the rapid colour (temperature) evolution provide robust evidence for the impostor nature of 2007sv, though some cases of faint transients exist in the literature that have been proposed to be true SNe. In fact, weak SNe can be produced via i) the core-collapse explosion of a peculiar SN through electron capture of a moderate-mass star; ii) the fall back event from a very massive star (Pumo et al. 2009, and references therein). Both mechanisms are believed to produce absolute light-curves fainter than those observed in canonical SN types.

In the former scenario, the ONeMg stellar core of a $8 - 10$ M$_\odot$ super-AGB star collapses generating a weak, low-energy event called electron-capture (EC) SN. The SN ejecta may eventually interact with an H-rich circumstellar environment generated by the stellar mass-loss during the super-AGB phase. As mentioned in Section 4.2.3, a promising candidate EC SN is SN 2008S (Botticella et al. 2009), an object that shares some similarity with a

SN impostor, but has a SN-like shaped light-curve and a late-time light-curve decline consistent with the ^{56}Co decay rate. In the latter scenario, the collapse of a very massive star ($> 25 - 30$ M$_\odot$; Zampieri et al. 2003) is followed by the fall-back of the inner stellar mantle onto the stellar core, generating eventually a black hole. In both scenarios a common feature is the faint absolute magnitude, which is generally due to the small amount of radioactive ^{56}Ni in the ejecta. The presence of radioactive material in the ejecta can be revealed from the decline rate of the late-time SN light-curve. However, in massive stars the interaction of the ejecta with the pre-existing CSM can induce a dramatic increase in the radiated energy, and cause significant deviations from the luminosity peak and light-curve decline rate expected in the radioactive decays, making the detection of ^{56}Co signatures problematic.

Another efficient mechanism proposed to explain transient events with a total radiated energy comparable with those of real SNe is the pulsational pair-instability in very massive stars. Woosley et al. (2007) showed that major instabilities produced by electron-positron pair production (pulsational-pair instability) cause the ejection of massive shells without necessarily unbinding the star (and hence without leading to a terminal SN explosion). These major mass-loss episodes might produce transients currently classified as SN impostors. In addition to this, when a new shell is ejected and collides with pre-existing material, the resulting radiated energy is comparable with that of a core-collapse SN (sometimes even one order of magnitude higher). If the impacting material is H-rich, the shell-shell collisions would produce a SN IIn-like spectrum and a slow-evolving, luminous light-curve that would make the transient practically indiscernible from true SNe IIn. All of this further complicates our attempts of discriminating SNe IIn from eruptive impostors.

A safe discrimination criterion would be the detection of the products of stellar and core-collapse explosive nucleosynthesis through the prominent α-element lines in the nebular spectra. But in many SNe IIn the inner ejecta are covered by the H-rich interaction region sometimes for very long timescales (up to many years), making the detection of the α-element spectral features difficult.

All the clues illustrated so far make us confident that 2007sv was not a terminal SN explosion, but very likely a major eruption mimicking the SN behaviour. If this is true, the progenitor star may have reached again a quiescent stage, returning to the pre-eruptive bolometric luminosity. This can be confirmed through an inspection of deep, high resolution images obtained years after the outburst, for example using the Hubble Space Telescope or the largest ground based telescopes which can deliver sub-arcsecond images. The identification of the quiescent progenitor in such high-quality images would be final evidence that the massive star producing 2007sv is still alive. Alternatively, a long timescale monitoring of 2007sv can eventually reveal further outbursts after the one registered in 2007, which would also prove that the 2007 episode was not the final stellar death. This strategy worked well for the 2000 transient observed in NGC 3432 (Wagner et al. 2004) that was recovered after 8 years during a subsequent eruptive phase (Pastorello et al. 2010b).

4.3.2 Is 2007sv heralding a SN explosion?

In order to identity further outbursts experienced by the progenitor of 2007sv, we analysed a number of images of the transient site obtained before and after the 2007 event. These data were mostly collected by amateur astronomers, with a few additional observations performed with the 1.82 m Telescopio Copernico of the Asiago Observatory. These observations are listed in Table 4.A.1 in Appendix 4.A. The unfiltered observations of amateur astronomers were scaled to R-band magnitudes using the magnitudes of references stars reported in Table 4.2.

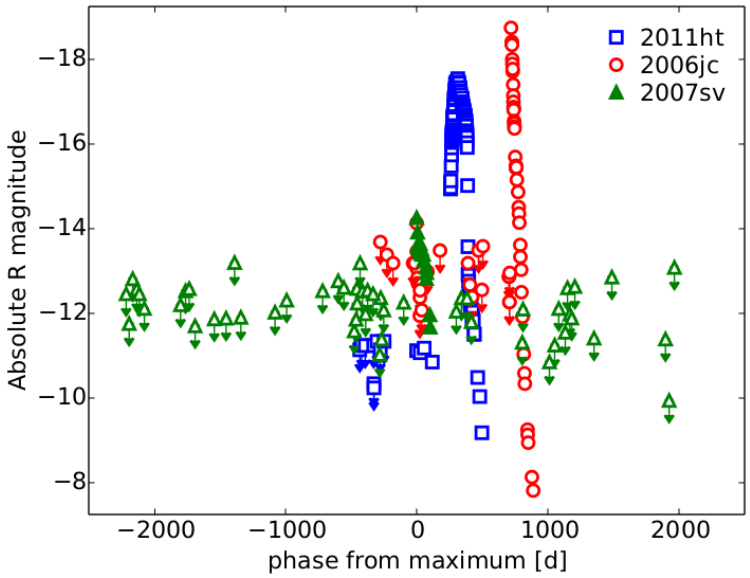

Figure 4.11: Plot of the photometric limits (open triangles) obtained from 2001 November 27 to 2014 January 07 and the absolute R-band light-curve of 2007sv. The absolute light-curve of the Type Ibn SN 2006jc and the Type IIn SN 2011ht are shown for comparison. The phases refer to the first recorded eruption.

These images of the 2007sv site span a period of almost one decade. In this temporal window, we did not detect any further signature of a variable source at the position of 2007sv (see Figure 4.11). The Pan-STARRS1 survey imaged this galaxy on 52 separate nights between 2010 February 25 (MJD 55252.30) and 2013 May 17 (MJD 56429.26) in one of the filters $g_{\rm P1}r_{\rm P1}i_{\rm P1}z_{\rm P1}$ (for a description of the Pan-STARRS1 3π survey, see Inserra et al. 2013; Magnier et al. 2013). No further detection of any outbursting activity was seen, and the magnitude limits of these individual epochs are typically 22.0, 21.6, 21.7, 21.4 and 19.3 mag respectively for $g_{\rm P1}r_{\rm P1}i_{\rm P1}z_{\rm P1}$ (as reported in Inserra et al. 2013). These magnitudes are in the AB system, as reported in Tonry et al. (2012).

Tracing the photometric history of a SN impostor has also another objective. As briefly mentioned in Section 1, there is growing evidence that some interacting SNe may be preceded by large stellar eruptions (i.e. impostor events). A similar sequence of events has been proposed for a number of SNe, from the remarkable case of SN 2006jc discovered by K. Itagaki (Nakano et al. 2006; Yamaoka et al. 2006; Pastorello et al. 2007) to a few recent Type IIn SNe (see Smith et al. 2014, and references therein). In several cases, a lower luminosity outburst was observed a few weeks before the brightest event (i.e. the putative SN). However, occasionally, a larger time delay was observed between the two episodes (1-2 years). In Figure 4.11, together with 2007sv, we also show two cases of SNe that were heralded by an outburst with a significant time delay. SN 2006jc is a stripped-envelope SN (of Type Ibn) whose ejecta were seen to interact with He-rich CSM (Pastorello et al. 2007, 2008; Foley et al. 2007). Its progenitor experienced an outburst 2 years before its explosion as a core-collapse SN, and the magnitude of this impostor ($M_R \simeq -14$ mag) was comparable with that expected in an LBV eruption, although the progenitor was very likely a WR star. SN 2011ht was initially classified as a SN impostor on the basis of its early spectral properties (Pastorello et al. 2011), and was later reclassified as a Type IIn SN after a major spectral metamorphosis (Prieto et al. 2011). However, the nature of SN 2011ht nature is not fully clarified. There are controversial interpretations on its SN-like observables (Roming et al. 2012; Humphreys et al. 2012; Mauerhan et al. 2013b; Fraser et al. 2013b), since collisions among massive shells might still

explain SN 2011ht without necessarily invoking a core-collapse. Interestingly, a posteriori, a weak transient has been observed about one year before the main episode (Fraser et al. 2013b). This weak source, (labelled as PSO J152.0441+51.8492 by Fraser et al. 2013b) was detected in archival data of the Panoramic Survey Telescope and Rapid Response System 1 (Pan-STARRS1) at an absolute magnitude $M_R \approx -11.8$ mag. Fraser et al. (2013b) provided strong arguments that the two sources were physically related. Recent studies (see Ofek et al. 2014) claim that pre-SN eruptions are quite common. Nonetheless, so far only an handful of impostors with solid detections have been observed to be followed by what is believed to be a true SN explosion.

The most intriguing issue is that, although there are some outliers with the absolute magnitudes brighter than -14 mag (Ofek et al. 2014), most pre-SN outbursts (those with robust detections) have absolute magnitudes close to or fainter than -14 mag, nearly coincident with absolute magnitude of 2007sv. Although there was no further detection of a re-brightening of 2007sv before and after 2007, its overall photometric similarity with the precursors of SN 2006jc and other interacting SNe, may lead to the speculation that impostors such as 2007sv are instability episodes of massive stars (some of them in the LBV stage) that can be followed on short timescales (months to decades) by a terminal stellar explosion, as an ejecta-CSM interacting SN.

4.4 Conclusions

In this Chapter we have reported the results of our follow-up campaign of the transient 2007sv. Our photometric monitoring spans a period of over 100d, whilst our spectroscopy data cover $\simeq 80$ d of the evolution of 2007sv. The spectra are largely dominated by a multi-component Hα line in emission. This spectral characteristic is common to both SN impostors and Type IIn SNe.

As we have illustrated, although there are uncertainties on the observational constraints and the discrimination between true interacting SNe and SN impostors is often a tricky issue, the lack of broad lines from α-elements, the fast colour/temperature evolutions, along with the relatively low velocity of the ejecta and the faint absolute magnitude at the discovery ($M_R = -14.25$ mag), support the SN impostor scenario for 2007sv, most likely a major eruption of an LBV. Although we do not have stringent pre-discovery limits, we claim that 2007sv was discovered soon after the outburst. Hence, we have adopted the discovery magnitude as an indicative guess for the peak magnitude. The rapid evolution of the colours and the temperature of the ejecta at early phases support this assumption.

However, some doubts still remain whether 2007sv was instead a very weak terminal explosion of a massive star. In absence of the detection of further outbursts or a future 'real' SN explosion (as observed in similar transients), the most promising method to definitely rule out the possibility that 2007sv was a faint interacting core-collapse SN is by obtaining deep and high spatial resolution images of the transient's site (e.g. with HST), in the attempt to detect some signatures from the surviving star. This method, that has been successfully tested to find the progenitors of a number of CC-SNe (see Smartt 2009, and references therein) and may well give the final answer to the enigma of 2007sv.

References

Berger, E., Soderberg, A. M., Chevalier, R. A. 2009, ApJ, 699, 1850

Bond, H. E., Bedin, L. R., Bonanos, A. Z., Humphreys, R. M,; Monard, L. A. G. B., Prieto, J. L.; Walter, F. M. 2009, ApJ, 695, L154

Botticella, M. T., Pastorello, A., Smartt, S. J., et al. 2009, MNRAS, 398, 1041

Cappellaro, E. (2014). SNOoPy: a package for SN photometry, `http://sngroup.oapd.inaf.it/snoopy.html`

Chevalier, R. A., Fransson, C. 1994, ApJ, 420, 268

Di Carlo, E., Massi, F., Valentini, G., et al. 2002, ApJ, 573, 144

Duszanowicz, G., Boles, T., & Corelli, P. 2007, Central Bureau Electronic Telegrams, 1182, 1

Foley, R. J., Smith, N., Ganeshalingam, M., Li, W., Chornock, R., Filippenko, A. V. 2007, ApJ, 657, L105

Foley, R. J., Berger, E., Fox, O., et al. 2011, ApJ, 732, 32

Fraser, M., Magee, M., Kotak, R., et al. 2013, ApJL, 779, L8

Gal-Yam, A., Leonard, D. C. 2009, Nature, 458, 865

Huchtmeier, W. K., & Skillman, E. D. 1998, A&Aps, 127, 269

Humphreys, R. M., Davidson, K., Jones, T. J., Pogge, R. W., Grammer, S. H., Prieto, J. L., Pritchard, T. A. 2012, ApJ, 760, 93

Inserra, C., Smartt, S. J., Jerkstrand, A., et al. 2013, ApJ, 770, 128

Khan, R., Stanek, K. Z., Prieto, J. L., Kochanek, C. S., Thompson, T. A., & Beacom, J. F. 2010, ApJ, 715, 1094

Kochanek, C. S. 2011, ApJ, 741, 37

Kotak, R., Vink, J. 2006, A&A, 460, L5

Itagaki, K., Nakano, S., Puckett, T., et al. 2006, IAU Circ., 8762, 1

Landolt, A. U. 1992, AJ, 104, 340

Magnier, E. A., Schlafly, E., Finkbeiner, D., et al. 2013, ApJs, 205, 20

Margutti, R., et al. 2014, ApJ, 780, 21

Mattila, S., Meikle, W. P. S., Lundqvist, P. et al. 2008, MNRAS, 389, 141

Nakano, S., Itagaki, K., Puckett, T., Gorelli, R. 2006, CBET, 666, 1

Nozawa, T., Kozasa, T., Tominaga, N. et al., 2008, ApJ, 684, 1343

Ofek et al. 2014, ApJ submitted ()arXiv:1401.5468

Pastorello, A., Turatto, M., Benetti, S. et al. 2002, MNRAS, 333, 27

Pastorello, A., Smartt, S. J., Mattila, S., et al. 2007, Nature, 447, 829

Pastorello, A., Mattila, S., Zampieri, L., et al. 2008, MNRAS, 389, 113

Pastorello, A., Botticella, M. T., Trundle, C., et al. 2012, MNRAS, 408, 181

Pastorello, A., Stanishev, V., Smartt, S. J., Fraser, M.; Lindborg, M. 2011, CBET, 2851, 2

Pastorello, A., Cappellaro, E., Inserra, C., et al. 2013, ApJ, 767, 1

Prieto, J. L., Kistler, M. D., Thompson, T. A. et al. 2008, ApJ, 681, L9

Prieto, J. L., McMillan, R., Bakos, G., & Grennan, D. 2011, Central Bureau Electronic Telegrams, 2903, 1

Pumo, M. L., Turatto, M., Botticella, M. T., et al. 2009, ApJl, 705, L138

Richardson, D.,; Branch, D., Casebeer, D., Millard, J., Thomas, R. C., Baron, E. 2002, AJ, 123, 745

Roming, P. W. A., Pritchard, T. A., Prieto, J. L. 2012, ApJ, 751, 92

Smartt, S. J. 2009, ARA&A, 47, 63

Szczygiel, D. M., Prieto, J. L., Kochanek, C. S., Stanek, K. Z., Thompson, T. A., Beacom, J. F., Garnavich, P. M., Woodward, C. E. 2012, ApJ, 750, 77

Smith, N. 2008, Nature, 455, 201

Smith, N., Foley, R. J., Filippenko, A. V. 2008, ApJ, 687, 1208

Smith, N., Ganeshalingam, M., Chornock, R. et al. 2009, ApJ, 679, L49

Smith, N., Miller, A., Li, W., et al. 2010, AJ, 139, 1451

Smith, N. Li, W., Miller, A. A. et al. 2011a, ApJ, 732, 63

Smith, N., Li, W., Silverman, J. M., Ganeshalingam, M., Filippenko, A. V. 2011b, MNRAS, 415, 773

Smith, N., Mauerhan, J. C., Kasliwal, M. M., & Burgasser, A. J. 2013, MNRAS, 434, 2721

Smith, N., Mauerhan, J. C., Prieto, J. 2014, MNRAS in press (arXiv:1308.0112)

Stritzinger, M., Taddia, F., Fransson, C., et al. 2012, ApJ, 756, 173

Tartaglia, L., Pastorello, A., Taubenberger, S., et al. 2015, MNRAS, 447, 117

Thompson, T. A., Prieto, J. L., Stanek, K. Z., et al. 2009, ApJ, 705, 1364

Tominaga, N., Blinnikov, S. I., Nomoto, K. 2013, ApJ, 771, L12

Tonry, J. L., Stubbs, C. W., Lykke, K. R., et al. 2012, ApJ, 750, 99

Trundle, C., Kotak, R., Vink, J. S., & Meikle, W. P. S. 2008, A&A, 483, L47

Trundle, C., Pastorello, A., Benetti, S., et al. 2009, A&A, 504, 945

Turatto, M., Cappellaro, E., Danziger, I. J., et al. 1993, MNRAS, 262, 128

Van Dyk, S. D., Peng, C. Y., King, J. Y., et al. 2000, PASP, 112, 1532

Wagner, R. M., Vrba, F. J., Henden, A. A., et al. 2004, PASP, 116, 326

Wesson, R., Barlow, M. J., Ercolano, B. et al. 2010, MNRAS, 403, 474

Woosley, S. E., Blinnikov, S., & Heger, A. 2007, Nature, 450, 390

Yamaoka, H., Nakano, S., Itagaki, K. 2006, CBET, 666, 2

Zampieri, L., Pastorello, A., Turatto, M., et al. 2003, MNRAS, 338, 711

Appendix

4.A Photometric limits of 2007sv

Table 4.A.1: Optical detection limits for 2007sv. No source was observed in the position of the transient at any epochs reported in the Table.

Date	MJD	R	Instrument
20011127	52240.11	> 18.96	Apogee AP7
20011220	52263.09	> 19.66	Apogee AP7
20020116	52290.20	> 18.60	Apogee AP7
20020215	52320.81	> 18.85	Apogee AP7
20020307	52340.86	> 18.96	Apogee AP7
20020414	52378.95	> 19.30	Apogee AP7
20030115	52654.91	> 19.22	Apogee AP7
20030222	52692.91	> 18.89	Apogee AP7
20030323	52721.03	> 18.84	Apogee AP7
20030506	52765.91	> 19.72	Apogee AP7
20030930	52912.17	> 19.55	Apogee AP7
20031229	53002.03	> 19.54	Apogee AP7
20040302	53066.83	> 18.22	Apogee AP7
20040419	53114.94	> 19.51	Apogee AP7
20050105	53375.00	> 19.39	Apogee AP7
20050403	53463.98	> 19.11	Apogee AP7
20060103	53738.05	> 18.89	SX
20060305	53899.87	> 18.81	Apogee AP7
20060501	53856.89	> 18.65	Apogee AP7
20060831	53978.90	> 19.84	SX
20060915	53993.00	> 19.56	SX
20060920	53998.95	> 18.83	SX
20060923	54001.87	> 19.18	SX
20061015	54023.78	> 18.23	SX
20061103	54042.08	> 18.89	SX
20061126	54065.91	> 19.43	SX
20061223	54081.06	> 18.88	SX
20070122	54122.88	> 18.96	SX
20070314	54173.86	> 20.39	SX
20070321	54180.88	> 19.05	Apogee AP7
20070328	54187.84	> 20.03	SX
20070413	54203.85	> 19.34	SX
20070913	54356.09	> 19.16	SX
20081017	54756.97	> 19.37	SX
20081125	54795.98	> 19.05	SX
20090107	54838.84	> 19.06	SX
20090209	54871.83	> 19.62	SX
20100304	55259.84	> 20.10	Apogee AP7
20100310	55265.80	> 19.32	SX
20100928	55467.13	> 20.57	SX
20101107	55507.13	> 20.17	SX

Table 4.A.1 Continued

Date	MJD	R	Instrument
20101207	55537.95	> 19.31	SX
20110126	55587.84	> 19.87	SX
20110212	55604.81	> 18.82	Apogee AP7
20110302	55622.86	> 19.44	SX
20110316	55636.87	> 19.53	SX
20110409	55660.94	> 18.79	Apogee AP7
20110903	55807.07	> 20.01	SX
20120117	55943.21	> 18.56	Apogee AP7
20130228	56351.89	> 20.03	ARTEMIS
20130315	56379.86	> 21.48	ARTEMIS
20130320	56371.10	> 21.88	AFOSC
20130507	56419.92	> 18.34	Apogee AP7
20131205	56631.19	> 22.15	AFOSC
20140107	56664.99	> 21.29	AFOSC

The observations, provided by Tom Boles (with a C-14 Celestron Schmidt Cassegrain reflector and an Apogee AP7 CCD camera at the Coddenham Astronomical Observatory, Suffolk, United Kingdom) and Gregor Duszanowicz (with a 0.32 m f/3.1 reflector and a Starlight Xpress MX716 CCD camera at Moonbase Observatory (Akersberga, Sweden)) were unfiltered images, with magnitudes rescaled to R-band.
Multi-band observations were obtained on March 20, 2013, with the following additional detection limits: $U > 19.93$, $B > 20.94$, $V > 21.02$, $I > 21.26$.

Chapter 5

The supernova impostor PSN J09132750+7627410 in NGC 2748

In most cases, SN impostors have been related to major outbursts of LBV stars (see e.g. Van Dyk et al. 2000; Maund et al. 2006; Smith et al. 2010; Tartaglia et al. 2015), given that narrow hydrogen lines present in their spectra have inferred velocities comparable to those of LBV winds (namely a few 10^{2-3} km s^{-1}). In addition, the study of line profiles in Type IIn SN spectra suggests the presence of a CSM with a complex density profile, likely formed through subsequent mass-loss events. Finally, LBVs have been directly seen to produce SNe IIn and/or SN impostors (e.g. Gal-Yam & Leonard 2009; Smith et al. 2010, 2011a). All of this supports the idea that many SN impostors are the extragalactic counterparts of the 'Giant Eruption' of η Car occurred in the 19th century (Davidson & Humphreys 2012), as mentioned in Chapter 4.

However, it has been argued that a fraction of these transients may also arise from stars less massive than LBVs (Smith et al. 2011) or even from stripped WR stars (e.g. Pastorello et al. 2007; Foley et al. 2007; Tominaga et al. 2008). Archival *Spitzer* data suggested a $8-10$ M$_\odot$ progenitor for the controversial SN 2008S (Botticella et al. 2009; Thompson et al. 2009), while a similar range of masses ($10-15$ M$_\odot$; Berger et al. 2009; Bond et al. 2009) have been proposed for both this object and the 2008 optical transient in NGC 300. Although the study of the nearby stellar populations surrounding NGC 300 2008OT-1 favoured a greater value for the initial mass of the progenitor (i.e. $12-25$ M$_\odot$; Gogarten et al. 2009), these masses are lower than those predicted for LBVs. This result supports the idea that LBV-like eruptions may involve different types of stars than previously thought, and mechanisms producing violent eruptions in less massive stars may be different than those producing LBV outbursts (Smith et al. 2011). The SED analysis on archival pre-outburst images of SNhunt248, for example, led Kankare et al. (2015) to conclude that the three peaks observed in its R-band light-curve in 2014 were the result of a non-terminal outburst of a lower mass 'yellow hypergiant', rather than a massive LBV star.

In this context, the results of the photometric and spectroscopic follow-up campaigns of the SN impostor PSN J09132750+7627410 (which will be presented in a forthcoming paper; Tartaglia et al. in preparation) are reported. Its discovery was announced on 2015 February 10 through a IAU Central Bureau for Astronomical Telegram[1]. The transient was observed

[1] `http://www.cbat.eps.harvard.edu/unconf/followups/\J09132750+7627410.html`

in the nearby galaxy NGC 2748 which already hosted two SNe in the past, namely the Type Ia SN 1985A (Wild & Schildknecht 1985; Wegner & McMahan 1987) and the Type Ic SN 2013ff (Brimacombe et al. 2013). PSN J09132750+7627410 was classified as a SN impostor by Tartaglia et al. (2015b) on 2015 February 12, using the 1.82 m Telescopio Copernico (Mt. Ekar, Asiago, Italy) with AFOSC.

Moreover, the detection of the progenitor star in archival images obtained with the Hubble Space Telescope (HST) and the Spitzer Space Telescope (SST) suggests that the precursor was most likely a blue-white supergiant with a mass between 18 and 20 $M_{\odot}$.

In the following, a luminosity distance $D_L = 23.8 \pm 2.0$ Mpc, and hence a distance modulus of $\mu = 31.88 \pm 0.18$ mag, will be adopted for NGC 2748, as reported by the Extragalactic Distance Database[2] (Tully et al. 2009). The foreground Galactic extinction is assumed to be $A(V) = 0.073$ mag, obtained from Schlafly & Finkbeiner (2011), as reported in the NASA/IPAC Extragalactic Database (NED[3]). No additional host galaxy contribution to the total extinction was adopted, as the spectroscopic analysis of PSN J09132750+7627410 revealed no evidences of narrow Na ID absorption features due to interstellar gas at the recessional velocity of NGC 2748.

5.1 Observations and data reduction

The photometric and spectroscopic follow-up campaigns of PSN J09132750+7627410 were carried out using the 1.82 m Copernico telescoped ewuipped with AFOSC (see above for a brief description), the 10.4 m Gran Telescopio Canarias (GTC) with OSIRIS and the 2.56 m Nordic Optical Telescope (NOT) with ALFOSC, both located at the Observatorio del Roque de los Muchachos, La Palma, Spain. We also collected archival data obtained with the 0.105 m Schmidt Telescope located at the Kiso Observatory of the Institute of Astronomy of the University of Tokyo with KWFC, and the GRB 0.5 m telescope located at the Okayama Astrophysical Observatory (National Astronomical Observatory of Japan), available through the public Subaru Mitaka Okayama Kiso Archive (SMOKA[4]). Additional photometric data, as well as several data covering the pre-eruptive phases of the transient were provided by amateur astronomers. The transient was also observed by the UV/Optical Telescope (UVOT) on board of the *Swift* Gamma-ray Observatory[5]. UVOT data (*uvw2, uvm2, uvw1, u, b, v* bands) were processed using the HEASARC software (HEASoft[6], version 6.17) following the prescription of Poole et al. (2008). The host galaxy was also observed by the *Hubble Space Telescope* (HST) in the optical domain and the *Spitzer Space Telescope* (SST) in Near-Infrared (NIR) and we used these images to perform our analysis on the progenitor of PSN J09132750+7627410 (see Section 5.4).

Ground-based spectroscopic and photometric data were pre-processed in the usual manner (overscan, bias and flat-field corrections) using standard IRAF[7] tasks. The final magnitudes were obtained through a dedicated pipeline (SNOoPY; Cappellaro 2014), and calibrated using the magnitudes of a set of stars in the field of the transient. The magnitudes of these local standards are reported in Tables 5.A.1 and 5.A.2 in Appendix 5.A. Unfiltered data from the amateur astronomers were calibrated to the r-band.

[2] http://edd.ifa.hawaii.edu/
[3] https://ned.ipac.caltech.edu/
[4] http://smoka.nao.ac.jp/
[5] http://swift.gsfc.nasa.gov/
[6] http://heasarc.nasa.gov/lheasoft/
[7] http://iraf.noao.edu/

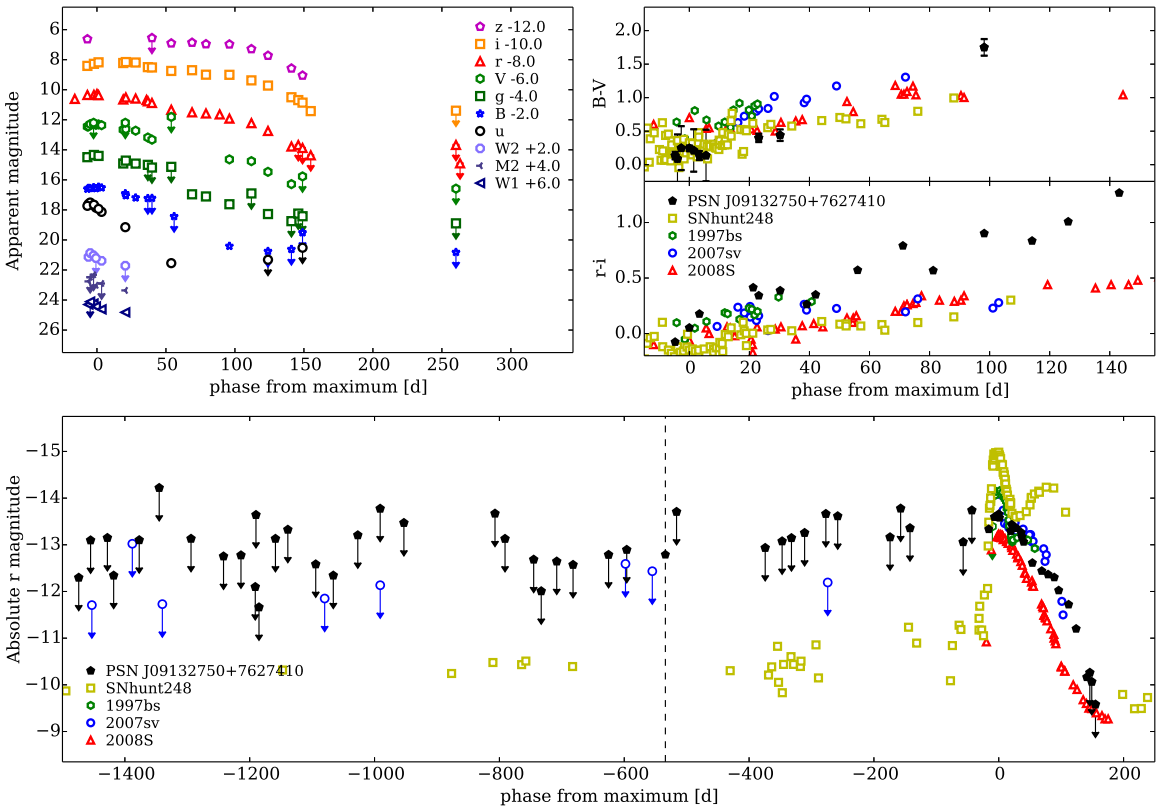

Figure 5.1: **a)** Multi-band light-curves of PSN J09132750+7627410. Arbitrary constants were added to the different magnitudes. **b)** $B-V$ and $r-i$ colour evolutions of PSN J09132750+7627410, compared to those of other SN impostors data. Distance moduli and reddening estimates of 1997bs (μ = 31.1 mag, A_V = 0.093 mag), 2007sv (μ = 31.38 mag, A_V = 0.056 mag), SNHunt248 (μ = 31.76 mag, A_V = 0.140 mag) and 2008S (μ = 28.74 mag, A_V = 1.13 mag) were taken from Van Dyk et al. (2000), Tartaglia et al. (2015), Kankare et al. (2015) and Botticella et al. (2009), respectively. **c)** Historical absolute r-band magnitudes of PSN J09132750+7627410 are compared with those of a sample of different transients. Ultraviolet and BV magnitudes were calibrated in the Vega system, while *griz* magnitudes in the AB photometric system. r and i-band magnitudes for 2007sv, 1997bs, 2008S and SNhunt248 were obtained from the R and I-band magnitudes adding the constant values 0.16 mag and 0.37 mag respectively, following the transformations given by Blanton & Roweis (2007).

The spectroscopic calibrations were performed using spectra of standard stars obtained during the same nights (for the flux calibration), while spectra of comparison lamps obtained with the same instrumental set-up used (for the wavelength calibration). The accuracy of the wavelength calibration was also checked using night sky lines, shifting the spectra in case of discrepancy. The flux calibration was checked using the magnitudes obtained on the closest nights, and a scaling factor was applied when necessary. Finally, we corrected the spectra os PSN J09132750+7627410 for the Galactic foreground extinction and for the redshift (z=0.0049) derived from the recessional heliocentric velocity of the host galaxy reported in NED (1476 ± 2 km s^{-1}).

5.2 Photometric analysis

The outcomes of our photometric analysis are shown in Figure 5.1, while the final magnitudes in the different bands are reported in Tables 5.1, 5.2 and 5.3 for the BV, *ugriz* and

Table 5.1: BV magnitudes of PSN J09132750+7627410. The magnitudes were calibrated to the Vega system.

Date	MJD	B	err	V	err	Instrument
20150212	57065.03	18.61	0.04	18.45	0.03	AFOSC
20150212	57065.81	18.55	0.13	18.44	0.34	UVOT
20150214	57067.06	18.56	0.17	18.29	0.28	UVOT
20150216	57069.50	18.51	0.20	> 18.2	–	UVOT
20150216	57069.78	18.53	0.03	18.27	0.03	AFOSC
20150218	57071.22	18.57	0.10	18.34	0.30	UVOT
20150220	57073.10	18.47	0.06	18.31	0.03	AFOSC
20150222	57075.31	18.52	0.34	18.36	0.18	UVOT
20150310	57091.00	–	–	18.66	0.20	AFOSC
20150311	57092.52	18.91	0.23	> 18.2	–	UVOT
20150311	57092.88	19.04	0.05	18.62	0.03	AFOSC
20150318	57100.00	19.19	0.08	18.73	0.04	AFOSC
20150327	57108.84	> 19.2	–	19.18	0.18	AFOSC
20150330	57111.85	> 19.2	–	19.32	0.18	AFOSC
20150413	57125.83	–	–	> 17.8	–	AFOSC
20150415	57127.89	> 20.4	–	–	–	AFOSC
20150525	57167.94	22.41	0.09	20.64	0.09	ALFOSC
20150610	57183.88	–	–	20.75	0.20	AFOSC
20150622	57195.90	–	–	21.47	0.22	ALFOSC
20150622	57195.90	> 22.8	–	–	–	ALFOSC
20150709	57212.89	–	–	22.28	0.18	ALFOSC
20150709	57212.89	> 22.6	–	–	–	ALFOSC
20150717	57220.95	> 21.5	–	> 21.8	–	AFOSC
20151106	57332.15	> 22.8	–	> 22.6	–	AFOSC

The observations were carried out using the 1.82 m Copernico Telescope with AFOSC and the UV/Optical Telescope (UVOT) on board of the *Swift* Gamma-ray Observatory.

UVOT filters, respectively. Final optical and near-UV magnitudes, obtained with the procedures described in Section 5.1, are shown in panel a). Our i-band image obtained on 2015 May 25 with ALFOSC (obtained with the best seeing condition, FWHM $\sim 0.5''$) was used to accurately pin-point the position of the transient (RA=09:13:27.408, Dec=+76:27:40.91; J2000). About 4 years of archival data were provided mostly by amateur astronomers, and revealed no further eruptive episodes similar to that observed in 2015. However, we report a marginal detection of a fainter transient on 2013 September 2, with absolute magnitude $r \simeq -12.8$, at the same position of the transient observed during the 2015 event (see Figure 5.1 and Table 5.B.1 in Appendix 5.B). The last non-detection prior to the 2015 event is dated 2015 January 6, $\sim$ 1 month before our first r-band point. The r-band maximum occurred on 2015 February 16 (MJD = 57069.76), and we will hereafter consider this as the reference epoch for the phases. After maximum, we note a relatively fast decline in the u-band light-curve with a slope of 6.8 mag/100 d. The light-curves decline more slowly in the other bands, with 4.3 mag/100 d, 2.8 mag/100 d and 3.3 mag/100 d in B, V and g-band respectively, while the r-band light-curve shows a decline rate of 1.9 mag/100 d in the first $\sim$ 130 d, while it steepens at later epochs. A similar behavior is observed in the i and z-band light-curves, with 1.3 mag/100 d and 0.4 mag/100 d in the first $\sim$ 100 d, while the slopes increase to 5.2 mag/100 d and 4.8 mag/100 d, respectively, at later phases.

The evolution of the $B - V$ and $r - i$ colours is shown in panel b). We notice that the colours become progressively redder, in agreement with a rapid decline of the temperature of the emitting gas. Although the colour evolution at early phases is similar to those of other impostors (namely the supernova impostors 2007sv and 1997bs and the peculiar transient 2008S, whose nature is still debated, see e.g. Prieto et al. 2008; Botticella et al. 2009; Pumo

Table 5.2: *ugriz* magnitudes of PSN J09132750+7627410 starting from 2015 February 2. All magnitudes, including the *u*-band UVOT data, were calibrated to the AB system.

Date	MJD	u(err)	g(err)	r(err)	i(err)	z(err)	Instrument
20150202	57055.89	–	–	18.61(0.43)	–	–	Starlight MX 916
20150212	57065.04	17.73(0.04)	18.49(0.08)	18.35(0.06	18.41(0.07)	18.63(0.24)	AFOSC
20150212	57065.81	17.61(0.21)	–	–	–	–	UVOT
20150214	57067.06	17.51(0.15)	–	–	–	–	UVOT
20150216	57069.50	17.68(0.16)	–	–	–	–	UVOT
20150216	57069.76	17.66(0.07)	18.34(0.08)	18.34(0.06)	18.27(0.05)	–	AFOSC
20150218	57071.22	17.85(0.16)	–	–	–	–	UVOT
20150218	57071.96	–	–	18.29(0.36)	–	–	Starlight MX 916
20150220	57073.12	17.94(0.06)	18.41(0.04)	18.37(0.09)	18.17(0.14)	–	AFOSC
20150222	57075.31	18.13(0.18)	–	–	–	–	UVOT
20150310	57091.02	–	18.91(0.08)	18.65(0.08)	18.22(0.06)	–	AFOSC
20150311	57092.51	19.15(0.41)	–	–	–	–	UVOT
20150311	57092.88	–	18.72(0.04)	18.51(0.03)	18.16(0.08)	–	AFOSC
20150319	57100.01	–	18.92(0.05)	18.59(0.06)	18.19(0.06)	–	AFOSC
20150326	57107.90	–	–	18.68(0.14)	–	–	OSIRIS
20150327	57108.87	–	> 19.0	18.77(0.08)	18.49(0.09)	–	AFOSC
20150330	57111.82	–	> 19.2	18.88(0.04)	18.52(0.08)	> 18.5	AFOSC
20150413	57125.82	–	> 19.1	19.33(0.12)	18.75(0.12)	–	AFOSC
20150415	57125.82	21.55(0.28)	–	–	–	18.90(0.05)	AFOSC
20150428	57140.88	–	20.96(0.08)	19.51(0.08)	18.70(0.08)	18.86(0.10)	ALFOSC_FASU
20150508	57150.97	–	21.10(0.04)	19.58(0.07)	19.00(0.06)	18.96(0.14)	ALFOSC_FASU
20150518	57160.92	–	–	19.64(0.06)	–	–	OSIRIS
20150525	57167.96	–	21.62(0.09)	19.92(0.08)	19.01(0.14)	18.97(0.16)	ALFOSC_FASU
20150610	57183.89	–	> 20.9	20.23(0.12)	19.38(0.06)	19.29(0.19)	AFOSC
20150622	57195.92	> 21.3	22.28(0.08)	20.74(0.04)	19.72(0.08)	19.73(0.23)	ALFOSC_FASU
20150709	57212.91	–	> 22.7	21.78(0.12)	20.50(0.07)	20.58(0.12)	ALFOSC_FASU
20150714	57217.86	–	> 22.2	> 21.7	20.69(0.24)	–	AFOSC
20150717	57220.96	> 20.5	> 22.4	> 21.9	20.86(0.26)	21.05(0.39)	AFOSC
20150723	57226.90	–	–	> 22.4	21.42(0.39)	–	ALFOSC_FASU
20151106	57332.16	–	> 22.9	> 21.7	> 21.4	–	AFOSC
20151109	57335.12	–	–	> 22.9	–	–	AFOSC

The observations were carried out using the 1.82 m Copernico Telescope with AFOSC, the 2.56 m Nordic Optical Telescope (NOT) with ALFOSC, the 10.4 m Gran Telescopio Canarias (GTC) with OSIRIS, the UV/Optical Telescope (UVOT) on board of the *Swift* Gamma-ray Observatory and ..... (Starlight MX 916)

et al. 2009; Smith et al. 2009; Thompson et al. 2009; Wesson et al. 2010; Kochanek 2011; Szczygieł et al. 2012; Adams et al. 2015), we note that PSN J09132750+7627410 has much redder colours than the other transients at phases later than ~ 70 d from maximum.

The *r*-band absolute light-curve is shown in panel c). Assuming the distance modulus and the extinction reported before, we infer an *r*-band absolute peak magnitude of -13.60 ± 0.19 mag, while the marginal 2013 detection corresponds to an absolute magnitude of -12.79 ± 0.50 mag. Different absolute peak-magnitudes were registered in the bluer bands, with -14.34 ± 0.19 mag and -13.63 ± 0.20 mag, -13.44 ± 0.18 mag, -13.69 ± 0.18 mag in the *u*, *g*, *B* and *V* bands, respectively. For the *i* and *z* bands, we measured -13.65 ± 0.19 mag and -13.29 ± 0.30 mag respectively. In the same panel, we show a comparison with the absolute curves of similar transients, proving that PSN J09132750+7627410 has an absolute light-curve similar to those of other SN impostors, with the main outburst having a light-curve resembling those of canonical CCSNe, but in general fainter peak-magnitudes. In panel c) we also mark the marginal detection revealing another minor burst on 2013 September 2 (dashed vertical line).

Table 5.3: UV magnitudes of PSN J09132750+7627410. The magnitudes were calibrated to the Vega system.

Date	MJD	$UVW1$	err	$UVM2$	err	$UVW2$	err	Instrument
20150212	57065.81	18.30	0.47	18.76	0.31	19.13	0.19	UVOT
20150214	57067.06	> 18.1	–	> 18.5	–	18.87	0.07	UVOT
20150216	57069.50	18.24	0.17	> 18.3	–	19.03	0.12	UVOT
20150218	57071.22	18.43	0.11	19.02	0.19	> 19.21	–	UVOT
20150222	57075.31	18.62	0.13	> 18.9	–	19.39	0.18	UVOT
20150311	57092.51	18.82	0.42	19.36	0.26	> 19.7	–	UVOT

The observations were carried out using the UV/Optical Telescope (UVOT) on board of the *Swift* Gamma-ray Observatory.

Table 5.1: Log of the spectroscopic observations of PSN J09132750+7627410. The phases are relative to the maximum.

Date	Phase (d)	Instrumental set-up	Grism or grating	Spectral range (Å)	Resolution (Å)	Exp. times (s)
20150212	-5	Ekar182+AFOSC	2xgm4	$3400 - 8200$	14.4	2×1800
20150216	0	Ekar182+AFOSC	gm4	$3400 - 8200$	14.4	2700
20150223	6	NOT+ALFOSC	gm4	$3500 - 9000$	18.1	2400
20150311	23	Ekar182+AFOSC	gm4	$3400 - 8200$	14.4	2×2700
20150326	38	GTC+OSIRIS	R1000B	$3600 - 8000$	7.0	2×1800
20150328	40	Ekar182+AFOSC	gm4	$3400 - 8200$	14.4	2×2700
20150518	92	GTC+OSIRIS	R1000R	$5000 - 10000$	8.0	2×1800

The spectra were obtained using the 1.82 m Copernico telescope with AFOSC, the 2.56 m Nordic Optical Telescope (NOT) with ALFOSC and the 10.4 m Gran Telescopio Canarias (GTC) with OSIRIS.

5.3 Spectroscopic analysis

The results of the spectroscopic analysis are shown in Figure 6.3. In panel a) we present the final sequence of spectra obtained during the nearly 90 days of our spectroscopic follow-up campaign.

The spectra at early phases are characterised by a blue continuum with sharp and narrow Balmer lines with P-Cygni profiles, as also noticed by Humphreys & Gordon (2015). A log of the spectroscopic observations is reported in Table 5.1, along with the information on the instrumental set-up used, the exposure times and the resolutions of the spectra. The temperature of the pseudo-continuum, estimated through a black-body fit, rapidly falls from 13360 ± 2470 K at -5 d to 3400 ± 420 K at $+92$ d, in agreement with the estimated broad-band colour evolution reported in Figure 5.1 (panel b). The Hα profile (the only Balmer line visible over the entire spectroscopic follow-up) is characterised by a prominent P-Cygni profile at all phases. In Figure 6.3 (panel b) we show a detail of the evolution of the Hα and Hβ regions. We note no significant evolution in the profiles of the Hα and Hβ emission components. The total Hα profile is well fitted using a Gaussian component in absorption and a single Lorentzian component in emission. From this fit, at early phases, we derive a FWHM velocity < 700 km s^{-1} for the emission component and a nearly constant ($900 - 1000$ km s^{-1}) expansion velocity, as deduced from the positions of the minimum of the absorption components. Nonetheless, at phases $+39$ d and $+92$ d from maximum, we note the presence of a second absorption component (Figure 6.3, panel c), suggesting the presence of a slower shell, moving at $300-450$ km s^{-1}, which is nearly the same value (within the errors) inferred from the FWHM of the narrow emission component at the same phases. The absence of this component at earlier phases, as well as in other spectra at similar phases, is most likely due to a resolution limitation. The presence of two velocity components in the Hα profile is supported by the fact that the velocity inferred from the blue wing of the faster absorption

components in the +39 d spectrum is consistent with that inferred from the red wing of the Hα emission profile. We do not detect the same unusual features in the Hβ profile, although this might be related to the lower SNR of our spectra at the corresponding wavelengths. The

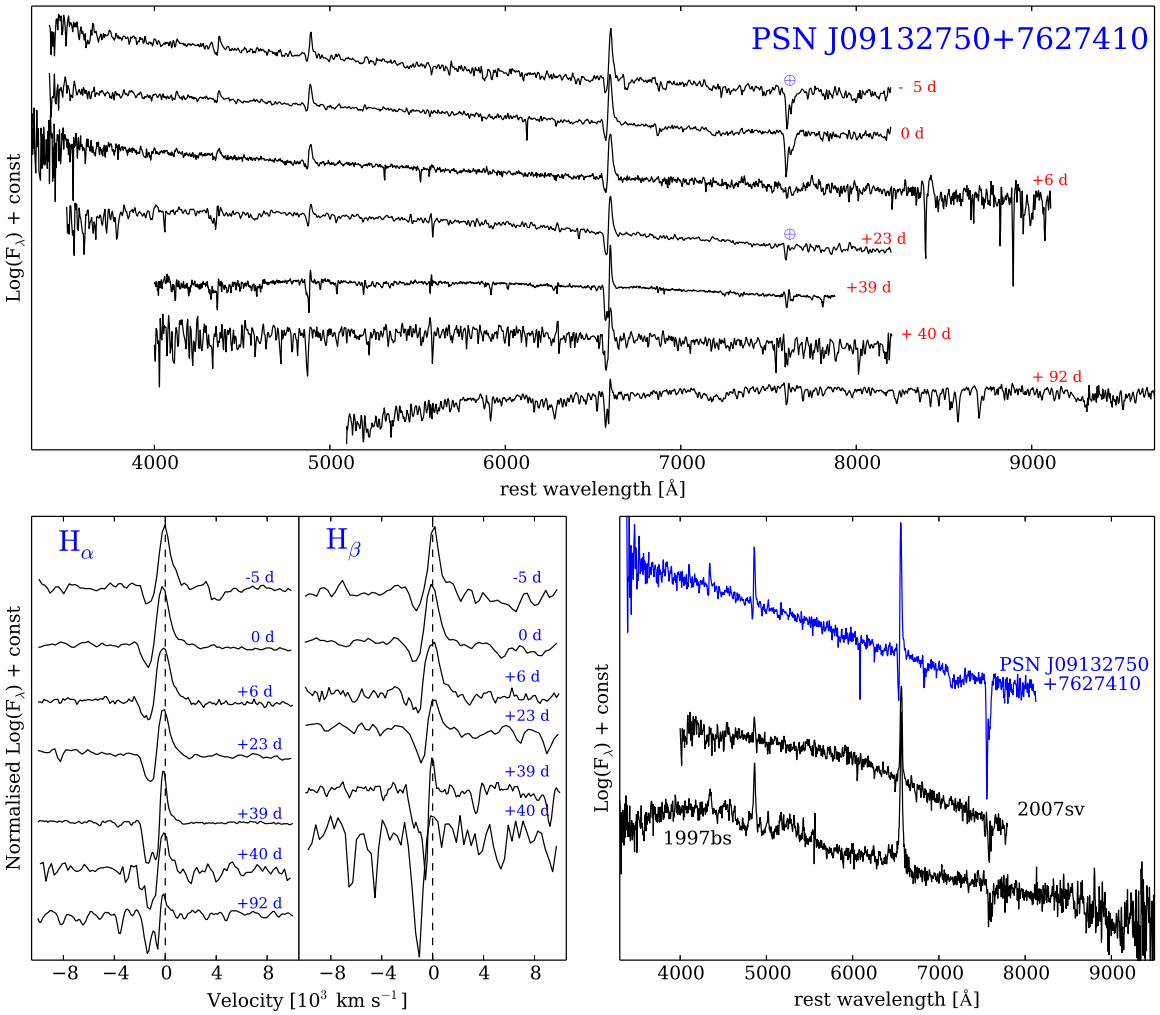

Figure 5.1: **a)** Spectral sequence of PSN J09132750+7627410. The phases are reported to the right and are relative to the r-band maximum. The $\oplus$ symbols mark the positions of the strongest telluric absorption bands. **b)** Evolution of the Hα (**left panel**) and Hβ (**right panel**) line profiles in the velocity space. Vertical dashed lines mark the rest-wavelength position of the two lines. **c)** Comparison of the spectrum of PSN J09132750+7627410 obtained at the epoch of the r-band maximum, and those of the SN impostors 2007sv and 1997bs obtained at similar phases. All spectra have been de-reddened and redshift corrected, and then shifted by an arbitrary constant.

Hγ line is also identified at early phases, while Hβ is clearly visible in all spectra, with the exception of our last (+92 d) spectrum, which does not have sufficient spectral coverage. In our +39 d spectrum, we also identify Fe II (multiplets 27, 37, 38, 42, 48, 49), Ba II $\lambda\lambda$4554.0, 4934.1, Na ID $\lambda\lambda$5889.9, 5895.9 Å, O I $\lambda\lambda$7772, 7775.4 and Ca II (H and K), Ti II (multiplets 1, 19, 20, 31, 34, 41, 51, 82, 105) and, tentatively, also the Ba I multiplet 2. We notice that our last (+92 d) spectrum has a much redder continuum, and broad features appear, most likely due to TiO molecular bands in the 6100 – 6400 Å and 7000 – 7400 Å regions.

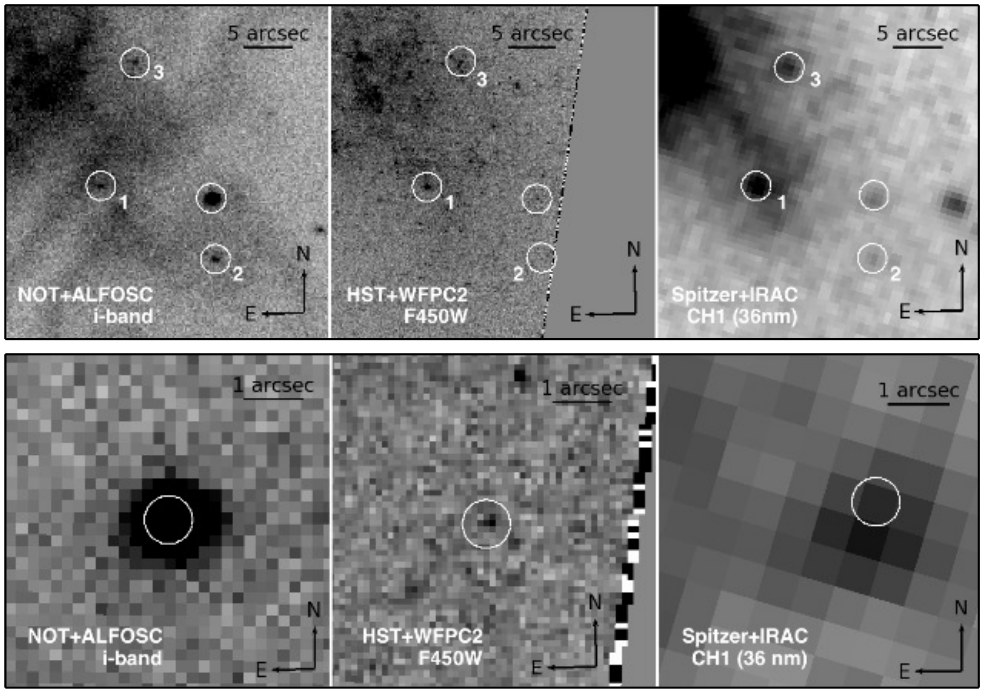

Figure 5.1: Pre-eruption archival images of the site of PSN J09132750+7627410. **Upper panel:** Details of the region of PSN J09132750+7627410 in the *i*-band ALFOSC image obtained on 2015 May 25, the HST $F450W$ and the SST images obtained on 2010 April 12. The positions of three reference stars are also shown. **Bottom panel:** Zoom in of the position coincident with that of PSN J09132750+7627410 in the ALFOSC images. The positions in the HST and SST images are those computed using the GEOMAP and GEOXYTRAN IRAF tasks.

5.4 The progenitor star of PSN J09132750+7627410

Deep archival HST and SST images of the host galaxy region were also available. HST images[8] were obtained on 2001 July 06 (*HST* ID proposal: 9042; PI: S. Smartt) using the Wide Field Planetary Camera 2 (WFPC2) $F450W$ ($\sim B$) and $F814W$ ($\sim I$) filters. Three sets of mid-infrared (MIR) SST images were obtained on 2009 December 2, 2010 April 12 (ID proposal: 61063; PI: K. Sheth) and 2014 January 2 (ID proposal: 10046; PI: D. Sanders) using the InfrarRed Array Camera (IRAC) with the 3.6 μm and 4.5 μm channels (channels 1 and 2 respectively). These data were provided by the *Spitzer* Heritage Archive[9] (SHA), hence fully co-added and calibrated. Drizzled HST images (resampled to a uniform grid to correct geometric distortions, with ~ 0.1 arcsec pixel^{-1}) obtained through the *Hubble* Legacy Archive[10] (HLA) and *Post Basic Calibrated Data* (pbcd) SST images (with ~ 0.6 arcsec pixel^{-1}), were used to align archival data to our *i*-band ALFOSC image (with 0.19 arcsec pixel^{-1}) obtained on 2015 May 8 (which is our ground-based image of PSN J09132750+7627410 obtained with the best sky conditions among our photometric data-set: seeing $\sim 0.5''$). Geometrical alignments were performed using the IRAF tasks GEOMAP, and a maximum of 17 common point-like sources between all sets of images. The errors of the geometric transformations are the root-mean-square (RMS) uncertainties given by GEOMAP, obtaining a precision in the

[8] `http://archive.stsci.edu/hst/search.php`
[9] `http://sha.ipac.caltech.edu/applications/Spitzer/SHA/`
[10] `http://hla.stsci.edu/`

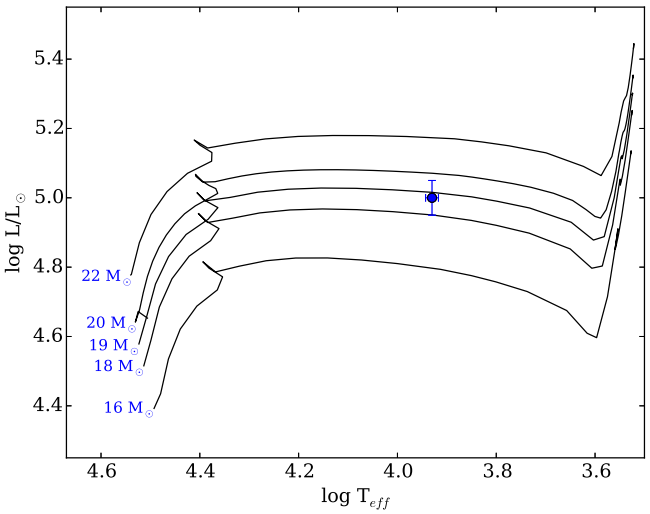

Figure 5.2: Hertzsprung-Russel diagram showing the position of the PSN J09132750+7627410 progenitor candidate (blue circle). Evolutionary tracks for stars from 16 $M_\odot$ to 23 $M_\odot$, computed using the Cambridge STARS (Eldridge & Tout 2004 models) are also shown. The tracks were obtained assuming solar metallicity.

corresponding position of PSN J09132750+7627410 of $< 0.020''$[11]

As a result, we identify a source at the position of the transient (within the transformation errors) in both HST and SST images although, given the different scales, the source in the SST images is most likely the blend of multiple sources (see Figure 5.1). HST magnitudes and errors of the source in the VEGAMAG flight-system ($F450W = 24.27 \pm 0.17$ and $F814W = 24.00 \pm 0.18$) were obtained using the DOLPHOT package[12] (Dolphin 2000). For both filters, before running DOLPHOT, it was necessary to measure small dithered offsets between exposures with respect to one fiducial image. The DOPLHOT output provides also a set of parameters which can be used to interpret the nature of the different sources. Hence, since the detected source has a 'object-type' flag of '1', which means that the source is likely stellar, we consider it as the most reliable progenitor of PSN J09132750+7627410. Accounting for the extinction and distance modulus reported before ($A_B = 0.097$ mag, $A_I = 0.040$ mag, $\mu = 31.88 \pm 0.18$ mag), we estimate for the progenitor candidate the absolute magnitudes of -7.71 ± 0.25 mag and -7.95 ± 0.25 mag for filters $F450W$ and $F814W$, respectively.

The final magnitudes in the SST images were measured using the SPOT[13] package, integrating the flux in a 4×4 pixels area around the position of the progenitor/transient, which included the whole extended source seen in Figure 5.1 (bottom-right panel). We obtained 3.1×10^{-19} and 1.7×10^{-19}, 3.0×10^{-19} and 0.8×10^{-19}, and 2.7×10^{-19} and 1.4×10^{-19} erg s^{-1} cm^{-2}/Å^{-1}, in the channel 1 and 2 from the images obtained with SST on 2009 December 2, 2010 April 12 and 2014 January 2, respectively. As we can see, there is no clear evidence of an excess of emission (e.g. due to dust formation) between years 2009 and 2014 at 3.6 μm, but some variability is perceptible at 4.5μm. However, we remark that the resulting magnitudes are likely due to the contribution of multiple sources in the vicinity of

[11] We obtained the following transformation uncertainties: $(x, y) = 0.013''$, $0.018''$ (11 stars used) and $(x, y) = 0.019''$, $0.020''$ (15 stars used) in the $F450W$ and $F814W$ images respectively, $(x, y)_1 = 0.066$, $0.072''$(16 stars), $(x, y)_2 = 0.047$, $0.084''$(16 stars), $(x, y)_1 = 0.078$, $0.060''$(17 stars), $(x, y)_2 = 0.066$, $0.072''$(16 stars), and $(x, y)_1 = 0.028$, $0.034''$(12 stars), $(x, y)_2 = 0.072$, $0.090''$(15 stars) for the channel 1 and 2 of images obtained with SST on 2009 December 02, 2010 April 12 and 2014 January 2, respectively.

[12] `http://americano.dolphinsim.com/dolphot/`. We used the WFPC2 Module, v.2.0 (updated in November 2014)

[13] `http://ssc.spitzer.caltech.edu/warmmission/propkit/spot/`

the impostor's progenitor. We obtained approximated magnitudes of 18.3 and 18.0, 18,3 and 18.8, and 18.5 and 18.2 in the channel 1 and 2 from the images obtained with SST on 2009 December 2, 2010 April 12 and 2014 January 2, respectively.

5.5 Discussion and conclusions

In this paper we have discussed the outcomes of our photometric and spectroscopic monitoring of the optical transient PSN J09132750+7627410. Its r-band absolute magnitude at peak ($M_r = -13.60 \pm 0.19$ mag) is consistent with that expected during giant outbursts of very massive stars. In Figure 5.1 (panels b and c), we showed that, although these transients have a similar nature, light-curves can differ in terms of absolute magnitudes and colour evolutions.
At all phases, the spectra are characterised by prominent Balmer lines showing sharp and narrow P-Cygni profiles. In our +39 d and +92 d best resolution spectra, we notice two components in absorption in the Hα profile. Our finding is supported by the fact that multiple absorptions were also reported in a moderate resolution spectrum obtained by Humphreys & Gordon (2015) around maximum. The clear detection of two absorption components suggests the presence of two expanding shells moving at different velocities (namely $\sim 1000\,\mathrm{km\,s^{-1}}$ and $\sim 340 - 450\,\mathrm{km\,s^{-1}}$). The velocity inferred for the slower component is comparable with the FWHM velocity of the narrow emission component visible in both +39 d and +92 d spectra. This shell, initially photo-ionised, quickly recombines, and contributes to a large fraction of the narrow Hα flux. The higher velocity component is likely due to the presence of a further shell, moving at a higher velocity. The absence (or the weakness) of the emission component is indicative that this shell is likely outer. Although the lack of any evidence of shell-shell collision from our data of PSN J09132750+7627410, we speculate that one of the shells may have been expelled in past outbursts similar to the 2013 event observed from the archival images.

The analysis of deep pre-outburst archival images obtained with HST and SST revealed the presence of a source at the position of PSN J09132750+7627410 (within the errors of our relative astrometry). In order to better constrain the nature of the candidate progenitor, we estimated the oxygen abundance at the position of the source following Hakobyan et al. (2009) and the prescriptions of Tremonti et al. (2004) and Pilyugin et al. (2004) (see also Pastorello et al. 2015, for more details), which resulted in $12 + \log[O/H] \simeq 8.59$ dex. This value is only marginally lower than the solar abundance, 8.69 ± 0.05 dex (Asplund et al. 2009). However, following Smartt et al. (2009), who sets $12 + \log[O/H] = 8.4$ dex as the dividing line between solar and subsolar metallicity evolutionary tracks, we conclude that the environment of PSN J09132750+7627410 is likely at solar metallicity. Assuming also a bolometric correction of ~ -0.14 mag (Kurucz Atlas 9 models; Kurucz 1993) given the intrinsic colour of the star obtained before $(B-I)_0 \simeq 0.2$ mag, we approximate the effective temperature of the quiescent progenitor to ~ 8500 K and estimate a luminosity of $\mathrm{Log}(\mathrm{L}/\,\mathrm{L}_\odot) \simeq 5$. These values of colour and luminosity of the recovered precursor candidate suggest a progenitor mass in the range $18 - 20$ $\mathrm{M}_\odot$(see Figure 5.2). Thus, the progenitor candidate of PSN J09132750+7627410 is likely a moderate-mass blue-white supergiant, likely an A-type star. An interesting implication is that we confirm the claim of Smith et al. (2011) that also moderate mass supergiants can experience large outburst and hence produce SN impostors.

References

Adams, S. M., Kochanek, C. S., Prieto, J. L., et al. 2015, arXiv:1511.07393

Asplund, M., Grevesse, N., Sauval, A. J., & Scott, P. 2009, ARA&A, 47, 481

Berger, E., Soderberg, A. M., Chevalier, R. A., et al. 2009, ApJ, 699, 1850

Blanton, M. R., & Roweis, S. 2007, AJ, 133, 734

Bond, H. E., Bedin, L. R., Bonanos, A. Z., et al. 2009, ApJ, 695, L154

Botticella, M. T., Pastorello, A., Smartt, S. J., et al. 2009, MNRAS, 398, 1041

Brimacombe, J., Zaggia, S., Barbieri, M., et al. 2013, Central Bureau Electronic Telegrams, 3647, 1

Cappellaro, E. (2014). SNOoPy: a package for SN photometry, `http://sngroup.oapd.inaf.it/snoopy.html`

Davidson, K., & Humphreys, R. M. 2012, Eta Carinae and the Supernova Impostors, 384

Dolphin, A. E. 2000, PASP, 112, 1383

Eldridge, J. J., & Tout, C. A. 2004, MNRAS, 353, 87

Foley, R. J., Smith, N., Ganeshalingam, M., et al. 2007, ApJ, 657, L105

Gogarten, S. M., Dalcanton, J. J., Murphy, J. W., et al. 2009, ApJ, 703, 300

Hakobyan, A. A., Mamon, G. A., Petrosian, A. R., Kunth, D., & Turatto, M. 2009, A&A, 508, 1259

Humphreys, R. M., & Gordon, M. S. 2015, The Astronomer's Telegram, 7172, 1

Kankare, E., Kotak, R., Pastorello, A., et al. 2015, A&A, 581, L4

Kochanek, C. S. 2011, ApJ, 741, 37

Kurucz, R. 1993, ATLAS9 Stellar Atmosphere Programs and 2 km/s grid. Kurucz CD-ROM No. 13. Cambridge, Mass.: Smithsonian Astrophysical Observatory, 1993., 13, 18

Maund, J. R., Smartt, S. J., Kudritzki, R.-P., et al. 2006, MNRAS, 369, 390

Pastorello, A., Smartt, S. J., Mattila, S., et al. 2007, Nature, 447, 829

Pastorello, A., Hadjiyska, E., Rabinowitz, D., et al. 2015, MNRAS, 449, 1954

Pilyugin, L. S., Vílchez, J. M., & Contini, T. 2004, A&A, 425, 849

Poole, T. S., Breeveld, A. A., Page, M. J., et al. 2008, MNRAS, 383, 627

Prieto, J. L., Kistler, M. D., Thompson, T. A., et al. 2008, ApJ, 681, L9

Pumo, M. L., Turatto, M., Botticella, M. T., et al. 2009, ApJ, 705, L138

Schlafly, E. F., & Finkbeiner, D. P. 2011, ApJ, 737, 103

Szczygieł, D. M., Prieto, J. L., Kochanek, C. S., et al. 2012, ApJ, 750, 77

Smartt, S. J., Eldridge, J. J., Crockett, R. M., & Maund, J. R. 2009, MNRAS, 395, 1409

Smith, N., Ganeshalingam, M., Chornock, R., et al. 2009, ApJ, 697, L49

Smith, N., Miller, A., Li, W., et al. 2010, AJ, 139, 1451

Smith, N., Li, W., Silverman, J. M., Ganeshalingam, M., & Filippenko, A. V. 2011a, MNRAS, 415, 773

Smith, N., Li, W., Miller, A. A., et al. 2011b, ApJ, 732, 63

Tartaglia, L., Pastorello, A., Taubenberger, S., et al. 2015a, MNRAS, 447, 117

Tartaglia, L., Pastorello, A., Benetti, S., et al. 2015b, The Astronomer's Telegram, 7051, 1

Thompson, T. A., Prieto, J. L., Stanek, K. Z., et al. 2009, ApJ, 705, 1364

Tominaga, N., Limongi, M., Suzuki, T., et al. 2008, ApJ, 687, 1208

Tremonti, C. A., Heckman, T. M., Kauffmann, G., et al. 2004, ApJ, 613, 898

Tully, R. B., Rizzi, L., Shaya, E. J., et al. 2009, AJ, 138, 323

Van Dyk, S. D., Peng, C. Y., King, J. Y., et al. 2000, PASP, 112, 1532

Wegner, G., & McMahan, R. K. 1987, AJ, 93, 287

Wesson, R., Barlow, M. J., Ercolano, B., et al. 2010, MNRAS, 403, 474

Wild, P., & Schildknecht, T. 1985, IAU Circ., 4031, 3

Appendix

5.A Stellar sequences

Table 5.A.1: Magnitudes of the stellar local sequence used for the $BVRI$ photometric calibration.

RA [J2000] (hh:mm:ss)	Dec [J2000] (dd:mm:ss)	B(err)	V(err)	R(err)	I(err)
09:12:18.71	76:30:11.17	11.66(0.06)	11.19(0.07)	10.92(0.06)	10.65(0.08)
09:12:31.44	76:26:50.94	16.86(0.08)	15.65(0.07)	14.96(0.08)	14.37(0.14)
09:12:37.61	76:25:08.75	12.94(0.06)	12.13(0.06)	11.65(0.06)	11.19(0.09)
09:12:50.34	76:22:37.45	15.90(0.04)	15.20(0.02)	14.87(0.03)	14.76(0.05)
09:13:02.46	76:22:45.59	13.49(0.06)	12.89(0.06)	12.54(0.06)	12.20(0.08)
09:13:06.97	76:25:43.61	17.43(0.10)	16.46(0.09)	15.88(0.04)	15.33(0.07)
09:13:23.48	76:24:07.71	16.29(0.07)	15.54(0.08)	15.10(0.10)	14.69(0.13)
09:13:27.62	76:27:09.53	15.76(0.07)	15.13(0.08)	14.77(0.07)	14.45(0.11)
09:13:38.84	76:22:04.53	14.71(0.06)	14.03(0.06)	13.63(0.06)	13.23(0.09)
09:13:42.90	76:28:32.47	14.78(0.07)	13.84(0.07)	13.26(0.08)	12.60(0.11)
09:13:45.59	76:30:44.30	17.09(0.12)	15.67(0.12)	14.82(0.10)	13.98(0.16)
09:13:50.49	76:29:48.30	16.70(0.09)	16.06(0.09)	15.66(0.05)	15.20(0.14)
09:13:51.47	76:26:36.78	15.86(0.07)	15.21(0.07)	14.84(0.06)	14.48(0.13)
09:13:54.00	76:31:09.48	14.42(0.06)	13.72(0.06)	13.32(0.06)	12.93(0.09)
09:14:00.27	76:24:32.85	14.74(0.06)	14.21(0.07)	13.90(0.06)	13.59(0.09)
09:14:02.49	76:25:26.03	14.65(0.06)	14.11(0.06)	13.79(0.07)	13.47(0.09)
09:14:02.71	76:31:46.69	16.13(0.07)	15.39(0.07)	14.94(0.08)	14.47(0.11)
09:14:13.79	76:23:15.51	16.32(0.08)	15.69(0.10)	15.31(0.14)	14.94(0.17)
09:14:14.63	76:30:49.70	17.32(0.08)	16.16(0.10)	15.48(0.17)	14.82(0.17)
09:14:28.43	76:22:49.60	16.29(0.07)	15.64(0.08)	15.25(0.10)	14.82(0.12)

Table 5.A.2: Magnitudes of the stellar local sequence used for the *ugriz* photometric calibration.

RA [J2000] (hh:mm:ss)	Dec [J2000] (dd:mm:ss)	u(err)	g(err)	r(err)	i(err)	z(err)
09:12:05.65	+76:28:56.05	–	16.55(0.05)	15.39(0.04)	14.90(0.08)	16.10(0.14)
09:12:12.64	+76:25:56.62	–	15.51(0.05)	15.40(0.03)	15.18(0.09)	16.75(0.10)
09:12:31.53	+76:26:50.71	–	16.16(0.05)	15.10(0.04)	14.50(0.08)	15.09(0.27)
09:12:37.41	+76:28:20.68	–	19.39(0.04)	17.96(0.04)	16.71(0.03)	16.63(0.06)
09:13:06.96	+76:25:44.27	–	16.62(0.02)	15.94(0.02)	15.54(0.04)	16.01(0.17)
09:13:06.98	+76:25:44.26	17.88(0.03)	16.64(0.07)	16.07(0.06)	15.81(0.15)	16.58(0.48)
09:13:10.22	+76:27:20.92	–	18.23(0.03)	17.09(0.04)	16.47(0.04)	16.64(0.03)
09:13:14.47	+76:25:16.67	–	16.55(0.02)	16.18(0.02)	15.85(0.05)	16.42(0.21)
09:13:14.49	+76:25:16.64	16.90(0.01)	16.59(0.08)	16.32(0.05)	16.20(0.10)	16.95(0.52)
09:13:23.50	+76:24:07.49	15.88(0.02)	15.74(0.04)	15.17(0.04)	14.77(0.09)	16.26(0.11)
09:13:27.66	+76:27:09.07	15.87(0.01)	15.29(0.07)	14.94(0.06)	14.72(0.12)	15.36(0.28)
09:13:38.81	+76:22:04.38	–	14.33(0.02)	13.83(0.02)	13.60(0.05)	14.90(0.14)
09:13:39.16	+76:31:12.54	–	17.44(0.03)	16.75(0.03)	16.28(0.05)	16.63(0.01)
09:13:45.75	+76:30:44.34	18.40(0.06)	16.37(0.06)	15.12(0.06)	14.43(0.13)	14.81(0.37)

Table 5.A.2 Continued

RA [J2000] (hh:mm:ss)	Dec [J2000] (dd:mm:ss)	u(err)	g(err)	r(err)	i(err)	z(err)
09:13:50.28	+76:25:50.29	19.84(0.02)	19.31(0.06)	19.05(0.02)	18.75(0.11)	19.09(0.02)
09:13:50.58	+76:29:49.21	16.63(0.02)	16.19(0.07)	15.78(0.07)	15.53(0.14)	16.26(0.25)
09:13:51.48	+76:26:36.80	16.10(0.01)	15.42(0.07)	14.98(0.06)	–	–
09:14:07.89	+76:28:29.38	17.07(0.03)	15.93(0.05)	15.37(0.03)	–	–
09:14:17.91	+76:29:10.59	–	17.41(0.03)	16.86(0.03)	16.45(0.05)	16.92(0.04)
09:14:36.45	+76:21:55.40	–	15.74(0.01)	15.18(0.01)	14.94(0.05)	16.20(0.13)

5.B Historical photometric data

Table 5.B.1: Historical photometric data of PSN J09132750+7627410 including optical detection limits.

Date	MJD	R	Instrument
20110206	55598.03	> 19.7	Starlight MX 916
20110225	55617.02	> 18.9	Starlight MX 916
20110323	55643.96	> 18.8	Starlight MX 916
20110402	55653.99	> 19.6	DSI
20110513	55694.94	> 18.8	Starlight MX 916
20110614	55726.96	> 17.7	Starlight MX 916
20110804	55777.93	> 18.8	Starlight MX 916
20110926	55830.00	> 19.2	Starlight MX 916
20111023	55857.95	> 19.2	Starlight MX 916
20111116	55881.98	> 18.3	Starlight MX 916
20111218	55913.17	> 18.8	Starlight MX 916
20120107	55933.03	> 18.6	Starlight MX 916
20120220	55977.72	> 19.4	Starlight MX 916
20120319	56005.86	> 19.6	Starlight MX 916
20120428	56045.11	> 18.7	Starlight MX 916
20120602	56080.95	> 18.2	Starlight MX 916
20120710	56118.98	> 18.5	Starlight MX 916
20121203	56264.91	> 18.3	Starlight MX 916
20121219	56280.98	> 18.8	Starlight MX 916
20130203	56326.89	> 19.3	Starlight MX 916
20130215	56338.97	> 19.9	Starlight MX 916
20130312	56363.81	> 19.3	Starlight MX 916
20130407	56389.96	> 19.4	Starlight MX 916
20130603	56446.87	> 19.2	Starlight MX 916
20130702	56475.95	> 19.1	Starlight MX 916
20130901	56536.80	> 18.8	Starlight MX 916
20130902	56537.79	> 18.1	Starlight MX 916
20130902	56537.87	19.16(0.47)	DSI
20130903	56538.79	> 18.5	Starlight MX 916
20130904	56539.79	> 19.0	Starlight MX 916
20130906	56541.78	> 18.4	Starlight MX 916
20130912	56547.78	> 18.3	Starlight MX 916
20130920	56555.78	> 18.2	Starlight MX 916
20140209	56697.80	> 19.0	Starlight MX 916
20140308	56724.89	> 18.9	Starlight MX 916
20140323	56739.86	> 18.8	Starlight MX 916
20140413	56760.93	> 18.7	Starlight MX 916
20140517	56794.97	> 18.3	Starlight MX 916
20140605	56813.94	> 18.3	Starlight MX 916
20140828	56897.80	> 18.8	Starlight MX 916

Table 5.B.1 Continued

Date	MJD	R	Instrument
20140914	56914.77	> 18.2	Starlight MX 916
20140929	56929.77	> 18.6	Starlight MX 916
20141223	57014.93	> 18.9	Starlight MX 916
20150106	57028.90	> 18.2	Starlight MX 916

The observations, provided by Fabio Briganti (using a C-14 Celestron Schmidt Cassegrain reflector with a Sarlight Xpress MX 916 CCD camera at the Monte Maggiore Observatory, Predappio, Forlì-Cesena, Italy) and and Giancarlo Cortini (using a 0.25 m Newton Telescope with a Meade DSI Pro camera with Sony EXView HAD CCD, Obs. R. Mancini, Associazione Astronomica Isaac Newton, Stazione di Gavena, Cerreto Guidi, Italy) were unfiltered images and have been re-scaled to the r-band in the AB photometric system.

Chapter 6

The controversial case of LSQ13zm

A key improvement in our comprehension of the final fate of massive stars resulted from the evidence of a connection (Kotak & Vink 2006; Smith & Owocki 2006) between some members of some Type IIn SNe and LBV stars. While this link has been firmly established through the detection of the quiescent progenitor stars of two type IIn SNe in archival Hubble Space Telescope (HST) images, (i.e. SN 2005gl and SN 2010jl; see Gal-Yam et al. 2007; Gal-Yam & Leonard 2009 and Smith et al. 2011a respectively), a further evidence comes from the study of the pre-SN photometric variability of the precursor stars, using archival images collected months to years before the SN explosion. The data archive inspection is, in fact, an invaluable tool to characterise the final stages of the progenitors of interacting transients. Weak transient events with luminosities consistent with those expected in LBV outbursts are occasionally detected weeks to years before major re-brightenings (e.g., Pastorello et al. 2013). Some of them have been proposed to be sequential events leading to a SN explosion (Mauerhan et al. 2013; Fraser et al. 2013b; Ofek et al. 2013a). Even more robust is the spatial coincidence between the CC SN 2006jc (a Type Ibn event, see Matheson et al. 2000; Pastorello et al. 2008, 2015, for more details on this subclass of stripped-envelope SNe) and a stellar outburst of $\simeq -14$ mag which had occurred ~ 2 years before (Pastorello et al. 2007; Foley et al. 2007). In that case, the massive precursor was likely a Wolf-Rayet (WR) star (Foley et al. 2007; Pastorello et al. 2007; Tominaga et al. 2008) with a residual LBV-like instability.

Nonetheless, in most cases, outbursts attributed to extragalactic massive stars are registered as isolated events. These are fainter than real SNe ($M \simeq -12$ to -14 mag), but mimic the behavior of Type IIn SNe, showing similar spectra dominated by prominent narrow Balmer lines in emission, and sometimes even similar light-curves and are usually labelled as 'SN impostors' (Van Dyk et al. 2000), as they are not terminal SN explosions. Accounting for the evidence of photometric variability from massive stars, a sequential event chain linking LBVs (but also other massive stellar types), SN impostors and SNe IIn has been proposed (Mauerhan et al. 2013).

In this context, it is worth mentioning the controversial case of SN 2009ip, an interacting transient whose real nature (SN explosion vs. non-terminal outburst) is still debated[1]. The detection of the progenitor star in archival HST images proved it to be consistent with a massive star – most likely an LBV – with a zero-age-main-sequence (ZAMS) mass of $\simeq 60$ $M_{\odot}$ (Smith

[1]Different interpretations have been proposed by Pastorello et al. (2013); Fraser et al. (2013a); Smith et al. (2013); Ofek et al. (2013); Prieto et al. (2013); Soker & Kashi (2013); Margutti et al. (2014); Smith et al. (2014); Mauerhan et al. (2014); Graham et al. (2014); Levesque et al. (2014); Moriya (2015); Martin et al. (2015); Fraser et al. (2015)

et al. 2010; Foley et al. 2011). SN 2009ip was well studied in the years ahead of the putative SN explosion and exhibited erratic luminosity oscillations since summer 2009 (Pastorello et al. 2013). In July 2012, it experienced a further re-brightening lasting a few weeks, ~ 20 days before a major outburst, in which the object reached an absolute magnitude competing with those of Type IIn SNe. However, a conclusive proof of the terminal SN explosion is still missing (Fraser et al. 2015), as the expected spectral signatures (such as nucleosynthesized elements) of a SN produced in the explosion of a very massive star have not been detected yet in the spectra of SN 2009ip (Fraser et al. 2013a). A similar sequence of events was observed also for SN 2010mc (Ofek et al. 2013a; Smith et al. 2014), with the detection of an outburst ~ 40 days before an even brighter light-curve peak.

SN 2011ht (Fraser et al. 2013b; Mauerhan et al. 2013b) is another interesting example. It was classified as a SN impostor (Pastorello et al. 2011), before showing a significant spectral metamorphosis which led Prieto et al. (2011) to suggest its re-classification as a Type IIn SN. Fraser et al. (2013b) later reported the detection of an outburst ~ 1 year prior to the SN explosion. Nonetheless, also in this case, its nature is also not fully clarified (Humphreys et al. 2012).

The LBV stage is a short-duration phase in the life of very massive stars ($M \gtrsim 30\ M_{\odot}$), which are then expected to become H-stripped WR stars before exploding – after a relatively long time (a few 10^5 yr, see Georgy et al. 2012) – as Type Ib/c SNe. However, current stellar evolution codes do not predict the explosion of a CCSN soon after a major instability phase (Groh et al. 2013). Nonetheless, in the light of the sequences of events involving interacting transients that have been observed in growing number, ad hoc scenarios have been proposed (see e.g. Justham et al. 2014), and some efforts have been devoted to include the effects of instabilities in stellar evolution codes (Smith & Arnett 2014).

In this Chapter, the results of the follow-up campaign of LSQ13zm, observed in the galaxy SDSS J102654.56+195254.8 are reported. These results will be published in a forthcoming paper (Tartaglia et al. 2016, submitted to MNRAS). The transient was discovered by the La Silla Quest (LSQ) survey[2], and later classified as a young Type IIn SN by the Nearby Supernova Factory (SNF[3]; Benitez et al. 2013) using the SuperNova Integral Field Spectrograph (SNIFS, Aldering et al. 2002) mounted on the University of Hawaii 2.2 m telescope. Archival data from different surveys, namely LSQ, the Intermediate Palomar Transient Factory (iPTF[4]; Law et al. 2009; Rau et al. 2009, where the transient was designated as iPTF13ajw) and the Catalina Real-Time Transient Survey (CRTS[5]; Drake et al. 2009; Djorgovski et al. 2012) revealed an outburst (reaching an absolute magnitude at peak of $M_R = -14.87 \pm 0.25$ mag) ~ 3 weeks before a major re-brightening, where the object reached an absolute magnitude $M_R = -18.46 \pm 0.21$ mag (see Section 6.2.1). Hereafter, the first outburst will be labelled as the '2013a event' while the second, more luminous re-brightening as the '2013b' event, in analogy to what has been proposed for SN 2009ip (Pastorello et al. 2013).

[2] http://hep.yale.edu/lasillaquest
[3] http://snfactory.lbl.gov/
[4] http://www.ptf.caltech.edu/iptf
[5] http://crts.caltech.edu/

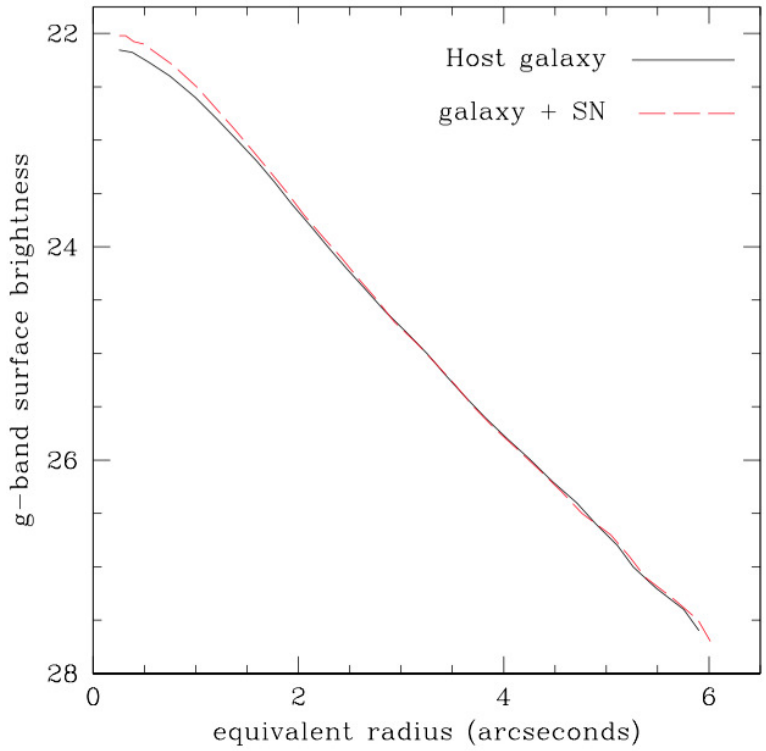

Figure 6.1: g-band surface brightness radial profiles of SDSS J102654.56+195254.8. The red dashed profile was obtained from a late phase image (+284 d) while the black one was obtained from our template image. Both images were obtained with the GTC.

6.1 The host galaxy

SDSS J102654.56+195254.8, the host galaxy of LSQ13zm, is a dwarf galaxy with an apparent g-band magnitude (as reported in the SDSS archive) of 18.95 ± 0.02 mag. Figure 6.1 shows the radial profile of the surface brightness of the host computed at different epochs, and suggests that the position of the SN (RA=10:26:54.591 and Dec= +19:52:54.91 [J2000]), accurately pin-pointed from a late-phase g-band template-subtracted image, is almost coincident with the coordinates of the host galaxy nucleus. A finding chart of LSQ13zm is shown in Figure 6.2. The field containing SDSS J102654.56+195254.8 was observed by the Sloan Digital Sky Survey (SDSS[6]) on 2005 March 10, and these data were used as template images for our *griz* early-phase photometric data. No source is visible at the galaxy position in the 2 Micron All Sky Survey (2MASS[7]), while the Wide-field Infrared Survey Explorer (WISE[8]) catalog reports the following magnitudes: $W_1 = 17.006 \pm 0.107$, $W_2 > 17.321$, $W_3 > 12.778$, suggesting a steep decline in the spectral energy distribution (SED) of the host from the optical to the infrared (IR) bands. From the average positions of the Balmer emission lines Hα and Hβ in the spectra of LSQ13zm (see Section 6.3), we derived a redshift of 0.029. Adopting a standard cosmology ($H_0 = 73$ km s^{-1} Mpc^{-1}, $\Omega_M = 0.27$, $\Omega_\Lambda = 0.73$) and using Ned Wright's Cosmological Calculator[9] (Wright 2006), we derived a luminosity distance $D_L = 122.0 \pm 8.2$ Mpc, and hence a distance modulus of $\mu = 35.43 \pm 0.21$ mag. For the foreground Galactic extinction, we adopt $A_V = 0.052$ mag, as derived from the Schlafly

[6] http://www.sdss.org/
[7] http://www.ipac.caltech.edu/2mass/
[8] http://www.nasa.gov/mission_pages/WISE/main/index.html
[9] http://www.astro.ucla.edu/~wright/CosmoCalc.html

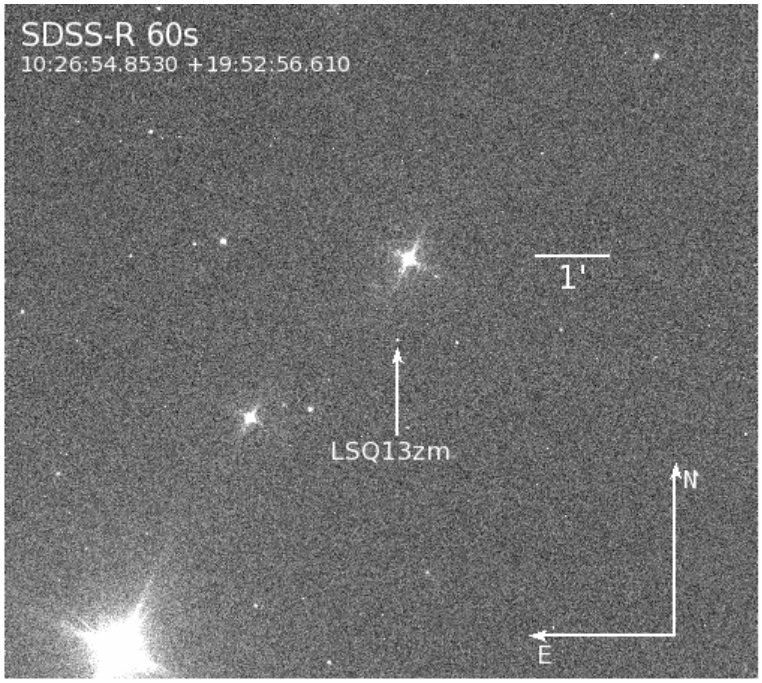

Figure 6.2: Finding chart of LSQ13zm. Information about the orientation, scale, filter and exposure time are reported.

& Finkbeiner (2011) infrared-based dust map available through the NED[10] database. Our spectroscopic analysis, detailed in Section 6.3, reveals no evidence of narrow absorption lines of the Na ID doublet at the recessional velocity of the host galaxy. For this reason, we will assume hereafter a negligible contribution of the host galaxy to the total extinction towards LSQ13zm.

An accurate study of the host galaxy was performed through our template images obtained with the 10.4 m Gran Telescopio Canarias (GTC) located at the Observatorio del Roque de los Muchachos (ORM, La Palma, Canary Islands, Spain) when the SN faded below the detection threshold. We first fit the isophotes with ellipses (1D fit), obtaining the following total magnitudes: $g = 19.68 \pm 0.01$ mag, $r = 19.14 \pm 0.02$ mag, $i = 18.97 \pm 0.01$ mag, $z = 18.73 \pm 0.02$ mag, significantly different than those reported in the SDSS archive, while the axial ratio and the position angle remain roughly constant in all bands with values of $\simeq 0.56°$ and $\simeq -46.5°$, respectively. Accounting for the redshift derived from the spectra of LSQ13zm and the foreground Galactic extinction reported by the NED archive, we infer an absolute magnitude $M_g = -15.99 \pm 0.21$ mag. The low absolute luminosity already suggests a significantly sub-solar global metallicity of $12 + \log[\mathrm{O/H}] = 8.21 \pm 0.37$ dex, following the relation of Pilyugin et al. (2004).

Global parameters were obtained using the GALFIT[11] code (Peng et al. 2010), hence performing 2D photometry fitting a Sersic law convolved with the local PSF. The effective radii range from $1.2''$ to $1.35''$ in the different filters. The results of this analysis confirmed our estimate on the actual position of LSQ13zm with respect to the centre of its host galaxy, that we assumed to be coincident with the centre of the isophotes (namely RA=10:26:54.638, Dec= +19:52:54.711 [J2000]). Their nearly coincident positions, in particular, suggest that

[10] http://ned.ipac.caltech.edu/
[11] http://users.obs.carnegiescience.edu/peng/work/galfit/galfit.html

the progenitor star belonged to a stellar population located in the central regions of the host galaxy. The Sersic index is low, ranging from 1.85 to 2.1 in the different bands. This, together with the visual appearance, suggests that the host could be a very early spiral galaxy, an S0, or a low luminosity elliptical galaxy. However, the SN spectra clearly show residual contamination of emission lines from a foreground H II region (see Section 6.3). For this reason, we rule out the elliptical galaxy classification. This choice is also supported by our estimated blue colours ($g-r=0.52$, $r-i=0.16$, $i-z=0.23$) as well as the clear detection of the host by the Galaxy Evolution Explorer (Galex[12]), which also provides the relatively bright total magnitudes 21.49 ± 0.14 mag and 21.64 ± 0.12 mag in the Far (1529 Å) and Near–Ultraviolet (2312 Å, FUV and NUV) respectively. In Figure 6.3 we show multi-wavelength images of the field of SDSS J102654.56+195254.8 obtained with SDSS, Galex and the NRAO VLA Sky Survey (NVSS[13]; Condon et al. 1998). Moreover, blue colours, along with [O II], [O III]

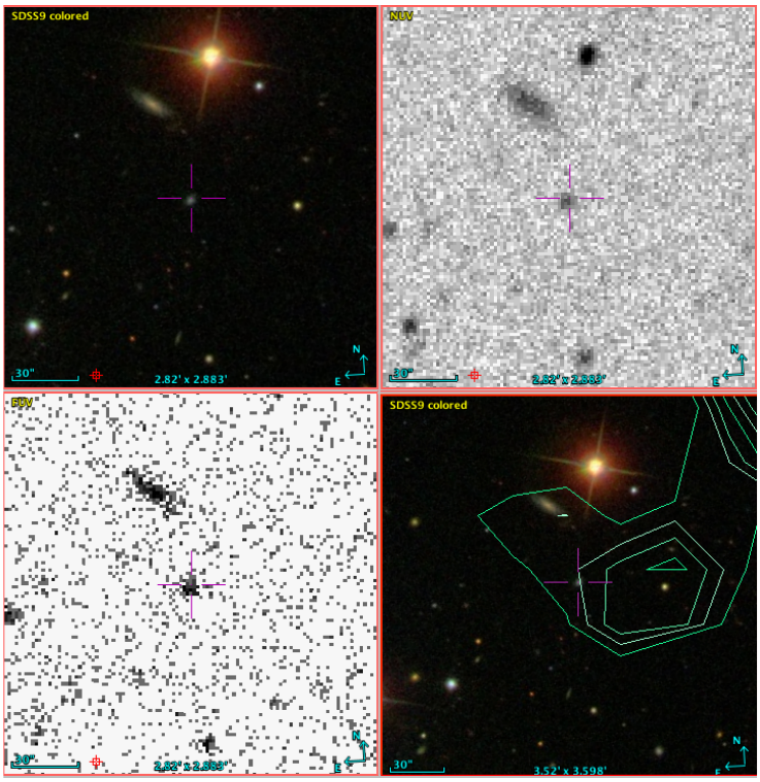

Figure 6.3: Sky region of SDSS J102654.56+195254.8 at different wavelength. **Top, left:** Polychromatic SDSS image. **Top, right:** NUV Galex frame. **Bottom left:** Galex FUV image. **Bottom right:** Polychromatic SDSS image with NVSS contour levels (1.0×10^{-3}, 4.8×10^{-4}, 4.6×10^{-4} and 4.3×10^{-4} mJy respectively); in all the images the position of the galaxy is marked.

and [S II] emission lines (clearly visible in the late time spectra of LSQ13zm, see Section 6.3) suggest high star formation rates (SFR), and are some of the common features of a class of galaxies known as 'Blue Compact Dwarf Galaxies' (BCDGs). BCDGs are active star–forming galaxies first identified by Haro (1956) and Zwicky et al. (1961). They are characterised by blue colours and compactness, but also by low luminosities and metallicities, and usually host stellar super-clusters (Adamo 2011). Some of them show spectra similar to those of H II regions of spiral galaxies, while the estimated SFRs range from 0.1 to 1 $M_\odot$ yr^{-1} (Fanelli et al. 1988; Cairós et al. 2001). According to this classification, and following Izotov et al. (2015),

[12] http://www.galex.caltech.edu/
[13] https://science.nrao.edu/science/surveys/vlass

we estimated a global metallicity of $12 + \log[\mathrm{O/H}] = 7.93 \pm 0.003$ dex. Low metallicities are common among the hosts of SN impostors, with values lower than those measured in galaxies hosting genuine Type IIn SNe (Taddia et al. 2015; Anderson et al. 2010). As a consequence, it is possible to argue that a fraction of interacting SNe does not belong to the same stellar population as SN impostors and that LBVs are not the only possible progenitor candidates for SNe IIn (Taddia et al. 2015).
The current SFR estimated from the FUV flux (9.2 μJy) obtained using the Kennicutt (1998) relation:

$$\mathrm{SFR_{FUV}}\ (\mathrm{M_\odot\ yr^{-1}}) = 1.4 \times 10^{-28}\ \mathrm{L_{FUV}}\ (\mathrm{erg\ s^{-1}\ Hz^{-1}}) \tag{6.1}$$

is 0.025 $\mathrm{M_\odot\ yr^{-1}}$, which is lower than the typical minimum value expected in this type of galaxies. We also computed an independent value using the integrated flux of the [O II] 3727 Å host galaxy line luminosity estimated from the +24 d LRS spectrum using the relation:

$$\mathrm{SFR_{[O\,II]}}\ (\mathrm{M_\odot\ yr^{-1}}) = 1.4 \times 10^{-41}\ \mathrm{L_{[O\,II]}}\ (\mathrm{erg\ s^{-1}}) \tag{6.2}$$

derived by Rosa-González et al. (2002), which gives a comparable low value of 0.028 $\mathrm{M_\odot\ yr^{-1}}$. Nonetheless, also the total mass derived adopting a 'diet' Salpeter Initial Mass Function (IMF Bell & de Jong 2001) and using the M/L – colour relation given in Bell et al. (2003), is relatively low, with a value (in stars) ranging from 8.65 to 8.8 $\mathrm{Log}(M/\mathrm{M_\odot})$. Adopting a Kroupa (2002) IMF, we derive an even lower mass ranging from 8.50 to 8.65 $\mathrm{Log}(M/\mathrm{M_\odot})$, suggesting an high specific SFR.

The above described parameters show that SDSS J102654.56+195254.8 is peculiar, since it shows compactness and morphological properties typically observed in early type galaxies, but also characterised by low metallicity and spectroscopic features typically observed in H II regions of star-forming spiral galaxies. The accurate characterisation of the host galaxies is an important tool in the study of peculiar transients, and could give an important improvement to our understanding of the physical processes occurring during the late phases of the evolution of massive stars.

6.2 Photometry

The multi-band photometric monitoring campaign started on 2013 April 27, and spanned a period of above 200 d. The 25 epochs of Sloan g, r, i and z photometry were primarily obtained using the 1 and 2-m telescopes of the Las Cumbres Observatory Global Telescope Network (LCOGT[14]; Brown et al. 2013) and are reported in Table 6.B.2. Near-Infrared (NIR) final magnitudes are reported in Table 6.B.3, while the observations in the Johnson–Cousins B, V and R bands were obtained using several facilities, all listed in Tables 6.B.1 and 6.C.1. Historical limits and the first detections of the pre-SN outburst (the 2013a event), were obtained by the Catalina Sky Survey (CSS) 0.7 m Schmidt telescope, which provided up to ~ 10 years of observations. Additional data were provided by the LSQ and the iPTF surveys. NIR data were obtained using the Rapid Eye Mount (REM) 0.6 m telescope with REMIR and the 2.54 m Nordic Optical Telescope (NOT) with NOTCam. The details about individual

[14] http://lcogt.net/

instrumental configurations are reported in the photometry tables (see Appendix **??**).

Photometric data were first pre-processed (applying overscan, bias and flat field corrections) using standard IRAF[15] procedures. Multiple NIR exposures were optimised subtracting clear sky images obtained median-combining dithered images, and then the resulting images were combined to increase the signal–to–noise ratio (SNR). The source instrumental magnitudes and their subsequent photometric calibration were obtained using a dedicated pipeline (Cappellaro 2014, SNoOpy). Template subtraction was performed with HOTPANTS by PSF matching, using archival SDSS images and very late images obtained with the GTC as templates to derive early- and late-phase optical magnitudes respectively. No templates were available for NIR bands, hence instrumental magnitudes for these bands were obtained using the PSF-fitting technique on un-subtracted images. Zero points and colour terms for the specific instrumental set-up were obtained with reference to a selected set of stars in the field. The 'local sequences' magnitudes were obtained from the SDSS and the 2MASS catalogues and were used to calibrate the SN magnitudes in the different images. BVR magnitudes of the reference stars were derived from the Sloan passband magnitudes, following Chonis & Gaskell (2008). Photometric errors were estimated through artificial star experiments, combining in quadrature the dispersions of individual measurements with the PSF-fit errors returned by DAOPHOT. For two epochs, multiband SNF synthetic photometry derived from flux-calibrated spectra was obtained using the procedures described in Buton et al. (2013), while the specific LSQ and PTF data reduction procedures are described in detail in Firth et al. (2015). The final magnitudes of LSQ13zm along with the photometric errors are listed in Tables 6.B.2, 6.B.3 and 6.B.1, while the resulting light-curves are shown in Figure 6.1. The first detection of the transient is dated 2013 March 18 (MJD = 56369.109) and was obtained by LSQ, followed by a marginal detection in a CRTS image obtained on 2013 March 19 (MJD = 56370.150). After these epochs, the R-band magnitude rose to $\simeq 20.6$ mag (corresponding to $M_R \simeq -14.8$ mag, with the distance modulus and extinction values reported in Section 6.1) until April 01, 2013 ($\simeq$ 13 d after the first detection), when the magnitude started to drop, reaching the value of $\simeq 21.3$ mag on April 7, 2013. Unfortunately, no information of the colours was obtained for the 2013a event, since the target was followed in the R-band only and no spectra were collected at these epochs (Section 6.3). On April 8, 2013 (MJD = 56390.285, the beginning of the 2013b event) a re-brightening was observed. After this epoch the R-band magnitude reached $\simeq 17$ mag, corresponding to $M_R \simeq -18.4$ mag, on April 24, 2013 (MJD = 56406.375, the peak of the 2013b event), that we will consider hereafter as a reference for both the photometric and spectroscopic analysis. During the re-brightening phase, we started to collect multi-band photometry and spectra using other facilities, as will be discussed in Sections 6.2.1 and 6.3. Over the 20 d prior to the 2013b maximum, we measure a rise of ~ 2.5 mag in R-band, while after maximum the light-curves evolve faster with a r-band decline-rate of $r \sim 5.6$ mag/100 d in the first ~ 25 d, decreasing to $r \sim 3$ mag/100 d until phase ~ 60 d. At later phases (namely after phase +200 d) we notice a slower decline, with a rate of $r \sim 0.2$ mag/100 d in the r-band light-curve, while the slopes in the g,i and z-bands are greater: 0.96, 3.62 and 3.28 mag/100 d respectively. This can be explained with an increased contribution of the Hα emission line relative to the continuum, although it has to be mentioned that we have no observations between phases +50 and +219 d in g and i-band, and between phases +63 and +219 d in z-band.

[15] `http://iraf.noao.edu/`

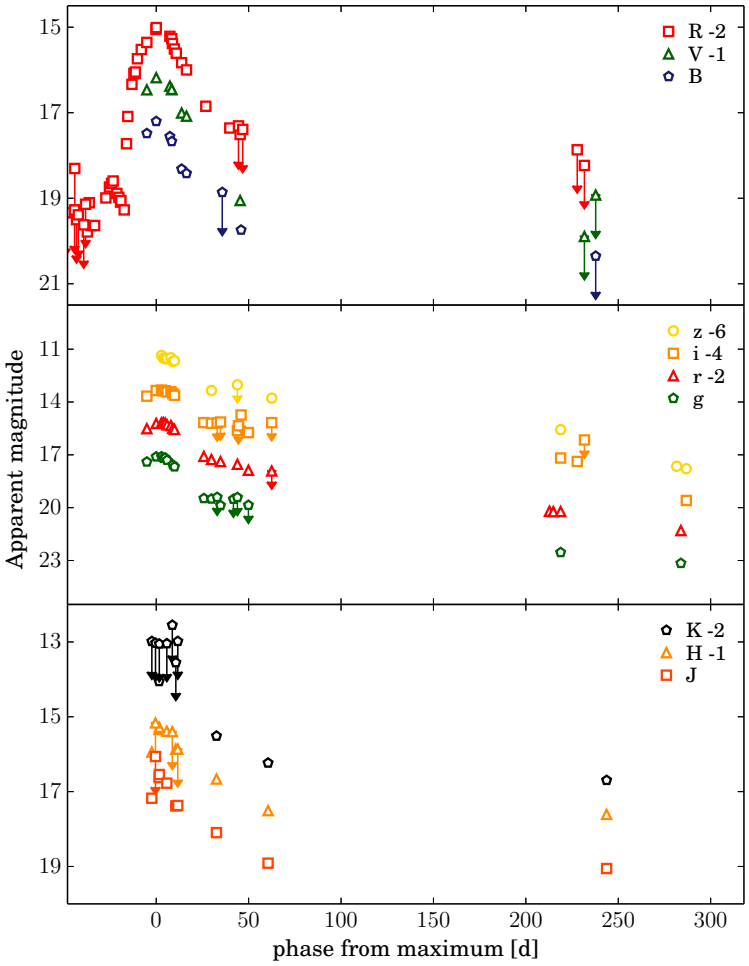

Figure 6.1: Multi-band light-curves of the transient LSQ13zm. BVR and JHK magnitudes are calibrated to the Vega system, while $griz$ magnitudes to the AB photometric system. Arbitrary constants were applied to the magnitudes of different bands.

6.2.1 Absolute light-curves and colour curves

Figure 6.2 shows the $g-r$ (top) and $r-i$ (bottom) colour evolution of LSQ13zm along with those of SN 2010mc (Ofek et al. 2013a) and SN 2009ip, two objects showing a similar photometric behavior, and the Type IIn SN 1999el (Di Carlo et al. 2002). The $g-r$ and $r-i$ colours become progressively redder with time, suggesting a rapid temperature decrease of the ejecta, as will be shown in the spectral analysis (Section 6.3).

The absolute R-band light-curve of LSQ13zm, referred to the 2013b event, is compared with those of the same SN sample as above in Figure 6.3. Adopting for LSQ13zm the distance modulus and extinction discussed in Section 6.1, we estimate an absolute peak magnitude of $M_R = -18.46 \pm 0.21$ mag for the 2013b event. As shown by this comparison, the absolute light-curve of the 2013b event of LSQ13zm is reminiscent of those of other Type IIn SNe, showing similar absolute peak magnitudes (in agreement with Kiewe et al. 2012, who found -18.4 mag as a mean value for the peak magnitudes for SNe IIn) and decline rates. In particular, there is a remarkable similarity between the 2013b absolute light-curve of LSQ13zm and that of SN 2010mc.

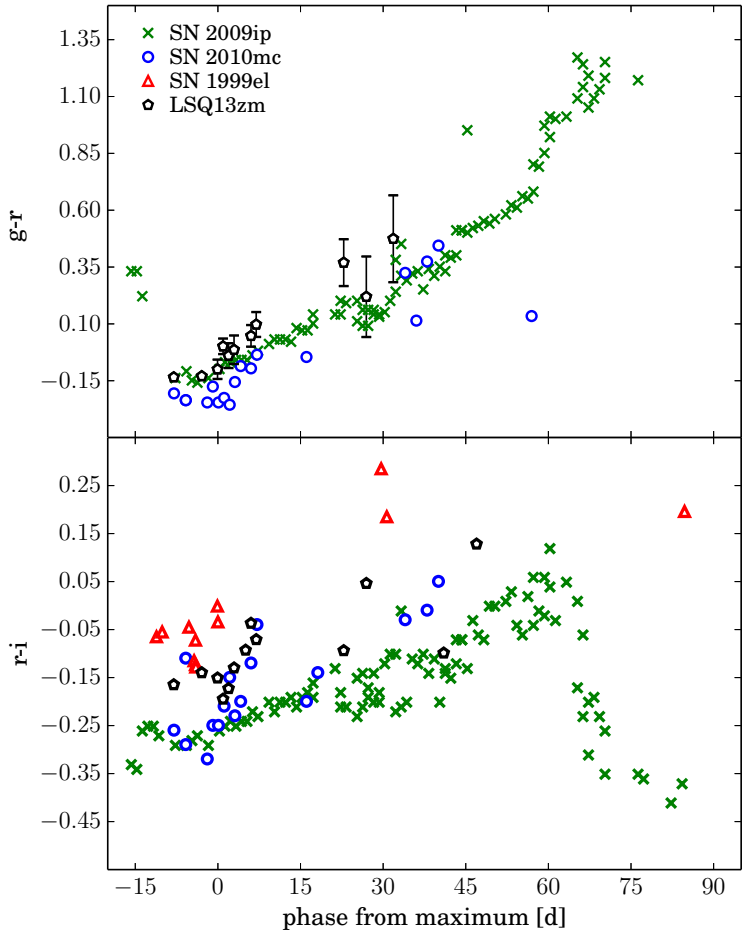

Figure 6.2: Comparison among the $g-r$ and $r-i$ colour curves of LSQ13zm, SN 2010mc, SN 1999el and SN 2009ip. Reddening estimates of SN 2009ip ($A_V = 0.055$ mag) and SN 2010mc ($A_V = 0.046$ mag) were obtained from the NED archive. For the total extinction to the direction of SN 1999el we adopted the value $A_V = 1.84$ mag, an average of the two extreme values reported by Di Carlo et al. (2002). Magnitudes were calibrated on the AB photometric system.

In Figure 6.4, we show the long-term photometric evolution of LSQ13zm (including the pre-discovery phases). Its R-band absolute light curve is compared with those of other objects classified as Type IIn SNe showing pre-explosion outbursts. Adopting the same values for the distance modulus and extinction, we infer an absolute peak magnitude of $M_R = -14.87 \pm 0.25$ mag for the 2013a event of LSQ13zm, comparable with the 2012a event of SN 2009ip.

Figure 6.4 also reports observations of the LSQ13zm site obtained prior to the 2013a,b episodes, including the photometric detection limits collected from CTRS, LSQ and iPTF archival images. The top panel shows that the pre-SN bursts of LSQ13zm, SN 2009ip and SN 2010mc are quite similar, with comparable absolute peak magnitudes, although the 2013a episode of LSQ13zm has a shorter duration. The Type IIn SN 2011ht, on the other hand, is slightly different, showing a pre-SN burst occurred ~ 1 year before the SN explosion (Fraser et al. 2013b). The bottom panel shows that no transient was observed in the past decade at the position of LSQ13zm, although the detection limits constrain the non-detections only to absolute magnitudes in the range between $M_R \approx -13.5$ mag and -15 mag. Of course, these observations cannot rule out that previous outburst episodes occurred in the gaps between

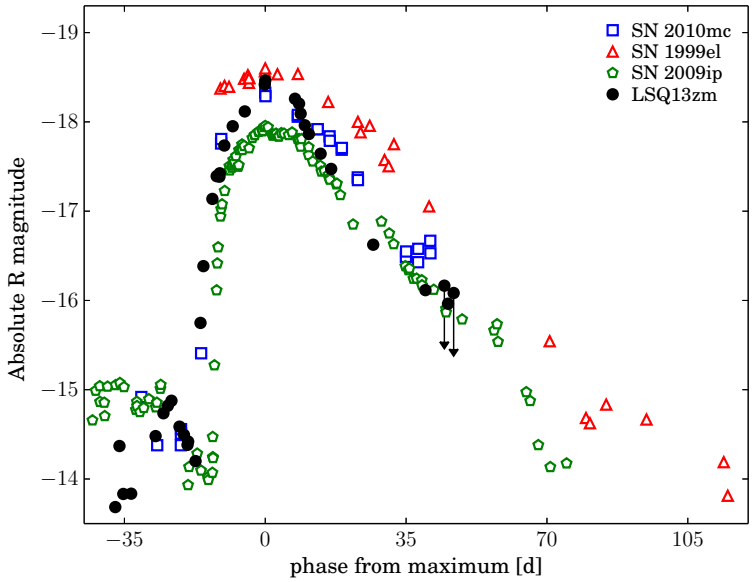

Figure 6.3: Comparison among the R-band absolute light curves of SN 1999el, SN 2010mc, SN 2009ip and LSQ13zm. The phases are relative to the maximum of the brightest event. The distance moduli of SN 1999el ($\mu = 32.1$ mag), SN 2009ip ($\mu = 31.55$ mag) and SN 2010mc ($\mu = 35.79$ mag) were taken from Di Carlo et al. (2002); Smith et al. (2010) and Ofek et al. (2013a), respectively.

the observations or at a fainter magnitude. In fact the detection limits of LSQ13zm (prior to the 2013a event) are not very stringent, as they are typically brighter than the erratic bursts observed in SN 2009ip during the period 2009-2011 (Pastorello et al. 2013).

6.3 Spectroscopy

Our spectroscopic follow-up campaign started on 2013 April 19 and lasted until 2014 November 23, hence covering almost 2 years. Essential information about the spectra is reported in Table 6.1. One-dimensional spectra were obtained using standard IRAF tasks for both pre-reduction (bias, flat field and overscan correction) and optimised extraction. Wavelength calibration was performed using the spectra of comparison lamps obtained during the same night. The accuracy of the wavelength calibration was then verified measuring the positions of night sky lines, in particular [O I] at 5577.34 Å and 6300.30 Å, and shifting the spectrum in wavelength in case of discrepancy. Flux calibration was performed using spectra of standard stars. Measured fluxes were checked against multi-band photometry obtained on the nearest nights and, when necessary, a scaling factor was applied. We did not perform any flux correction on the last two OSIRIS spectra, since they were both strongly contaminated by the flux of the host galaxy. Spectral resolutions, reported in Table 6.1, were computed measuring the mean values of the FWHM of unblended night sky lines.

6.3.1 Line identification and spectral evolution

The full spectral sequence of LSQ13zm is shown in Figure 6.1. The spectra show a blue continuum that becomes progressively redder with time, as the temperature at the photosphere decreases. A significant evolution in the relative strengths of the spectral features can also be noted. The first two spectra are dominated by narrow Balmer lines in emission, probably arising from a photo-ionised thin shell expelled a relatively short time ahead of

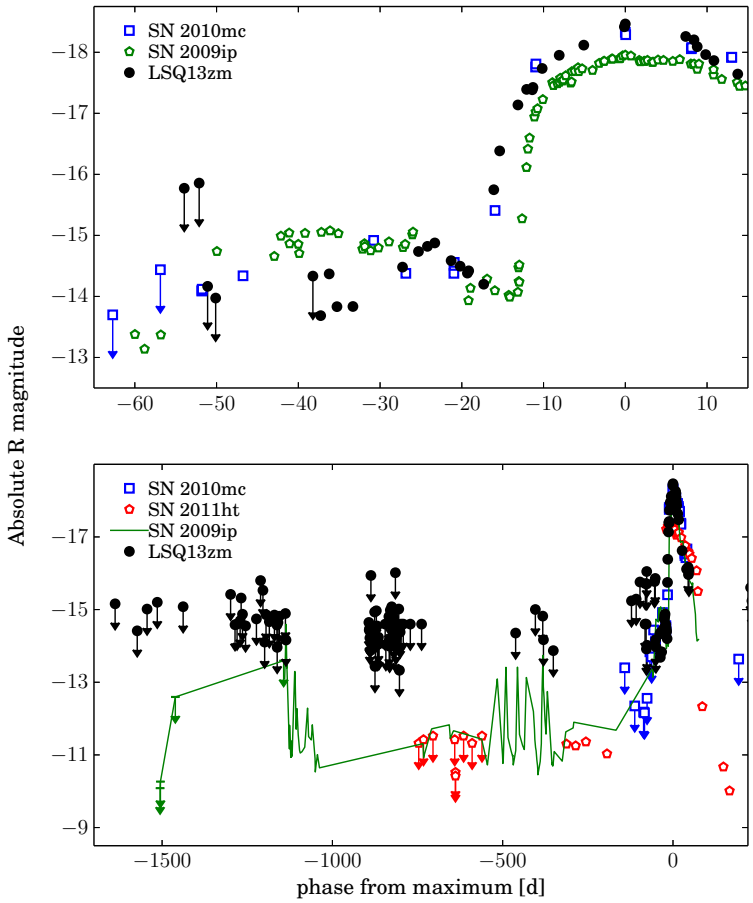

Figure 6.4: Comparison of the long-term R-band absolute light curves of LSQ13zm, SN 2011ht and SN 2009ip. **Top:** blow-up of the pre-SN outbursts of LSQ13zm (2013a) and SN 2009ip (2012a, Pastorello et al. 2013). **Bottom:** comparison of historical observations of LSQ13zm, SN 2011ht and SN 2009ip. References are indicated in the main text. The indicated phases are relative to the maximum of the most luminous event, possibly corresponding to the final SN explosion. The distance modulus of SN 2011ht ($\mu = 31.42$ mag) was taken from Roming et al. (2012) while, the reddening estimate ($A_V = 0.029$ mag) is from the NED archive.

the 2013b event. Around +8 d, the spectrum begins to show broad shallow features with P-Cygni profiles, most clearly visible in Hα and Hβ. From +16 d onwards, broad P-Cygni absorptions dominate the spectrum, including those of Hβ and other blended lines, as will be discussed in the following sections. We also identify blended Fe II, Mg II and Ca II lines, taking as a comparison the super-luminous Type Ic SN 2010gx (Figure 6.5; Pastorello et al. 2010a). From +44 d to +67 d, the interaction of the ejecta with the CSM becomes dominant, resulting in a progressively stronger contribution of the Hα intermediate component, which merges with the broad line wings of the profile. At +67 d, the intermediate component dominates the Hα profile over the other components.

In the early spectra, we marked the two He I lines in emission at 5875.6 and 7065.2 Å (see Figure 6.1), which are clearly detectable until +8 d. On the basis of the available data (resolution and SNR), we cannot rule out the presence of a weak He I (5875.6 Å) line in absorption also at later phases. At +8 d, we note the presence of the [O III] $\lambda\lambda$4958.5, 5006.8 doublet, although the single lines remain un-resolved. In addition, at late phases, also the [S II] $\lambda\lambda$6717-6731 doublet becomes detectable. Unresolved [S II] lines are uncommon in the nebular spectra of CCSNe, suggesting that they are an evidence of host galaxy contamination. Although these

Table 6.1: Log of the spectroscopical observations.

20130419	56401.3	−5	2.2 m UH+SNIFS	Channels B+R	3180-9420	9.7	2×1820
20130425	56406.4	0	2.2 m UH+SNIFS	Channels B+R	3180-9420	9.4	2×1820
20130428	56410.3	+4	FLOYDS	Channels red+blue	3200-6600	8.9	2×3600
20130502	56414.5	+8	BTA6 m+SCORPIO	VPHG550G	3100-7300	12.7	2550
20130508	56421.3	+15	Ekar182+AFOSC	Gm4	3600-7900	24	2700
20130510	56422.5	+16	BTA6 m+SCORPIO	VPHG550G	3600-7660	12.7	3600
20150517	56429.9	+24	TNG+LRS	LR-B	3200-7700	11.9	3600
20130523	56435.9	+30	TNG+LRS	LR-B	3200-7700	11.1	3000
20130606	56449.9	+44	TNG+LRS	LR-B	3200-7700	15.2	3000
20130629	56472.9	+67	TNG+LRS	LR-B	3200-7700	18.8	2×2700
20131225	56651.9	+245	GTC+OSIRIS	R500R	4670-9000	16.2	1800
20141124	56985.2	+579	GTC+OSIRIS	R300B	4000-9770	17.1	2×1800

The observations were carried out using the 6.05 m Bolshoi Teleskop Alt-azimutalnyi (BTA) of the Special Astronomical Observatory equipped with the Spectral Camera with Optical Reducer for Photometrical and Interferometrical Observations (SCORPIO; Zelenchuksky District, Caucasus Mountains, Russia), 2.2 m telescope of the University of Hawaii with the SuperNova Integral Field Spectrograph (SNIFS; Mauna Kea, Hawaii), the 10.4 m Gran Telescopio Canarias (GTC) with OSIRIS and the 3.58 m Telescopio Nazionale Galileo (TNG) with DOLoRes (LRS; both located at Roque de Los Muchachos, La Palma, Canary Islands, Spain), the 1.82 m Copernico telescope with AFOSC (Mt. Ekar, Asiago, Italy) and the LCOGT 2 m Faulkes North Telescope with FLOYDS.

unresolved forbidden lines appear to increase in flux with time, this is likely a consequence of the growing contamination of the galaxy foreground sources. This is clearly shown in Figure 6.A.1, where the latest two-dimensional spectrum of LSQ13zm including the host galaxy is shown for two wavelength windows: the Hα + [S II] 6717-6731 Å doublet (top panel in the figure), and Hβ + [O III] $\lambda\lambda$ 4958.5, 5006.8 doublet (bottom panel). In both cases, while the H lines are broader, [O III] and [S II] are narrower and spatially offset with respect to the peak of the H emissions. The relatively strong and unresolved [O II] $\lambda\lambda$ 3726-3729 doublet is also visible in the spectra from +24 d to +67 d, most likely due to the host contamination as well.

From +8 d to +67 d, we identify a very broad Hα component and, at the location of the Na ID doublet, another shallow feature in absorption showing a 'boxy' profile. The close-by comparisons in Figure 6.2 show the temporal evolution of these two spectral regions in the velocity space, where the absorption features observed in Hα and He I/Na ID are compared. We note that broad P-Cygni absorptions are clearly visible in the Hα profile since phase +8 d, indicating the presence of a significant amount of material moving at $\simeq 10^4$ km s^{-1}, with a maximum inferred velocity of $\simeq 22000$ km s^{-1}. The existence of fast-moving material is also confirmed by the absorption features observed in the He I/Na ID region. The range of velocities inferred from the two different lines at +44 d also agrees, with a velocity $\simeq 5 \times 10^3$ km s^{-1} for the bulk of the ejected material, and a maximum velocity of the line wing of $\simeq 10^4$ km s^{-1}, indicating that they arise from the same regions. We also notice a second absorption component in the He I (5876 Å)/Na ID (5891, 5897 Å) P-Cygni profile. This could be explained with the blended contribution of the two He I and Na ID lines. Such high velocity absorption features are generally observed in the ejecta of CCSNe at early phases, and are not typical of LBV eruptions. This is one of the main arguments that supports the SN scenario for the 2013b event (see Section 6.5).

Figure 6.3 displays the evolution of the Hα and Hβ emission line profiles. These two features are the only Balmer lines visible in all the spectra of our sequence, since Hγ disappears after a few days. We do not observe a significant shift in the position of the broad Hα and

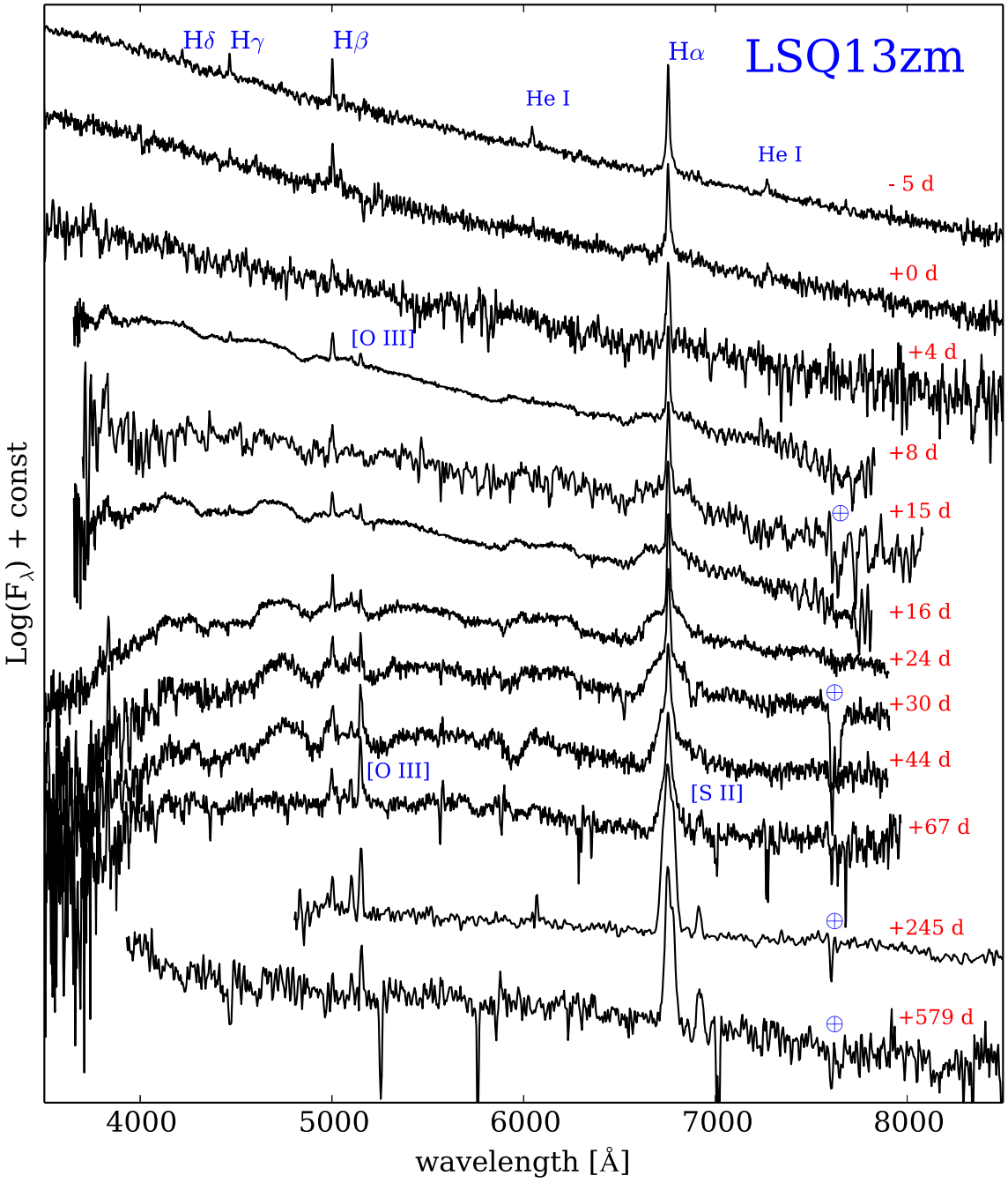

Figure 6.1: Spectral sequence of LSQ13zm. The phases, in days, are reported to the right, and are relative to the light-curve maximum of the 2013b event. The ⊕ symbols mark the positions, when visible, of the strongest telluric absorption bands. All spectra are flux-calibrated using the information obtained from the photometric data, with the exception of the last two OSIRIS spectra for which the galaxy contamination could not be removed. The spectra have been shifted by an arbitrary constant. The strongest lines visible in emission are also marked. The spectra are in the observed frame, and no reddening correction has been applied.

Hβ components, very likely arguing against a prompt dust formation.

Figure 6.4 shows the evolution of a few spectral parameters, viz. continuum temperature (top), velocity (middle) and luminosity (bottom) of the three line components, after correct-

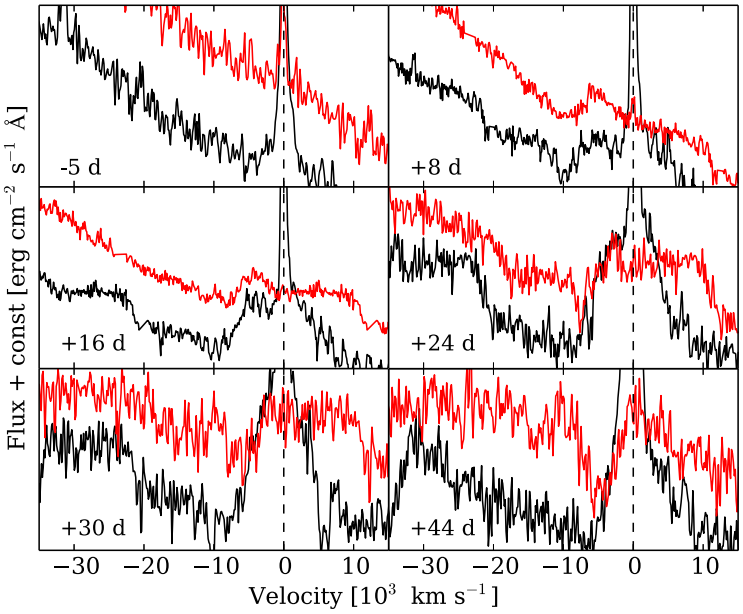

Figure 6.2: Blow-up of the H_α (black line) and He I/Na ID features (red line) at $= -5, +8, 16, 24, 30$ and 44 d, respectively. The dashed line is centred at the corresponding zero velocity of the Hα and He I 5875.6Å transitions. The fluxes are re-scaled and a constant is applied.

ing the spectra for foreground extinction and redshift. Their values are listed in Table 6.2. The velocities for the different line components are obtained through a multicomponent fit, using Gaussian and Lorentzian functions to reproduce the different Hα emission profiles. In the two earliest spectra, we obtain a good fit is reached using a single Lorentzian component, while in all other spectra a fair result is obtained using a combination of multiple Gaussians. This choice is based on the fit results, mostly affected by different resolution and SNR of the spectra. When the different components have widths which are larger than the resolution of the spectra, we compute the final velocity $v = \frac{width}{\lambda_0} \times c$ from the measured width corrected for the spectral resolution ($width = \sqrt{\mathrm{FWHM}^2 - \mathrm{res}^2}$). When the components are un-resolved, we adopt the resolution of the spectra as an upper limit of the velocities. For the narrow component we infer a nearly constant velocity, ranging from 250 ± 10 km s^{-1} to 470 ± 20 km s^{-1} (but strongly affected by spectral resolution limitations), while the broad component has a fast decline in velocity at early phases, from 11500 ± 1080 km s^{-1} to 4110 ± 300 km s^{-1} in the first 67 d.

From +67 d onwards, we include an intermediate component with velocities declining from 2560 ± 350 km s^{-1} to 1900 ± 400 km s^{-1}. As discussed in (Turatto et al. 1993b; **?** and Kiewe et al. 2012), spectra with multicomponent line profiles are common in interacting objects. The narrow line components have velocities consistent with those expected for the material expelled from an LBV, and are interpreted as recombination lines emitted by an outer un-shocked CSM. The FWHM velocities of the broad component are consistent with those measured in the expanding ejecta of a CCSN, although occasionally large velocities have been observed during major eruptions of LBVs (see e.g. SN 2009ip, Pastorello et al. 2013, during the period 2009-2011). Finally, the velocities of the intermediate component are fully consistent with those predicted for shocked gas, lying in the region between the forward and the reverse shock fronts.

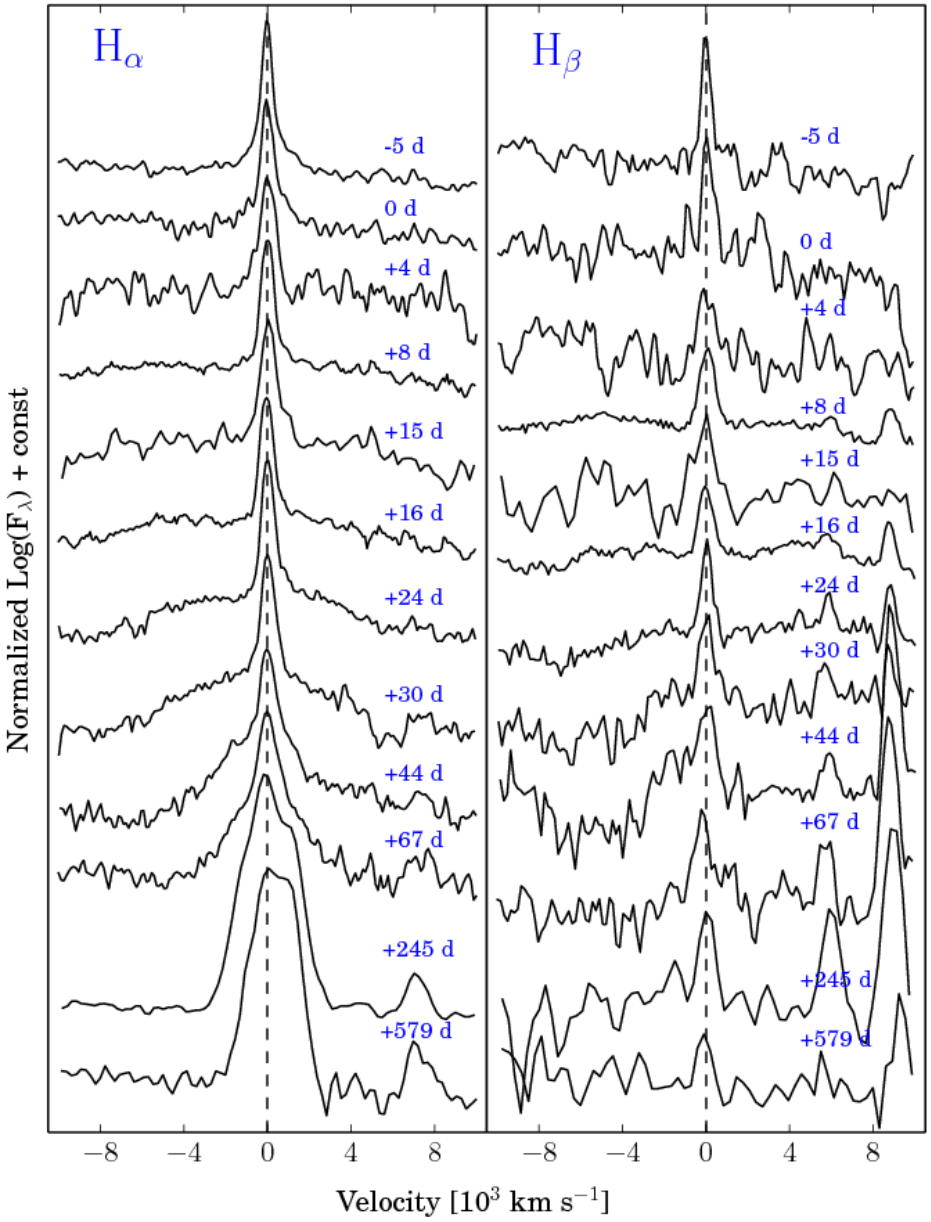

Figure 6.3: Evolution of the profiles of Hα (**left panel**) and Hβ (**right panel**) in the velocity space. The fluxes are re-scaled and a constant is applied. The vertical dashed lines mark the rest wavelength positions of the two lines.

The evolution of the temperature of the photosphere (Figure 6.4, top) is inferred through a black-body fit to the spectral continuum, since the spectra at early and intermediate phases (from +30 d to +67 d) are all characterised by a significant contribution of the continuum to the total emission. The temperature rapidly decreases from 12540 ± 770 K to 6170 ± 250 K in the first two months after maximum light. We do not compute a temperature in the last two spectra, since at this phase the continuum is strongly contaminated by the emission of the host galaxy. The temperature evolution is consistent with that of the broad-band colours discussed in Section 6.2.1 (see also Figure 6.2).

We also derive the luminosity evolution for the different components of Hα(Figure 6.4, bottom). The luminosity declines from 1.50×10^{40} to 1.30×10^{38} erg s^{-1} for the narrow com-

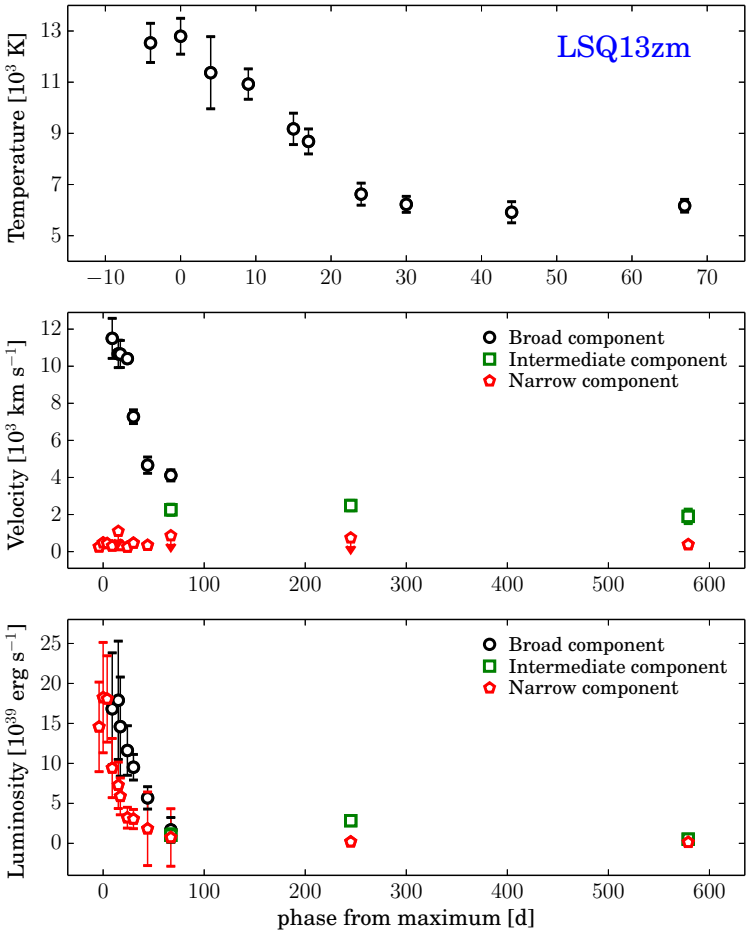

Figure 6.4: **Top:** Evolution of the temperature of the ejecta obtained through black-body fits. **Middle:** FWHM evolution for the broad (black dots), intermediate (green squares) and narrow (red pentagons) of the Hα components. **Bottom:** Luminosity evolution of the three Hα components.

ponent, from 1.80×10^{40} to 1.80×10^{39} erg s^{-1} for the broad component and from 1.10×10^{39} to 5.50×10^{38} erg s^{-1} for the intermediate components over the period of the spectroscopic monitoring.

6.3.2 Comparison with spectra of interacting SNe

A comparison with the spectra of different CCSNe is shown in Figure 6.5 (top). The comparison Is made on the basis of the best match to the +16 d and the +24 d spectra with those of other CCSNe obtained using the GELATO[16] comparison tool (Harutyunyan et al. 2008). A fair agreement is obtained with the Type IIb SN 1993J (Guinan et al. 1993; Baron et al. 1993; Barbon et al. 1995) and the Type II SNe 2007od (Andrews et al. 2010; Inserra et al. 2011) and 2009bw (Inserra et al. 2012). Nonetheless, we note that a better match is provided by a sample of superluminous SNe (SLSNe; Gal-Yam 2012, Figure 6.5, bottom), in particular SN 2008es (Miller et al. 2009; Gezari et al. 2009). SN 2008es is an overluminous Type II-L SN at z=0.205 with an absolute R-band magnitude of $\simeq -22$ mag. Although it reached a much higher luminosity, it showed a temperature evolution similar to that observed

[16] `https://gelato.tng.iac.es/`

Table 6.2: Main spectral parameters, as result from the analysis performed on the H_α line profiles.

phase (d)	Temperature (K)	$FWHM_{nar}$ (km s^{-1})	$FWHM_{brd}$ (km s^{-1})	$FWHM_{int}$ (km s^{-1})	L_{nar} (erg s^{-1})	L_{brd} (erg s^{-1})	L_{int} (erg s^{-1})
−5	12540(770)	~ 250*	–	–	$1.50(0.55) \times 10^{40}$	–	–
0	12800(700)	470*(20)	–	–	$1.90(0.70) \times 10^{40}$	–	–
+4	11370(1410)	440(50)	–	–	$1.90(0.50) \times 10^{40}$	–	–
+8	10930(590)	300(10)	11500(1080)	–	$9.90(0.40) \times 10^{39}$	$1.80(0.30) \times 10^{40}$	–
+15	91780610)	< 1100	10670(740)	–	$7.60(0.30) \times 10^{39}$	$1.90(0.30) \times 10^{40}$	–
+16	8680(490)	∼330	10660(730)	–	$6.20(0.35) \times 10^{39}$	$1.50(0.20) \times 10^{40}$	–
+24	6620(430)	~ 250	10410(720)	–	$3.40(0.30) \times 10^{39}$	$1.20(0.30) \times 10^{40}$	–
+30	6230(310)	460(10)	7280(440)	–	$3.20(0.40) \times 10^{39}$	$1.00(0.40) \times 10^{40}$	–
+44	5920(410)	~ 340	4660(560)	–	$1.90(0.50) \times 10^{39}$	$6.00(0.35) \times 10^{39}$	–
+67	6170(250)	< 8600	4110(300)	2560(350)	$7.70(0.40) \times 10^{38}$	$1.80(0.30) \times 10^{39}$	$1.10(0.50) \times 10^{39}$
+245	–	< 740	–	2490(280)	$2.00(0.30) \times 10^{38}$	–	$3.00(0.60) \times 10^{39}$
+579	–	380(10)	–	1900(400)	$1.30(0.60) \times 10^{38}$	–	$5.50(0.50) \times 10^{39}$

Column 1 reports the phases relative to the light-curve maximum, column 2 lists the temperatures derived through a black-body fit on the spectra continuum, columns 3,4 and 5 report the FWHM velocities inferred from multi-component fits of the Hα emission profiles for the narrow (nar), broad (brd) and intermediate (int) components, respectively. Columns 6,7 and 8 report the total luminosities inferred from the same Hα emission line components. We remark that values for the luminosities of the narrow and intermediate components in the last two spectra (phases +245 and +579 d) are strongly affected by the contamination of the host galaxy emission lines. The * symbol refers to the velocities inferred through a Lorentzian fit only. The $\sim$ symbol refers to narrow lines marginally resolved.

for LSQ13zm (namely from $\sim$ 14000 K to $\sim$ 6400 K during the first 65 d after maximum), along with comparable line velocities ($\simeq$ 10000 km s^{-1}) for the broad components. The Type II SN CSS121015:004244+132827, likely an interacting object (Benetti et al. 2014), has also a similar spectrum. This object has a B-band absolute magnitude of $\simeq -22.6$ mag, and shows a linearly declining light-curve.

Among the sample of SNe with H-rich CSM, also the energetic Type IIn SN 2008fz (Drake et al. 2010) provides a good match with our spectrum of LSQ13zm. SN 2008fz reaches an absolute V-band magnitude of $\simeq -22$ mag with an inferred radiated energy of $\gtrsim 1.4 \times 10^{51}$ erg s^{-1}, showing slow-evolving light-curves and spectra with multi-components emission lines. The comparison in Figure 6.5 (bottom) suggests that all these luminous, CSM-interacting SNe are likely CCSN events.

In Figure 6.6, we also report a comparison of the −5 d, +16 d and +44 d spectra of LSQ13zm (2013b event), with the spectra of SN 2009ip (Pastorello et al. 2013) and SN 2010mc (Ofek et al. 2013a) at similar phases. These two comparison objects are characterised by a similar sequence of events as those observed in LSQ13zm. The strong similarity in the spectroscopic and photometric properties of the three objects is remarkable, although this does not necessarily imply that their sequence of photometric outbursts has to be interpreted in a similar way (see Section 6.5).

6.4 Dating mass-loss episodes

In Section 6.3, we reported the results of our spectroscopic follow-up campaign of LSQ13zm. A blue continuum with prominent narrow Balmer lines in emission characterises the spectra at around the 2013b maximum, suggesting the presence of a photo-ionised un-shocked CSM, which recombines and re-emits photons. If the 2013b event was a genuine SN explosion, one might claim that this ionised gas was expelled during the 2013a outburst.

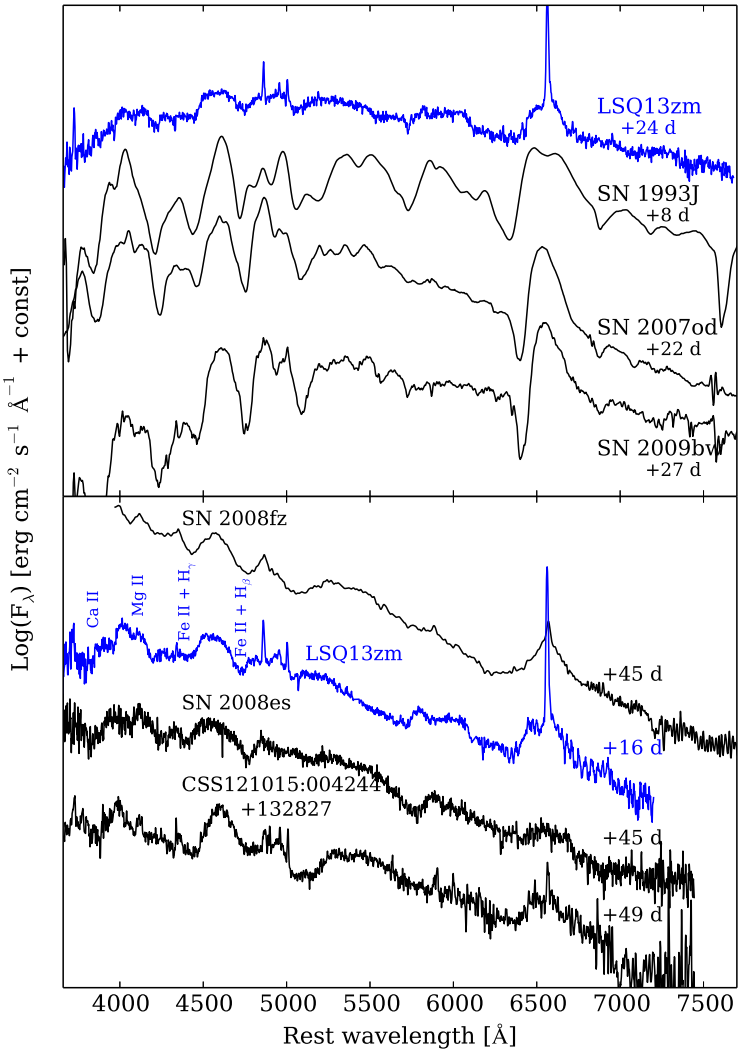

Figure 6.5: Comparison of the +16 d and the +24 d spectra with those of a sample of CCSNe and SLSNe. The objects were selected on the basis of good fits obtained using GELATO. Different constants have been applied to the logarithm of the fluxes.

The spectra show the first unequivocal signs of interaction (namely the rise of the intermediate Hα component) between +44 d and +67 d after maximum. Hereafter, we will assume that the SN explosion occurred 16 d before maximum ($\mathrm{MJD_{expl}} = 56387.9 \pm 2.5$, computed from a parabolic fit to the *R*-band light-curve of the 2013b event). Considering an intermediate phase (namely day 55 post-max) as the indicative epoch when the SN ejecta reach the pre-existing CSM, we can approximately estimate the epoch of the ejection of this circumstellar shell. Adopting 11500 km s^{-1} as an indicative velocity for the SN ejecta (the velocity inferred from the broad component of the +8 d spectrum) and 470 km s^{-1} as the velocity of the un-shocked CSM (as inferred from our highest resolution spectrum), we find that this gas was expelled by the star $\simeq$ 4 yr before the putative SN explosion. Therefore this material had been lost well ahead the 2013a event. Under the same gross assumptions, we can infer that the gas moving at 470 km s^{-1} and expelled at the beginning of the 2013a event (that we assume to be on $\mathrm{MJD_{out}} = 56366.1 \pm 3.0$, i.e. $\sim$ 22 d before the epoch of the explosion; also estimated through a polynomial fit of the *R*-band light-curve) has been blown away by the SN ejecta in $\sim$ 1 d.

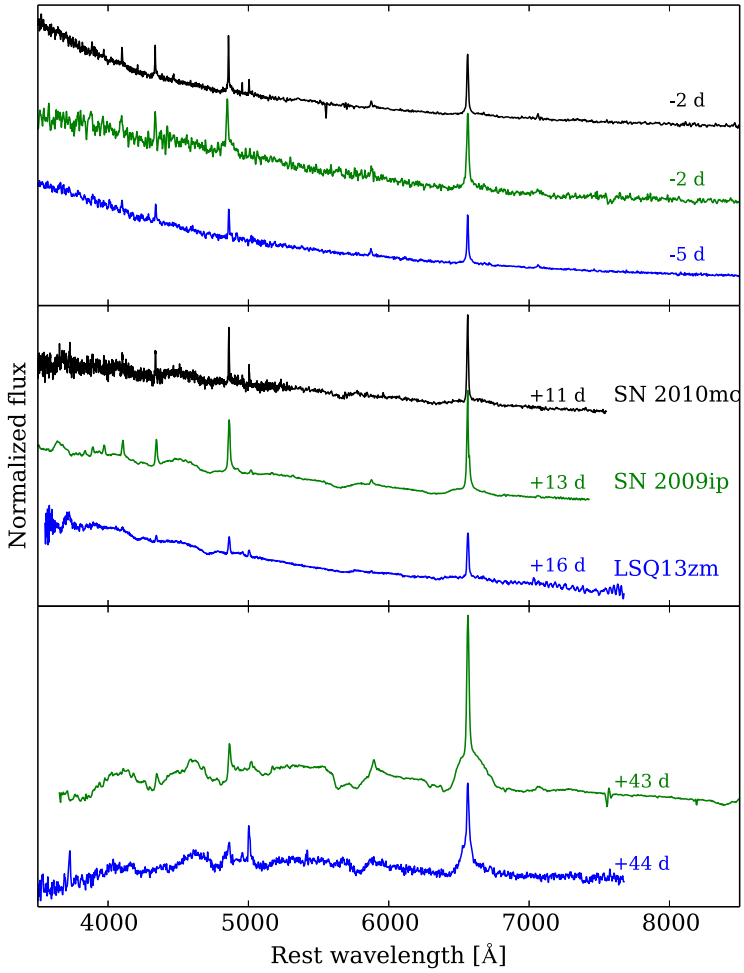

Figure 6.6: Comparison of the spectra of LSQ13zm, SN 2009ip and SN 2010mc at similar phases. The phases of SN 2009ip refer to the 2012b maximum, those of SN 2010mc to the maximum light.

The SN shock breakout and the early interaction between SN ejecta and inner CSM would provide enough energy to ionise the outer CSM expelled in past, unobserved mass-loss events. The latter mechanism would the most natural explanation for injecting ionizing radiation to power the narrow Hα line produced in the outer CSM, and observed from our first spectrum of LSQ13zm to that at $\sim$ 44 d after light curve peak. We note that some spectroscopic indicators would argue against strong ejecta-CSM interaction at early phases in LSQ13zm. In fact, until day +44, there is no direct evidence for the presence intermediate-width line components typical of shocked gas shells, and broad features from un-shocked SN ejecta are clearly detected. Nonetheless, higher-density clumps in more diluted gas and/or geometrical effects may produce the above mentioned spectral observables.

At epoch later than +44 d, the interaction between the ejecta of LSQ13zm and outer CSM becomes more evident, with the detection of intermediate-width line components. This provides a sufficient amount of high-energy photons to ionise the un-shocked external material, as proposed by Chugai & Danziger (1994) to explain the observed spectroscopic features of SN 1988Z. We will widely discuss the implications of the photometric and spectroscopic properties of LSQ13zm in Section 6.5.

6.5 On the nature of LSQ13zm

In Sections 6.2 and 6.3, we reported the photometric and spectroscopic analysis of the optical transient LSQ13zm. In a remarkable sequence of events, this object showed a first outburst, the '2013a event', during which it reached the absolute magnitude $M_R = -14.87 \pm 0.25$ mag. This brightening was followed after ~ 3 weeks by another episode, the '2013b event', with an absolute peak magnitude $M_R = -18.46 \pm 0.21$ mag, similar to those observed in Type IIn SNe. We need to remark that the presence of previous outbursts in the past decade cannot be ruled out since, as shown in Figure 6.4, our historical limits are not deep enough to detect eruptive episodes fainter than $M_R \simeq -15$ mag. Moreover, as discussed in Section 6.4, the results of our photometric and spectroscopic analysis suggest that an unobserved eruptive event might have occurred $\gtrsim 4$ years before the 2013a event.

Our spectra, covering almost 2 years after the 2013b episode, are characterised by three main phases. At early phases (before and around the 2013b masimum), the spectra show a blue continuum (with an inferred black-body temperature of ~ 13000 K) with narrow Balmer lines in emission characterised by Lorentzian profiles. At intermediate epochs (namely during the decline after the 2013b light-curve maximum) the spectra show broad absorption features, particularly evident in the Hα, Hβ and He I/Na ID, suggesting the presence of underlying high-velocity ejecta. Finally, late-phase spectra are dominated by the intermediate-width features typical of ejecta-CSM interaction, although the contamination of the host galaxy strongly contributes to the shape of the continuum at these phases.

While early-phase spectra show unequivocal evidence of a surrounding dense CSM, different physical mechanisms can produce the ionising photons required to explain the observed features. Lorentzian wings are, in fact, typical of hot ionised gas and are usually related to Thomson scattering due to free electrons in the medium. While inner ejecta-CSM collisions may produce the sufficient amount of energy to ionise pre-existing H-rich material, narrow recombination lines may also be powered by a long-lived shock-breakout within a dense, optically thick surrounding CSM. The lower velocity limit for SN shocks breaking out in such dense media was found to be $\sim 10^4$ km s^{-1}, supporting the conclusion that the rising in the light-curves of some Type IIn SNe might be powered by shock break-out within a dense CSM (Ofek et al. 2014b). Ofek et al. (2010) also explained the fast rising in the UV emission with shock break-out through a dense CSM for the Type IIn SN PTF 09uj. The subsequent visible emission at later times was then interpreted as the diffusion of the energy deposited in the CMS by the shock itself.

The spectroscopic evolution during the early decline phases is characterised by prominent absorption features strengthening with time, with relatively fast and constant expansion velocities ($\sim 10^4$ km s^{-1}, inferred from the minima of the absorption profiles). The absorption feature observed for Hα and He I/Na ID is of particular interest, showing boxy profiles with wing velocities extending to ~ 22000 km s^{-1} (see Figure 6.2), without showing a significant evolution from $\sim +8$ d to $\sim +44$ d after maximum. High velocities, along with the peculiar profile of Hα and He I/Na ID, were never observed in SN 2009ip, which, on the other hand, showed blue wings with an inferred velocity of ~ 13000 km s^{-1} only.

Clear signatures of ejecta-CSM interaction become unequivocally visible only at late phases, from phase +67 d, when an intermediate component clearly appears in the Hα line profile. Moreover, like in many other interacting transients, the late spectra show no trace of α- or Fe-peak elements produced in the explosive nucleosynthesis.

The case of SN 2009ip is widely debated, and different interpretations to the nature of the two 2012 events are offered in the literature. While the photometric properties of the 2012a event were comparable with those displayed by SN impostors, the spectroscopic analysis at these epochs showed broad P-Cygni line components. However, broad absorptions had already been observed during the numerous re-brightenings during the 2009-2011 period, and this was an indication that a relatively small amount of gas was expanding at velocities much higher than those typically observed in erupting LBVs.

The effects of a particular geometrical configuration on such observables was the subject of recent studies performed by Mauerhan et al. (2014) using spectropolarimetry data of SN 2009ip. Their analysis revealed that the two eruptive episodes occurred in 2012 were both highly aspherical (with the second episode showing an higher level of asphericity) and, most importantly, exhibited orthogonal geometries on the sky. Their results supported the scenario in which SN 2009ip exploded during the 2012a event with a prolate/bipolar photosphere geometry partially obstructed by a toroidal (disc- or ring-shaped) dense CSM (see Figure 9 in Mauerhan et al. 2014). Toroidal geometry for the surrounding CSM of SN 2009ip was already suggested by Levesque et al. (2014) on the basis of spectroscopic arguments, while bipolar geometry was already proposed by Wang et al. (2001) to explain other cases of highly polarised CCSNe. We cannot rule out that high asphericity can characterise also LSQ13zm, although we do not have spectropolarimetry observations to verify this speculation.

In the forthcoming sections, we compare the photometric and spectroscopic properties of LSQ13zm with those of other similar transients, in particular SN 2009ip, in order to infer the true nature of the 2013a,b events. To do that, we consider for LSQ13zm the most plausible scenarios on the basis of the different interpretations given for SN 2009ip. In Section 6.5.1 we will discuss the scenario proposed by Pastorello et al. (2013), which supports a pulsational pair-instability (PPI) event powered by collisions between shells expelled at different times, while in Section 6.5.2 we will inspect the scenario proposed by Mauerhan et al. (2013), suggesting a SN explosion followed by ejecta-CSM interaction. In Section 6.5.3 we will briefly analyse the possibility that the 2013a event is the result of binary interactions between an evolved LBV star with a un-evolved, less massive star, with the 2013b event triggered by a violent merger (following the interpretation proposed by Soker & Kashi 2013; Kashi et al. 2013, for SN 2009ip). Finally, in Section 6.5.4, we will discuss the scenario in which the giant eruption of a massive progenitor (most likely an LBV star) is followed by a terminal explosion.

6.5.1 2013b as a pulsation pair-instability event powered by shell-shell collisions

The first scenario illustrated for LSQ13zm is that of an unusual SN impostor, where the first, weaker light curve peak would be produced by a giant, non-terminal outburst, followed by a major re-brightening due to interaction between two dense circumstellar-shells. To support this, we first compare in Figure 6.1 (top panel) the absolute light curve of the LSQ13zm 2013a event with those of proposed SN impostors, and with the 2012a event of SN 2009ip. All these transients show very similar absolute peak magnitudes, which are relatively faint for SNe (but see Figure 6.1, bottom panel, and Section 6.5.2), and frequently observed in non-terminal eruptions of massive stars (see, e.g. Smith et al. 2011, and references therein). What triggers these eruptions is still debated. One possibility is that 'pulsation pair-instability' (PPI) in very massive stars may produce some of these impostors.

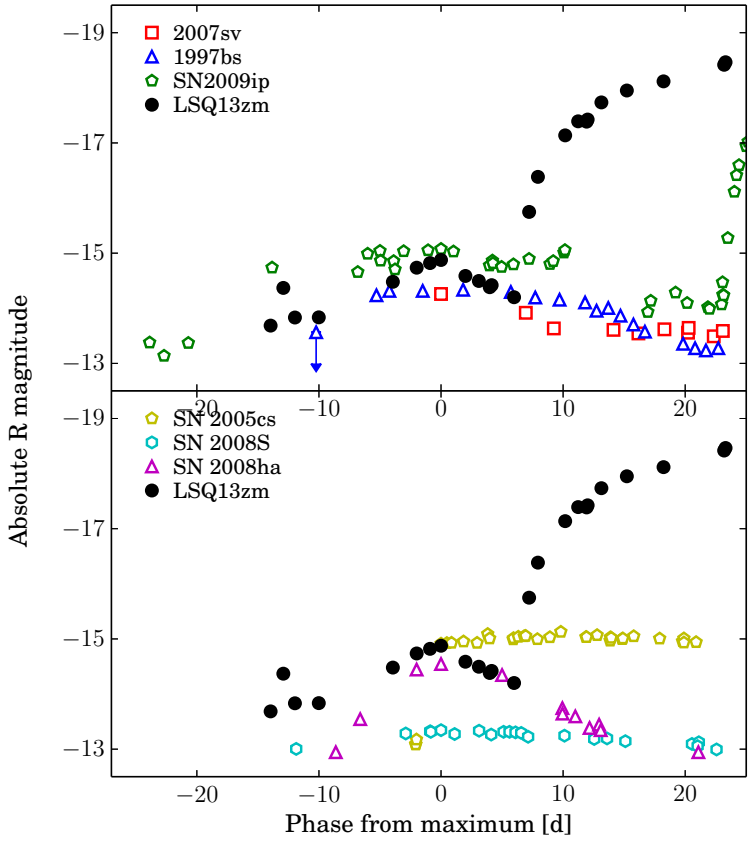

Figure 6.1: **Top:** Comparison of the absolute R-band light curve of LSQ13zm with those of known SN impostors. The distance moduli of 2007sv ($\mu = 31.38$ mag), 1997bs ($\mu = 31.1$ mag) were taken from Tartaglia et al. (2015) and Van Dyk et al. (2000) respectively, while the reddening estimates for the same two objects ($A_V = 0.056$ mag and $A_V = 0.093$ mag respectively) were taken from the NED archive. The phases are relative to the maximum light. For LSQ13zm we refer to the maximum of the 2013a episode, for SN 2009ip to the maximum of the 2012a event (Pastorello et al. 2013). **Bottom:** Comparison with the absolute R-band magnitudes of a sample of faint SNe. The distance moduli and the reddening estimates for SN 2005cs ($\mu = 29.26$ mag, $A_V = 0.155$ mag), SN 2008S ($\mu = 28.74$ mag, $A_V = 1.13$ mag) and SN 2008ha ($\mu = 31.55$ mag, $A_V = 0.236$ mag) and they were taken from Pastorello et al. (2009a); Botticella et al. (2009) and Valenti et al. (2009) respectively. The phases are relative to the maximum light. Phase 0 in LSQ13zm is coincident with the epoch of the 2013a event maximum.

During a PPI event, the production of electron-positron pairs due to high temperatures leads to a reduction of the radiative pressure inside the core followed by a partial collapse and runaway thermonuclear explosions. However, these explosive events have not necessarily sufficient energy to unbind the entire star causing the disruption of the progenitor, but can provide a sufficient amount of energy to trigger violent ejections of several solar masses of the envelope. If the remaining core mass is high enough, subsequent eruptions may happen, and collisions of shells expelled at different times would eventually lead to a dramatic increase in the luminosity of the transient. The conversion of kinetic energy into radiation can be extremely efficient, providing an energy output up to 10^{50} erg, much greater than that measured even in CCSNe. For this reason, PPI is one of the mechanisms proposed to explain the major eruption of LBVs (Woosley et al. 2007).

In a detailed spectroscopic analysis, Pastorello et al. (2013) compared the spectra of

SN 2009ip collected during the erratic variability in 2009-2011, and during the 2012a episode with those of the SN impostor NGC 3432-LBV1 (aka 2000ch; Wagner et al. 2004; Pastorello et al. 2010b), very likely an hyper-active LBV. In their paper, Pastorello et al. showed that high velocity ejecta can be observed also during major eruptions of LBVs, with broad wings extending up to 9000 km s^{-1}. As the erratic variability observed in SN 2009ip from 2009 to 2011 closely resemble that still experienced by NGC 3432-LBV1, one of the main conclusions of Pastorello et al. (2013) was that the major re-brightening of SN 2009ip (called 2012b) was the consequence of a PPI event, in which the gas expelled in a major outburst (possibly the event 2012a) collided with pre-existing CSM, likely collected during the previous erratic variability phase of the massive LBV precursor. The consequence was that SN 2009ip did not undergo core-collapse during the 2012b event, but was the result of collisions among shells expelled at different times. Multiple repeated outbursts, similar to those observed in SN impostors and not leading to a terminal SN explosion are a possible scenario, and have already been observed (see e.g. the case of SNHunt248; Kankare et al. (2015); Mauerhan et al. (2015) or SN 1994W; Dessart et al. (2009)). According to the above scenario, the 2013a event in LSQ13zm would be a major outburst produced by PPI, while the light-curve of the 2013b event would be a large re-brightening powered by the conversion of kinetic energy into radiation. With the above scenario, there would be no need of additional energy input from the decay of radioactive material.

Nonetheless, the PPI plus shell-shell collision does not convincingly explain all the observables of LSQ13zm. First of all, some concerns derive from energetic consideration. As we do not have any data in the ultraviolet (UV) domain for LSQ13zm, we estimate its quasi-bolometric peak luminosity assuming a UV contribution to the total luminosity similar to that of SN 2009ip. We obtain a peak luminosity for LSQ13zm of $\gtrsim 10^{43}$ erg s^{-1}. Even assuming a 10% of efficiency, the conversion of the kinetic energy of 1 $M_{\odot}$ of gas moving at 11500 km s^{-1} (a crude estimate of the velocity of the ejecta based on our early spectra of LSQ13zm) into radiation would give $\sim 10^{51}$ erg of total radiated energy, which is a factor ~ 10 larger than the total energy radiated during the 2013b event. We also remark that this value might even be significantly underestimated since, as pointed out by Mauerhan et al. (2014), particular geometrical configurations may lead to a reduction in the ejecta-CSM interacting surface and hence a less efficient conversion of kinetic energy into radiation. Nonetheless, the spectral properties of LSQ13zm, including the presence of very broad features similar to those observed in CCSNe spectra (see Figure 6.5 and discussion in Section 6.3.2), do not favour the PPI mechanism and shell-shell collision, and favour a terminal SN explosion.

6.5.2 The 2013a event was a faint SN, with 2013b being powered by ejecta-CSM interaction

Another possibility is that we first observed a very weak CCSN followed by the interaction between the ejecta and pre-existing CSM. This scenario was first proposed by Mauerhan et al. (2013) to explain the chain of events producing the final brightenings of SN 2009ip, and should be re-discussed in the context of LSQ13zm. The faint absolute magnitude of the 2013a event is not a major problem, since weak CCSNe do exist (e.g., Figure 6.1, bottom panel). Weak explosions may result from the CC of moderate-mass (8-10 $M_{\odot}$) super–AGB stars producing so-called 'electron-capture (EC) SNe' (e.g. Pumo et al. 2009), as well as from the core-collapse of more massive stars (above 25-30 $M_{\odot}$) where a large fraction of the progenitor's mantle falls back onto the nucleus, likely producing a black hole (Heger et al. 2003). In both terminal explosion scenarios, the final outcomes are expected to be faint CCSNe with absolute magnitudes ranging from -13 mag to -15 mag.

Although faint absolute magnitudes at maximum are often arguments used to discriminate SN impostors from genuine SNe (see e.g. Tartaglia et al. 2015), as pointed out by Pastorello et al. (2007b) there are a few classes of genuine SNe characterised by weak peak magnitudes, including the most common CCSNe, i.e. Type II-P events. The faintest member of this class was SN 1999br (Pastorello et al. 2004), reaching an absolute peak magnitude of $\simeq -14.2$ mag, but also SN 2010id showed a similarly faint magnitude ($M_R < -14$mag; Gal-Yam et al. 2011). This evidence was also used by Mauerhan et al. (2013) and Smith et al. (2014) to state that the weakness of the 2012a event in SN 2009ip was not a strong argument to rule out the CCSN scenario.

Consequently, the photometric analysis alone is not sufficient to rule out either the genuine SN or the SN impostor scenarios for this class of transients (Tartaglia et al. 2015). Therefore, additional clues are needed to discriminate between the different types of explosions. One plausible clue is the width of the broadest line components, that can be associated with the velocities of the fastest-moving ejected material. In the spectra of SN 2009ip, the detection of broad Hα line components led Mauerhan et al. (2013) to conclude that it was indeed the final explosion of an LBV progenitor, although this argument has been questioned by other authors, (e.g., Pastorello et al. 2013; Fraser et al. 2015; Margutti et al. 2014).

Following Mauerhan et al. (2013), in Figure 6.1 (bottom panel) we compare the absolute light-curve of the 2013a event in LSQ13zm with those of a sample of faint SNe, including the Type II-P SN 2005cs (Pastorello et al. 2006), the peculiar Type IIn SN 2008S (Botticella et al. 2009) and SN 2008ha (Valenti et al. 2009). Clearly, the absolute magnitude and the evolution of the light-curve of the 2013a event of LSQ13zm are consistent with those of faint SNe. For this reason, assuming that 2013a is a true SN explosion, we then need to provide a coherent interpretation for the 2013b event. As mentioned in the previous section, we consider the possibility that the 2013b re-brightening is powered by the interaction of the SN-ejecta with a dense CSM expelled during past mass loss episodes.

Collisions between H-rich SN ejecta and circum-stellar gas usually produce spectra with a blue continuum and strong Balmer lines in emission, with prominent intermediate-width components (namely with FWHM velocities of a few $\sim 10^3$ km s^{-1}). Intermediate-velocity components are typical of the spectra of interacting objects, and arise in the gas interface between the forward and reverse shocks (see Chevalier & Fransson 1994). However, the first two spectra in Figure 6.1 are characterised by a blue continuum with narrow H and He I lines in emission, with low FWHM velocities (a few 10^2 km s^{-1}), and no evidence of intermediate components. Nonetheless, narrow lines are generally indicative of a slow-moving ionised thin shell, that may eventually produce an opaque pseudo-photospere masking the underlying ejecta-CSM interaction. After the 2013b event peak, the spectra evolve showing very broad features similar to those of canonical non-interacting CCSNe, and likely attributed to the SN ejecta. The fact that the spectral signatures can be now directly observed, can be explained with a peculiar geometrical configuration of the CSM (e.g. Mauerhan et al. 2014), or a non-homogeneus clumpy CSM structure. Nonetheless, the characteristic boxy absorption detected in both the Hα and He I/Na ID regions up to $\sim +44$ d after the 2013b maximum, suggests the presence of a fraction of expelled gas moving at very high velocities (up to 22000 km s^{-1}). Adopting a scenario according to which the 2013a event is a faint SN followed by ejecta-CSM interaction (2013b), the very high expansion velocities would be measured at over 90 d after the explosion. Such high velocities have never been observed at late SN phases in any CCSN Type. Hence this doeas not favour the SN scenario for the 2013a event of LSQ13zm.

6.5.3 2013a and 2013b events generated by repeated binary interactions and a final merger-burst

A further scenario that could potentially explain the unusual light curve of LSQ13zm was first proposed for SN 2009ip by Soker & Kashi (2013); Kashi et al. (2013). An overall similarity, in fact, should be remarked between the light curves of SN 2009ip (and - consequently - LSQ13zm) and the binary merger V838 Mon (Brown et al. 2002; Kimeswenger et al. 2002; Munari et al. 2002; Crause et al. 2003; Soker & Tylenda 2003; Kipper et al. 2004; Tylenda 2005). According to this scenario, the sequence of outbursts experienced by SN 2009ip before the main 2012b event, is explained with mass transfer in a strongly interacting binary system consisting in an evolved massive (M_1 = 60-100 $M_\odot$) star with a lower mass main-sequence companion of M_2 = 12-50 $M_\odot$ lying in an eccentric orbit. A final merger-burst would be responsible for the re-brightening observed during 2012b. A binary merger (e.g., Soker & Tylenda 2006) is a violent event in which two (or more) stars merge, due to direct collision or interaction. As the primary star evolves beyond the main sequence, it expands triggering the merging event, although also orbital angular momentum losses via tidal interaction can lead the binary system to a collision. Extreme cases of mass transfer at very high rates have also been suggested as an alternative mechanism to trigger outbursts or eruptive episodes of evolved massive stars like LBVs (see e.g. Kashi & Soker 2010). The presence of multiple minor peaks in the light-curve of SN 2009ip after the 2012b maximum, carefully analysed by Martin et al. (2015), is in fact reminiscent of the secondary luminosity peaks observed during the Giant Eruption of η Car, and attributed to binary interaction at periastron passages (Damineli 1996; Kashi & Soker 2010; Smith & Frew 2011). These bumps, superposed to the main light curve of the 2012b event, were observed with amplitudes of several tenths of magnitude (Martin et al. 2015). Soker & Kashi (2013) and Kashi et al. (2013) focused their discussion, in particular, on one major fluctuation, which occurred at +30 d after the 2013b maximum. In their scenario, this peak is due to interaction of the gas expelled during the merger event, with a low mass shell expelled in a previous binary interaction episode.

As LSQ13zm, SN 2009ip and (more marginally) V838 Mon show similar light-curves, the above scenario has to be considered also to explain the photometric properties of LSQ13zm. While erratic variability has been registered for SN 2009ip in the period 2009-2011 (Soker & Kashi 2013), these were not detected in the historical data of LSQ13zm. However, as mentioned in Section 6.2.1, these detection limits were not deep enough to rule out that outbursts fainter than -15 mag had occurred in the past, including eruptive mass-loss events triggered by binary interaction. On the other hand, luminosity fluctuations similar to those observed during the 2012b event in SN 2009ip are not observed during the 2013b event of LSQ13zm, whose light curve shows a monotonic decline in all bands. For this reason the binary merger scenario is less plausible for LSQ13zm, although we have to remark that our data are not sufficiently well sampled to rule out this hypothesis.

6.5.4 2013a was an eruption, 2013b the SN explosion

The most promising scenario which explains fairly well the double brightening observed in the light curve of LSQ13zm includes an initial outburst similar to those observed in some LBVs (i.e. a SN impostor), followed by the genuine SN explosion a short time later. The photometric similarity of the 2013a event with light-curves of SN impostors, viz. 1997bs (Van Dyk et al. 2000) and 2007sv (Tartaglia et al. 2015) has been remarked in Section 6.5.1 (see also top panel in Figure 6.1), and provides support to the non-terminal burst for the first brightening of LSQ13zm.

SN impostors are believed to be stellar outbursts with light-curves similar to those of genuine Type IIn SNe, though (on average) with fainter peak luminosities. As discussed in Section 1, their spectra share some similarity with those of Type IIn SNe, although they usually display a faster evolution in the continuum temperature, and weak or no evidence of multicomponent line profiles (in particular, very broad line wings). In addition, strong high-velocity α– or Fe-peak element lines typically identified in the spectra of CCSNe are not comfortably detected in those of SN impostors. Therefore, the spectra and the photometric data together give crucial information to discriminate between SNe and SN impostors.

Since we do not have any direct information on the spectroscopic properties of LSQ13zm during the 2013a event, we have to extrapolate useful information from the available light curve and the spectroscopic features of the 2013b event. If we assume that 2013b was the real SN light curve, 2013a was necessarily a pre-SN outburst. As mentioned above, a conclusive proof for establishing the SN nature of the 2013b brightening would be the detection of α– or Fe-peak nebular lines in the late spectra. However, the late spectra are contaminated by strong residual features from foreground emission and heavily affected by features produced in the ejecta-CSM interaction. This is a common issue for many interacting transients, since the signatures of the interaction usually dominate the spectral emission for months to years after the explosion, veiling the typical features of the SN ejecta during the nebular phase. Interestingly, from +16 d past-maximum, a broad Hα emission component and other shallower spectral features with blue-shifted P-Cygni components (cfr. Section 6.3.1) become prominent, and are interpreted as the first direct evidence of the underlying SN ejecta. The broad component of Hα dominates the total line flux until +67 d, when the intermediate component become preponderant over the others. The high photospheric velocities and the ions producing the broad lines in the spectrum of LSQ13zm, are normally observed in the spectra of H-rich CCSNe (see the excellent match of the +16 d spectrum of LSQ13zm with that of SN 2008es in Figure 6.5).

As a natural consequence, if the 2013b event of LSQ13zm is the real SN explosion, as suggested by the detection of broad P-Cygni lines in the spectra taken during that episode, then 2013a should be regarded as the last burp of the progenitor. In other words, the 2013a event is a luminous outburst similar to those observed in active LBVs. This conclusion is also supported by the similarity of the light-curve of the 2013a event with those of some SN impostors (Figure 6.1, top.)

6.6 Conclusions

We presented our study on the photometric and spectroscopic evolution of the optical transient LSQ13zm, that exploded in the galaxy SDSS J102654.56+195254.8, most likely a BDCG with low mass (8.65 to 8.8 Log(M/ $M_\odot$)) and a relatively low global SFR (0.025 $M_\odot$ yr^{-1}). The transient object experienced two main brightenings: the former – labelled as 2013a – reached an absolute magnitude of $M_R = -14.87 \pm 0.25$ mag, and the latter – named 2013b – with a peak magnitude of $M_R = -18.46 \pm 0.21$ mag. The multi-band light curves indicate that LSQ13zm was photometrically similar to the debated SNe 2009ip and 2010mc. In particular, the photometric properties (peak magnitude and colours) of the 2013b event of LSQ13zm are consistent with those of a true SN. On the other hand, the light-curve of the 2013a event is strikingly similar to outbursts of massive stars known as SN impostors, including its faint absolute magnitude at peak and the rapid luminosity decline.

The spectroscopic properties of the transient observed during the 2013b episode (namely,

the presence of high velocity ejecta with wings up to $\simeq 20000$ km s^{-1}), support the terminal SN explosion, most likely occurred during the 2013b event. Hence, the 2013a event can be regarded as an outburst of a massive star, likely an LBV, which occurred few weeks before the stellar core-collapse. Other considerations on the spectroscopic evolution of LSQ13zm suggest that 2012a is likely the last episode of a sequence of mass-loss events that produced as final outcome the observables of a Type IIn SN.

The lack of a clear evidence of synthetised α- or Fe-peak elements in the spectra of LSQ13zm is a common feature of Type IIn SNe and does not constitute a problem for the SN explosion of LSQ13zm. In fact, the presence of an opaque ionised CSM expelled during the latest stages of the progenitor's life frequently masks the spectral signatures of the SN ejecta.

Although most observational clues suggest that the 2013b event observed during the LSQ13zm evolution was actually a genuine CCSN explosion, we cannot definitely rule out the alternative scenarios discussed in this Chapter. We finally remark that - although LSQ13zm and SN 2009ip are photometrically very similar - they have subtle spectroscopic differences suggesting a somewhat different explosion scenarios.

References

Adamo, A. 2011, Ph.D. Thesis,

Aldering, G., Adam, G., Antilogus, P., et al. 2002, Proc. SPIE, 4836, 61

Anderson, J. P., Covarrubias, R. A., James, P. A., Hamuy, M., & Habergham, S. M. 2010, MNRAS, 407, 2660

Andrews, J. E., Gallagher, J. S., Clayton, G. C., et al. 2010, ApJ, 715, 541

Barnes, J. E., & Hernquist, L. 1992, ARA&A, 30, 705

Barbon, R., Benetti, S., Cappellaro, E., et al. 1995, A&AS, 110, 513

Baron, E., Hauschildt, P. H., & Branch, D. 1993, Bulletin of the American Astronomical Society, 25, 1348

Bell, E. F., & de Jong, R. S. 2001, ApJ, 550, 212

Bell, E. F., McIntosh, D. H., Katz, N., & Weinberg, M. D. 2003, ApJS, 149, 289

Benetti, S., Nicholl, M., Cappellaro, E., et al. 2014, MNRAS, 441, 289

Benitez, S., Hillebrandt, W., Kromer, M., et al. 2013, The Astronomer's Telegram, 4994, 1

Botticella, M. T., Pastorello, A., Smartt, S. J., et al. 2009, MNRAS, 398, 1041

Brown, N. J., Waagen, E. O., Scovil, C., et al. 2002, IAU Circ., 7785, 1

Brown, T. M., Baliber, N., Bianco, F. B., et al. 2013, PASP, 125, 1031

Buton, C., Copin, Y., Aldering, G., et al. 2013, A&A, 549, A8

Cairós, L. M., Vílchez, J. M., González Pérez, J. N., Iglesias-Páramo, J., & Caon, N. 2001, ApJS, 133, 321

Cappellaro, E. (2014). SNOoPy: a package for SN photometry, `http://sngroup.oapd.inaf.it/snoopy.html`

Chevalier, R. A., Fransson, C. 1994, ApJ, 420, 268

Chonis, T. S., & Gaskell, C. M. 2008, AJ, 135, 264

Chugai, N. N., & Danziger, I. J. 1994, MNRAS, 268, 173

Condon, J. J., Cotton, W. D., Greisen, E. W., et al. 1998, AJ, 115, 1693

Crause, L. A., Lawson, W. A., Kilkenny, D., et al. 2003, MNRAS, 341, 785

Damineli, A. 1996, ApJ, 460, L49

Dessart, L., Hillier, D. J., Gezari, S., Basa, S., & Matheson, T. 2009, MNRAS, 394, 21

Di Carlo, E., Massi, F., Valentini, G., et al. 2002, ApJ, 573, 144

Dilday, B., Howell, D. A., Cenko, S. B., et al. 2012, Science, 337, 942

Djorgovski, S. G., Drake, A., A. Mahabal, Graham M., Donalek, C., Williams, R., Beshore, E., Larson, S., Prieto, J., Catelan, M., Christensen, E., McNaught, R. 2012: The Catalina Real-Time Transient Survey (CRTS). In: The First Year of MAXI: Monitoring Variable X-ray Sources, eds. T. Mihara, M. Serino, Special Publ. IPCR-127, p. 263, Tokyo: RIKEN

Drake, A. J., Djorgovski, S. G., Mahabal, A., et al. 2009, ApJ, 696, 870

Drake, A. J., Djorgovski, S. G., Prieto, J. L., et al. 2010, ApJ, 718, L127

Fanelli, M. N., O'Connell, R. W., & Thuan, T. X. 1988, ApJ, 334, 665

Fassia, A., Meikle, W. P. S., Vacca, W. D., et al. 2000, MNRAS, 318, 1093

Fassia, A., Meikle, W. P. S., Chugai, N., et al. 2001, MNRAS, 325, 907

Filippenko, A. V. 1997, ARA&A, 35, 309

Firth, R. E., Sullivan, M., Gal-Yam, A., et al. 2015, MNRAS, 446, 3895

Fisher, A., Branch, D., Nugent, P., & Baron, E. 1997, ApJ, 481, L89

Foley, R. J., Smith, N., Ganeshalingam, M., et al. 2007, ApJ, 657, L105

Foley, R. J., Berger, E., Fox, O., et al. 2011, ApJ, 732, 32

Fransson, C., Chevalier, R. A., Filippenko, A. V., et al. 2002, ApJ, 572, 350

Fraser, M., Inserra, C., Jerkstrand, A., et al. 2013a, MNRAS, 433, 1312

Fraser, M., Magee, M., Kotak, R., et al. 2013b, ApJ, 779, L8

Fraser, M., Kotak, R., Pastorello, A., et al. 2015, MNRAS, 453, 3886

Gal-Yam, A., Leonard, D. C., Fox, D. B., et al. 2007, ApJ, 656, 372

Gal-Yam, A., Leonard, D. C. 2009, Nature, 458, 865

Gal-Yam, A., Kasliwal, M. M., Arcavi, I., et al. 2011, ApJ, 736, 159

Gal-Yam, A. 2012, Science, 337, 927

Georgy, C., Ekström, S., Meynet, G., et al. 2012, A&A, 542, A29

Gezari, S., Halpern, J. P., Grupe, D., et al. 2009, ApJ, 690, 1313

Graham, M. L., Sand, D. J., Valenti, S., et al. 2014, ApJ, 787, 163

Groh, J. H., Hillier, D. J., Damineli, A., et al. 2009, ApJ, 698, 1698

Groh, J. H., Meynet, G., & Ekström, S. 2013, A&A, 550, L7

Guinan, E. F., Marshall, J., & McCook, G. P. 1993, Bulletin of the American Astronomical Society, 25, 1349

Haro, G. 1956, Boletin de los Observatorios Tonantzintla y Tacubaya, 2, 8

Harutyunyan, A. H., Pfahler, P., Pastorello, A., et al. 2008, A&A, 488, 383

Heger, A., Fryer, C. L., Woosley, S. E., Langer, N., & Hartmann, D. H. 2003, ApJ, 591, 288

Humphreys, R. M., & Davidson, K. 1994, PASP, 106, 1025

Humphreys, R. M., Davidson, K., Jones, T. J., et al. 2012, ApJ, 760, 93

Inserra, C., Turatto, M., Pastorello, A., et al. 2011, MNRAS, 417, 261

Inserra, C., Turatto, M., Pastorello, A., et al. 2012, MNRAS, 422, 1122

Izotov, Y. I., Guseva, N. G., Fricke, K. J., & Henkel, C. 2015, MNRAS, 451, 2251

Kankare, E., Kotak, R., Pastorello, A., et al. 2015, A&A, 581, L4

Kashi, A., & Soker, N. 2010, ApJ, 723, 602

Kashi, A., Soker, N., & Moskovitz, N. 2013, MNRAS, 436, 2484

Kennicutt, R. C., Jr. 1998, ARA&A, 36, 189

Kiewe, M., Gal-Yam, A., Arcavi, I., et al. 2012, ApJ, 744, 10

Kimeswenger, S., Lederle, C., Schmeja, S., & Armsdorfer, B. 2002, MNRAS, 336, L43

Kipper, T., Klochkova, V. G., Annuk, K., et al. 2004, A&A, 416, 1107

Kroupa, P. 2002, Science, 295, 82

Justham, S., Podsiadlowski, P., & Vink, J. S. 2014, ApJ, 796, 121

Law, N. M., Kulkarni, S. R., Dekany, R. G., et al. 2009, PASP, 121, 1395

Levesque, E. M., Stringfellow, G. S., Ginsburg, A. G., Bally, J., & Keeney, B. A. 2014, AJ, 147, 23

Margutti, R., Milisavljevic, D., Soderberg, A. M., et al. 2014, ApJ, 780, 21

Martin, J. C., Hambsch, F.-J., Margutti, R., et al. 2015, AJ, 149, 9

Matheson, T., Filippenko, A. V., Chornock, R., Leonard, D. C., & Li, W. 2000, AJ, 119, 2303

Mauerhan, J. C., Smith, N., Filippenko, A. V., et al. 2013a, MNRAS, 430, 1801

Mauerhan, J. C., Smith, N., Silverman, J. M., et al. 2013b, MNRAS, 431, 2599

Mauerhan, J., Williams, G. G., Smith, N., et al. 2014, MNRAS, 442, 1166

Mauerhan, J. C., Van Dyk, S. D., Graham, M. L., et al. 2015, MNRAS, 447, 1922

Moriya, T. J. 2015, ApJ, 803, L26

Miller, A. A., Chornock, R., Perley, D. A., et al. 2009, ApJ, 690, 1303

Munari, U., Henden, A., Kiyota, S., et al. 2002, A&A, 389, L51

Ofek, E. O., Rabinak, I., Neill, J. D., et al. 2010, ApJ, 724, 1396

Ofek, E. O., Sullivan, M., Cenko, S. B., et al. 2013a, Nature, 494, 65

Ofek, E. O., Lin, L., Kouveliotou, C., et al. 2013b, ApJ, 768, 47

Ofek, E. O., Sullivan, M., Shaviv, N. J., et al. 2014a, ApJ, 789, 104

Ofek, E. O., Arcavi, I., Tal, D., et al. 2014b, ApJ, 788, 154

Pastorello, A., Zampieri, L., Turatto, M., et al. 2004, MNRAS, 347, 74

Pastorello, A., Sauer, D., Taubenberger, S., et al. 2006, MNRAS, 370, 1752

Pastorello, A., Smartt, S. J., Mattila, S., et al. 2007a, Nature, 447, 829

Pastorello, A., Della Valle, M., Smartt, S. J., et al. 2007b, Nature, 449, 1

Pastorello, A., Quimby, R. M., Smartt, S. J., et al. 2008, MNRAS, 389, 131

Pastorello, A., Valenti, S., Zampieri, L., et al. 2009a, MNRAS, 394, 2266

Pastorello, A., Smartt, S. J., Botticella, M. T., et al. 2010a, ApJ, 724, L16

Pastorello, A., Botticella, M. T., Trundle, C., et al. 2010b, MNRAS, 408, 181

Pastorello, A., Stanishev, V., Smartt, S. J., Fraser, M.; Lindborg, M. 2011, CBET, 2851, 2

Pastorello, A., Cappellaro, E., Inserra, C., et al. 2013, ApJ, 767, 1

Pastorello, A., Hadjiyska, E., Rabinowitz, D., et al. 2015, MNRAS, 449, 1954

Peng, C. Y., Ho, L. C., Impey, C. D., & Rix, H.-W. 2010, AJ, 139, 2097

Pilyugin, L. S., Contini, T., & Vílchez, J. M. 2004, A&A, 423, 427

Prieto, J. L., McMillan, R., Bakos, G., & Grennan, D. 2011, Central Bureau Electronic Telegrams, 2903, 1

Prieto, J. L., Brimacombe, J., Drake, A. J., & Howerton, S. 2013, ApJ, 763, L27

Pumo, M. L., Turatto, M., Botticella, M. T., et al. 2009, ApJl, 705, L138

Rau, A., Kulkarni, S. R., Law, N. M., et al. 2009, PASP, 121, 1334

Roming, P. W. A., Pritchard, T. A., Prieto, J. L., et al. 2012, ApJ, 751, 92

Rosa-González, D., Terlevich, E., & Terlevich, R. 2002, MNRAS, 332, 283

Schlafly, E. F., & Finkbeiner, D. P. 2011, ApJ, 737, 103

Schlegel, E. M. 1990, MNRAS, 244, 269

Smith, N., Vink, J. S., & de Koter, A. 2004, ApJ, 615, 475

Smith, N., & Owocki, S. P. 2006, ApJ, 645, L45

Smith, N., Miller, A., Li, W., et al. 2010, AJ, 139, 1451

Smith, N., & Frew, D. J. 2011, MNRAS, 415, 2009

Smith, N., Li, W., Miller, A. A., et al. 2011a, ApJ, 732, 63

Smith, N., Li, W., Silverman, J. M., Ganeshalingam, M., & Filippenko, A. V. 2011b, MNRAS, 773

Smith, N., Mauerhan, J. C., Kasliwal, M. M., & Burgasser, A. J. 2013, MNRAS, 434, 2721

Smith, N., Mauerhan, J. C., & Prieto, J. L. 2014, MNRAS, 438, 1191

Smith, N., & Arnett, W. D. 2014, ApJ, 785, 82

Soker, N., & Tylenda, R. 2003, ApJ, 582, L105

Soker, N., & Tylenda, R. 2006, MNRAS, 373, 733

Soker, N., & Kashi, A. 2013, ApJ, 764, L6

Stritzinger, M., Taddia, F., Fransson, C., et al. 2012, ApJ, 756, 173

Taddia, F., Sollerman, J., Fremling, C., et al. 2015, arXiv:1505.04719

Tartaglia, L., Pastorello, A., Taubenberger, S., et al. 2015, MNRAS, 447, 117

Tominaga, N., Limongi, M., Suzuki, T., et al. 2008, ApJ, 687, 1208

Trundle, C., Kotak, R., Vink, J. S., & Meikle, W. P. S. 2008, A&A, 483, L47

Turatto, M., Cappellaro, E., Danziger, I. J., et al. 1993a, MNRAS, 262, 128

Turatto, M., Cappellaro, E., Benetti, S., & Danziger, I. J. 1993b, MNRAS, 265, 471

Tylenda, R. 2005, A&A, 436, 1009

Valenti, S., Pastorello, A., Cappellaro, E., et al. 2009, Nature, 459, 674

van den Bergh, S. 1960, ApJ, 131, 215

Van Dyk, S. D., Peng, C. Y., King, J. Y., et al. 2000, PASP, 112, 1532

Wagner, R. M., Vrba, F. J., Henden, A. A., et al. 2004, PASP, 116, 326

Wang, L., Howell, D. A., Höflich, P., & Wheeler, J. C. 2001, ApJ, 550, 1030

Wolf, B. 1989, A&A, 217, 87

Woosley, S. E., Blinnikov, S., & Heger, A. 2007, Nature, 450, 390

Zwicky, F., Herzog, E., Wild, P., Karpowicz, M., & Kowal, C. T. 1961, Pasadena: California Institute of Technology (CIT), |c1961

Wright, E. L. 2006, PASP, 118, 1711

Levesque, E. M., Stringfellow, G. S., Ginsburg, A. G., Bally, J., & Keeney, B. A. 2014, AJ, 147, 23

Appendix

6.A [O III] lines in the spectra of LSQ13zm

Figure 6.A.1 shows a zoom-in of the Hα/S II region and of the Hβ/[O III] region in the last +579 d two-dimensional spectrum. The narrow Hα component, as well as the [O III] doublet, have clearly a broader spatial extension than the SN emission region. We believe that these lines are not related to the SN CSM, but are part of the strong flux-contamination of the host galaxy.

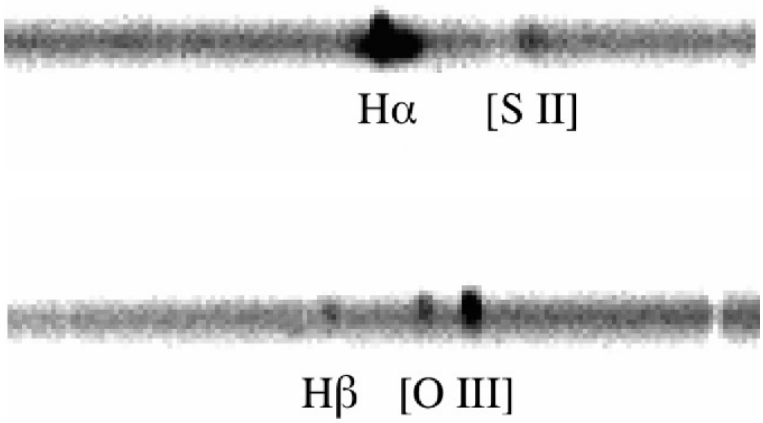

Figure 6.A.1: Zoom-in of the Hα and O III/ Hβ regions of the two-dimensional +579 d spectrum.

6.B Photometric data of LSQ13zm

Table 6.B.1: BVR light-curves starting from the first 2013a event detection.

Date	MJD	B(err)	V(err)	R(err)	Instrument
20130318	56369.11	–	–	21.79(0.25)	QUEST
20130318	56369.16	–	–	>20.9	CFH12K
20130319	56370.15	–	–	21.10(0.65)	SI 600-277
20130319	56370.30	–	–	>21.0	CFH12K
20130320	56371.10	–	–	21.64(0.26)	QUEST
20130321	56372.17	–	–	>19.4	CFH12K
20130322	56373.06	–	–	21.64(1.01)	QUEST
20130322	56373.28	–	–	>20.8	CFH12K
20130328	56379.12	–	–	20.99(0.64)	QUEST

Table 6.B.1 Continued

Date	MJD	B(err)	V(err)	R(err)	Instrument
20130330	56381.07	–	–	20.74(0.14)	QUEST
20130331	56382.17	–	–	20.65(0.19)	CFH12K
20130401	56383.07	–	–	20.60(0.14)	QUEST
20130402	56384.26	–	–	19.65(0.44)	SI 600-277
20130403	56385.07	–	–	20.89(0.12)	QUEST
20130404	56386.17	–	–	20.98(0.25)	CFH12K
20130405	56387.06	–	–	21.09(0.15)	QUEST
20130405	56387.22	–	–	21.05(0.26)	CFH12K
20130407	56389.05	–	–	21.27(0.16)	QUEST
20130408	56390.29	–	–	19.73(0.10)	CFH12K
20130409	56391.01	–	–	19.09(0.03)	QUEST
20130411	56393.24	–	–	18.34(0.03)	CFH12K
20130412	56394.30	–	–	18.08(0.02)	CFH12K
20130412	56394.99	–	–	18.09(0.01)	QUEST
20130413	56395.08	–	–	18.05(0.01)	QUEST
20130414	56396.21	–	–	17.74(0.02)	CFH12K
20130416	56398.29	–	–	17.52(0.20)	SI 600-277
20130419	56401.30	17.48(0.01)	17.47(0.01)	17.36(0.01)	SNIFS
20130424	56406.26	–	–	17.06(0.04)	SI 600-386
20130424	56406.38	17.20(0.05)	17.18(0.05)	17.01(0.05)	SNIFS
20130501	56413.77	17.56(0.03)	17.38(0.02)	17.21(0.04)	Zeiss-1000
20130502	56414.77	–	17.46(0.14)	–	SCORPIO
20130502	56414.78	17.67(0.03)	17.45(0.01)	17.27(0.01)	Zeiss-1000
20130503	56415.17	–	–	17.38(0.21)	SI 600-277
20130504	56416.20	–	–	17.51(0.02)	CFH12K
20130505	56417.21	–	–	17.61(0.02)	CFH12K
20130508	56420.13	18.32(0.05)	18.01(0.04)	17.83(0.14)	Alta
20130510	56422.76	18.42(0.03)	18.08(0.06)	18.00(0.25)	SCORPIO
20130521	56433.20	–	–	18.85(0.07)	CFH12K
20130530	56442.11	>18.9	–	–	Alta
20130603	56446.18	–	–	19.36(0.21)	SI 600-277
20130607	56450.88	–	–	>19.3	AFOSC
20130608	56451.79	–	20.05(0.05)	19.51(0.21)	SCORPIO
20130609	56452.30	19.74(0.28)	–	–	Spectral Camera
20130610	56453.19	–	–	19.39(0.00)	SI 600-277
20130627	56470.87	>18.2	–	–	RATCam
20131208	56634.17	–	–	>19.9	AFOSC
20131212	56638.06	–	–	>20.2	AFOSC
20131218	56644.17	>20.4	>19.9	–	IO:O

AFOSC: 1.82 m Telescopio Copernico with AFOSC.
SNIFS: 2.2 m telescope of the University of Hawaii with SNIFS.
SCORPIO: 6 m Bolshoi Teleskop Alt-azimutalnyi (BTA) with SCORPIO
Zeiss-1000: 1 m Zeiss-1000 telescope.
QUEST: 60" ESO Schmidt Telescope of the La Silla Quest (LSQ) survey with QUEST.
SI 300-386: 1.5 m Cassegrain reflector of the Mt. Lemmon Survey (MLS) with SI 300-386.
SI 600-277: 0.7 m Schmidt telescope of the Catalina Sky Survey (CSS) with SI 600-277.
CFH12K: 1.2 m Samuel Oschin Telescope of the Intermediate Palomar Transient Factory (iPTF) with CFH12K.
Spectral Camera: LCOGT 2.0-m Faulkes North Telescope.
IO:O: 2 m Liverpool Telescope with IO:O.
Alta: 20" telescope of the UIS Barber Research Observatory with an Alta U42 CCD Camera.

Table 6.B.2: *griz* light-curves.

Date	MJD	g(err)	r(err)	i(err)	z(err)	Instrument
20130419	56401.30	17.40(0.01)	17.52(0.01)	17.67(0.01)	–	SNIFS
20130424	56406.38	17.11(0.05)	17.22(0.05)	17.35(0.05)	–	SNIFS
20130427	56409.24	17.10(0.03)	17.18(0.03)	17.32(0.06)	17.36(0.15)	Spectral Camera
20130428	56410.25	17.20(0.02)	17.18(0.03)	17.36(0.06)	17.50(0.09)	Spectral Camera
20130429	56411.24	17.17(0.04)	17.20(0.04)	17.36(0.06)	17.54(0.12)	Spectral Camera
20130430	56412.24	17.30(0.04)	17.30(0.05)	17.42(0.05)	17.54(0.14)	Spectral Camera
20130502	56414.34	–	17.34(0.03)	17.42(0.03)	17.49(0.30)	Spectral Camera
20130503	56415.32	17.57(0.03)	17.50(0.04)	17.53(0.03)	17.70(0.19)	Spectral Camera
20130504	56416.27	17.68(0.04)	17.56(0.04)	17.62(0.04)	17.66(0.10)	Spectral Camera
20130520	56432.15	19.47(0.06)	19.09(0.08)	19.17(0.12)	–	SBIG
20130524	56436.26	19.50(0.16)	19.27(0.08)	19.21(0.07)	19.35(0.24)	Spectral Camera
20130527	56439.35	>19.4	–	>19.2	–	Spectral Camera
20130529	56441.15	19.87(0.17)	19.38(0.08)	–	–	SBIG
20130529	56441.15	–	–	>19.1	–	SBIG
20130605	56448.16	>19.5	–	–	–	SBIG
20130607	56450.88	–	–	>19.4	–	AFOSC
20130607	56450.31	–	19.54(0.11)	19.62(0.16)	–	Spectral Camera
20130607	56450.31	>19.4	–	–	>19.0	Spectral Camera
20130609	56452.30	–	–	>18.7	–	Spectral Camera
20130613	56456.27	–	19.88(0.17)	19.74(0.15)	–	Spectral Camera
20130613	56456.27	>19.9	–	–	–	Spectral Camera
20130625	56468.88	–	–	–	19.78(0.33)	RATCam
20130625	56468.88	–	>19.9	>19.2	–	RATCam
20131123	56619.17	–	22.20(0.35)	–	–	IO:O
20131125	56621.22	–	22.23(0.40)	–	–	IO:O
20131129	56625.21	22.54(0.29)	22.22(0.18)	21.18(0.16)	21.57(0.19)	ACAM
20131208	56634.20	–	–	21.38(0.61)	–	AFOSC
20131212	56638.09	–	–	>20.2	–	AFOSC
20140202	56690.26	23.16(0.27)	23.30(0.18)	–	–	OSIRIS
12341234	56688.00	–	–	–	23.65(0.40)	OSIRIS
20140205	56693.21	–	–	23.59(0.12)	23.79(0.36)	OSIRIS

AFOSC: 1.82 m Telescopio Copernico with AFOSC.
SBIG: LCOGT 1.0-m telescope at McDonald Observatory (Texas, USA) equipped with an SBIG camera.
Spectral Camera: 2.0-m FSTN + FLOYDS.
SNIFS: 2.2 m telescope of the University of Hawaii with SNIFS.
IO:O, RATCam: 2 m Liverpool Telescope with IO:O and RATCam.
OSIRIS: 10.4 m Gran Telescopio Canarias (GTC) with OSIRIS.
ACAM: 4.2 m William Herschel Telescope (WHT) with ACAM.

Table 6.B.3: JHK light-curves.

Date	MJD	J(err)	H(err)	K(err)	Instrument
20130421	56403.99	17.18(0.42)	16.94(0.28)	–	REMIR
20130422	56404.01	–	–	>15.0	REMIR
20130423	56405.98	>16.1	>16.2	>15.0	REMIR
20130425	56407.93	16.63(0.07)	16.34(0.07)	16.054(0.32)	NOTCam
20130426	56408.06	16.54(0.30)	16.28(0.30)	>15.0	REMIR
20130430	56412.11	16.77(0.20)	16.39(0.45)	>15.0	REMIR
20130503	56415.07	–	>16.4	>14.6	REMIR
20130504	56416.97	17.38(0.38)	16.87(0.29)	>15.6	REMIR
20130506	56418.04	17.37(0.47)	>16.9	>15.0	REMIR
20130526	56438.98	18.10(0.20)	17.66(0.17)	17.514(0.15)	NOTCam
20130623	56466.90	18.91(0.18)	18.51(0.19)	18.233(0.13)	NOTCam
20131224	56650.07	19.06(0.20)	18.61(0.27)	18.696(0.25)	NICS

REMIR: 0.6 m Rapid Eye Mount (REM) telescope with REMIR.
NOTCam: 2.56 m Nordic Optical Telescope (NOT) with NOTCam.
NICS: 3.58 m Telescopio Nazionale Galileo (TNG) with NICS.

6.C Photometric limits of LSQ13zm

Table 6.C.1: R-band detection limits of LSQ13zm prior to the 2013a event. The transient was not detected at any reported epoch in the table.

Date	MJD	R	Instrument
20040128	53032.26	>21.2	SI 600-277
20050109	53379.35	>20.4	SI 600-277
20060104	53739.41	>20.5	SI 600-277
20070110	54110.46	>20.9	SI 600-277
20070314	54173.30	>20.3	SI 600-386
20080111	54476.37	>20.8	SI 600-277
20080302	54527.40	>20.1	SI 600-386
20081029	54768.49	>20.3	SI 600-386
20090102	54833.39	>21.1	SI 600-277
20090131	54862.31	>20.5	SI 600-386
20090302	54892.27	>20.3	SI 600-386
20090517	54968.19	>20.4	SI 600-386
20090930	55104.53	>18.7	CFH12K
20091003	55107.52	>20.1	CFH12K
20091016	55120.52	>20.9	CFH12K
20091022	55126.49	>20.9	CFH12K
20091031	55135.51	>20.8	CFH12K
20091103	55138.46	>20.2	CFH12K
20091107	55142.45	>20.6	CFH12K
20091116	55151.44	>20.9	CFH12K
20091218	55183.35	>20.7	CFH12K
20091230	55195.50	>19.7	CFH12K
20100106	55202.47	>19.9	CFH12K
20100108	55204.53	>18.9	CFH12K
20100111	55207.48	>21.4	CFH12K
20100115	55211.55	>20.6	CFH12K
20100125	55221.23	>20.8	CFH12K
20100129	55225.29	>18.3	CFH12K
20100209	55236.26	>20.6	SI 600-277
20100216	55243.54	>20.9	CFH12K

Table 6.C.1 Continued

Date	MJD	R	Instrument
20100217	55244.31	>21.5	CFH12K
20100219	55246.49	>20.8	CFH12K
20100223	55250.53	>20.7	CFH12K
20100224	55251.15	>18.8	CFH12K
20100313	55268.49	>20.6	CFH12K
20100315	55270.18	>21.3	CFH12K
20101113	55513.47	>20.8	CFH12K
20101114	55514.51	>21.0	CFH12K
20101115	55515.55	>21.0	CFH12K
20101116	55516.46	>21.3	CFH12K
20101117	55517.46	>21.1	CFH12K
20101118	55518.46	>21.6	CFH12K
20101119	55519.48	>19.5	CFH12K
20101130	55530.44	>20.5	CFH12K
20101201	55531.45	>22.0	CFH12K
20101202	55532.53	>21.4	CFH12K
20101205	55535.43	>20.5	CFH12K
20101207	55537.38	>20.9	CFH12K
20101208	55538.42	>21.4	CFH12K
20101209	55539.50	>21.4	CFH12K
20101211	55541.52	>21.2	CFH12K
20101213	55543.53	>21.4	CFH12K
20101231	55561.36	>20.9	CFH12K
20110102	55563.39	>21.4	SI 600-277
20110111	55572.27	>20.7	CFH12K
20110112	55573.39	>21.3	CFH12K
20110113	55574.43	>21.5	CFH12K
20110114	55575.41	>21.4	CFH12K
20110115	55576.43	>20.5	CFH12K
20110116	55577.45	>20.6	CFH12K
20110117	55578.45	>20.8	CFH12K
20110118	55579.46	>20.9	CFH12K
20110119	55580.54	>20.4	CFH12K
20110124	55585.37	>20.7	CFH12K
20110125	55586.38	>21.1	CFH12K
20110126	55587.46	>20.8	CFH12K
20110128	55589.26	>20.9	CFH12K
20110129	55590.33	>21.5	CFH12K
20110130	55591.36	>19.5	CFH12K
20110201	55593.43	>21.3	CFH12K
20110209	55601.25	>20.5	CFH12K
20110211	55603.25	>22.1	CFH12K
20110212	55604.26	>21.0	CFH12K
20110213	55605.28	>21.1	CFH12K
20110214	55606.33	>17.9	CFH12K
20110216	55608.26	>20.9	CFH12K
20110222	55614.43	>20.9	CFH12K
20110315	55635.15	>20.9	CFH12K
20110417	55668.25	>20.9	CFH12K
20120118	55944.36	>21.1	SI 600-277
20120316	56002.29	>20.5	SI 600-386
20120407	56024.01	>20.7	QUEST
20120409	56026.05	>21.3	QUEST
20120507	56055.00	>21.6	QUEST
20121223	56284.48	>20.2	SI 600-386
20130106	56298.29	>20.2	SI 600-277
20130117	56309.46	>19.7	SI 600-277
20130201	56324.35	>20.9	CFH12K
20130202	56325.26	>19.8	SI 600-277

Table 6.C.1 Continued

Date	MJD	R	Instrument
20130204	56327.38	>20.9	CFH12K
20130205	56328.27	>21.6	CFH12K
20130206	56329.24	>19.4	CFH12K
20130206	56329.36	>19.8	SI 600-277
20130207	56330.28	>21.5	CFH12K
20130301	56352.42	>19.7	SI 600-277
20130303	56354.24	>19.6	CFH12K
20130304	56355.28	>21.3	CFH12K
20130305	56356.26	>21.5	CFH12K
20130306	56357.23	>21.3	CFH12K
20130311	56362.21	>21.3	CFH12K
20130311	56362.31	>20.3	SI 600-386
20130312	56363.26	>21.5	CFH12K
20130313	56364.22	>21.4	CFH12K
20130316	56367.17	>21.6	CFH12K
20130317	56368.16	>21.1	CFH12K

SI 600-277: 0.7 m Schmidt telescope of the Catalina Sky Survey (CSS) with SI 600-277
SI 300-386: 1.5 m Cassegrain reflector of the Mt. Lemmon Survey (MLS) with SI 300-386
CFH12K: 1.2 m Samuel Oschin Telescope of the Intermediate Palomar Transient Factory (iPTF) with CFH12K
QUEST: 60" ESO Schmidt Telescope of the La Silla Quest (LSQ) survey with QUEST.

Chapter 7

Conclusions

In the last two decades, thanks to the significant improvements in the available technology and observational tools, our understanding on the variety of SNe and, more in general, stellar outbursts has significantly grown. As a consequence, the interest of the astronomical community has focused on new types of stellar explosions. In fact, as a major product of the currently running panoramic surveys, the discovery of new types of transient events that are challenging the existing stellar evolutionary models should be remarked. Many new transients, in particular, show unprecedented observational characteristics and cannot be comfortable explained with traditional explosion channels, hence requiring the development of novel explosion models.

Interacting SNe spanning a huge luminosity range and SN impostors are among the most interesting products of these new unbiased surveys. SN impostors have been constrained in a new class of stellar explosions in relatively recent times (Van Dyk et al. 2000), and have been shown to be luminous, single or repeated outbursts experienced by massive stars that - under particular circumstances - may mimic the "true" SN behavior.

Both interacting SNe and SN impostors are related to the enormous mass-loss experienced by the very massive progenitor stars in the latest stages of their life. Although large mass-loss can be produced via binary interaction, also large eruptions in very massive stars can accumulate dense and massive circumstellar environments. The mechanisms triggering these major eruptions are still unknown, and only marginally explored by the theory.

In this thesis, the two SN impostors 2007sv and PSN J09132750+7627410 and the Type IIn SN LSQ13zm have been presented.

The analysis of 2007sv, which we proved to be the major outburst experienced by a massive LBV, supported our claim that the discrimination between genuine SNe and SN impostors is not always an easy task (Chapter 4). Some impostors, in fact, appear very similar to Type IIn SNe, showing both spectroscopic and photometric features cloning those of genuine SNe. Nonetheless, as discussed in a recent paper (Tartaglia et al. 2015), a number of combined indicators, including the absolute peak magnitudes, the inferred temperatures of the pseudo-photospheres and the FWHM velocities of the ejecta, can provide the required clues. Detailed long-term photometric and spectroscopic campaigns are therefore needed to safely discriminate between SNe and SN impostors in such cases.

A number of spectroscopic properties (namely the presence of prominent H lines with inferred FWHM velocities comparable with those of LBV winds in their spectra) suggest a

strong connection between SN impostors and LBVs. However, recent observational evidences have suggested that even stars less massive than LBVs can produce SN impostors. SNhunt248 (Mauerhan et al. 2015; Kankare et al. 2015) has been proved to be an eruption of a cool hypergiant. In addition, the 2004 outburst that heralded the Type Ibn SN 2006jc (Foley et al. 2007; Pastorello et al. 2007) was likely produced by a WR stars with a residual LBV-like instability. In this context, we have analysed the case of PSN J09132750+7627410 (Chapter 5). Its peak luminosity was compatible with those usually encountered during giant outbursts of very massive stars, with an r-band absolute magnitude at peak of $M_r = -13.60 \pm 0.19$ mag and spectra showing prominent Balmer lines in emission with sharp and narrow P Cyg profiles at any phases of the spectroscopic evolution. Two distinct absorption features were also observed in our higher resolution spectra, suggesting the presence of two shells expanding with different velocities. The most important result of this study is that the analysis of archival HST images resulted in the detection of a quiescent stellar precursor, which was likely a ~ 20 $M_\odot$ white supergiant. This finding supports the claim of Smith et al. (2011), that the mass range of stars susceptible to giant eruptions extends below the LBV typical values.

The above mentioned SN 2006jc has also opened a new window on our understanding of the final fate of massive stars, since its progenitor was the first star that was directly observed to experience a major outburst before finally exploding as a SN. Since then, a growing number of interacting SNe have been observed to be heralded by major optical outbursts occurred weeks to years before their terminal explosion (Mauerhan et al. 2013; Ofek et al. 2013). This findings suggest that massive stars (more frequently LBV, buts occasionally also other stellar types, see Section 5) are very unstable in their late phases. The main consequence is that SN impostors may surprisingly be considered as a sort of joining link between massive stars and SNe (specifically, Type IIn and Type Ibn events). In Chapter 6 we have presented the controversial case of LSQ13zm, which is similar in many properties to the well-studied SN 2009ip (Mauerhan et al. 2013; Pastorello et al. 2013; Margutti et al. 2014; Smith et al. 2014). This object showed two main brightenings in 2013, that we labelled 2013a,b following the example of SN 2009ip (Pastorello et al. 2013). In particular, the light-curve of the 2013a event strongly resembles SN impostor outbursts, from the faint absolute magnitude at peak ($M_R = -14.87 \pm 0.25$ mag) to the rapid luminosity decline, while the peak of 2013b event ($M_R = -18.46 \pm 0.21$ mag) is consistent with those of genuine CCSNe. Moreover, the spectroscopic analysis of the 2013b event revealed the presence of high velocity ejecta with wings up to $\simeq 20000$ km s^{-1} up to ~ 44 d after the main maximum, favouring the scenario in which the terminal SN explosion occurred ~ 3 weeks after the major outburst of a very massive star.

A lot of work still needs to be done to improve our knowledge on the mechanisms triggering luminous stellar outbursts and major eruptions. So far, little efforts have been devoted to properly modeling instabilities occurring in the late stages of life of massive stars. A lot of observational time also needs to be spent to clarify why SN impostors display a such huge variety of properties, as well as whether this heterogeneity is somewhat connected with the different stellar parameters (mass, radius, chemical composition, rotation, binarity). Only the discovery of a large number of similar transients, extensive follow-up campaigns in a wide wavelength range, and the availability of rich archives with deep images at different domains will allow us to give more robust conclusions on these open issues.

Major improvements are expected when the new generation of telescopes will be operative. The Large Synoptic Survey Telescope (LSST; see *LSST Science Book 2009*), is expected to start operations on 2021-2022. It will survey the entire Southern sky every a few nights. Thanks to its large diameter (8.2 m), its effective field of view (9.6 square degrees), and the

multiple survey strategies, it will have a primary role in the study of the transient sky. The survey will discover new types of transients, and will largely increase the existing samples. During operations, it will provide well-sampled light curves for young objects to redshift $z \simeq 1$.

More detailed information on the explosion sites will be provided by high spatial resolution images from the existing telescopes and from the future 39 m European Extremely Large Telescope (E-ELT). Thanks to its huge diameter and the fully adaptive and diffraction-limited optics, it will gather much more light and spatial resolution than any existing ground based (or even space) telescope. This will allow us to inspect in detail the environments of transient events, to monitor the intrinsically faintest objects, and to study SN and impostors to very high redshifts.

Additional key information will be given by the next generation of space telescopes, in particular those operating at different domains than the optical window. In particular, the 6.5 m mirror of the James Webb Space Telescope will provide infrared images with unprecedented quality, depths and spatial resolution and will allow us to detect and study transients even in dusty regions of the host galaxies. With these new instruments, we will largely improve our understanding on the physics that determines the latest moments of the life of stars, how the different stellar types are related to the different transients, and which is the role of the environment in the fate of stars. Finally, we will understand how the rates of the different types of stellar transients (including interacting SNe and impostors) depend on the redshift.

References

Foley, R. J., Smith, N., Ganeshalingam, M., et al. 2007, ApJ, 657, L105

Kankare, E., Kotak, R., Pastorello, A., et al. 2015, A&A, 581, L4

Margutti, R., Milisavljevic, D., Soderberg, A. M., et al. 2014, ApJ, 780, 21

Mauerhan, J. C., Smith, N., Filippenko, A. V., et al. 2013, MNRAS, 430, 1801

Mauerhan, J. C., Van Dyk, S. D., Graham, M. L., et al. 2015, MNRAS, 447, 1922

Ofek, E. O., Lin, L., Kouveliotou, C., et al. 2013, ApJ, 768, 47

Pastorello, A., Cappellaro, E., Inserra, C., et al. 2013, ApJ, 767, 1

Pastorello, A., Smartt, S. J., Mattila, S., et al. 2007, Nature, 447, 829

Smith, N., Li, W., Silverman, J. M., Ganeshalingam, M., & Filippenko, A. V. 2011, MNRAS, 415, 773

Smith, N., Mauerhan, J. C., & Prieto, J. L. 2014, MNRAS, 438, 1191

Tartaglia, L., Pastorello, A., Taubenberger, S., et al. 2015, MNRAS, 447, 117

Van Dyk, S. D., Peng, C. Y., King, J. Y., et al. 2000, PASP, 112, 1532